KOCAELI JOURNAL OF SCIENCE AND ENGINEERING

Kocaeli University

Kocaeli Journal of Science and Engineering

http://dergipark.org.tr/kojose

Development of a Neural Network Model for Recognizing Red Palm Weevil Insects Based on Image Processing

Radhwan Ali Abdulghani SALEH [1, *] (iD) , H.Metin ERTUNÇ [2] (iD)

[1] Department of Mechatronics Engineering, Kocaeli University, Kocaeli, 41380, Turkey, **ORCID:** 0000-0001-9945-3672
[2] Department of Mechatronics Engineering, Kocaeli University, Kocaeli, 41380, Turkey, **ORCID:** 0000-0003-1874-3104

Abstract

The red palm weevil (RPW) is an invasive pest insect that attacks palm trees and threatens their existence. Accordingly, RPW causes significant and massive economic losses during the last two decades. This issue makes the early detection of RPW is a hot research topic. This study proposes a machine learning technique based on image processing to easily recognize these insect species for people who do not know them. The basic idea of the proposed research is to develop a neural network model that can use image processing to identify RPW and distinguish it from other insects found in palm tree habitats. This model consists of three stages: image pre-processing (image enhancement and segmentation using Otsu's thresholding), feature extraction (texture and color moments features), and classification (artificial neural network). The dataset used in this study includes 913 images, where 448 are RPWs' images, and the rest are ants' images. The experimental results of the ten-fold cross-validation show that the accuracy of the proposed model is 92.22%.

1. Introduction

Many pests have adverse effects on plants, where some of them may damage the trees and cause many losses in agriculture production. This fact leads to economic loss and high rates of poverty. Although various kinds of pests infest trees, such as bacteria, viruses, insects, and harmful parasites, the Red Palm Weevil (RPW) is one of the most destructive insects in infested trees. RPW is considered a global disease, destroying trees, raising the temperature of the tree, and creating water stress. It places the eggs inside the tree trunk, continues to feed on the tree's tissue, and starts moving into it until the tree dies, then moves onto the following plants. It is not easy to diagnose this weevil early; the noticeable signs of the infection only occur when the disease is in a dangerous stage.

In literature, different detection methods are used to discover the infected trees, such as Acoustic Detection, Chemical Detection, Thermal remote sensing, and Visual Inspection. In [1] survey article, these techniques were discussed in detail. And they concluded that there are drawbacks in each of these techniques, and there is a need to propose a novel model to detect RPW early.

In the literature, a limited number of studies have used image processing techniques to identify RPW. In [2] paper, a novel model is proposed. This model is based on image processing techniques and artificial neural networks. In this paper, nine features are extracted from each image (three from the regional properties technique and six from the Zernike moments technique). Then artificial neural networks are used as a classification model. The data set used in this paper consists of 326 RPW and 93 other insects' images. Two separate training algorithms have been used to train the neural network: Conjugate Gradient with Powell/Beale restarts (CGB) and Scaled Conjugate Gradient (SCG). The results obtained in this paper are 100% identification rates for RPW's images and 93% for other insects' images. The same author has published another article using the same data set and image

---

processing techniques. But instead of using artificial neural networks for classification, he has used the Support Vector Machine (SVM) with the polynomial kernel. The suggested method succeeded in detecting RPW and other insects by rates of 97% and 93%, respectively [3]. In 2020, the Linear SVC algorithm was used for the early detection of RPW. The proposed model has achieved 92.8% of accuracy [4]. Despite numerous attempts and research to combat this pest, none of them have been successful enough to discuss a way for detecting RPW in its early phases [5].

This study proposed an artificial intelligence technique to recognize RPW for people who do not understand easily. The proposed model consists of three stages. The first stage is called image pre-processing. This stage aims to enhance the quality of images and segment the body of the insects into separate images. In order to enhance images, Erodes and Dilates filters are used [6]. In contrast, Otsu's thresholding method is used for segmentation tasks [7]. The second stage is called feature extraction, which is an essential step in machine learning. In this stage, four texture and nine color moments features are extracted from the segmented images [8]. The final stage is called the classification stage, done by artificial neural networks (ANN).

The rest of the paper is organized as follows. First, the proposed image processing techniques are introduced. Then the proposed feature extraction techniques are presented. After that, the proposed classification model is illustrated. Finally, the obtained results are discussed.

2. Materials and Methods

In this section, we discuss our model in detail. In order to do that, we divide this section into three main subsections as the following.

2.1. Pre-processing

This stage focuses on enhancing the image to increase the classification accuracy and decrease the blur that happened by morphology operations. In this stage, the sample images are enhanced using Erodes and Dilates filter after resizing them into 256×256. The techniques of image rescaling are applied due to the lack of the same and standard size of images as our data set is collected from different sources. We can see the original image and the image after enhancement in Figures 1 and 2, respectively. We have also plotted the histograms in order to show whether it is possible to segment the background from the foreground of the image or not. After that, the image is passed to the segmentation method concerned with

extracting the insects' bodies from the inserted image. It is clear in the histogram figures that it is possible to segment the insect region from the background by finding the optimal threshold. However, this is not the case in all images, which may negatively affect the performance of the proposed model. Therefore, we have used Otsu's thresholding method to find the optimal threshold for each image. Then we have used this threshold value to convert the image into a binary image representing the mask filter that will be used to segment the image, as shown in Figure 3. The obtained mask is then multiplied by the three-color channels (Red, Green, and Blue) to extract the region of interest, as is shown in Figure 4. Finally, we have extracted the proposed features from the segmented image that is shown in Figure 4.
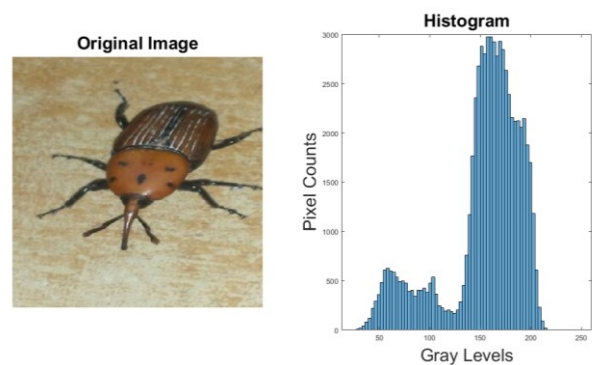
Figure 1. Sample of the dataset with its histogram.
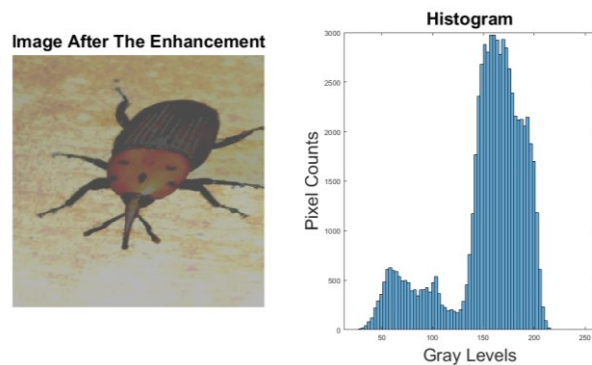
Figure 2. Results after the enhancement step.
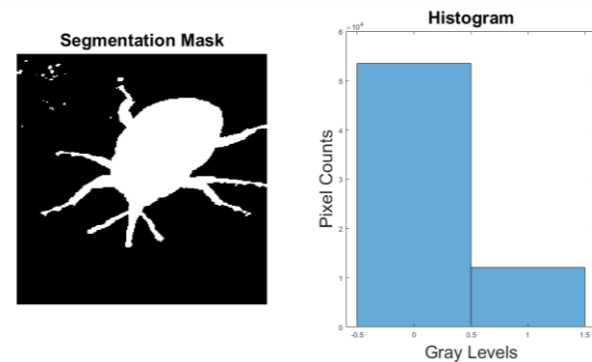
Figure 3. Binary mask obtained by Otsu's method.
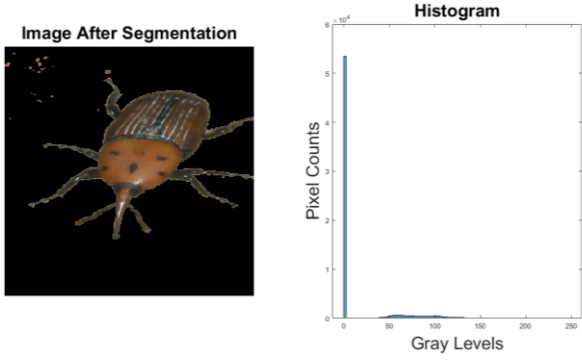
Figure 4. Results after the segmentation step.

2.2. Feature Extraction

This stage concentrateson transforming the input images from a matrix of pixels into a specific number of features. Those features arethen used as inputs to the classification models and help differentiate between input patterns (in this project, help distinguish between PRW and Ant). This study proposed hybridizing texture features (four features) with color moments features (nine features). Since insects differentiate from each other in texture and color, the proposed feature extraction model concurrently calculates each kind of feature. In order to extract texture features, Gray Level Co-Occurrence Matrix (GLCM) should be calculated from the segmented image. Then, there are many statistics exist that can be derived from GLCM [9]. But in our study, we have just used four texture properties: Energy, Contrast, Correlation, and Homogeneity. Concurrently, the Red Green Blue (RGB) image isseparated into three layers wherein three-color moments are extracted. These moments are called first, second, and third moments and their equations are shown in Eqs. (1-3).

$$M = \frac{1}{N}\sum_{j=1}^{N} P(i,j) \tag{1}$$

$$\sigma = \sqrt{\frac{1}{N}\left(\sum_{j=1}^{N}(P(i,j) - M)^2\right)} \tag{2}$$

$$S = \sqrt[3]{\frac{1}{N}\left(\sum_{j=1}^{N}(P(i,j) - M)^3\right)} \tag{3}$$

2.3. Classification

This stage focuses on training the artificial neural networks to classify whether the input features are for RPW or ant. ANNs can identify and learn correlated patterns between input data sets and corresponding target values. The configuration of ANNs used in this study is one input layer with 13 nodes, one hidden layer with 92 nodes, and one output layer with 2 nodes. The trial and error method is used to find the optimal number of hidden layer nodes, as it is suggested in [10]. The training

algorithm used in training is Levenberg-Marquardt backpropagation [11].

3. Results and Discussion

Due to the lack of data set of PRW images in the literature, we have collected a new data set. The collected data set consists of 913 images, where 448 are RPWs' images, and the rest are Ants' images. Since our problem is a classification problem, and our data set is balanced, the accuracy metric is enough to test the performance of the proposed model. However, a confusion matrix is also used in order to test the performance of the proposed model. Moreover, the classification model was trained for 30 independent runs and tested using 10-fold cross-validation to study the stability and variance of the model. Table 1 shows the Best, the Mean, and Standard Deviation of the classification accuracy metric over the 30 runs of ANNs. Table 2 shows the confusion matrix of the best run for ANNs.

Table 1. Classification accuracy results of the 30 runs.

Model	Best%	Mean%	Standard Deviation%
ANN	92.2217	87.7475	1.7215

Table 2. Confusion matrix of the best run for ANNs.

		Actual		
		RPW	Ant	Sum
Predicted	RPW	421 46.11%	44 4.82%	465 90.54%
	Ant	27 2.96%	421 46.11%	448 93.97%
	Sum	448 93.97%	465 90.54%	913 92.22%

The 10-fold cross-validation means the dataset is randomly partitioned into ten equal subsamples, and the proposed model is trained ten times using nine parts of the dataset, wherein each time is tested using a different part of the ten parts. After that, the average of the ten times represents the accuracy of this run. We have used 10-fold cross-validation as a performance measurement metric to ensure no bias in the dataset. Moreover, we have examined the model's performance for 30 runs to check the stability of the results.

As it is shown in Table 1, the proposed model archives competitive accuracy on 10-fold cross-validation experiments (92.22%). Moreover, the mean accuracy of the 30 runs proves that the proposed model can be generalized and used in real-time applications with high accuracy. The standard deviation that is shown in Table 1 proves that the proposed model has low variance. Furthermore, if the

model is trained again, it will give a similar performance. The results shown in the confusion matrix tell us that the accuracy rate for RPWs' images is 93.97% and 90.54% for Ants' images. That means our model can identify RPWs' images so efficiently.

4. Conclusions

This study proposed an artificial intelligence model to easily recognize RPW insects to decrease the massive economic losses that occur due to the damage happened to the trees because of the RPW. In this model, each image has to go through the following steps. First, the image is enhanced using erodes and delites filters. Next, the insect region is segmented using Otsu's method. Then, four texture and nine color moments features are extracted from the segmented part of the image. Finally, the artificial neural network is used to recognize whether the image is RPW or not. The experimental results of the 10-fold cross-validation show that the accuracy of the proposed model is very competitive, and that is 92.22%. Moreover, the proposed model can be used in real-world applications since we have used a new dataset that consists of images with different backgrounds. However, in future studies, we are planning to collect more images in order to be able to use deep learning techniques like Convolutional Neural Networks. Furthermore, other kinds of machine learning models could be proposed, such as using different types of features. If there were enough images and deep learning techniques were used, the accuracy would exceed 95%.

Declaration of Ethical Standards

The authors of this article declare that the materials and methods used in this study do not require ethical committee permission and/or legal-special permission.

Conflict of Interest

The authors declare that they have no known competing financial interests or personal relationships that could have appeared to influence the work reported in this paper.

References

[1] Ahmed H., 2020. Red Palm Weevil Detection Methods: A Survey. Journal of Cybersecurity and Information Management (JCIM), **1**(1), pp. 17-20.

[2] Al-Saqer S. M., 2012. A reliable identification system for red palm weevil. American Journal of Applied Sciences, **9**(8), p. 1150.

[3] Hassan G. M., Al-Saqer S. M., 2012. Support vector machine based red palm weevil (Rynchophorus ferrugineous, Olivier) recognition system. American Journal of Agricultural and Biological Sciences, **7**(1), pp. 36-42.

[4] Alaa H., Waleed K., Samir M., Tarek M., Sobeah H., Salam M. A., 2020. An intelligent approach for detecting palm trees diseases using image processing and machine learning. Int. J. Adv. Comput. Sci. Appl., **11**(7), pp. 434-441.

[5] Eldin H. A., Waleed K., Samir M., Tarek M., Sobeah H., Salam M. A., 2020. A Survey on Detection of Red Palm Weevil Inside Palm Trees: Challenges and Applications. In Proceedings of the 2020 9th International Conference on Software and Information Engineering (ICSIE), Cairo, Egypt, 11-13 November, pp. 119-125.

[6] Haralick R. M., Shapiro L. G., 1992. Computer and robot vision. Vol. 1. Reading: Addison-wesley.

[7] Otsu N., 1979. A threshold selection method from gray-level histograms. IEEE transactions on systems, man, and cybernetics, **9**(1), pp. 62-66.

[8] Saleh R. A. A., Rüştü A. K. A. Y., 2019. Classification of melanoma images using modified teaching learning based artificial bee colony. Avrupa Bilim ve Teknoloji Dergisi, pp. 225-232.

[9] Haralick R. M., Shanmugam K., Dinstein I. H., 1973. Textural features for image classification. IEEE Transactions on systems, man, and cybernetics, (6), pp. 610-621.

[10] Saleh N. A., Ertunç H. M., Saleh R. A., Rassam M. A., 2021. A Simple Mask Detection Model Based On A Multi-Layer Perception Neural Network. In 2021 International Conference of Technology, Science and Administration (ICTSA), 22-24 March, pp. 1-5. IEEE.

[11] Moré J. J., 1978. The Levenberg-Marquardt algorithm: implementation and theory. In Numerical analysis, pp. 105-116. Springer, Berlin, Heidelberg.

Kocaeli University

Kocaeli Journal of Science and Engineering

http://dergipark.org.tr/kojose
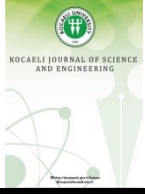
Providing the Ratio of Micro Hydroelectric Generation of the Municipal Wastewater Treatment Plant to Turkey's Total Electricity Consumption

Burhan BARAN [1, *] (iD)

[1] Department of Electrical and Electronics Engineering, İnönü University, Malatya, 44280, Turkey, **ORCID:** 0000-0001-6394-412X

Abstract

In this study, it was aimed to determine to provide the ratio of municipal wastewater treatment plant (WWTP) micro-hydropower generation to Turkey's total electricity consumption. Primarily, population and treated wastewater flow predictions of Turkey were made between 2020 and 2023 years. The power predictions that micro-hydroelectric power plants could generate were made by using 2 meters drop height and predicted flow data. Then, for the same years, Turkey's total electricity consumption prediction was made. For forecasting data for the coming years, a forecast sheet application was used. Finally, the total predicted electrical energies that could be generated with micro-hydroelectric at municipal WWTPs were compared with Turkey's predicted electricity consumption from 2020 to 2023 years. Thus, the ratio of these two parameters to each other was determined. The population was predicted as 87873632 people and the total amount of treated wastewater (TWW) was predicted as 5117528600 m^3 for the year 2023. Total annual electricity generation that could be generated from micro-hydroelectric power plants was predicted as 2231 GW/year for 2023 year, while the total electrical power consumption value was predicted as 312547 GW/year. It was predicted that the supplying ratio of micro-hydropower generation in municipal WWTPs to total electricity consumption would be 0.00714% on average between 2020-2023 years.

1. Introduction

Climate change and its social, environmental, and economic consequences are interrelated problems facing humanity. The effects and costs are great. The main reason behind global warming is energy consumption based on fossil fuels by people for different purposes. In order to obtain secondary energy, fossil fuels such as coal and oil are usually burned. In the past when consumption was less, power plants operated locally and fed a certain area. With the advancement of technology, energy need has increased as a result of the establishment of industrial facilities and local productions have become unable to meet this [1]. Renewable energy sources such as solar, hydroelectric, wind, geothermal and biomass energy are offered as alternative energy sources to meet the increasing demand [2]. Throughout history, water has played an important role

not only as a source of life but also as an energy source. In addition, the fact that it was considered a major energy-related resource in recent years carries water to a special point [3]. We are more likely to be more dependent on energy in the future. In the energy hierarchy, electrical energy is at the top. However, traditional sources of electricity generation are limited. One of the most useful sources of electricity generation today is the hydroelectric power plant established in municipal sewage WWTP. Wastewater in municipal sewage WWTPs is generated by housing, public and commercial buildings [4].

Hydroelectric is a renewable, non-polluting energy source that is relatively less harmful to the environment than other sources. Municipal sewage wastewater has hydroelectric potential. Generating electrical energy by using this potential energy of wastewater in municipal sewage WWTPs can be considered an alternative energy source. This energy is defined as a micro-hydroelectric power plant. The micro hydroelectric system has become one of the popular renewable energy sources in developing

countries. These plants are environmentally friendly as they do not produce greenhouse gas emissions [5]. Renewable energy sources are the most important points to consider when designing the social and economic system on a global scale. At this point, hydropower plants in municipal sewage WWTPs can also be considered a renewable energy source [6]. Micro-hydroelectric technology used in municipal sewage WWTPs is a clean and sustainable energy source. Since it is not fossil-based, it may also contribute to carbon emission reduction [2]. Today, in addition to large hydroelectric power plants, small hydroelectric power plants with a maximum output capacity of 10 MW are also utilized. The aim of these plants is to convert the potential energy of water into electrical energy with the help of a turbine and a generator. The power generated from the plants is proportional to the flow and drop height of the water. Since the flow rate and amount of water depending on the amount of rainfall received in the water basin according to the seasons, the water flow rate may vary non-linearly [7]. Small-scale hydroelectric investment is a renewable energy source that is clean, sustainable and emission-free, and its usage is increasing day by day all over the world. Small-scale hydroelectric power can be classified as small, mini, micro or pico depending on the output power and type. Micro-hydropower typically corresponds to power generation below 100 kW, while pico-hydropower generally corresponds to an installed power of less than 5 kW.

A study was carried out by Abbas et al. (2019) on the energy savings and power output that would occur if a hydro turbine was used in a WWTP in Wisconsin. The waste flow rate of the wastewater treatment plant under consideration was 190 million gallons (836927 m^3) per day. There was a height of 3 meters between the wastewater treatment plant and the discharge point. A computational fluid dynamics software had been applied to evaluate the performance of the system. The value of the savings was estimated to be 1564 MWh/year. The hydroelectric potential of the WWTPs in Switzerland had been evaluated in the study carried out by Bousquet et al. (2017). Hydroelectric generation estimates were made separately for 19 WWTPs with different head heights. 55 m^3/s in total from nineteen WWTPs. An algorithm had been developed for the economic evaluation of each plan. As a result of the study, it was estimated that annual potential energy generation of 9.3 GWh/year could be realized for nineteen project areas in the country. Chae et al. (2015) conducted a study on the applicability of small-scale municipal WWTPs with different flow levels in a micro-hydro system with flow variable turbines in South Korea. As a result of the study, they concluded that the type of turbine that gives the highest performance is the semi-tiger turbine. However, in South Korea, wastewater-

based hydroelectric turbine efficiency was not considered feasible due to low efficiency. As a result of this study, micro-hydropower plants from WWTP had been proposed as a clean energy source due to their simple installation, economic contribution and minimum environmental impact. Power et al. (2014) developed a method for estimating potential forces and payback periods for hydroelectric power recovery studies in more than 100 WWTPs in Ireland and the UK. A sensitivity analysis was performed based on changes in flow, turbine selection, electricity pricing and financial incentives. A method had been developed to optimize a design that could accommodate flow change without hindering turbine efficiency. In addition, the effect of future flow rate changes on the design was investigated. Concerning turbine selection, it was concluded that the Kaplan brand turbine had the highest potential power output. Furthermore, electricity pricing had been found to have a major impact on the economic viability of hydroelectric energy recovery. In the study conducted by Kose et al. (2013) a hybrid system consisting of wind and hydroelectric power plants was analyzed to meet the energy demand of the Konya water treatment plant. In addition to 250 kW HEPP (Hydroelectric Power Plants) and 250 kW WPP (Wind Power Plant), two 250 kW or one 500 kW wind turbine were added to the HEPP in order to meet the electrical energy requirements of the Konya water treatment plant. In this case, the energy demand of the power plant could be met with HEPP for 10 months per year. It had concluded that a WPP was required to provide uninterrupted energy. Bhandari et al. (2017) conducted a study on how the micro hydroelectric power plant can meet high electricity demands. They conducted a study on the advantages and disadvantages of generating micro-hydroelectric power from WWTP. They concluded that they could generate at 11.32 kWh of electricity with a 0.57 m^3/s flow rate and 1.8-meter drop height. In the study made by Albany et al. (2011) an integrated 15 kW turbine/generator system had been designed and evaluated to obtain energy from the flow in WWTPs. The prototype system was designed to supply 15 kW of electrical power to the power grid when fed with 12 million gallons (52858 m^3) per day. A case study on a hydroelectric system had been conducted by Kusakana (2019) in Zeekoegat WWTP, South Africa. The WWTP's electricity load demand, water resources and potential energy that could be recovered using the proposed hydroelectric power plant were evaluated to determine the projected cost savings over a proposed 20-year operating period. According to the economic analysis obtained in the study, the breakeven point was 6.35 years. For the foreseen 20 years, it had been concluded that 45.63% of the total electricity to be consumed could be met by WWTP hydro. In the study by

Never (2016), the dependency between India's wastewater and energy availability was analyzed. It was analyzed under which conditions and which vehicles were useful in wastewater systems. In addition, land and water scarcity caused changes in planning depending on local conditions.

The aim of this study was to reveal the hydroelectric potential of municipal sewage WWTPs in Turkey. For this aim, the amount of TWW that belongs to past years was taken from Turkey Statistical Institute (TUIK). In the Microsoft excel environment, forecast sheet application was used to predict the flow rates for the coming years. According to the obtained flow values, total micro-hydroelectric energy values which could be generated from municipal sewage WWTPs were obtained according to 2 meters head height. Also, by using previous years data, next years electricity consumption values of Turkey were predicted. Finally, micro-hydropower generation values obtained from municipal sewer WWTPs and Turkey's next years predicted electricity consumption values were compared. In this context, it was thought that the electrical energy to be obtained from the TWW, which was released directly to the discharge environment after treatment, would be a guide in terms of how much of the total electricity consumption, which was constantly increasing, could be met.

The next part of the study consists of four sections. In the second section, hydroelectric theory and its calculation were explained and population and TWW estimates were made. In the third section, the predicted flow rate until the year 2023 was calculated according to the predicted amount of electricity that can be generated according to 2 meters of drop height. Then, Turkey's total electricity consumption value was compared with these total generations. The fourth section was the conclusion part, and the results obtained in the study were compared.

2. Materials and Methods

2.1. Hydroelectric Theory

The potential energy of water with a certain height is called hydroelectric energy. This energy is first converted to mechanical energy and then to electrical energy by the rotation of the generator motor connected to the turbine wheel. Thus, hydroelectric power plants convert the power of the flowing water into electricity. The flow or drop rate of water is directly related to the amount of energy that the flowing water will have. When this relationship is taken into consideration, it is concluded that a high amount of energy can be obtained by decreasing the water from a very high point [17]. In hydroelectric technology, there are two basic parameters, namely the height of the head and

the flow rate enough to generate electricity [2]. Accordingly, in order to determine the potential of the power of the water flowing into the sewer, it is necessary to determine both the flow rate of the water and the head height of the water. The flow rate is the amount of water flowing from a point at a given time. Flow units are liters per second or cubic meters per second. The head refers to the vertical height.

Accordingly, the potential power calculation that can be obtained from a micro-hydroelectric power plant is as follows. The potential energy of water at a given height can be calculated by Eq. (1) and Eq. (2) [17]:

$$P_E(joule) = m \times g \times h \qquad (1)$$

where m is the weight of water (kg), g is the gravitational acceleration (9.81 m/s^2), and h is the height of the drop (m).

$$P_E(Wh) = Q * 1000 \left(\frac{kg}{m^3}\right) \times g \times h \times R \qquad (2)$$

$$P_E(kWh) = Q * 1 \left(\frac{kg}{m^3}\right) \times g \times h \times R \qquad (3)$$

where PE is the power (kWh), Q is the flow rate (m^3/s), g is the gravity coefficient (9.81 m/s^2), h is the drop (m), and R is the efficiency coefficient [18].

2.2. Forecast Sheet Application

The "Forecast Sheet" is a forecasting tool that quickly and easily predicts based on historical data grouped by time. The ability to recognize seasonality in historical data and take it into account is something that traditional linear projections do not. Also, the speed at which you can forecast using this tool is also unique [19].

2.3. Curve Fitting

The data generated in experimental studies are usually punctual. A continuous function cannot be obtained. In this case the data is $(x_1, y_1), \ldots, (x_n, y_n)$ are given as pairs of points. Determining another function closest to the function at given values for each point of a function is defined as the "curve fitting" problem [20]. It is aimed to find a suitable curve equation that will best represent the relationship between two variables.

2.4. Matlab

MATLAB is expressed as the 4th generation programming language. Developed by MathWorks. It

offers many possibilities such as matrix operation, drawing and scientific programming. It also contains many tools. Examples of these are signal processing, optimization, statistics, signal and image processing toolboxes [21]. R2015a version was used in this study. It was used to obtain the polynomial equations of population by years, TWW related to population and total electricity generation related to population value. The curve fitting method was used as a method.

2.5. Prediction Studies

In this chapter, predictions of Turkey's population and TWW were made. Predictions were made until 2023. Turkey's population values between the years 2000-2018 are given in Table 1. These data were taken from TUIK [22]. Population predictions between 2019 and 2023 years were made by using the forecast sheet application in Microsoft excel [23].

Table 1. Current and Predicted Population Values (Turkey).

Years	Population	Years	Population	Predicted Population
2000	64729501	2012	75627384	-
2001	65603160	2013	76667864	-
2002	66401851	2014	77695904	-
2003	67187251	2015	78741053	-
2004	68010215	2016	79814871	-
2005	68860539	2017	80810525	-
2006	69729967	2018	82003882	-
2007	70586256	2019		83177528
2008	71517100	2020		84351554
2009	72561312	2021		85525580
2010	73722988	2022		86699606
2011	74724269	2023		87873632

When Table 1 is examined, the population growth rate would increase by 1.431% in the year 2019 compared to the previous year, 1.411% in 2020, 1.392 in 2021, 1.373% in 2022, 1.354% in 2023. Also, the total predicted population would be 87.873.632 in 2023. When the predicted data in Table 1 is applied to the curve fitting algorithm written in Matlab [24] environment, Eq. (4) is obtained.

$$Population = 1.009 \times 10^6 \times (year) - 1.953 * 10^9 \quad (4)$$
R-square: 1

The total amount of TWW by municipal sewage WWTPs in Turkey between 2001 and 2016 years are shown in Table 2. In addition, the flow prediction between 2017-2023 years was made. These data were taken from TUIK [22]. Microsoft excel forecast sheet application was used for prediction. When this table was analyzed, it was predicted that the rate of increase at the amount of TWW

would increase by 4.682% in 2017 and 3.700% in 2023 compared to the previous year, and the total amount of TWW would be 5117528600 m³ in 2023.

Table 2. Current and Predicted Amount of TWW (Turkey).

Years	Current and Predicted Flow Rate (thousand m³/year)	Years	Current and Predicted Flow Rate (thousand m³/year)
2001	1193975	2016	3842350.0
2002	1312379	2017	4022246.4
2003	1586550	2018	4204793.4
2004	1901040	2019	4387340.5
2006	2140494	2020	4569887.5
2008	2251581	2021	4752434.5
2010	2719151	2022	4934981.5
2012	3256980	2023	5117528.6
2014	3483787		

The predicted data in Table 2 was applied to the curve fitting algorithm written in Matlab environment. The resulting equation was shown in Figure 1. Figure 1 is a graphical representation of the data obtained in Table 2. The values to be obtained by the equation in Figure 1 are very close to the values in Table 2. Coefficients were with 95% confidence bounds.
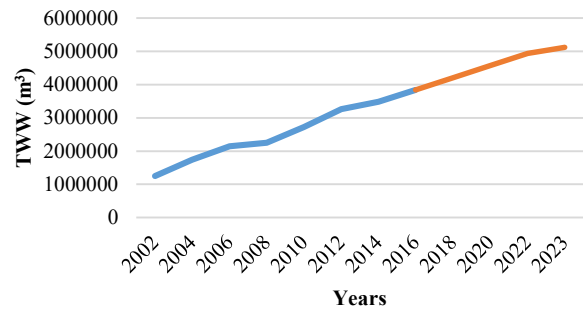
Figure 1. Turkey's Current and Predicted Flow Rate Amounts

When Table 1 and Table 2 are compared, the population growth rate from 2001 to the year 2019 was 26.79%, while the rate of increase in TWW by municipal sewage WWTPs is 267.46%. The rate of increase at the amount of TWW is ten times the population growth rate. Similarly, while the predicted population growth rate from 2019 to the year 2023 is 5.65%, the predicted amount of TWW by municipal sewage WWTPs increases by 16.64%. Using the annual flow rates obtained in Table 2, if the desired flow rate per second is calculated, Table 3 is obtained. While calculating the flow rate obtained per second, annual flow rate is obtained by dividing into 365 days, 24 hours, 60 minutes and finally 60 seconds respectively.

Table 3. Predicted Amount of TWW (Turkey)

Years	Predicted Amount of Wastewater (m³/year)	Predicted Amount of Wastewater (m³/sec.)
2020	4569887500	144.90
2021	4752434500	150.70
2022	4934981500	156.49
2023	5117528600	162.28

The relationship between population growth and the amount of TWW was analyzed. All data for both parameters were used for this purpose. When the related parameters were written to the above-mentioned Matlab algorithm, the polynomial of the 3rd order is as in Eq. (5). Here, P is the population. The coefficients in the obtained equation were with 95% confidence bounds.

$$TWW(year) = -1.301 * 10^{-6} * P^2 + 372.9 * P - 1.762 * 10^{10} \quad (5)$$

R-square: 0.9968

3. Results and Discussion

3.1. Micro-hydropower Generation in Case of Drop Height is 2 Meters

In the studies in literature, the drop height varies between 1.8-3 meters, and in this study, calculations were made according to the drop height of 2 meters.

Eq. (3) was used to calculate the amount of energy that could be generated according to the amount of wastewater treated. Here R yield coefficient is accepted as 0.80 in this study. Accordingly, using the flow values in Table 3, the energy value calculations obtained for the year 2020 at a height of 2-meter head are obtained as at Table 4:

Table 4. Power generation calculations obtained for the year 2020 at height of 2 meters head

Power Generation	Hourly (kW)	Daily (kW)	Yearly (kW)	Yearly (GW)
	2274.35	54584.41	19923309.5	19.92

Like this calculation, if the predicted electricity generation values of the other years were calculated, the power values in Table 4 are obtained. Table 5 shows the predicted hourly flow that could be obtained from municipal sewage WWTPs between 2020-2023 years, annual power available for one hour and annual power values obtained in one year. Predicted wastewater amounts to be treated in Table 3 were used to calculate the generation values of these years. As could be seen in Table 5, the amount of electricity to be generated increased every

year. However, it is predicted that these increase rates would decrease as a percentage compared to the previous year. While the value increased by 4.02% in 2021 compared to 2020, it is predicted that these percentage values would increase by 3.86% and 3.67% in the following years.

Table 5. Predicted flow rate and power values for the coming years at a height of 2 meters

Years	Predicted Flow Rate (m³/sec)	Generated Electricity (kWh)	Generated Electricity (GW/year)
2020	144.90	2274.35	19.92
2021	150.70	2365.39	20.72
2022	156.49	2456.27	21.52
2023	162.28	2547.15	22.31

If the similar study between the population and TWW amount was made between amount of predicted wastewater to be treated and predicted electric power to be generated in 2020-2023 years, the polynomial equation obtained was as at Eq. (6). GE means generated electricity. Coefficients were with 95% confidence bounds.

$$GE\ (GW/year) = 2.182 \times 10^{-8} \times TWW - 0.09253 \quad (6)$$

R-square: 1

Accordingly, if the Eq. (5) and Eq. (6) were combined based on wastewater to be treated between the population and the generated energy, Eq. (7) is obtained.

$$GE\ (GW/year) = 2.182 \times 10^{-8} \times (-1.301 \times 10^{-6} \times P^2 + 372.9 \times P - 1.762 \times 10^{10}) - 0.09253 \quad (7)$$

Using the Eq. (7) obtained, the predicted generation of electricity based on the wastewater to be treated depending on the population of the following years could be obtained.

3.2. Supplying Ratio of Municipal WWTP Micro-hydroelectric Generation to Turkey's Total Electricity Consumption

At this stage, a study was conducted to determine the supplying ratio of municipal WWTP micro-hydroelectric that generated from municipal sewage WWTPs to Turkey's total electricity consumption (TEC) at 2020-2023 years. Predicted electricity generation values obtained from municipal sewage WWTPs, which was one of the two data required for this comparison, are obtained in Table 5. Predicted electricity consumption values between the years 2020-2023 have been obtained with the excel forecast

sheet application. Figure 2 shows the values obtained by this embodiment.
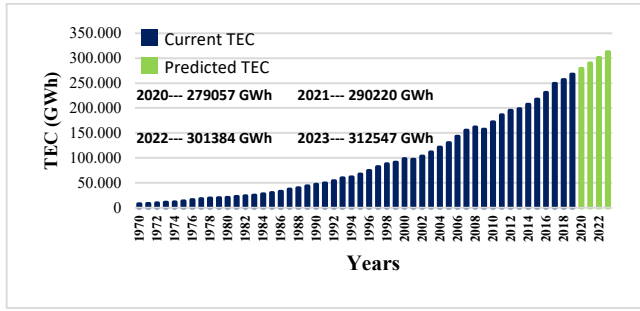
Figure 2. Turkey's Current and Predicted TEC

When Figure 2 is examined, it is seen that TEC continuously increases. However, when analyzed in more detail, the consumption rate shows a decrease compared to the previous year. For example, while the consumption of electricity consumed in the 2020-year increase by 4.17% compared to the previous year, the year 2019, increase rate was predicted to be 4.00%, 3.85% and 3.70% in the following years, respectively. To determine whether the municipal WWTP micro-hydroelectric generation of Turkey meets TEC to what extent, the data of Figure 2 and Table 5 are used. The supply ratios obtained are as in Figure 3.
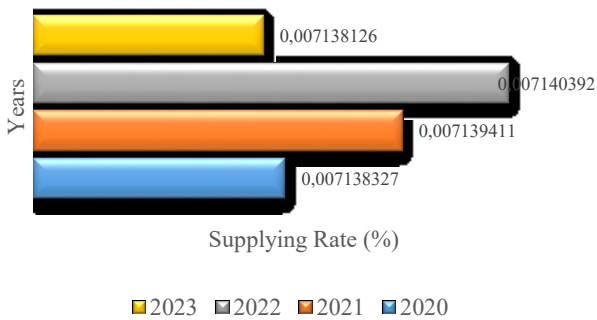
Figure 3. Supplying Ratio of Municipal WWTP Micro-hydroelectric Generation to Turkey's TEC

As can be seen from Figure 3, similar supply-to-demand ratio emerges in four years. These values are around 0.00714%. The reason for the close supply-demand ratios is that between 2020-2023 years, both municipal WWTP electricity generation and total electricity consumption increased at close rates.

When the studies mentioned in the literature review section above were examined, generally the appropriate turbine selection for electricity generation from WWTP, the amount of generation that could be obtained, and similar studies could have been made. In addition, in this study, the contribution rate of the hydroelectric that could be obtained from WWTPs to the total electricity generation

of the country had been investigated. In addition, in the studies in the literature, either for a single WWTP or separate generations of different WWTPs were evaluated. In this study, the total hydroelectric calculation that could be obtained by considering the total amount of TWW in Turkey was performed. In addition, in this study, the ratio of the generated hydroelectricity to the electricity consumption of the country was calculated. Compared to the study conducted by Bousquet, Samora, Manso, Rossi, Heller & Schleiss (2017), it was predicted 9.3 GWh/year hydroelectric generation for 55 m^3 total flow rate from nineteen WWTP, whereas in this study, 22.31 GWh/year generation was predicted for 162.28 m^3 flow rate for 2023 year. While the flow rate was 295 times, the amount of hydroelectric produced was 240 times in Turkey. The slight difference in generation was thought to be due to the drop height and the use of different models of turbines. In the study conducted by Bhandari & Rahate (2017), the flow rate was taken as 0.57 m^3/s and the drop height as 1.8 meters, and 11.32 kWh was obtained. In this study, 2547.15 kWh electricity generation was predicted for the year 2023 with 162.28 m^3 flow rate. While the flow rate was 285 times, the amount of hydroelectric generated was 225 times in Turkey. The small difference in the generation amount was thought to be due to the use of different model turbines and the selection of parameters used in the calculations.

4. Conclusions

This paper aimed to determine the supplying ratio of municipal WWTP micro-hydroelectric that generated from municipal sewage WWTPs to Turkey's TEC. The head height was assumed to be 2 meters. The prediction years were between 2020-2023 years. According to the predictions made for this purpose, the population growth rate would increase by 1.431% in 2019 compared to the previous year, 1.411% in the year 2020, 1.392 in the year 2021, 1.373% in the year 2022, 1.354% in the year 2023, and the total population would be 87873632 in the year 2023. The rate of increase in the amount of TWW was predicted to increase by 4.682% in 2017 and 3.700% in the year 2023 compared to the previous year, and the total amount of TWW was predicted to be 5117528600 m^3 in the year 2023. Furthermore, both municipal WWTP micro-hydroelectric power generation and the total electric consumption predicts were made for Turkey. According to the prediction studies, a total of 2231 GW/year electricity generation was predicted in 2023 year, while the TEC was predicted to be 312547 GW/year. For the following years, the supplying ratios were similar for four years. These values are around 0.00714%. The reason for the close

supplying ratio was that both the predicted electricity generation predicts from the municipal WWTP and the TEC predicts have increased over the years. As a result, energy from WWTPs supports future-oriented renewable energy generation plans. In this respect, it should be taken into consideration in energy policies in the sustainable development of countries.

Declaration of Ethical Standards

The author(s) of this article declare that the materials and methods used in this study do not require ethical committee permission and/or legal-special permission.
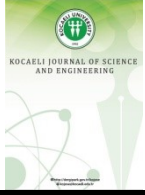
Conflict of Interest

The authors declare that they have no known competing financial interests or personal relationships that could have appeared to influence the work reported in this paper.

References

[1] Özgören Y., Koyuncu S., 2018. Current Status and ptimization of Electrical Grids in Çanakkale Region for Renewable Energy Systems as Future Technology. Journal of Advanced Research in Natural and Applied Sciences, **4**(2), pp. 212-236.

[2] Patel D., Jardosh H., 2018. Application of Hydropower Technology in Wastewater Treatment Plants Step towards Sustainable Environment. International Journal of Innovative Research in Science, Engineering and Technology, **7**(2), pp. 1818-1821.

[3] Beltran H., Vidal R., Basiero L., Santos J.M., Basiero J.A., Belenguer E., 2014. Micro hydro installation analysis in a wastewater treatment plant. International Conference on Renewable Energies and Power Quality (ICREPQ'14), April 08-10, pp. 15-20.

[4] Özaktürk M., Yanıkoğlu E., Çavuş T. F. Metin A., 2006. Küçük Hidroelektrik Santrallerin Gücünün Bulanık Mantık Yöntemiyle Tahmini. ELECO, Bursa, December 2006.

[5] Tamrakar A., Pandey S.K., Dubey S., 2015. Hydro Power Opportunity in the Sewage Waste Water. American International Journal of Research in Science, Technology, Engineering &Mathematics, AIJRSTEM,15-369, pp. 179-183.

[6] Gómez-Llanos E., Arias-Trujillo J., Durán-Barroso P., Ceballos-Martínez J.M., Torrecilla-Pinero J.A., Urueña-Fernández C., Candel-Pérez M., 2018. Hydropower Potential Assessment in Water Supply Systems. Proceedings, **2**(20):1299.

[7] Baran B., Mamis M.S., Alagoz, B.B., 2016. Utilization of energy from waste potential in Turkey as distributed secondary renewable energy source. Renewable Energy, **90**, pp.493-500.

[8] Abbas A.I., Qandil M. D., Al-Haddad M.R., Saravani M.S., Amano R.S., 2019. Utilization of Hydroturbines in Wastewater Treatment Plants, The Journal of Energy Resources Technology, **141**(6): 062011.

[9] Bousquet C., Samora I., Manso P., Rossi L., Heller P., Schleiss A.J., 2017. Assessment of hydropower potential in wastewater systems and application to Switzerland, Renewable Energy, **113**, pp. 64-73.

[10] Chae K.J., Kim I.S., Ren X., Cheon K.H., 2015. Reliable energy recovery in an existing municipal wastewater treatment plant with a flow-variable micro-hydropower system. Energy Conversion and Management, **101**, pp. 681-688.

[11] Power C., McNabola A., Coughlan P., 2014. Development of an evaluation method for hydropower energy recovery in wastewater treatment plants: Case studies in Ireland and the UK. Sustainable Energy Technologies and Assessments, **7**, pp. 166-177.

[12] Kose F., Kaya M.N., 2013. Analysis on meeting the electric energy demand of an active plant with a wind-hydro hybrid power station in Konya, Turkey: Konya water treatment plant. Renewable Energy, **55**, pp. 196-201.

[13] Bhandari K., Rahate O.P., 2017. Micro Hydro Electricity Generation in S.T.P, A Case Study of S.T.P, Salawas-Jodhpur. International Research Journal of Engineering and Technology (IRJET), 04 (03), pp. 278-281.

[14] Albany N.Y., O'Connor K., Torrey D.A., 2011. Hydropower from Wastewater, New York State Energy Research and Development Authority, Final Report, 12-04, pp. 1-46.

[15] Kusakana, K., 2019. Hydropower Energy Recovery from Wastewater Treatment Plant: Case of Zeekoegat Plant, 2019 IEEE PES Asia-Pacific Power and Energy Engineering Conference (APPEEC), Macao, Macao, pp. 1-5.

[16] Never B., 2016. Wastewater Systems and Energy Saving in Urban India: Governing the Water-Energy-Food Nexus Series, Deutsches Institut für Entwicklungspolitik Discussion Paper No. 12/2016.

[17] Hydroelectric Energy, 2019. Hydroelectric Energy, https://enerjiteknolojileri.wordpress.com/2014/12/17/126/

[18] Bayer Company, 2018. Hydraulic Turbines for Low Height. www.bayercompany.com

[19] Forecast Sheet, 2020. Forecast Sheet Application. https://www.k2e.com/tech-tips/excel-forecast-sheet/

[20] Curve Fitting, 2019. Curve Fitting Method. www.yildiz.edu.tr/~nguzel/Egri_Uydurma_ve_En_K ucuk_Kareler_Yontemi.docx

[21] Matlab-b, 2021. Matrix Laboratory. https://cvw.cac.cornell.edu/matlab/default

[22] TUIK, 2019. The Statistical Institute of the Republic of Turkey. Turkey population, treated wastewater amount and total electricity consumption. www.tuik.gov.tr.

[23] Excel, 2019. Microsoft Office. Excel. https://products.office.com/tr-tr/excel

[24] Matlab-a, 2019. Matrix Laboratory. www.mathworks.com/products/matlab.html.

Paper-Based Biosensor System for Fast and Sensitive Phenolic Compounds Detection

Nimet YILDIRIM TİRGİL [1, 2, *]   iD

[1] Department of Biomedikal Engineering, Ankara Yıldırım Beyazıt University, Keçiören, Ankara, Turkey, **ORCID:** 0000-0002-5973-8830
[2] Department of Metalurgican and Materials Engineering, Ankara Yıldırım Beyazıt University, Keçiören, Ankara, Turkey, **ORCID:** 0000-0002-5973-8830

Abstract

In this original paper, the development of a paper-based, sensitive, low-cost, quantitative and consistent biosensor system was demonstrated for the suitable "naked-eye" detection of phenolic compounds (specifical catechol). The Paper-based system depends on the enzymatic color-changing reaction that observed by using chromogenic agent of 4-AAP (4-aminoantipyrine) which has a specific color changing reaction in the presence of horseradish peroxidase (HRP) enzyme, phenol and H_2O_2. The visual result was associated with the catechol concentration by using image processing software to evaluate the quantitative detection. The developed biosensor system demonstrated a linear detection range from catechol between 2,5 μM to 100 μM with 2.6% to 9.3 % of sd results. The detection limit was also calculated as 2,25 μM. Specificity, selectivity, stability and direct real sample analysis demonstrated the potential applicability of the developed paper-based biosensor system for catechol detection in food samples with minimal investment and an easy-to-use method.

1. Introduction

Phenolic compounds are widely used in food processing, petrochemical engineering, chemical production, printing, dyeing, etc. When these compounds discharge to the environment during or after the processes, they become one of the most harmful pollutants due to phenolic compounds' high toxicity and low biodegradability in the environment [1]. They contaminate agricultural products, poison marine animals, and affect the functions of the human nervous, urinary, and digestive systems. Other than their usage on different production processes, they also existing in many natural sources such as tea, vegetables, fruits, and other plants [2, 3, 4]. For example, catechol (1,2-benzenediol/1,2-dihydroxybenzene) is a critical dihydroxybenzene, and it is recognized as one of the key fragments of tea catechins. Catechol's concentration can be high up to 18-36% weight of the fresh dry tea and it is believed to be the source of many claims made regarding tea's health benefits. Catechol quantification is also

essential due to its biological importance such as anti-oxidation, anti-virus activities and affecting of some enzymes. because of its biological roles and environmental significance in such topics as antioxidation, antivirus, toxicity, and carcinogenicity [5, 6, 7]. Therefore, phenolic compound detection is crucial in food quality monitoring and also environmental water pollutants analysis. Several physical and chemical-based analytical methods are available to detect and determine phenolic compounds in various samples. HPLC with fluorimetric detection GC/MS, colorimetric methods or fluorescence excitation-emission matrix (EEM) are the most commonly used ones [8, 9]. Nevertheless, these methods involve complex sample pre-treatment, cost, increasing time, and expert personnel needs. Thus, it is precious to develop a simple, rapid, reliable, and low-cost method to detect phenolic pollutants in environmental and food matrices.

It has been observed that biosensors provide analysis that is less costly, easy, less time consuming, highly sensitive, and selective to various analytes. This has inspired

---

to development of easy-to-use, low-cost, and reliable platforms for monitoring several targets with following the "ASSURED" standards ("affordable, sensitive, specific, user-friendly, rapid and robust, equipment-free, and deliverable") by giving results even in the most restricted facilities [10, 11]. Among other biosensor systems, paper-based sensors can accomplish most of the ASSURED criteria' requirements and present some significant advantages such as high surface-to-volume ratio, biocompatibility, low-cost, biodegradability, lightness, and flexibility [10]. The analysis by using paper-based biosensors can be performed with colorimetric and electrochemical transducers, however the colorimetric strategies offer benefits like affectability, soundness, and straightforwardness of location through direct perception rather than the perusers needed for electrochemical gadgets. [12, 13]. However, a significant weakness of colorimetric transduction is the lack of sensitivity and quantitative detection. In the literature, most researchers used a mobile phone with a camera as the detection device, and so the software could be calculated the values by converting images of paper-based systems from the color scale into grayscale [14]. However, they sometimes suffered from adjustable changes in light conditions. Additionally, some people used a scanner to implement testing. However, it was challenging to be portable for on-site detection. Thus, well-standardized smartphone apps can solve these problems and are suited for on-site and real-time detection modes.

Typically, the colorimetric analysis of phenolic compounds can be accomplished by monitoring the target's oxidative coupling with 4-aminoantipyrine (4-AAP). In detail, the colorless 4-AAP can react with phenolic compounds to procedure a colored quinone imine molecule. To enable the chromogenic reaction, H_2O_2 and enzymes are frequently used to analyze phenol in diverse conditions rapidly. For example, Lin and co-workers described a colorimetric platform with horseradish peroxidase (HRP) for visually detection of phenol [15, 16, 17]. Figure 1 presents the colorimetric reaction of phenolic compounds and 4-AAP that catalysis by HRP in the presence of H_2O_2. While the approach displays a good performance for phenol monitoring, there is still plenty of opportunity to the enhance of the colorimetric method.
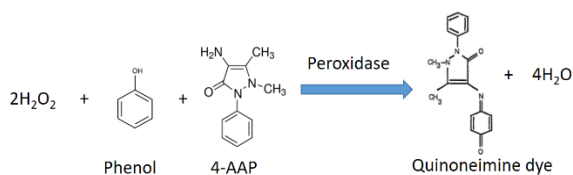
Figure 1. The colorimetric reaction of 4-aminoantipyrine and phenol produced a red color dye in the presence of horseradish peroxidase (HRP) and H_2O_2.

In this work, we demonstrated the establishment of a sensitive, quantitative, low-cost, portable and reliable paper-based biosensor system for the straight "naked-eye" detection of phenolic compounds (specifical catechol). Onto the paper filter material, biocompatible zones were prepared by chitosan modification and enzyme immobilization. The color changing reactions of phenolic compounds were observed by using the chromogenic agent of 4-AAP which has a specific color-changing reaction in the presence of HRP enzyme, phenol and H_2O_2. The visual outcome was corresponded with the catechol focus by the unaided eye and with picture handling programming to assess the quantitative recognition. Thus, catechol analysis, which will be performed using only a smartphone and a prepared paper-based biosensor system without extra equipment, will significantly benefit the time/cost benefit. Accuracy, selectivity, stability, and direct real sample tests showed the promising usage of the created paper-based biosensor framework for catechol recognition in food tests with the insignificant venture and a simple to-utilize technique.

2. Materials and Methods

Reagents and chemicals: RP type II (210 U/mg), chitosan powder (CAS 9012-76-4), Cathecol (1,2-Dihydroxybenzene- CAS 120-80-9), phenol (CAS 108-95-2), 4-nitrophenol (100-02-7), Hydroxyquinone (615-94-1), gallic acid (149-91-7), 4-aminoantipyrine (CAS 83-07-08), acetic acid (CAS 64-19-7), paraffin (CAS 8002-74-2), and # 40 WhatmanTM filter paper (210 μm of thickness and 8 μm of pore size) were ordered from (Sigma-Aldrich, Germany). 100 mM of phosphate buffer solution, distinct pH ranges, was set up from potassium phosphate monobasic and sodium phosphate dibasic, both acquired likewise from Sigma-Aldrich. The working solutions of catechol were prepared in PBS and green tea samples (prepared by regular brewing method).

Detection zone Preparation: Delimited round recognition zones were made utilizing a stamping process (figure 2, A-C), like the philosophy for paper gadgets represented by de Tarso-García et al. [18]. A metal stamp was planned and produced in aluminum to get location zones 6 mm in distance across. The metal stamp incorporates only a metal body and round meager edges which produce the hydrophobic boundaries around the detection zones. During the manufacture, a piece of Whatman paper was submerged into fluid paraffin for ≈2 seconds and put into a non-covered Whatman paper surface. At that point, the aluminum form was warmed at ≈110 °C and squeezed against the paraffin covered paper for ≈5 seconds. This brought about the exchange of paraffin from the upper paper to the non-covered channel paper and encompassed discovery zones with hydrophobic paraffin boundaries. The interaction is meant in Figure 2 with the means of A to C.
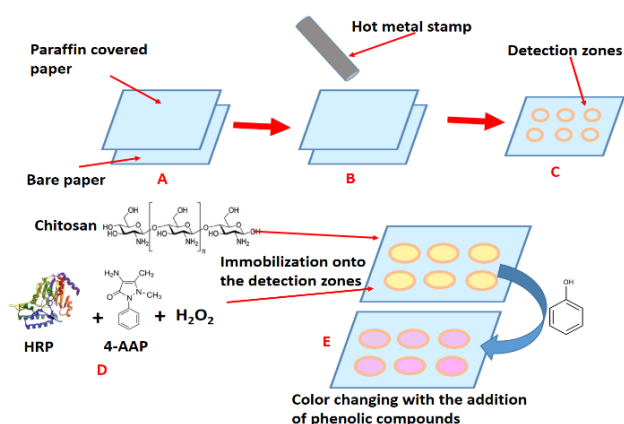
Figure 2. Portrayal of the paper-based sensor manufacture steps. (A) to (C); the advancement of the detection zone. (D) to (E); chemical and enzymatic modification of detection zone is presented.

Chitosan, Enzyme and chromogenic agent immobilization onto the detection zones: Chitosan was used as supporting material for the immobilization of HRP enzyme and 4-AAP chromogenic agent onto the prepared detection zones. The detection zones were firstly modified with chitosan solutions at 0.25%, 0.5%, 1%, and 2% (m/v) concentrations in acetic acid at 2% (v/v). After the chitosan modification the HRP (250 U/mL) enzyme was prepared in PBS at pH 6.0, 6.5, 7.0, 7,5, and 8.0 to immobilize onto the paper surfaces. Different pH values were prepared to investigate the enzymatic reaction efficiency in these pH conditions. The chromogenic agent, 4-AAP solution of 0,1 M, was prepared within PBS (100 mM, Ph 7.2). Paper-based biosensor framework was set up by consecutively adding the entirety of the reagents as introduced in Figure 2,D–E. 6 uL of chitosan solution, 3 uL of the enzyme solution and 3 uL of chromophore solution were added to the detection zones step by step and allowed to dry at room temperature. The prepared paper materials for the developed biosensor system were stored at 4°C not exposed to direct light. H_2O_2, the color-changing reaction indicator, was tested both by immobilizing onto the detection zones and adding to the phenolic compounds solutions. To optimize the H_2O_2 amount, the different percent composition of H_2O_2 solutions (0.05 % to 0.01 %) were mixed with 4-AAP or samples then injected onto the detection zones.

Color Detection Procedure: The obtained color change results were analyzed using a smartphone app, 'ON Color Measure,' to process the information with the RGB model [19, 20]. The smart phone apps for color intensity analysis is going to be an exciting filed on biosensor application that some of the recent works alrady tested their validation and verification [21]. In the RGB model red (R), green (G), and blue (B) light are added together in various ways to generate a broad array of colors. The name of the model comes from the initials of the three additive primary colors, red, green, and blue. Each tone is described on a scale from 0 to 225

when 0 addresses no commitment to the tone, and 225 addresses the R+G+B parts' top-level input. Ordinarily, in this model, the white tone is shown as the top level augmentation of the R+G+B parts, and the dark tone is the minimum value. Since the enzymatic response creates a color change from the white substrate to a colorful product, during the detection, the white introductory substrate was perceived as the maximum value for the entirety of the R+G+B parts, and the product color intensity was addressed with a decrease of these RGB values. Thus, lower phenolic compounds amount described as high RGB values, and higher concentrations formed low RGB values (Fig. 3). To accomplish a precise explanation, the total distribution of the R+G+B prices were measured, and the average values were used at each experimental part of this work. In the calibration curves an opposite relationship between mean RGB values and phenolic compounds concentration were observed in PBS and tea samples.

Figure 3. A smartphone app, 'ON Color Measure,' analysis process with the RGB model.

Biosensor performance optimization: After preparation of the detection zones and immobilization of the enzyme+4-AAP onto them, a fixed concentration (50 µM) of phenolic compounds including catechol, phenol, N-nitrophenol, Hydroxyquinone, and gallic acid were added to the zones. Afterward, different concentrations of catechol (the most sensitive and selective target for the system) solutions were added to the detection zones in optimum conditions to determine the calibration curve and limit of detection of the developed biosensor system. To research the stability of the created biosensor framework, the colorimetric reaction for a catechol test of 50 µM was recorded over 30 days.

Real sample testing: By using the optimum performance conditions for the developed biosensor system, real tea samples were tested. 10 µM, 50 µM, and 100 µM concentrations of catechol spiked onto the teas samples, and catechol detection was performed by the developed biosensor system. Percentage of recovery and cv (coefficient of variation) results were calculated for each concentration using three independent experiments.

3. Results and Discussion

Manufacture and Optimization of the Paper-Based Sensor: The created detection zones were covered with chitosan to accomplish an appropriate spot for analysis. The chitosan was utilized in concentrations from 0.25 to 2 % (mass to volume), which framed the meager film above the cellulose substrate of paper with a thickness reliant on the concentration. Figure 4 shows the morphology got for a paper-based biosensor framework before and after chitosan adjustment. Scanning electron microscopy (SEM) exposed the commonplace porous fibrillar design of the clear cellulose substrate and a chitosan film covering the cellulose filaments and obstructing the porous regions. It is found in figure 4 that the most uniform modification was accomplished with a 1% concentration of chitosan (Figure 4, D), which is likewise thick enough to cover the entire paper surface. After the enzyme immobilization onto the chitosan-covered paper surface, we got SEM images of Figure 4, F, representing the successful enzyme entrapping on chitosan layers.
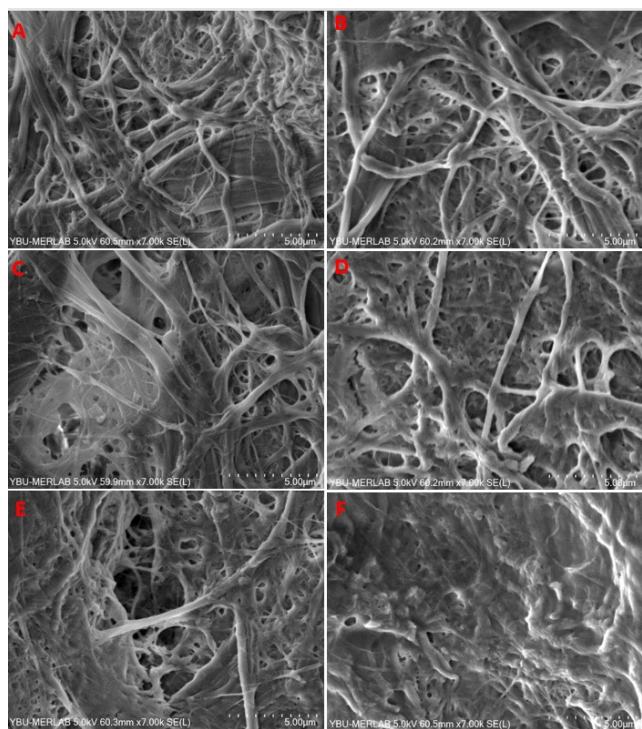
Figure 4. SEM images of modified papers with different chitosan concentrations; A) Blank paper, B) 0.25 %, C) 0.5 %, D) 1 %, E) 2 % and F) enzyme immobilized paper surface with % 2 concentration of chitosan (scale bars are 5.0 μm for each figure).
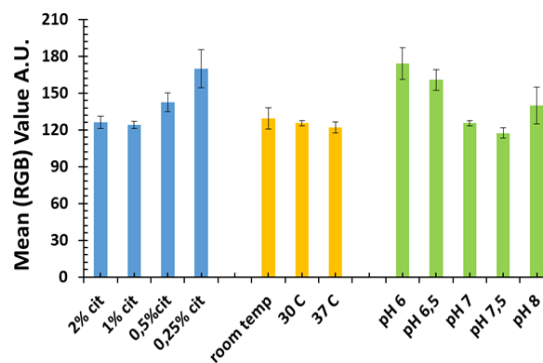
Figure 5. Impact of the concentration of chitosan solutions, detection temperature, and pH over the mean RGB values for the concentration of 50 μM of catechol.

The impact of the concentration of chitosan, pH ranges, and detection temperature over the colorimetric reaction was examined before catechol detection. The tests were directed with a sample concentration of 50 μM, which is inside the recognition range for catechol in food tests. Figure 5 shows the distinctions in the mean RGB values for the equivalent catechol concentration under various conditions.

It is seen from figure 5 that when the chitosan concentration increases, the means of RGB values decrease, which represents enhancing the activity of catechol's enzymatic reaction. The improved colorimetric reaction can be qualified initially to the surrounded detection zones, which expanded the entrapped enzyme concentration in the detection zone with a homogeny profile. In addition, the change with higher chitosan concentration gave to establishing a biocompatible climate for the enzymatic assay, given the chitosan's high affinity for proteins. Thus, the optimum chitosan percentage for the enzyme immobilization onto the detection zones was concluded as 1%.

Detection temperature is another essential condition for the maximum enzymatic activity, which is generally observed at 37 °C for most enzymes. Thus, we tested 37 °C, 30 °C, and room temperature (≈22 °C) to observe the temperature effect on the developed biosensor system performance. As seen from figure 5, even the maximum activity observed at 37 °C, even at the room temperature enzyme, had acceptable activity and closed RGB values to the higher temperatures. Thus, performing of biosensor system at room temperature was concluded, which helps to perform real-time and on-site detection of real samples.

In addition to the chitosan percentage and detection temperature, the pH values for the immobilized enzyme solution were tested with the range of pH 6.0, 6.5, 7.0, 7,5, and 8.0. As it was estimated, the maximum activity was observed at pH 7.5, which is generally the optimum pH value for biological molecules.

After the immobilization condition optimization, which was performed by the addition of 0.03 % of H_2O_2 solution directly onto the 4-AAP, the percentage amount of

H_2O_2 and the additional way for the H_2O_2 was evaluated (results are represented in Figure 6). Firstly, 0.05 %, 0.03 %, and 0.01 % of H_2O_2 were added onto the 50 µM of catechol and injected onto the detection zones, prepared using optimum conditions. In a second way, 0.05 %, 0.03 %, and 0.01 % of H_2O_2 were added to the 4-AAP solution during the immobilization. The results for the additional way of the H_2O_2 solutions were quite the same for the freshly used biosensor systems, but when we stored them ready to use the paper-based device, H_2O_2 and 4-AAP reacted by time in the presence of HRP enzyme (stability tests also represents this results). Thus we concluded to add H_2O_2 after immobilization and freshly before catechol testing on the developed biosensor system.
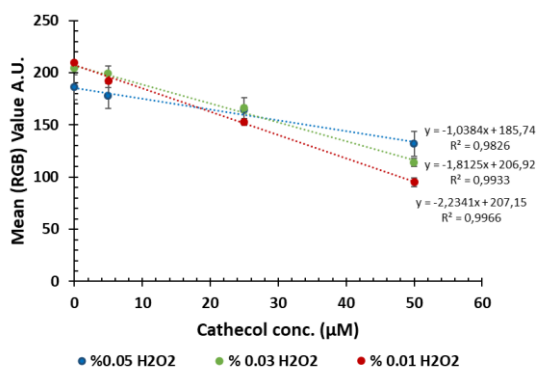
Figure 6. Effect of H_2O_2 amount on the developed paper-based biosensor system with different concentrations of catechol.

On the other hand, different H_2O_2 percentages gave different biosensor responses with different catechol concentrations. When the concentration ratios of catechol that range from 0 to 50 µM were tested, the test by using 0.01 % of H_2O_2 solution represented the most linear and distinguished results depending on the catechol concentrations (Fig. 6). The access amount of H_2O_2 generated undesired color changing not related to the catechol but also a non-specific reaction between 4-AAP and H_2O_2. Thus, we concluded to use 0.01 % of H_2O_2 freshly and after immobilization of all molecules onto the paper device.
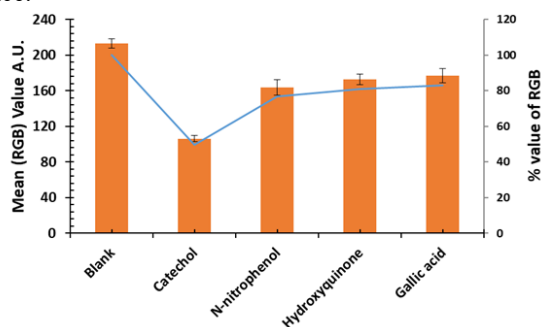
Figure 7. Selectivity analysis for the manufactured biosensor framework with mean colorimetric RGB values for catechol and diverse phenolic compounds (each was applied on 50 µM concentrations).

After preparation of the detection zones and immobilization of the enzyme and 4-AAP onto the paper surfaces on the optimized conditions, a fixed concentration (50 µM) of phenolic compounds including catechol, phenol, N-nitrophenol, Hydroxyquinone, and gallic acid were added to the zones with including 0.01 % of H_2O_2. In addition to these phenolic compounds, the blank solution, which includes only BPS, was tested. After measuring the RGB values of the color changed detection zones with the 'ON Color Measure' app, catechol, N-nitrophenol, Hydroxiquinone, and gallic acid generates % of RGB values of 49.9, 76.8, 80.8, and 83.1 depends on the blank experiment values (Fig. 7). The results represent that the developed biosensor system is not 100 percent selective for catechol, but the system also has more sensitivity and selectivity for catechol than the other phenolic compounds. Thus the developed biosensor system could be used for sensitive catechol detection and has potential usage for total phenolic compound detection on real food samples.

Afterward, different concentrations of catechol (the most sensitive and selective target for the system) solutions were added to the detection zones, which were prepared with optimized conditions, to determine the calibration curve and limit of detection of the developed biosensor system. Figure 8 shows the linear response (RGB values) obtained for the developed paper-based biosensor system after increasing the catechol amounts from 2,5 µM to 100 µM with 2.6% to 9.3 % of sd results. The detection limit was also calculated as 2,25 µM using the 3 times Standard Deviation value SD± that prepared most of the biosensor-related works [22, 23, 24, 25]. In addition to these measure responses, the color-changing for the different catechol concentrations represented naked eye observation between 0 µM and 200 µM.
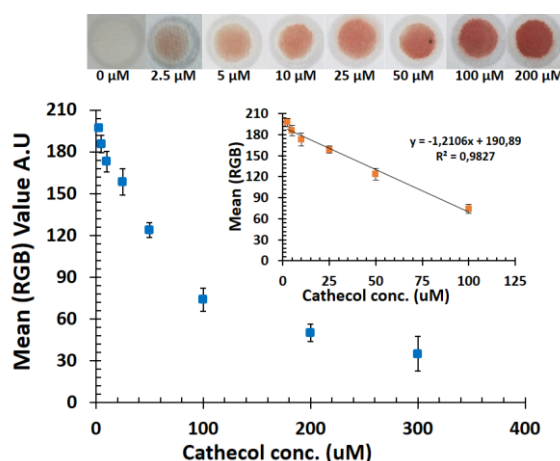
Figure 8. Calibration curve acquired for catechol detection in PBS with an inset figure representing the linear range and naked-eye visual scale achieved for catechol detection.

The RGB profile of the created biosensor framework stored under standard conditions was examined for 5 weeks, as demonstrated in Figure 9. The paper-based biosensor systems were prepared with and without immobilization of H_2O_2 onto the detection zones. The stability was accomplished with storage in the dark environment and +4 °C conditions, which is effortlessly accessible with a standard fridge. It is clearly seen from Figure 9 that immobilization without H_2O_2 gave more stable results than immobilization with H_2O_2. This is because the enzyme denaturation with acidic H_2O_2 and the non-specific reaction between 4-AAP and H_2O_2, even without phenolic compounds. The average deviation for immobilization without H_2O_2 was 6.32 %, and 21,2 % for the immobilization with H_2O_2 comparing the measured RGB values of the last day's results with the first day. Thus, we concluded that the paper-based biosensor systems should be prepared without immobilization of H_2O_2 during the initial preparation process, and the H_2O_2 solution should be added to the phenolic compound included solution just before the analysis. This proposes the practicality of the paper-based biosensor in restricted supply conditions within an acceptable performance over a period of time.
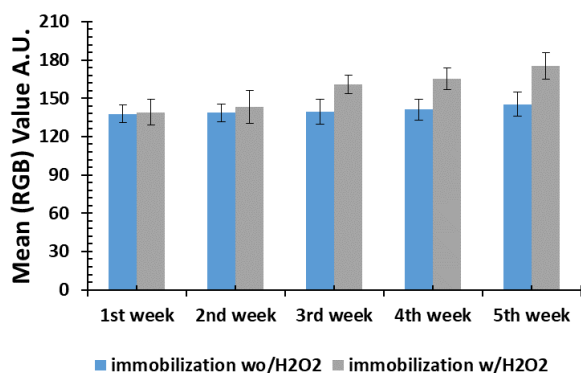
Figure 9. Stability test for fabricated paper-based sensors stored at 4 °C in dark conditions over 30 days.

Detection of Catechol in Tea Samples: To demonstrate the paper-based sensor's applicability for monitoring real samples, the detection of catechol in tea samples was performed. By using the optimum performance conditions for the developed biosensor system, real tea samples were tested. 10 μM, 50 μM, and 100 μM concentrations of catechol spiked onto the tea samples prepared by brewing in hot water. These different catechol concentrations were detected by the developed biosensor system, and the accuracy was evaluated through recovery percentages, achieving results from 92 to 114% (for three independent experiments), as shown in Table 1. also represents the calibration curves for catechol detection in BPS and tea samples, representing the closeness of the results with PBS and complex matrix.

Table 1. Results for catechol determination in real samples by using the developed paper-based biosensor system.

Added	Found (ave. value)	Recovery %	cv %
10	15,23	152,30	8,20
50	52,59	105,18	12,16
100	88,38	88,38	7,11

4. Conclusions

Compared to other reported works for catechol detection, our results demonstrate better sensitivity, wider linear detection range and better stability efficiency than most of them. Additionally, comparing the cost of them precious system, the developed paper-based biosensor system serves more efficient usage for real samples over 5 weeks of storage (Table 2). Additionally, we can conclude that this approach can be visually observed with the "naked eye," without the need for exterior analyzers or additional necessities, which according to the ASSURED criteria, is highly convenient for zones with restricted resources.

Table 2. Comparison of some analytical characteristics of the proposed methods with those of previously reported

Detection System	Biosensor system	Detection range	Stability/ Reusability	Real sample testing	Ref.
Colorimetric Sensor	Polymer modified enzyme based system	2.5 μM to 50 μM	1 months	Wine and fruit juice samples	[26]
Colorimetric Sensor	Non-enzymatic system	0.87 μM to 56 μM	Not Specified	Water and plasma samples	[27]
Electrochemical impedance spectroscopy (EIS)	PANI modified enzymatic system	1.0 μM to 100 μM	5 months	Wastewater samples	[28]
Amperometric Sensor	PANI copolymer based enzymatic system	5.0 μM to 80 μM	over 120 times	Not Specified	[29]
Potentiometric Sensor	Polypyrrole film based enzymatic system	1 μM to 16 μM	1 month	Not Specified	[30]

Table 2. (Cont.) Comparison of some analytical characteristics of the proposed methods with those of previously reported

Detection System	Biosensor system	Detection range	Stability/ Reusability	Real sample testing	Ref.
Cyclic voltammetry Sensor	Carbon nanofibers used enzymatic system	1 µM to 310 µM	30 days	Water samples	[31]
Fluorescent Sensor	Carbon dots based enzymatic system	2,66 µM to 341 µM	Not Specified	Not Specified	[32]
Fluorescent Sensor	carbon quantum dots based non-enzymatic system	0.002 µM to 0.05 µM	Not Specified	River water samples	[33]
Paper based colorimetric Sensor	4-AAP based enzymatic system	2,5 µM to 100 µM	5 weeks	Green tea sample	This work

Declaration of Ethical Standards

The author(s) of this article declare that the materials and methods used in this study do not require ethical committee permission and/or legal-special permission.

Conflict of Interest

The authors declare that they have no known competing financial interests or personal relationships that could have appeared to influence the work reported in this paper.

References

[1] Mahugo Santana, C., Sosa Ferrera, Z., Esther Torres Padrón, M. and Juan Santana Rodríguez, J. 2009, Methodologies for the extraction of phenolic compounds from environmental samples: new approaches. Molecules, Molecular Diversity Preservation International. **14**, pp. 298–320.

[2] Abad-García, B., Berrueta, L.A., Garmón-Lobato, S., Gallo, B. and Vicente, F. 2009, A general analytical strategy for the characterization of phenolic compounds in fruit juices by high-performance liquid chromatography with diode array detection coupled to electrospray ionization and triple quadrupole mass spectrometry. Journal of Chromatography A, Elsevier. **1216**, pp. 5398–415.

[3] Herchi, W., Arráez-Román, D., Trabelsi, H., Bouali, I., Boukhchina, S., Kallel, H. et al. 2014, Phenolic compounds in flaxseed: a review of their properties and analytical methods. An overview of the last decade. Journal of Oleo Science, Japan Oil Chemists' Society. **63**, pp. 7–14.

[4] Escarpa, A., Morales, M.D. and González, M.C. 2002, Analytical performance of commercially available and unavailable phenolic compounds using real samples by high-performance liquid chromatography–diode-array detection. Analytica Chimica Acta, Elsevier. **460**, pp. 61–72.

[5] Sandeep, S., Santhosh, A.S., Swamy, N.K., Suresh, G.S. and Melo, J.S. 2019, Detection of Catechol using a Biosensor Based on Biosynthesized Silver nanoparticles and Polyphenol Oxidase Enzymes. Portugaliae Electrochimica Acta, Sociedade Portuguesa de Electroquímica. **37**, pp. 257–70.

[6] Wang, G., He, X., Zhou, F., Li, Z., Fang, B., Zhang, X. et al. 2012, Application of gold nanoparticles/TiO2 modified electrode for the electrooxidative determination of catechol in tea samples. Food Chemistry, Elsevier. **135**, pp. 446–51.

[7] Li, M., Ni, F., Wang, Y., Xu, S., Zhang, D., Chen, S. et al. 2009, Sensitive and facile determination of catechol and hydroquinone simultaneously under coexistence of resorcinol with a Zn/Al layered double hydroxide film modified glassy carbon electrode. Electroanalysis: An International Journal Devoted to Fundamental and Practical Aspects of Electroanalysis, Wiley Online Library. **21**, pp. 1521–6.

[8] Ciulu, M., Spano, N., Pilo, M.I. and Sanna, G. 2016, Recent advances in the analysis of phenolic compounds in unifloral honeys. Molecules, Multidisciplinary Digital Publishing Institute. **21**, pp. 451.

[9] Petrovic, M., Farré, M., De Alda, M.L., Perez, S., Postigo, C., Köck, M. et al. 2010, Recent trends in the liquid chromatography–mass spectrometry analysis of organic contaminants in environmental samples. Journal of Chromatography A, Elsevier. **1217**, pp. 4004–17.

[10] Lee, V.B.C., Mohd-Naim, N.F., Tamiya, E. and Ahmed, M.U. 2018, Trends in paper-based electrochemical biosensors: from design to application. Analytical Sciences, The Japan Society for Analytical Chemistry. **34**, pp. 7–18.

[11] Liu, B., Zhuang, J. and Wei, G. 2020, Recent advances in the design of colorimetric sensors for environmental monitoring. Environmental Science: Nano, Royal Society of Chemistry. **7**, pp. 2195–213.

[12] Zhang, Y., Zhou, C., Nie, J., Le, S., Qin, Q., Liu, F. et al. 2014, Equipment-free quantitative measurement for microfluidic paper-based analytical devices fabricated using the principles of movable-type printing. Analytical Chemistry, ACS Publications. **86**, pp. 5–12.

[13] Russell, S.M., Doménech-Sánchez, A. and de la Rica, R. 2017, Augmented reality for real-time detection and interpretation of colorimetric signals generated by paper-based biosensors. Acs Sensors, ACS Publications. **2**, 8, pp. 48–53.

[14] Mahato, K., Srivastava, A. and Chandra, P. 2017, Paper based diagnostics for personalized health care: Emerging technologies and commercial aspects. Biosensors and Bioelectronics, Elsevier. **96, 2**, pp. 46–59.

[15] Emerson, E. 1943, The condensation of aminoantipyrine. II. A new color test for phenolic compounds. The Journal of Organic Chemistry, ACS Publications. **8, 4**, pp. 17–28.

[16] Varadaraju, C., Tamilselvan, G., Enoch, I. M. V. M., & Selvakumar, M. 2018, Phenol sensing studies by 4-aminoantipyrine method—a review. Org. and Med. Chem, **5(2)**, 1-7.

[17] Fiamegos, Y., Stalikas, C. and Pilidis, G. 2002, 4-Aminoantipyrine spectrophotometric method of phenol analysis: Study of the reaction products via liquid chromatography with diode-array and mass spectrometric detection. Analytica Chimica Acta, Elsevier. **467, 1**, pp. 05–14.

[18] de Tarso Garcia, P., Cardoso, T. M. G., Garcia, C. D., Carrilho, E., & Coltro, W. K. T. 2014, A handheld stamping process to fabricate microfluidic paper-based analytical devices with chemically modified surface for clinical assays. Rsc Advances, **4, 71**, pp. 37637-37644.

[19] Soni, A. and Jha, S.K. 2015, A paper strip based non-invasive glucose biosensor for salivary analysis. Biosensors and Bioelectronics, Elsevier. **67, 76**, pp. 3–8.

[20] Christodouleas, D.C., Nemiroski, A., Kumar, A.A. and Whitesides, G.M. 2015, Broadly available imaging devices enable high-quality low-cost photometry. Analytical Chemistry, ACS Publications. **87,** 917, pp. 0–8.

[21] Safarik, I., Baldikova, E., Prochazkova, J., & Pospiskova, K. 2019, Smartphone-based image analysis for evaluation of magnetic textile solid phase extraction of colored compounds. Heliyon, **5(12)**, e02995.

[22] Şengül, Ü. 2016, Comparing determination methods of detection and quantification limits for aflatoxin analysis in hazelnut. Journal of Food and Drug Analysis, Elsevier. **24**, pp. 56–62.

[23] Desimoni, E. and Brunetti, B. 2015, About estimating the limit of detection by the signal to noise approach. OMICS Publishing group.

[24] Vial, J. and Jardy, A. 1999, Experimental comparison of the different approaches to estimate LOD and LOQ of an HPLC method. Analytical Chemistry, ACS Publications. **71**, 267, pp. 2–7.

[25] Lavín, Á., Vicente, J. De, Holgado, M., Laguna, M.F., Casquel, R., Santamaría, B. et al. 2018, On the determination of uncertainty and limit of detection in label-free biosensors. Sensors, Multidisciplinary Digital Publishing Institute. **18**, 2038.

[26] Hosu, O., Lettieri, M., Papara, N., Ravalli, A., Sandulescu, R., Cristea, C. et al. 2019, Colorimetric multienzymatic smart sensors for hydrogen peroxide, glucose and catechol screening analysis. Talanta, Elsevier. **204**, 5, pp. 25–32.

[27] Keshvari, F. and Bahram, M. 2017, Selective, sensitive and reliable colorimetric sensor for catechol detection based on anti-aggregation of unmodified gold nanoparticles utilizing boronic acid–diol reaction: optimization by experimental design methodology. Journal of the Iranian Chemical Society, Springer. **14**, 9, pp. 77–84.

[28] Chen, H., Li, S., Wang, S., Tan, Y. and Kan, J. 2013, A new catechol biosensor immobilized polyphenol oxidase by combining electropolymerization and cross-linking process. International Journal of Polymeric Materials and Polymeric Biomaterials, Taylor & Francis. **62,** 62, pp. 0–6.

[29] Mu, S. 2006, Catechol sensor using poly (aniline-co-o-aminophenol) as an electron transfer mediator. Biosensors and Bioelectronics, Elsevier. **21**, 12, pp. 37–43.

[30] Ameer, Q. and Adeloju, S.B. 2009, Development of a potentiometric catechol biosensor by entrapment of tyrosinase within polypyrrole film. Sensors and Actuators B: Chemical, Elsevier. **140**, pp. 5–11.

[31] Li, D., Pang, Z., Chen, X., Luo, L., Cai, Y. and Wei, Q. 2014, A catechol biosensor based on electrospun carbon nanofibers. Beilstein Journal of Nanotechnology, Beilstein-Institut. **5**, 3, pp. 46–54.

[32] Li, H., Kong, W., Liu, J., Liu, N., Huang, H., Liu, Y. et al. 2015, Fluorescent N-doped carbon dots for both cellular imaging and highly-sensitive catechol detection. Carbon, Elsevier. **91**, pp. 66–75.

[33] Ma, Y., Chen, A.Y., Huang, Y.Y., He, X., Xie, X.F., He, B. et al. 2020, Off-on fluorescent switching of boron-doped carbon quantum dots for ultrasensitive sensing of catechol and glutathione. Carbon, Elsevier. **162**, 2, pp. 34–44.

Kocaeli University

Kocaeli Journal of Science and Engineering
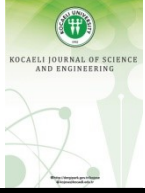
Two Dimensional and Stereo PIV Comparison for Port Applications

Burak YELKEN [1, *] (iD) , İsmail Hakkı SAVCI [2] (iD) , Zafer DÜLGER [3] (iD)

[1] *Department of Mechanical Engineering, Kocaeli University, Kocaeli, 41310, Turkey,* **ORCID:** *0000-0001-6902-8528*
[2] *Ford Otosan R&D Center, İstanbul, 34885, Turkey,* **ORCID:** *0000-0002-7923-6061*
[3] *Department of Mechanical Engineering, Kocaeli University, Kocaeli, 41310, Turkey,* **ORCID:** *0000-0002-5043-788X*

Article Info	Abstract
Research paper *Received* : September 02, 2021 *Accepted* : November 03, 2021 **Keywords** *Swirl* *2D PIV* *Stereo PIV* *Uncertainty Analyze*	Fuel-air movements in-cylinder are one of the most critical diesel engine parameters to determine engine performance and emission. Swirling movement in the engine combustion chamber is investigated advanced experimental techniques to improve the air intake design. Honeycomb measurement method and PIV (particle image velocimetry) method are used to measure the swirling airflow. The honeycomb measurement method can directly measure the swirl. However, it does not give detail information about the flow field. On the other hand, the PIV technique is one of the non-invasive measurement methods for swirl measurement. PIV can directly measure the velocity vector of the cylinder section. In this study, the honeycomb measurement method was performed to measure the swirl ratio of 13L and 9L engines. The uncertainty analysis was determined for the reliability ratio of the measurement. In addition, PIV measurements are performed to understand the velocity field of the cylinder section. This velocity field gives detailed information about the center of the swirl and the velocity index of the velocity field.

1. Introduction

The most important fundamental parameters affecting engine performance are air intake quality, fuel injection values and air-fuel mixture. Therefore, the diesel engine's power, torque, and emissions are specified depending on these three basic parameters.

It is challenging to optimize the combustion phenomenon in the cylinder due to the fuel's high number of combustion parameters and the physics complexity. [1]. Some of these parameters, fuel pressure and droplet size, play a critical role in combustion efficiency. Another factor affecting the combustion quality is the flow structure inside the cylinder at the end of the compression process. The characteristics of flow start from the inlet of the intake port and develop during the combustion process.

When air enters the cylinder, two types of flow motion occur. The first is a swirl motion for a diesel engine and the other is a tumble motion for a gasoline engine. In Figure 1, the left flow represents swirl motion and the right one represents tumble motion [2].
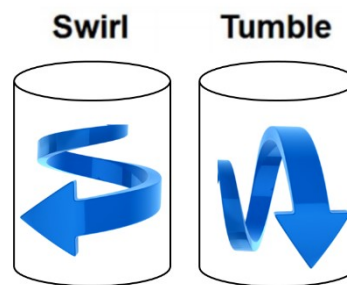
Figure 1. Swirl and Tumble notation [2]

Studies on the vortex motion properties in the cylinder and its effects on the combustion performance are still published. Different test rigs are used for design optimization to obtain the desired swirl pattern in the cylinder.

One of the critical parameters affecting the vortex motion is the engine's air intake duct design. The angular position of the air inlet duct is examined with particle

* Corresponding Author: yelkenburak@yahoo.com

imaging velocity measurement. With this method, the effects of various air intake geometries at different angular positions on the engine performance were analyzed on a test engine. It was found that the swirl and tumble properties were similar between other ports. However, they differ according to angular positions [3]. In terms of the valve's openings in the cylinder head, it has been observed that while the fully open valve gives the most vital large-scale structures, more significant amounts of kinetic energy are converted into small-scale turbulence with smaller openings [4].

One of the biggest challenges of the particle imaging velocity measurement technique is that the swirl motion occurs inside the cylinder. Tests were carried out using a particle imaging velocity measurement technique on a transparent diesel engine to overcome this challenge. The obtained measurement results were analyzed statistically, and the movements between motorcycles were determined by grouping. It has been determined that the swirling motion of the flow, especially between cycles, changes from a vortex to circular type [5]. When using the particle imaging velocity measurement method, the selection of the surface being measured is essential. The swirl mechanism's behavior against time has been studied by taking measurements from different characters and making 2-dimensional and 3-dimensional measurements in the steady-flow state [6]. Similar inspections and tests have been carried out on various engines, such as heavy diesel engines. In the tests performed on the engine, swirl was measured by both torque meter and particle imaging velocity measurement methods. With these measurements, the tangential velocity profile was determined, the measurement results obtained by theoretical calculations were compared, and the turbulence characteristic of the flow was determined [7].

With all these studies, the particle imaging velocimetry measurement technique contains errors and uncertainties as in every measurement. In some studies, velocity measurement with particle imaging has focused on error sources. Mainly, particle density, particle diameter, velocity gradient and particle displacement parameters were studied. A four-dimensional uncertainty surface was created; a methodology was developed by creating a particle imaging measurement method algorithm [8]. Simultaneously, two-dimensional and 3-dimensional measurements were performed using particle imaging velocimetry to minimize the uncertainties in size and reduce the error rate. The error rate was focused on improvements that have been made by making calibration changes [9]. The particle imaging velocimetry measurement method is a technique used by researchers but is still under development. A correlation was obtained in a study between particle image density, particle

properties, and how the peak sizes in the system change for particle imaging velocimetry measurement. As a continuation of this study, interrogation region size, illumination intensity, image size parameters and effects were investigated [10].

Using CFD tools, developing a computational fluid dynamics method for flow factor and swirl ratio is also efficient for studies. It is possible to generate different velocity vectors for various valve openings and compare them with analysis results. It was found that a difference between 5 and 25 percent was observed in the swirl ratio values. However, the analysis could only estimate flow factor values with a difference of 5 percent. [11].

In the literature review studies, it was seen that the particle imaging velocimetry measurement method is still being developed. There are different uncertainty calculation approaches, and it is used by various researchers in other applications and studies. Besides, studies in the literature are carried out with simple test setups [5-7,12]. Therefore, different particle imaging velocimetry measurement methodologies in complex applications such as engine in-cylinder flow are discussed in the completed task.

This study aims to examine different swirl ratio measurement methods and other approaches. Within the study's scope, torque bench measurements at steady flow condition, 2D and 3D particle imaging velocimetry measurements were made on both the 13L engine cylinder head and the prototype part simulating the 9L engine. Swirl rates and swirl properties were investigated. Uncertainty analysis of the measurement results has been completed. The most accurate swirl measurement approach for an engine port in the automotive industry will be examined in detail by comparing different measurement methods.

2. Materials and Methods

Many experimental techniques can be used for performance reviews of internal combustion engines. However, the results for performance review and verification purposes must be collected accurately and in detail. Firstly, the test device's calibration, the test method's repeatability, and the measurement's quality should be assured.

There are different experimental techniques to measure the swirl in diesel engines. These techniques are Laser Doppler Velocitymeter, Anemometer with Hotwire and Particle Image Velocimeter (PIV). Due to the technical imaging used for Laser Doppler Velocitymeter and Particle Imaging Velocitymeter methods, test engines must be designed and manufactured with transparent, optically accessible materials. For this reason, their application is

costly. This reality has led to the creation and development of different swirl ratio measurement methods over time. Engineering firms such as FEV, AVL, and Ricardo have developed their techniques and designed test setups to measure the vortex ratio precisely in a continuous flow state.

In this study, the port swirl ratio measurements were made with the test setup developed by FEV.

2.1 Swirl Ratio Measuring Device – Steady Flow Test Bench

In this study, a steady flow test bench is used to measure the swirl ratio. This method does not include the effect of valve and piston movements. Measurement is performed with constant valve openings and under steady flow conditions.

A steady flow testing mechanism enables air movement measurement, depending on the air suction channel geometry in the engine cylinder. Thus, the performance of the air intake duct to produce swirl and tumble movements can be examined.

In this study, since the vortex movement of the air inside the cylinder in diesel combustion engines is examined, the vortex ratio measurement mechanism will be explained in this section. The steady flow test device, which is used during the tests, is shown in Figure 2. This system determines the swirl ratio for diesel engines and has a module for particle imaging velocity measurement.
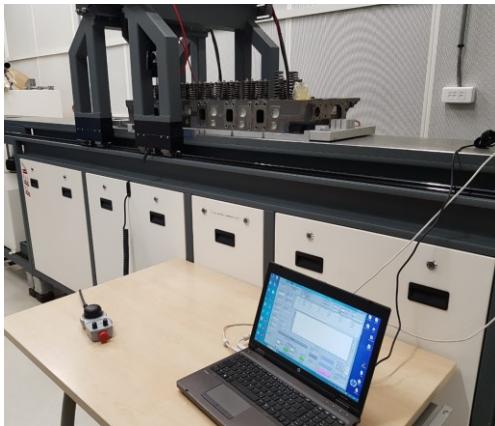
Figure 2. The steady flow test device

In this study, steady-state swirl ratio measurement results will be used as baseline reference measurements. Steady-state swirl ratio measurement with honeycomb is the state-of-the-art method. The honeycomb swirl anemometer's working principle measures the torque value from the honeycomb mounted in the cylinder at the test bench. A blower obtains airflow with constant pressure. The mounted honeycomb does not have any motion. The

tangential component of the airflow creates momentum on the honeycomb geometry in the test bench. The force on the honeycomb is measured with a torque meter. By using this angular momentum value, the swirl ratio is calculated by using the swirl ratio equation. This measurement is repeating for each valve lift starting from 1mm up to maximum valve lift values.

3. Uncertainty Analysis

Test results as a result of each measurement contain uncertainty. Therefore, the first step, PIV testing, should be focused on repeatability. The measured and calculated value's uncertainty should always be determined, expressed numerically. Besides, minimizing these errors will increase the reliability of the study.

It is essential to have a process that characterizes the measurement's quality, is immediately applicable, easily understandable, and generally accepted. This is to calculate and express the uncertainty of the value obtained as a result of the measurement.

The error in the data obtained at the end of the experimental studies can emerge in two different ways. One may be due to the experiment set's structure and measuring devices; the other may be caused by the person experimenting. It is possible to correct such errors with a skilled or trained meter or experimenter. However, it may not always be possible to identify the mistakes caused by test equipment [13].

Many methods can be applied to determine the error rate of the test results values calculated with the data collected from the measuring instruments used in the experiments. One of these is the error analysis of the experimental findings with the uncertainty analysis method developed by Kline and McClintock [14].

Let the magnitude be "R," which is the result function desired to be obtained or determined due to an experimental study if this magnitude is expressed by a function in the format R = R (v1, v2, ...,vn) depending on the measurement sizes v1, v2, ... vn. And, the uncertainty values of these variables are w1, w2, ... wn if the measurement uncertainty of the R-result function is found by the RSS (root sum square) method [13] [15].

Uncertainty w of a variable v is found with the expression;

$$\pm w = k\sqrt{(A_1)^2 + (A_2)^2 + .. + (B_1)^2 + (B_1)^2 + ..} \qquad (1)$$

Here A1, A2, ... show random errors and B1, B2, ... show systematic errors. After the uncertainties resulting from these two types of errors are converted to the same reliability level, they are collected in a vector. The "k"

value here is the "coverage factor" defined above. This method is applied to all measurement variables to find w_1, w_2, ... w_n.

In the Kline and McClintock uncertainty analysis method, if the error rates for each independent variable x_1, x_2, x_3 ..... x_n are w_1, w_2, w_3, ... w_n and the error rate of R size is shown with w_R, Kline and McClintock uncertainty analysis equation is shown as below;

$$w_R = \pm \left[\left(\frac{\partial R}{\partial x_1} w_1 \right)^2 + \left(\frac{\partial R}{\partial x_2} w_2 \right)^2 + \left(\frac{\partial R}{\partial x_3} w_3 \right)^2 + \ldots + \left(\frac{\partial R}{\partial x_n} w_n \right)^2 \right]^{\frac{1}{2}} \quad (2)$$

or

$$\frac{w_R}{R} = \left[\left(\frac{w_{x1}}{x_1} \right)^2 + \left(\frac{w_{x2}}{x_2} \right)^2 + \left(\frac{w_{x3}}{x_3} \right)^2 + \ldots + \left(\frac{w_{xn}}{x_n} \right)^2 \right]^{\frac{1}{2}} \quad (3)$$

The most significant advantage of uncertainty analysis is that the variable causing the most significant error can be detected immediately.

The swirl coefficient value is a dimensionless flow value, and the swirl coefficient formula is given below;

$$D = \frac{M*R_{cyl}}{\rho_{cyl}*\dot{V}_{cyl}^2} = \frac{M*R_{cyl}*\rho_{cyl}}{\dot{m}^2} \quad (4)$$

Here;

D = Swirl coefficient
V_{cyl} = Air flow rate (m^3/s)
M = Moment on honeycomb (Nm)
R_{cyl} = Cylindrical tube radius (m)
ρ_{cyl} = Air density before honeycomb (kg/m^3)

Parameters measured during the experiments are; airflow, temperature, pressure and torque. The error rates given by the test device manufacturer for these parameter measurements are as follows;

Pressure sensor error value;	+/- 0.05 %
Temperature sensor error value;	+/- 0.5 ^{0}C
Flowmeter error value;	+/- 2 %
Torquemeter sensor error value;	+/- 0.1 %

If the formula for value D is remembered to find the uncertainty value of the swirl coefficient,

$$D = \frac{M*R_{cyl}}{\rho_{cyl}*\dot{V}_{cyl}^2} \quad (5)$$

Here;

$$\rho_S = \frac{p_1}{R*T} * \left(\frac{p_2}{p_1} \right)^{\frac{1}{K}} \quad (6)$$

If it is substituted in equation number 5;

$$D = \frac{M*R_{cyl}}{\frac{P_1}{R*T}*\left(\frac{P_2}{P_1}\right)^{\frac{1}{K}}*\dot{V}_{cyl}^2} \quad (7)$$

The uncertainty formula is expressed in the following ways.

$$w_D = \pm \left[\left(\frac{\partial D}{\partial M} w_M \right)^2 + \left(\frac{\partial D}{\partial T} w_T \right)^2 + \left(\frac{\partial D}{\partial P} w_P \right)^2 + \left(\frac{\partial D}{\partial \dot{V}} w_V \right)^2 \right]^{\frac{1}{2}} \quad (8)$$

or

$$\frac{w_D}{D} = \pm \left[\left(\frac{w_M}{M} \right)^2 + \left(\frac{w_T}{T} \right)^2 + \left(\frac{w_P}{P} \right)^2 + \left(\frac{w_V}{V} \right)^2 \right]^{\frac{1}{2}} \quad (9)$$

Similarly, formulas calculated for uncertainty analysis within the mass flow and flow coefficient are given as below.

Mass flow uncertainty analysis;

$$\frac{w_{\dot{m}}}{\dot{m}} = \pm \left[\left(\frac{w_T}{T} \right)^2 + \left(\frac{w_P}{P} \right)^2 + \left(\frac{w_V}{V} \right)^2 \right]^{\frac{1}{2}} \quad (10)$$

Flow coefficient uncertainty analysis;

$$\frac{w_D}{D} = \pm \left[\left(\frac{w_M}{M} \right)^2 + \left(\frac{w_T}{T} \right)^2 + \left(\frac{w_P}{P} \right)^2 + \left(\frac{w_V}{V} \right)^2 \right]^{\frac{1}{2}} \quad (11)$$

If the uncertainty analysis numerical calculation is made for the swirl ratio;

For 13L engine measurements for;

$$\frac{w_D}{D} = \pm \left[\left(\frac{0.1}{70.36} \right)^2 + \left(\frac{0.5}{26.64} \right)^2 + \left(\frac{0.0005}{679,19} \right)^2 + \left(\frac{0.02}{514,67} \right)^2 \right]^{\frac{1}{2}} \quad (12)$$

Uncertainty is calculated as 0,019.
For prototype part measurements that simulate 9L engine;

$$\frac{w_D}{D} = \pm \left[\left(\frac{0.1}{90.44} \right)^2 + \left(\frac{0.5}{27.92} \right)^2 + \left(\frac{0.0005}{610,39} \right)^2 + \left(\frac{0.02}{396,07} \right)^2 \right]^{\frac{1}{2}} \quad (13)$$

Uncertainty is calculated as 0,018.

Uncertainty value has been calculated for all valve openings. It is seen that the uncertainty value of each valve opening is the same when the initial valve openings are ignored. The uncertainty graph for the 9L engine is shown as follows (Figure3).
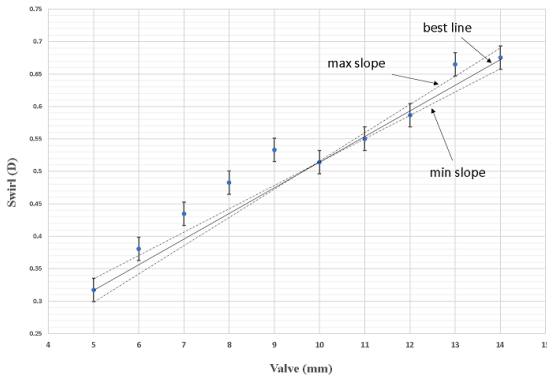
Figure 3. Uncertainty graph of swirl measurement

If numerical calculation is made for uncertainty analysis for mass flow and flow coefficient;

The uncertainty value for mass flow is calculated as 0,019. The uncertainty value for the flow coefficient was calculated as 0,019.

4. Particle Imaging Velocitymeter

A particle imaging velocimeter (PIV) measurement system has a technique that can generate experimental data without interfering with the flow field. Imaging the flow field and obtaining velocity vectors are the outputs of this measurement technique. The PIV system examines the flow field in many branches and verifies the results obtained using the developed computational fluid dynamics methods.

The PIV systems, main elements are double-pulsed laser, high-resolution speed camera, particle generation system, data acquisition system, and computer (Figure 4). The particles whose size and density are determined depending on the fluid type and flow conditions of interest are illuminated on a laser plane. The light scattered from the particles is recorded one after another by the high-resolution speed camera. Velocity vectors are obtained using the particles displacement measurements in a specific time interval by examining two consecutive images.
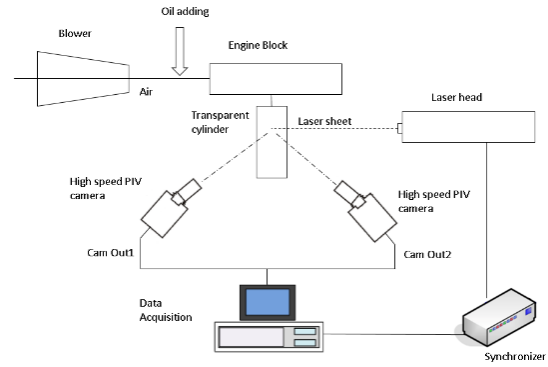
Figure 4. PIV working principle

Depending on the number of high-speed cameras, the test setup is called 2D PIV or 2d/2c if only a single camera is used. A single camera is used to record images and, in turn, measure two velocity components. If two high-speed cameras are used, it is called Stereo PIV or 2d/3c. In this case, two cameras are using different observation angles. So that information on the third (out-of-plane) velocity component can be retrieved (Figure 5).
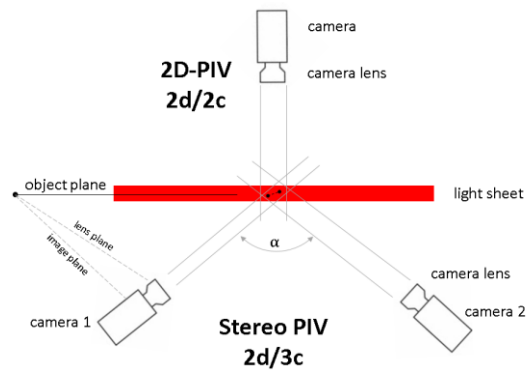
Figure 5. 2d/2c vs 2d/3c PIV measurement system

To perform measurements, the cylinder wall is produced with a transparent material, as shown in Figure 6. In this way, with the two air intake valves opening in the figure, the cylinder's air movements can be displayed by the PIV system. During the transparent cylinder measurement, it is fixed to the cylinder head with the help of a lower piston, and it is ensured that no leakage occurs.
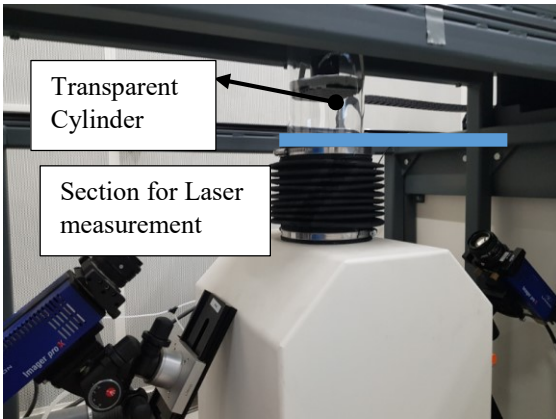
Figure 6. PIV measuring system transparent cylinder wall

4.1. 2D and 3D Particle Imaging Velocitymeter

The particulate air flow sent into the cylinder will be displayed with a CCD camera's help on the created laser plane, as shown in the figure below. (Figure 7)

Before starting the measurement process, calibration of the high-resolution speed camera and the laser plane to be created is required. The calibration plane shown in Figure 8 is used for this calibration process.

After the calibration plane is placed in the transparent cylinder wall for calibration, as in Figure 9, it is determined that the laser beam plane and the calibration plane are matched, and these points appear with the high-resolution speed camera.

Figure 7. 2D PIV test setup PIV

Figure 8. Calibration plane

Figure 9. Calibration plane assembled

Each point on the calibration plane must be seen and marked before testing by the high-resolution speed camera. In the test setup, the high-resolution speed camera angle was measured as 47.6º. As seen in Figure 10, points at this angle were determined, marked and corrected to the computer screen's x-y plane.
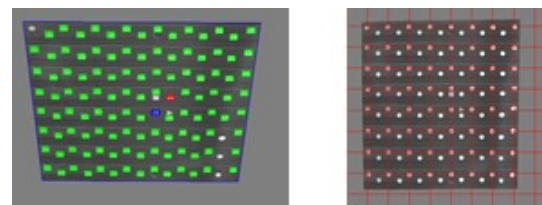
Figure 10. Calibration plane point scan and correction images

Two high-speed cameras (CCD) are used in the 3D PIV measurement system (Figure 11).
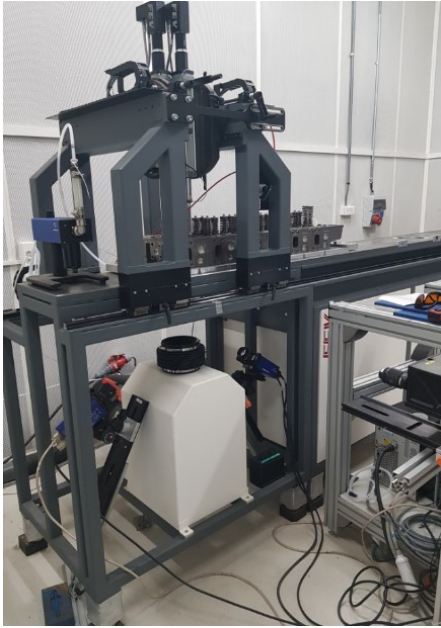
Figure 11. 3D PIV test setup

After the calibration processes are completed, the calibration plane is taken from the transparent cylinder, and the tests are carried out.

5. Steady Flow Test Bench (Honeycomb) and Particle Imaging Velocitymeter Measurement Results

The results are obtained for the steady flow bench for two different engine configurations, as shown in figure 12.

The details of the engine configurations are shown in Table 1

Table 1. Engine Dimensions

	A	B
Cylinder Diameter (mm)	115	130
Number of Cylinder	6	6
Number of Valves	4	4
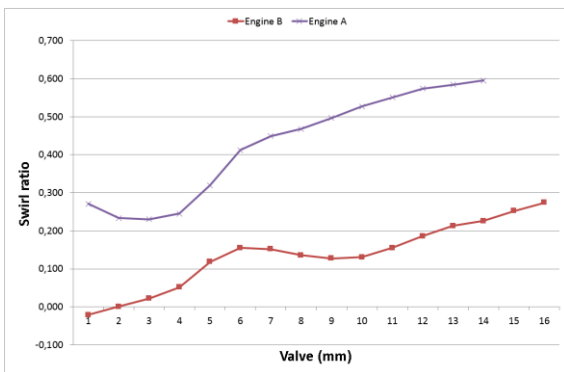
Figure 12. Comparison of the swirl level of two engines

Figure 12 shows the results of the swirl measurement of two engines with different port designs. Engine B has a swirl rate of at least 4-5 times higher than the honeycomb technique measured in engine A. All results at this figure. However, measuring the air distribution from the ports in the cylinder is critical to understand the swirl rates. For this, the PIV method can be used to measure the airflow in the cylinder. When measuring at different valve heights, it is sufficient to measure with a single camera when using the 2d PIV method, while two cameras should be used for 2d / 3c PIV. However, in 2d PIV, fast but low-accuracy measurements are made by a single camera, while the 2d / 3c PIV method enables complex but highly accurate measurements. With this study, the measurement approaches will be discussed for the engine port application.

For the 2d / 2c setup, measurements are made on a slice parallel to the y-z plane along the piston bowl's axis. The laser plate illuminates the plane in the negative z-direction, and the camera focuses the aircraft from a 45-degree perspective. The spatial resolution is about 2mm. The data were averaged from 100 snapshots. The left side of the plane becomes a distorted image due to its angular appearance. Velocity information cannot be captured accurately at the edges. The 2d / 3c PIV experiments use the setup shown in figure 4. The two cameras are mounted between 45 degrees in the opposite direction. Calibration adjustments are made with the images obtained from two cameras.

Figure 13 shows the 2d flow distribution of Engine A for an 11mm valve lift. Test results are shown that the swirl value of the honeycomb measurement and 2d PIV measurement is slightly different. The swirl ratio of the honeycomb measurement is 0.55, but the 2d PIV measurement is 0.68. So, PIV measurement techniques should be improved.
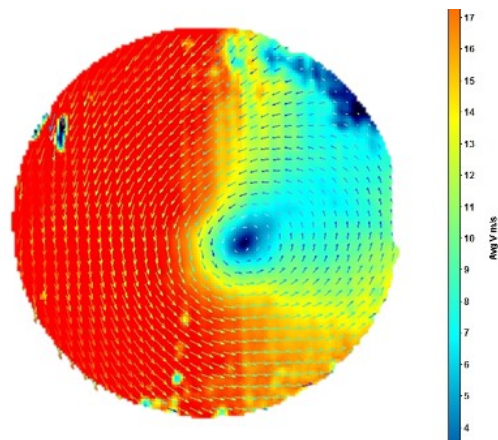
Figure 13. 2d PIV Measurement

Figure 14 shows the 2d/3c flow distribution of Engine A for an 11mm valve lift. The center of the velocity is close to the center of the circle. Velocity index is typically used to define the location of the high-velocity flow. [16] The swirl ratio of the 2d/3c measurement results is 0.58.
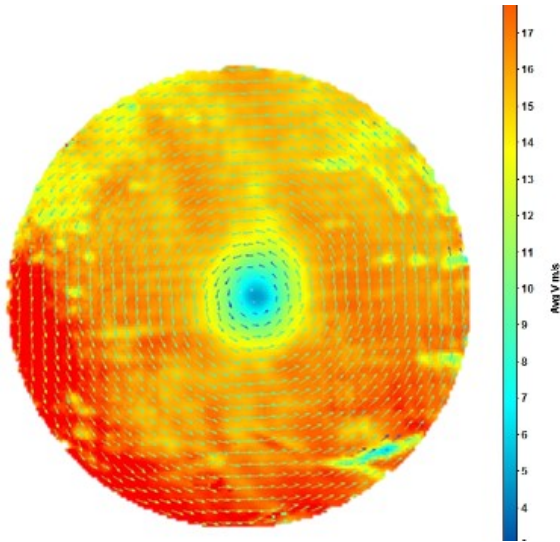
Figure 14. 2d/3c PIV Measurement

Figure 15 shows Engine A's 2d and 2d / 3c flow distributions for an 11 mm valve lift. The 2d and 2d / 3c measurement techniques were compared in terms of velocity index and swirl ratio. The velocity index of 2d PIV is 0.45, and the 2d / 3c PIV speed index is 0.51. The differences are 11.8%. As a result of the measurement made with these two methods, the swirl ratio difference is 12 percent. Besides, making the comparison with the reference measurement shows that the 2d / 3c method gives a closer result.

2d/2c and 2d/3c methods were compared with Engine B, lower swirl ratio. Figure 16 shows the 2d and 2d/3c flow distributions of Engine B for an 11 mm valve lift. Velocity distributions of the two methods for Engine B have similar results to Engine A.
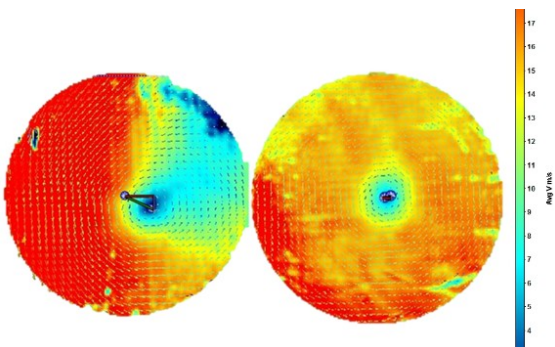
Figure 15. 2d-2d/3c PIV measurement results for a high swirl case (Engine A)

Figure 16 shows the 2d and 2d / 3c flow distributions of Engine B for an 11mm valve lift. Again, the results of the 2d and 2d / 3c measurement techniques are comparable for Engine B in terms of the velocity index and swirl ratio.
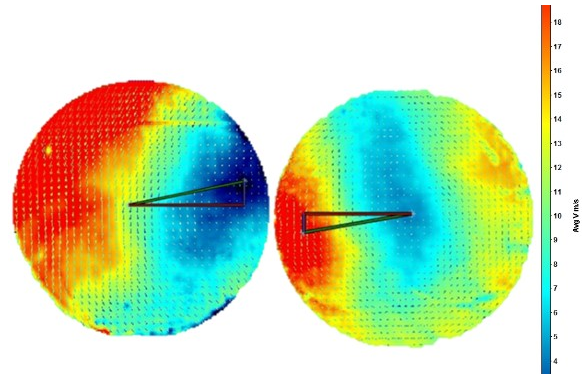
Figure 16. 2d-2d/3c PIV measurement results for low swirl case (Engine B)

When compared to the measurement results in figure 15 and figure 16, it is seen that while a swirl center of Engine B is formed slightly in the cylinder, the speed distribution has accumulated on one side of the cylinder. On the contrary, in Engine A, the flow rate is spread more homogeneously around the swirl center.

6. Conclusions

In this work, port performance is investigated experimentally by honeycomb torque measurement and PIV methods. Nevertheless, the PIV measurements are provided by insightful information on port measurement's velocity structure in terms of the velocity magnitude and velocity structure. MATLAB tool is developed based on the PIV results. This tool generates the velocity index, flow distributions and distance of the velocity index from the center.

An objective of the study was the investigation of the suitability of the PIV techniques for port measurement. PIV measurements can be performed by either 2d PIV or 2d/3c PIV. The advantage of the 2d PIV is being easy to setup and measure.

Furthermore, the experimental measurements demonstrate that 2d PIV cannot measure velocity distribution and velocity index for high swirl ratio case well, but 2d/3c measurement is comparable with the honeycomb measurement method. Besides, 2d PIV and 2d/3c PIV measurements show a similar velocity index but a different velocity distribution for the low swirl ratio case.

Declaration of Ethical Standards

The authors of this article declare that the materials and methods used in this study do not require ethical committee permission and/or legal-special permission.

Conflict of Interest

The authors declare that they have no known competing financial interests or personal relationships that could have appeared to influence the work reported in this paper.

References

[1] Heywood, J., 1988. Internal Combustion Engine Fundamentals, McGraw-Hill, New York, USA.

[2] Yelken, B., Savcı, İ.H., Dülger, Z., 2021. Investigation of air movement in cylinder in diesel internal combustion engines and comparison of measurement methods. Engineers and Machinery, **62**(703), pp.221-244.

[3] Bottom, K.E., 2003. PIV measurements of in-cylinder flow and correlation with engine performance, Ph.D. thesis, University of Wisconsin – Madison, Wisconsin.

[4] Vester, A.K., Nishio, Y., Alfredsson, P.H., 2019. Investigating swirl and tumble using two prototype inlet port designs by means of multiplanar PIV. International Journal of Heat and Fluid Flow, **75**, pp.61-76.

[5] Cosadia, I., Bore´e, J., Charnay, G., Dumont, P., 2006. Cyclic variations of the swirling flow in a diesel transparent engine. Experiments in Fluids, **41**, pp.115–134.

[6] Rabault, Jean, Vernet, Julie, Alfredson, Per-Henrik, 2016. A study using PIV of the intake flow in a diesel engine cylinder. International Journal of Heat and Fluid Flow, **62**, pp.56-67.

[7] Doosje, E., Bastiaans R.J.M., Baert, R.S.G., 2004. Application of PIV to characterize the Flow-Phenomena of a Heavy-Duty Cylinder Head on a Stationary Flow-Bench. In Particle Image Velocimetry: Recent Improvements, pp. 301-313.

[8] Timmins, Benjamin H, 2011. Automatic particle image velocimetry uncertainty quantification, Utah State University Ms.C. thesis, pp. 67-68.

[9] Abe, M., Longmire, E. K., Hishida, K. and Maeda, M., 2000. A Comparison of 2D and 3D PIV Measurements in an Oblique Jet. Journal of Visualization, **3** (2), pp.165-173.

[10] Warner, Scott O., 2012. Autocorrelation-based estimate of particle image density in particle image velocimetry, Utah State University Ms.C. thesis, pp. 49-51.

[11] Dwarshala, S., Vandana, S., and Rambhaji, G., 2016. Computation and validation of in-cylinder flow field, swirl and flow coefficients for a naturally aspirated single-cylinder diesel engine. SAE Technical Paper, 2016-28-0018.

[12] Özgün, Ö., Kumlutaş, D., Yücekaya, U. A., 2017. Investigation of flow structures with three dimensional background positioned density difference (schlieren) method and verification with particle imaging velocity measurement. Engineers and Machinery, **58**(687), pp.29-40.

[13] Onan, Cenk, 2013. Investigation of heat and mass transfer from moving liquid film at the exterior surface of pipes, Ph.D. Thesis, pp.104-111.

[14] Kline, S.J. ve McClintock, F.A., 1953. Describing uncertainties in single-sample experiments. Mechanical Engineering, **75,** pp.3–8.

[15] Sadıkov E., Kangı R., Uğur S, 1995. Measurement uncertainty, TÜBİTAK Marmara Research Center National Metrology Institute, pp.55-61.

[16] Leong W.A., Eroglu S and Guryuva S.,2012. Using STAR-CCM+ for Catalyst Utilization Analysis. Paper presented at Star Global Conference, Amsterdam, 19-21 March.
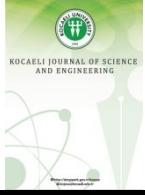
The Effects of Design Parameters on The UNICORE Type Transformer Inrush Current

Mehlika SENGUL [1, *] (iD) , Bora ALBOYACI [2] (iD) , Mehmet Aytac CINAR [3] (iD) , I. Gursu TEKDEMİR [4] (iD)

[1] Faculty of Aeronautics and Astronautics, Kocaeli University, Kocaeli, 41285, Turkey, **ORCID:** 0000-0003-0882-3901
[2] Faculty of Engineering, Kocaeli University, Kocaeli, 41380, Turkey, **ORCID:** 0000-0002-1117-0326
[3] Izmit Vocational School, Kocaeli University, Kocaeli, 41285, Turkey, **ORCID:** 0000-0002-1655-4281
[4] Faculty of Engineering and Natural Sciences, Bursa Technical University, Bursa, 16310, Turkey, **ORCID:** 0000-0003-1381-3513

Abstract

In this study, it is aimed to fill the information gap about the effects of designed parameters in UNICORE type transformers inrush current. Considered prameters are the flux density, the core construction and the lamination thickness of the transformers. In this context, the UNICORE transformer was compared with the conventional wound core (CWC) transformer by using three-dimensional finite-element configuration. In order to get real system response, the study was carried out experimentally. Analyzing the test results, the effects of the core material and design parameters on the magnitude, duration and harmonic content of inrush current on these types of transformers were detected. Tests were performed by using a programmable power source and analyzed data sets were recorded by scopemeter.

1. Introduction

A transformer is a static machine used for transforming electrical power from one alternating voltage level to another with the same frequency by electromagnetic induction [1].

Transformer energization is a workaday operation which is being performed frequently in an electric power system. A transformer no-load current is generally at a level of 1-2% of the rated current, but it may be as high as 10-20 times of the rated current, which decreases to a magnetizing current over time when the transformer is energized [2-3]. This current is called magnetizing inrush current. The decaying time of the inrush current depends on the resistance and reactance of the transformer equivalent circuit. If the inductance is high, it takes longer time for the circuit to switch to a steady state condition. The critical inductance value here is directly related to the transformer's magnetizing reactance.

So, design parameters of the transformer core have become more of an issue to reduce excitation current and so reducing the inrush current. For the last few years, core design has been getting more importance. The development of the transformer design philosophy has been extended by use of computers and numerical tools. By means of these tools, it is enabled to model the geometrical complexities as well as the nonlinear material characteristics accurately for problem analysis. And using this program, different transformer designs have been generated and tested to get more efficient models. One of these new transformer core designs is called UNICORE.

UNICORE is a new type of magnetic core technology which was developed in 1997 in an attempt to make the conventional machine structure simpler and to improve the performance of electric machine magnetics behaviour [4,5].

Important advantages of this manufacturing technology are the decreased magnetic flux saturation by means of healed magnetic flux density distribution reduced

---

* Corresponding Author: mehlika@kocaeli.edu.tr

eddy-current losses and excitation current by means of uniformed magnetic flux density, increased efficiency and improved performance [6].

In this study, with the present detrimental effects of major inrush currents of transformers in mind, it is intended to understand the effect of core material and design parameters on the inrush current and to present the improved effects of the UNICORE technology.

2. Magnetizing Inrush Current at Transformers and Analized Parameters

Magnetizing current occurs in both no-load and loaded working conditions at transformers. No-load current is the sum of magnetizing current and core-loss, and it is about 1-2% of the rated current of the transformer in a steady-state condition, so it is neglected generally. But this is not always the case. When the transformer is energized, the amount of the current increases dramatically [2,3,7].

When a transformer is de-energized, the excitation current becomes zero by following the hysteresis curve. However, the flux drops to a steady-state Ør (remanent flux) value - not to zero - during the same process. When the applied voltage is zero, and the transformer is re-energized, flux starts to rise from the remanent flux level and reaches its peak value after an energization for a time period of 180° in sine. Because of the increment of the flux in the core, magnetizing current may reach 10-20 times the rated current [9]. This event is called magnetizing inrush [10]. The voltage considering the change in flux can be defined as below.

$$u = N\frac{d\Phi}{dt} \qquad (1)$$

where N and Φ are the turns number of the primary winding and magnetic flux in the core, respectively. Applied voltage is:

$$u = U_m sin(\omega t + \varphi) \qquad (2)$$

where U_m and φ are the maximum value of the applied voltage wave and the phase angle of the voltage wave, respectively. Substituting Eq. (2) in Eq. (1) and by using integration;

$$\frac{d\Phi}{dt} = \frac{U_m}{N}sin(\omega t + \varphi) \qquad (3)$$

$$\Phi = -\frac{U_m}{N\omega}cos(\omega t + \varphi) + k \qquad (4)$$

is obtained. Thus, as it is seen in Eq. (5) the maximum flux is equal to coefficient of the cosine function.

$$\Phi_m = \frac{U_m}{N\omega} \qquad (5)$$

The k is calculated by considering the initial condition which is t=0 and $\Phi(0) = \Phi_r$,

$$k = \Phi(t) + \Phi_m cos(\omega t + \varphi) \qquad (6)$$

where Φ_r is the remanent flux in the core. The final equation of the flux in the core is given by;

$$\Phi(t) = \Phi_r + \Phi_m[cos\varphi - cos(\omega t + \varphi)] \qquad (7)$$

The flux in the core is related to the energization angle and the remanent flux as can be seen from Eq. (7). The transient component of the flux wave decreases in conjunction with the primary winding resistance (R1) and the inductance (L1) values of the transformer - with a ratio of R1/L1 [6].

From the above-defined Eq. (7), it can be seen that if the transformer is switched on at the zero angle of the voltage wave, flux starts to rise from a remanent flux level and reaches its peak value after an energization for a time period of 180° in sine. The peak value of flux is two times of nominal maximum (Øm) plus remanent flux (Ør) in the core.

$$\Phi = \Phi_r + 2\Phi_m \qquad (8)$$

As in no-load energizing, similar transients can occur when the loaded transformer is energized. However, when the load resistance is included in the transformer equivalent circuit, the damping speeds up and the level of harmonic distortion in total current decreases.

Inrush current magnitude is related to some magnetic parameters like the core material magnetic characteristics, magnetic remanence and mechanical parameters like the moment when the transformer is energized, etc [11,12].

Remanent flux can be positive or negative. This can cause an increment or decrement in magnetizing inrush current. If the remanent flux has same the direction with the created flux at the first instant after switching the transformer, in the positive half cycle the inrush current occurs otherwise causes to reduce the inrush current and in the negative half cycle, the inrush current will be maximized [13,14].

In this study, remanent flux is reduced to zero. For this purpose, transformers were energized randomly and then de-energized at the instant of positive maximum voltage level by using a programmable power source. And then inrush currents of the tested transformers were analyzed in terms of point-on-voltage wave and transformer core material and design.

And also, since the magnetizing inrush current is

nonlinear, it contains harmonic components. By using Fourier series analysis, the harmonic levels of the magnetizing inrush current are estimated. During the transformer inrush conditions, even harmonics are dominant and especially the second harmonic component is effective. Thus, the second harmonic component is selected as the basis for inrush current.

2.1. The Effect of Point-on-Voltage Wave

The most significant factor is the point-on-voltage wave at the moment of energization. Transformer energization angle affects the peak value of inrush current. From the above-defined Eq. (7), it can be seen that if the transformer is switched on at the zero angle of the voltage wave, flux starts to rise from the remanent flux level and reaches its peak value after 180° of energization. The peak value of flux is two times of nominal maximum Φ_m plus remanent flux Φ_r in the core.

Under normal operating condition, the core flux is Φ_m and the core of the transformer is operating at the knee of the B-H curve. In order to produce the flux in Eq. (8), the current required will be extremely high because of the nonlinear nature of the B-H curve and drives the core material into saturation. This results in heavy inrush current into the transformer.

2.2. The Effect of The Core Material and Design

The power transformer design affects the transformer core saturation during inrush events. The design of the core, the flux density of the steel and the connection method of the laminations all impact the magnitude and characteristics of the magnetizing inrush current [16].

Due to ongoing research and development efforts [17] by steel and transformer manufacturers, core materials with improved characteristics are getting developed and applied with better core building technologies. Remarkable stages of core material development are cold rolled grain oriented (CRGO), hot rolled grain oriented (HRGO), high permeability cold rolled grain oriented (Hi-B), non-oriented, mechanically scribed and laser scribed. Thus, using lower thickness laminations eddy losses are reduced. The decrease in the lamination thickness leads to a quadratic decrease of the classical eddy current loss [18-20]. The popular thickness range is 0.23 mm to 0.35 mm for power transformers. Core materials are generally sorted as M2 (H1), M3 (H0), M4, M5, M6 and MOH.

A more significant change has been in the construction of the core. Stacking laminations on top of each other, an air gap between each lamination is created. As a result of this, the reluctance of the core increases.

Laminations are now constructed such that they overlap each other to provide a continuous path for the flux when the laminations are stacked one above the other. The reluctance in the core is reduced in this construction, and, therefore, the flux density increases, and the exciting current reduces. But there is still an air gap.

The most common used transformer joint types are non-mitred and mitred joints. Manufacturing of nonmitred joints, in which the overlap angle is 90°, is quite simple, but the corner joint losses are more since the flux in the joint region is not along the direction of grain orientation. In the case of mitred joints, the angle of overlap (α) is of the order of 30° to 60°, the most commonly used angle is 45°. In mitred joints, the flux crosses from limb to yoke along the grain orientation minimizing losses.

In recent years, studies about core designing for decreasing the core loss have been continued. In this study, test transformers with core designs, which are called UNICORE, are examined in terms of inrush current. The test transformers were analyzed at the energization conditions. Magnitude, decaying time and the harmonic component of inrush current of the test transformers were examined in terms of core material and design.

3. Unicore Transformers and Performed Analysis

3.1. Unicore Transformers and Comperation with The Conventional Wound Core (CWC) Transformer

In a bolted yoke construction, which ensures rigidity of the core, holes are punched in the yoke laminations. Small guiding holes are needed to facilitate the placement of laminations and core buildings.

There is a significant contribution of limbs and yokes joints to the core loss due to cross-fluxing and crowding of flux lines in them. Hence, if the corner area and weight are higher, the core loss will be higher. So UNICORE type transformers have less core loss from classically designed transformers.

UNICORE constitutes a new line of cores of magnetic circuits. It was the aim to simplify the existing technology and improve the parameters of electrical machines of the manufacturing technology development in 1997. The technology of OWC (octagonal wound core), called Unicore technology [21], is very flexible, highly accurate, repeatable, and reliable. Unlike the production of CWC [20,21]. Cores can be supplied with an annealed or unannealed finish. Depending on the core size, subsequent annealing of cores decreases losses by 10 to 30%. The core angle of a UNICORE can be either 30°, 45° or 90° depending on their use.
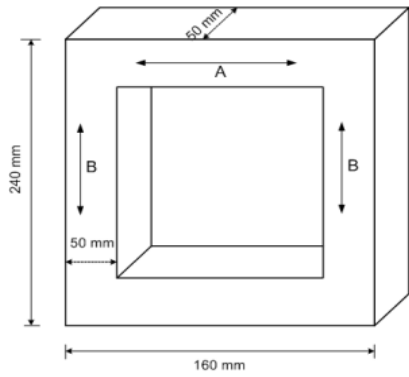
Figure 1. Dimensions of the tested transformers.

To compare the UNICORE transformer and CWC transformer, sample transformers were designed. The dimensions of the designed transformer are seen in Figure 1. It is targeted to determine the magnetic flux distributions and excitations currents of these two types of transformers. So three-dimensional finite-element method (FEM) was used.

The magnetic flux density of shell-type tested transformer is seen in Fig.2-a. It is seen that the distribution of magnetic flux density in the corners is so weak.
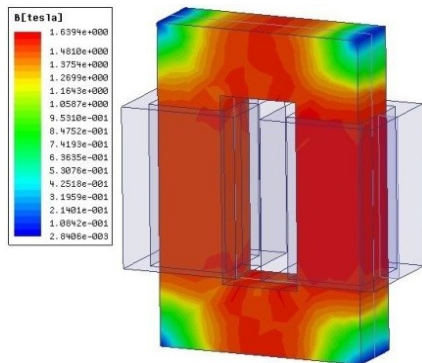
Figure 2. (a) Shell-type single phase transformer core analysis
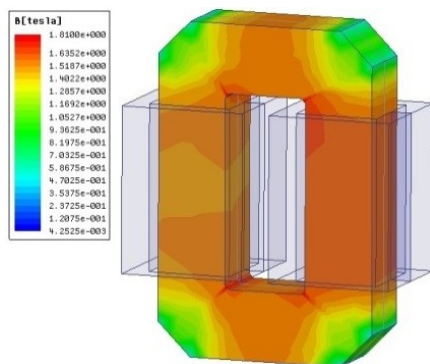
Figure 2. (b) UNICORE single phase transformer core analysis.

The same transformer parameters are used for analyzing the UNICORE transformer. It is seen in Fig.2-b that there is no unused region in the core. So, the eddy-current losses of this type of transformer are less than the conventional transformers. And also, excitation currents of these two types of transformers are shown in Fig.3. It is shown that the no-load current of the UNICORE type transformer is less than classical core type transformer one.
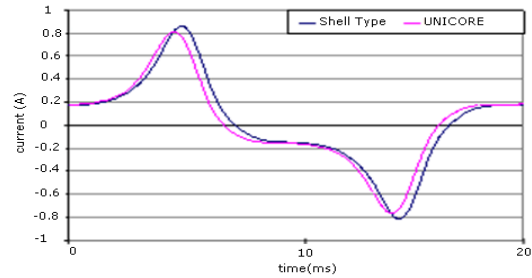
Figure 3. No-load currents of CWC and UNICORE transformers [22].

So, in this study for the detailed analysis of the UNICORE transformers, nine different UNICORE transformers whose constructions and design parameters are different from each other were used. The parameters of the designed transformers are given in Table-1.

3.2. Laboratory Test Set Up for The Measurement and Performed Analysis

The experiments were set up according to Fig.4. Nominal voltage magnitude was applied to the test transformers by using California Instruments 4500LX programmable power source. Data sets were recorded by Scopemeter 199-C. Obtained data sets were analyzed by using MATLAB software. Recorded data sets are sampled at 1kHz (which means 20 samples on 50 Hz power frequency) and harmonic components are obtained by using Fourier Analysis in MATLAB.
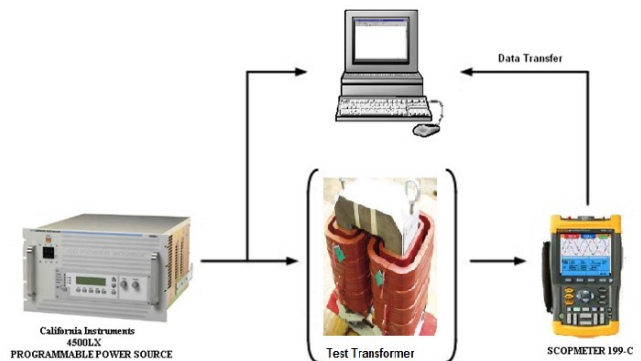
Figure 4. Experimental set up

To compare the transformer's true behaviors, test transformers were energized at the zero-flux level. For this purpose, transformers were energized randomly and after the transformer has reached steady state-conditions deenergized at the instant of positive maximum voltage level by using a programmable power source.

After that, each tested transformer is energized at different points of the sine wave. The applied energization angles (t_i) are 0º, 10º, 20º, 30º, 40º and 50º. (Fig.5)
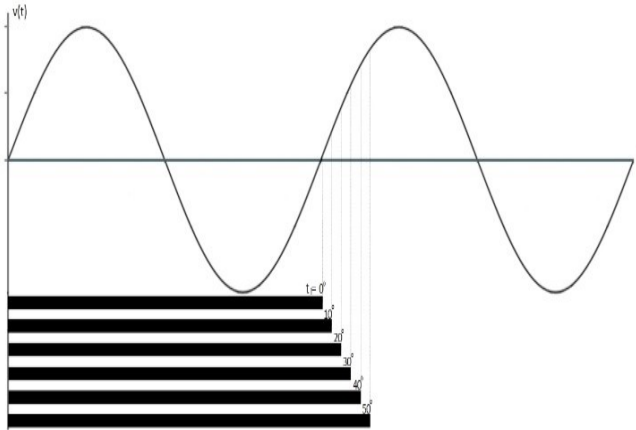
Figure 5. The transformer energization points of sine wave

Before each energization, residual fluxes of all tested transformers were made zero.

Comparing inrush currents of transformers, it is seen that the relationships of these currents are similar for each energization angle. So that in this study the current waveforms are given for just energization at 0º of sine wave.

3.3. The Tested Unicore Transformers and The Analyzed Parameters

In this study, 1kVA, 220/110V single phase UNICORE transformers with core materials M5 and MOH, were analyzed. All used transformer design parameters and core materials are given in Table-1 and construction of the core is given in Figure 1.

The flux density of the steel, the material of the core, and the method of connecting the laminations all affect the amount and characteristics of the magnetizing inrush current. In this section, maximum value, harmonic components, decaying time of inrush current and the ratio of second harmonic current to the fundamental current were analyzed using test transformers. The transformers are grouped such that only one of their design parameters is different.

Table 1. Design parameters and core materials of the test transformers.

Core construction	Core material	Designed flux density	Primary and secondary winding turn numbers
	TR1-M5	1	396/198
	TR2-M5	1,5	264/132
	TR3-M5	1,7	232/116
	TR4-M5	1,5	264/132
	TR5-M5	1,5	264/132
C-CORE	TR6-M5	1,5	264/132
	TR7-MOH H2-0.23	1,5	264/132
	TR8 MOH-0.27	1,5	264/132
	TR9-MOH-0.35	1,5	264/132

3.3.1. The Effect of Core Design on Unicore Transformer

In this section, four transformers (tr2-tr4-tr5-tr6) are compared. Primary and secondary winding section areas and turn numbers, lamination thickness and used materials, yoke and leg dimensions and designed flux densities of these transformers are the same. The only difference is the core construction. Each tested transformer is energized at different points of sine a wave. The applied energization angles are 0º, 10º, 20º, 30º, 40º and 50º. Before the

energization residual fluxes of all tested transformers were made zero by deenergizing the randomly energized tested transformers at the instant of positive maximum voltage level. Comparing inrush currents of transformers, it is seen that the relationships of these currents are similar for each energization angle. So that in this study the current waveforms are given for just energization at 0º of sine wave. Inrush currents of these transformers are as in Figure 6.

It is seen that tr-6 has maximum inrush current magnitude in the first cycle. When core constructions are examined, it is realized that the air gap in this transformer is larger than the others. Core reluctance increases by the air gap so that magnetic efficiency of the core decreases. So, the flux density decreases and exciting current increases. An increase in the required exciting current leads to an increase in the magnetizing inrush current. Steady-state exciting currents can be seen in Figure 6 (in detail).

Harmonic content is as important as the magnitude of inrush current when inrush detection is in question. To maintain the security of the system, transformer differential relays are restrained by the second harmonic component during transformer inrush case. So harmonic components and ratio of the second harmonic component to fundamental harmonic component of inrush currents are analyzed too. In Figure 7 the ratio of second harmonic current to the fundamental current of four transformers are given.

Maximum inrush current is observed in tr-6, but decaying time of the ratio of second harmonic component to the fundamental component is the shortest one. Because the exciting current of this transformer is maximum (zoomed part in Figure 6), the fundamental component of this current is also maximum (Figure 8). So that decaying time is shorter than the others.

3.3.2. The Effect of Core Lamination Thickness on Unicore Transformer

In this section, three transformers (tr7-tr8-tr9) are compared. Primary and secondary winding section areas and turn numbers, used materials, yoke and leg dimensions, designed flux densities and core constructions of these transformers are the same. Only the core lamination thickness is different.

Transformer core is made of thin isolated steel called laminations and carries flux linked to windings. If the laminations have lower thickness, the eddy losses will be lower too for the same level of flux density (Eq. (9)).

$$P_e = k_1 f^2 t^2 B_{rms}^2 \tag{9}$$
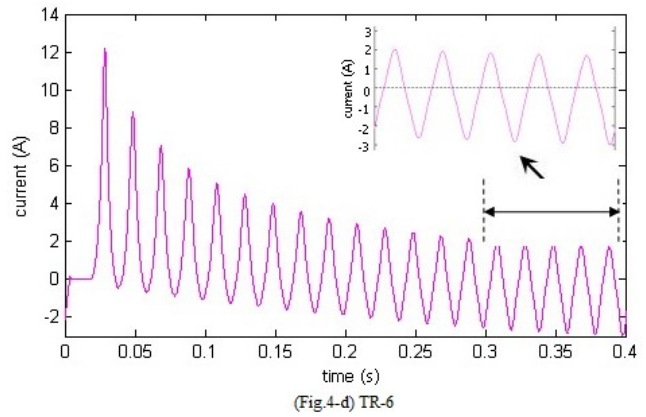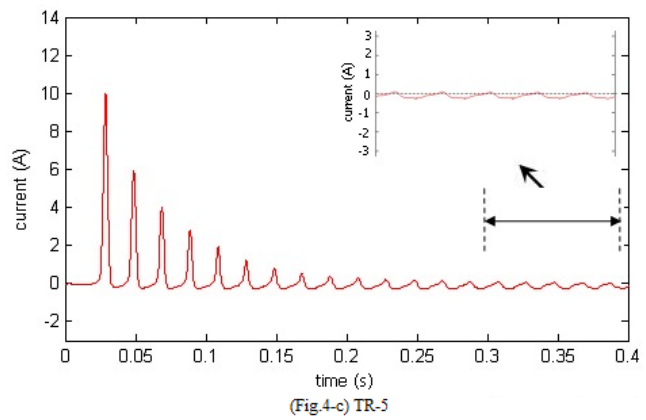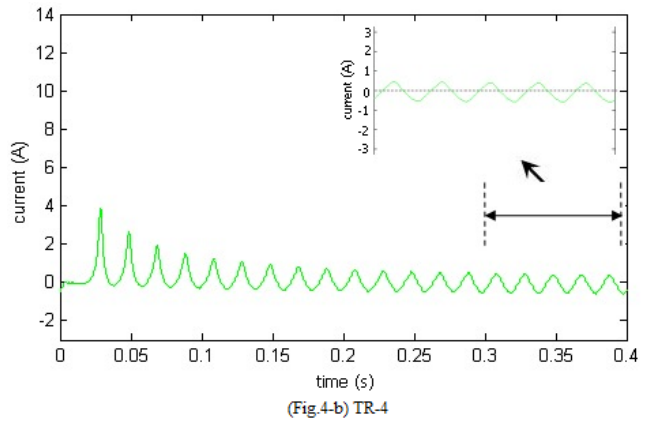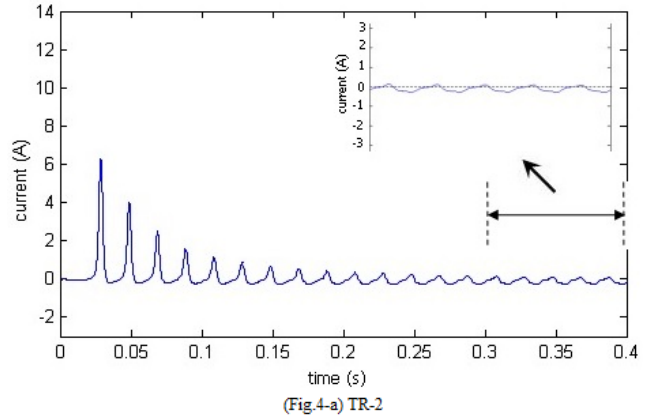
Figure 6. Inrush currents of the transformers-2-4-5-6.

(Fig.5-a) TR-2

(Fig.5-b) TR-4

(Fig.5-c) TR-5

(Fig.5-d) TR-6
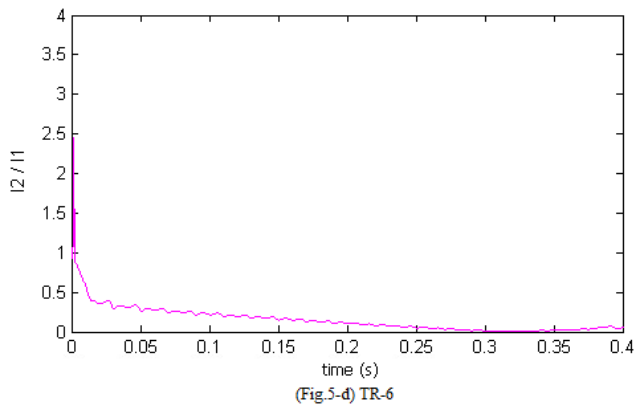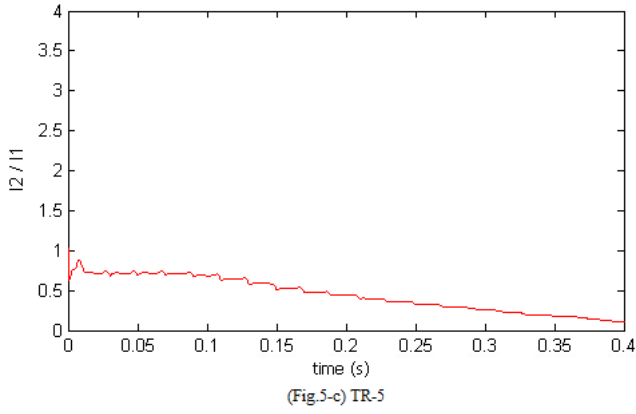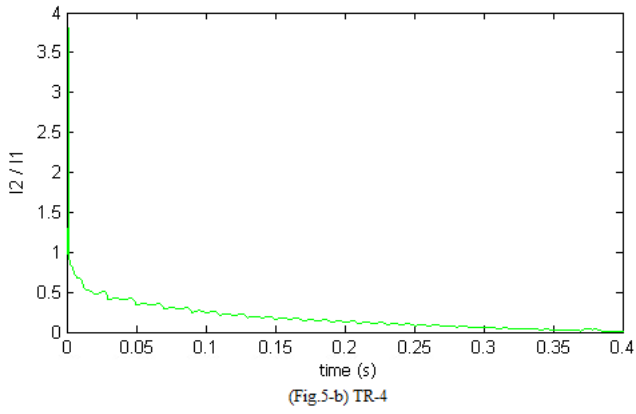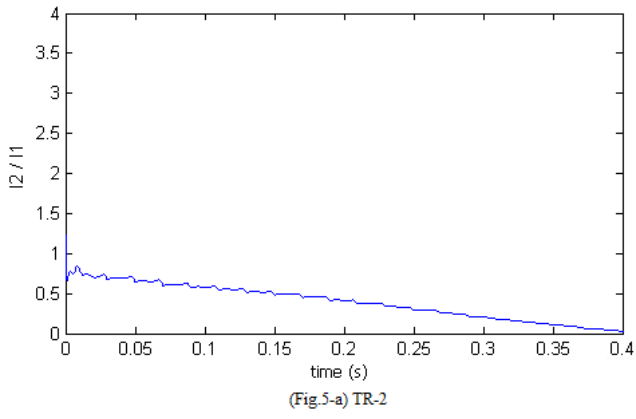
Figure 7. The ratio of the second harmonic current to the fundamental current of the transformers-2-4-5-6.

Figure 8. Harmonic components of inrush currents of the transformers-2-4-5-6.

(Fig.7-a) TR-7

(Fig.7-b) TR-8

(Fig.7-c) TR-9
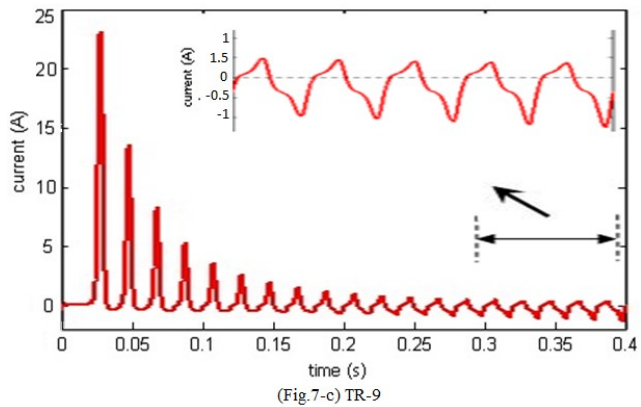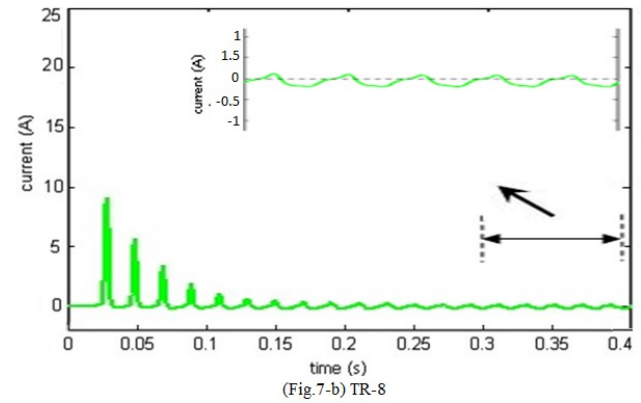
Figure 9. Inrush currents of the transformers-7-8-9.

where P_e, t, k_1, f and B_{rms} are the eddy loss, thickness of individual lamination, constant which depends on material, frequency and the rated effective flux density related with the actual rms voltage on the sine wave basis, respectively.

In this test group, the lamination thickness of the TR-9 is the greatest one, so eddy losses of this transformer are greater than the others. If eddy losses of a transformer, which is a part of iron losses that is called no-load losses of a transformer, are high, then the no-load current will also be high. At the zoomed part in Figure 9, it is seen that the steady state no load current (exciting current) of the TR-9 is higher than the others. An increase in the required exciting current leads to an increase in the magnetizing inrush current (Figure 9).

Because the exciting current of the TR-9 is the maximum (zoomed part in Figure 9), the fundamental component of this current is also maximum (Figure 11). So that, decaying time is less than the other transformers (Figure 10). On the other hand, the exciting current and therefore inrush current of the tr-11 is higher than the others, that's why the harmonic components of the tr-9 are higher. It is seen in Figure 11.

3.3.3. The Effect of Designed B (Flux Density) on Unicore Transformer

In this section, three transformers (tr1-tr2-tr3) are compared. Primary and secondary winding section areas, used materials, yoke and leg dimensions, core constructions and core lamination thickness of these transformers are the same. The only difference is the designed flux densities obtained by different turn numbers.

If the transformer design induction level increases, the hysteresis loss will increase. Because the hysteresis loss is a part of the no-load loss; the no-load loss will increase at the same time. High no-load loss causes high steady state no-load current. At the zoomed part in Figure 12, it is seen that exciting current of the TR-3 is higher than the others. Increase in the required exciting current leads to an increase in the magnetizing inrush current (Figure 12). Peak inrush current increases as the design induction level increases. The reason of this is the core saturation for a greater part of the voltage cycle [23].
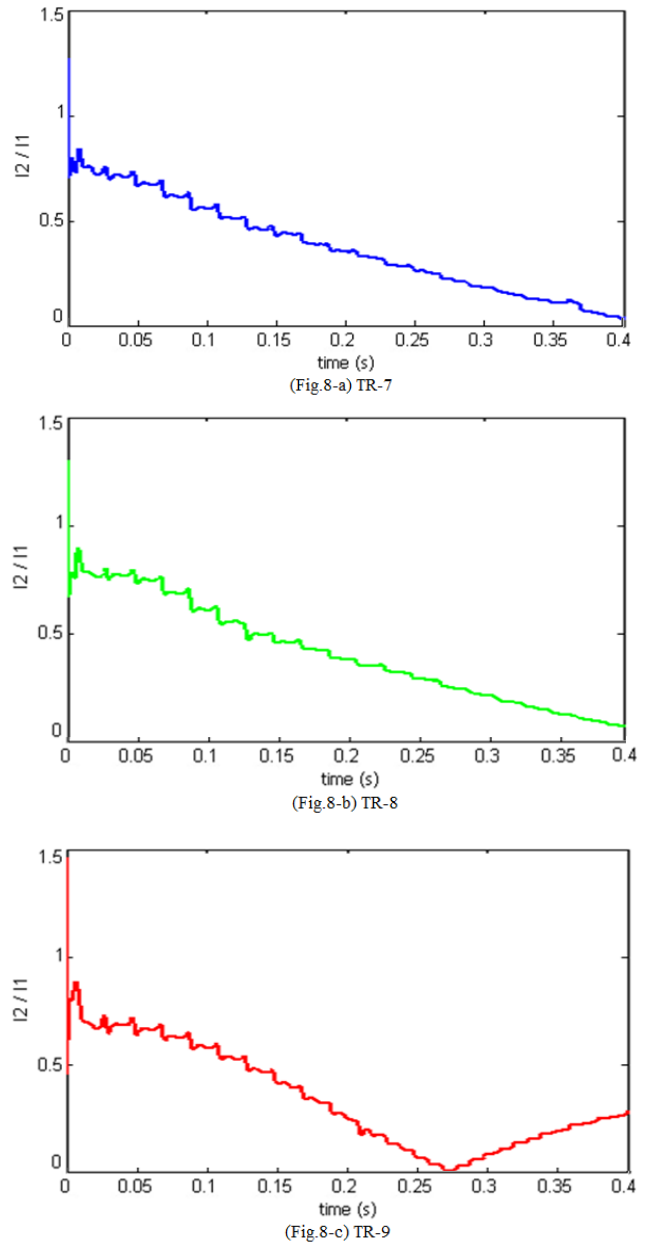
Figure 10. The ratio of the second harmonic current to the fundamental current of the transformers-7-8-9.
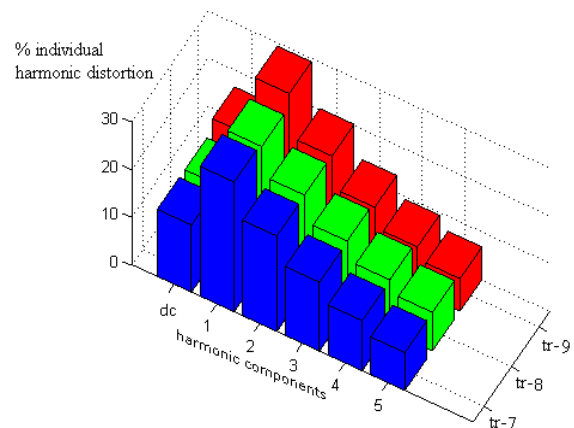
Figure 11. Harmonic components of inrush currents of the transformers-7-8-9.
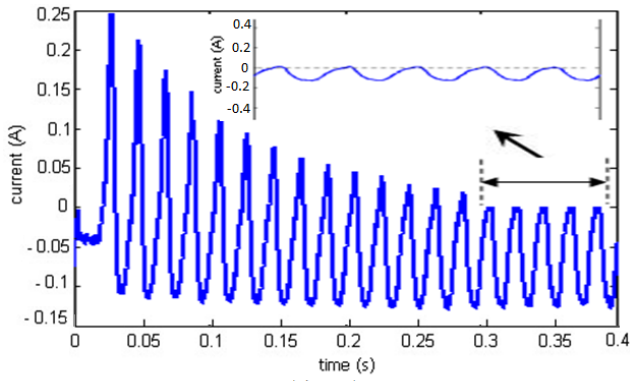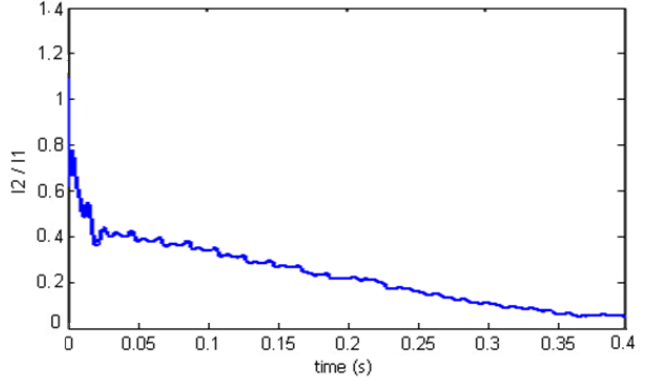
(Fig.10-a) TR-1
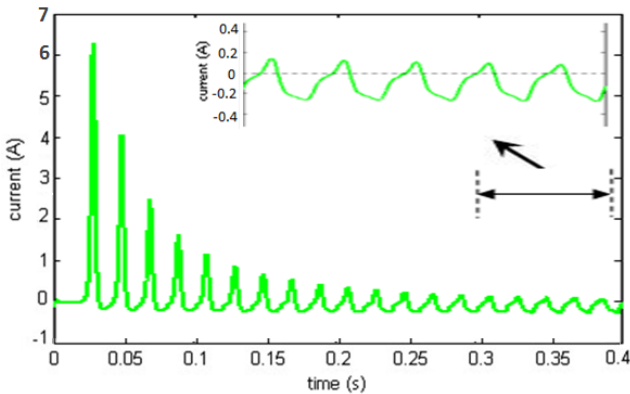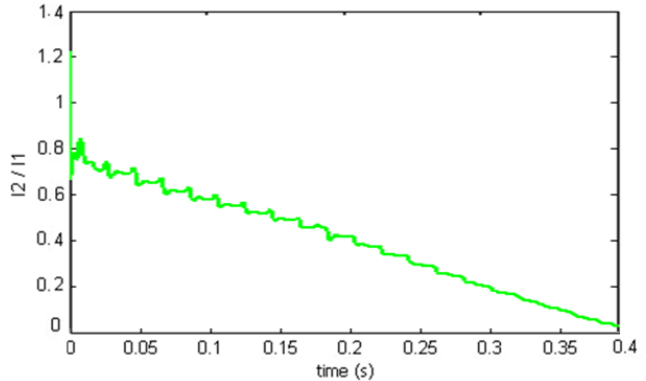
(Fig. 10-b) TR-2
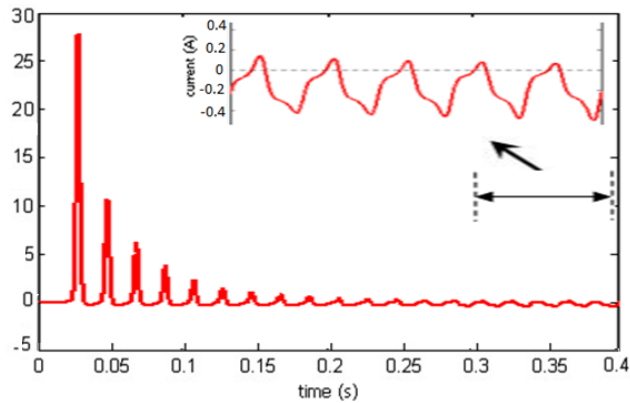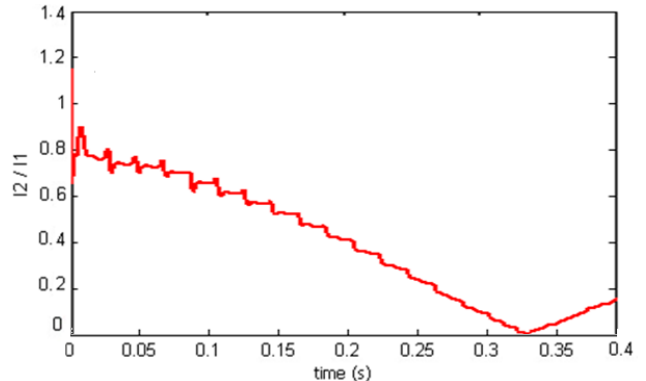
(Fig.10-c) TR-3

Figure 12. Inrush currents of the transformers-1-2-3.

(Fig.11-a) TR-1

(Fig.11-b) TR-2

(Fig.11-c) TR-3

Figure 13. The ratio of the second harmonic current to the fundamental current of the transformers-1-2-3.

The distortion of the exciting current may be reduced if the transformer core is designed for and operated at very low flux densities. The TR-1 is designed at low flux density, and it is seen that the exciting current is nearly linear. So, the inrush current of this transformer contains a low level of harmonic currents. If the designed flux level of a transformer is increased, the exciting current waveform will be away from linearity (zoomed part in Figure 12) and so harmonic components of this current will increase. It is seen in Figure 14.

Figure 14. Harmonic components of inrush currents of the transformers-1-2-3.

4. Conclusions

Comparing the CWC transformers with the UNICORE transformers, it is seen that the excitation current and eddy-current losses are less in the UNICORE transformers. So, in this study, the transformers which are constructed by using this new line cores were analyzed in terms of magnetizing inrush current magnitude, duration and harmonic content. To reduce the exciting current and the magnetizing inrush current, it is important to construct the transformer with lower losses. For this purpose, more efficient steel must be used in the core and designed flux density must be limited. In this study, inrush currents of the nine different UNICORE transformers were compared by considering the parameters below:

If the length of the air gap in the joint regions increases, the reluctance of the core increases. So, the flux density decreases and exciting current increases. Increase in the required exciting current leads to an increase in the magnetizing inrush current. If the exciting current increases, the fundamental component of inrush current increases. So, the decaying time of the ratio of the second harmonic component to the fundamental component is reduced.
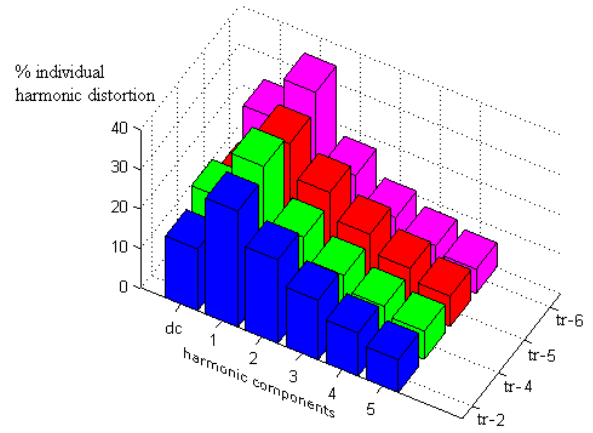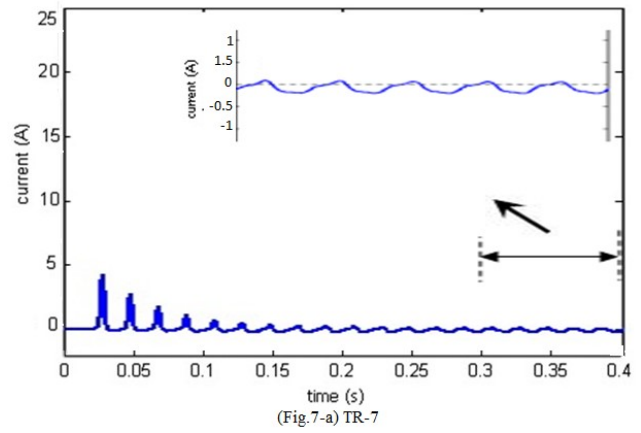
If the lamination thickness of the transformer is increased, eddy losses of the transformer increase. If the eddy-current losses are high, the excitation current will also be high. An increase in the required exciting current leads to an increase in the magnetizing inrush current. If the exciting current increases, the fundamental component of inrush current also increases. So, the decaying time of the ratio of the second harmonic component to the fundamental component is reduced.

If the design induction level of a transformer is higher, the hysteresis loss will be greater. Because of the fact that hysteresis loss is a part of the no-load loss; the no-load loss will rise at the same time. High no-load loss causes high steady state exciting current. Increase in the required exciting current leads to an increase in the magnetizing inrush current. So, the decaying time of the ratio of the second harmonic component to the fundamental component is reduced.

Declaration of Ethical Standards

The authors of this article declare that the materials and methods used in this study do not require ethical committee permission and/or legal-special permission.

Conflict of Interest

The authors declare that they have no known competing financial interests or personal relationships that could have appeared to influence the work reported in this paper.

References

[1] Georgilakis P. S., 2009. Spotlight on Modern Transformer Design, London, U.K.: Springer.

[2] Blume L. F., Camilli G., Farnham S. B., and Peterson H. A., 1994. Transformer magnetizing inrush currents and influence on system operation. AIEE Trans., **63**, pp. 366-375.

[3] Tseng H. T., Chen C. F., 2012. Voltage compensation-type inrush limiter for reducing power transformer inrush current. IET Electric Power Appl., **6**(2), pp. 101-110.

[4] Hernandez I., Olivares-Galvan J.C., Georgilakis P. S., Canedo J. M., 2010. A Novel Octagonal Wound Core for Distribution Transformers Validated by Electromagnetic Field Analysis and Comparison with Conventional Wound Core. IEEE Transactions on Magnetics, **46**(5), pp. 1251-1258.

[5] Hernandez I., Olivares-Galvan J.C., Georgilakis P. S., Canedo J. M., 2014. Core loss and excitation current model for wound core distribution transformers. International Transactions on Electrical Energy Systems, **24**(1), pp. 30-42.

[6] Hernandez I., Olivares-Galvan J.C., Georgilakis P.S., Canedo J.M., 2010. A Novel Octagonal Wound Core for Distribution Transformers Validated by Electromagnetic Field Analysis and Comparison with Conventional Wound Core. IEEE Transactions on Magnetics, **46**(5), pp.1251-1258.

[7] Yabe K., 1997. Power Differential Method for Discrimination between Fault and Magnetizing Inrush Current in Transformers. IEEE Transactions on Power Delivery, **12**(3), pp. 1109-1118.

[8] Shrikrishna V., KulkarnI.,Khaparde S.A. , 2004. Transformer engineering: design and practice.Marcel Dekker Inc.

[9] Wang F., 2001. On Power Quality and Protection Technical Report. Department of Electric Power Engineering Chalmers University of Technology Gutenberg, Sweden.

[10] Hurwitz S.H., Padre A.G., 1995. Power System Relaying. John Wiley Sons Ltd.

[11] Kulidjian A., Kasztenny B., Campbell B., 2001. New magnetizing inrush restraining algorithm for power transformer protection. IEEE Developments in Power Sys. Protec. Conf., pp. 181-184.

[12] Bronzeado H.S., Brogan P.B., Yacamini R., 1996. Harmonic Analysis of Transient Currents During Sympathetic Interaction. IEEE Transactions on Power Systems, **11**(4), pp. 2051-2056.

[13] Sengul M, Ozturk S., Cetinkaya H.B., Erfidan T., 2006. New Phenemenon on Power Transformers and Fault Identification Using Artificial Neural Networks. ICANN, Lecture Notes in Computer Science, **4132**, pp. 767-776.

[14] Darabi A., Khosravi M., 2009. Inrush current analyzing in the transformers based on preisach model. IJTPE Journal, **1**(1), pp. 48-53.

[15] Lin C.E., Cheng C.L., Huang C.L., Yeh. J.C., 1993. Investigation of Magnetizing Inrush Current in Transformers. IEEE Transactions on Power Delivery, **8**(1), pp. 255-263.

[16] Hunt R., Schaefer J., Bentert B., 2008. Practical experience in setting transformer differential inrush restraint. Protective Relay Engineers 61st Annual Conference, pp. 118-141.

[17] Baehr R., 1993. Up-to-date possibilities for further improvement of power transformer magnetic circuit features. International Summer School of Transformers, ISST'93, Lodz, Poland.

[18] Olivares-Galvan J C., Georgilakis P. S., Campero-Littlewood E., Escarela-Perez R., 2013. Core lamination selection for distribution transformers based on sensitivity analysis. ElectrEng, Springer-Verlag, **95**(1), pp. 33-42.

[19] Ionel D., Popescu M., McGilp M. I., Miller T. J. E., Dellinger S. J., Heinemann R. J., 2007. Computation of core losses in electrical machines using improved models for laminated steel. IEEE Trans. Ind. Appl., **43**(6), pp.1554-1564.

[20] Ionel D., Popescu M., Dellinger S. J., Miller T. J. E., Heinemann R. J., McGilp M. I., 2006. On the variation with flux and frequency of the core loss coefficients in electrical machines. IEEE Trans. Ind. Appl., **42**(3), pp.658-667.

[21] Aem Unicore-Innovation in Transformer Cores and Manufacturing Data Catalog. Gillman, Australia: Aem cores PTY, LTD., Oct. 2008.

[22] Alboyaci B., Cinar M.A., Sengul M., 2011. Transformator Manyetik Yapisinin Bosta Calisma Akimina Etkisi (The effect of magnetic structure on the no-load current of the transformer). IV.EVK Symposium, pp.88-91.

[23] Girgis R. S., Tenyenhuis E. G., 2007. Characteristics of inrush current of present designs of power transformers. IEEE PES, pp.1-6.

Kocaeli University

Kocaeli Journal of Science and Engineering

http://dergipark.org.tr/kojose
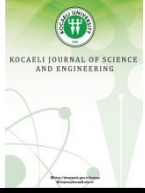
Arsenic Removal Technologies: Mapping Global Research Activities (1970-2019)

Kemal AKTAŞ [1, *] (iD) , I. Ethen KARADIREK [2] (iD) , Duygu Hazal GOKTEPE [3] (iD) , Meltem ASILTURK [4] (iD) , Ayca ERDEM UNSAR [5] (iD)

[1] Department of Environmental Engineering, Akdeniz University, Antalya, 07058, Turkey, **ORCID:** 0000-0001-5526-110X
[2] Department of Environmental Engineering, Akdeniz University, Antalya, 07058, Turkey, **ORCID:** 0000-0003-3689-4125
[3] Department of Environmental Engineering, Akdeniz University, Antalya, 07058, Turkey, **ORCID:** 0000-0002-1374-7424
[4] Department of Material Science and Engineering, Akdeniz University, Antalya, 07058, Turkey, **ORCID:** 0000-0001-8447-5684
[5] Department of Environmental Engineering, Akdeniz University, Antalya, 07058, Turkey, **ORCID:** 0000-0003-3296-1247

Abstract

Arsenic contamination in drinking water poses worldwide threat to public health and requires emergency actions in some parts of the world. Several technologies have been used to overcome arsenic contamination issues and to meet the arsenic concentration limitations for public health. In this study, research tendencies on arsenic removal technologies were evaluated. A total of 4083 publications, published between 1970 and 2019, on arsenic removal from drinking water, groundwater and wastewater were retrieved from Web of Science (WoS) database. A bibliometric analysis was carried out and word frequency along with visualization map analysis were used to provide a quantitative analysis, and an overview on the current research trends and research prospects. The results showed that annual output of the "arsenic removal" subject increased significantly after the year 2000. "Article" was the most preferable publication type, and "Journal of Hazardous Materials" had the highest publication number. The most productive country in terms of number of total articles on arsenic removal was China. Also, the South-East Asian countries highly contributed to the literature. "Adsorption" was found to be the most frequently researched arsenic removal technology and nanotechnology plays a significant role in the adsorption development.

1. Introduction

Arsenic (As) is a prevalent element which can be found in air, soil, water, and living organisms. It is the 18th most common element in the universe, the 20th in the earth's crust, the 14th in the seawater, and the 12th in the human body [1]. This abundance is mostly caused by soil erosion, mineral ore formation, volcanic, geothermal, and hydrothermal activity [2]. It has several oxidation states (-III, 0, +III, +V), among those forms +III and +V states are mostly found in natural systems [3] as a part of dissolved oxyanions such as, arsenite (AsO_3^{-3}) and arsenate (AsO_4^{-3}) [4]. Inorganic As compounds are classified as "Group 1" carcinogens by International Agency for Research on

Cancer [5] and recognized as toxic by many authorities such as World Health Organization (WHO) and United States Environmental Protection Agency (USEPA). Toxicity of As depends on chemical forms and oxidation states, and is due to reversible reactions with thiol groups and phosphorus substitution [6]. In addition, physical state, particle size, absorption rate and chemical structure of arsenic compounds have important role on toxicity as well [7]. Inorganic arsenic is highly associated with skin, lung, urinary system, liver cancers, and other serious cancer types [8]. 200 million people are exposed to As concentration of higher than 50 μg L^{-1} globally,[9]. In South and South-East Asia, 100 million people face risk of arsenic contamination. As contamination is critical in countries like Bangladesh [10], Chile [11], Taiwan [12], Vietnam [13], Argentina [14] due to geological characteristics. Arsenic crisis has been affecting millions

---

* Corresponding Author: kemalaktas301@gmail.com

of people in nearly 70 countries and causing adverse health effects [15]. On the ground of high toxicity and serious health effects induced by As, WHO lowered As limit in drinking water to 10 µg L^{-1} in 1993 [16]. European Union (EU) passed council directive that accepted the same limit for bottled water in 1998 [17]. USEPA accepted the same limit for drinking water in 2001 [18]. There are numerous As removal technologies, such as oxidation, coagulation, ion exchange, membrane filtration and adsorption technologies [19,20]. Researchers have often used nanomaterials for As removal as nanomaterials provide exceptionally high surface areas, catalytic activity and versatility via surface-functionalization [21,22]. However, residual contamination levels are higher than the water quality standard [19]. Coagulation process uses positively charged coagulants to stabilize negatively charged suspended solids. Usually, addition of metal salts, such as alum salt, starts the flocculation process and can be removed from the bottom of the tank. Oxidation processes uses different oxidants (chloride and ozone) to oxidize and remove pollutants from water. Ion exchange is a physical-chemical process that exchanges ions within solid resin. There are two types of resins: anion and cation. Membrane filtration is a barrier between two phases. These phases could be layers, film, or different structures. Usually, arsenic removal technologies are successful at removing highly contaminated water to certain levels.

Bibliometric analysis uses scientific data within science by quantitative analysis [23]. Basically, it is a methodology that conducts quantitative analysis and statistics to illustrate patterns, global trends, and research productivity of certain constituents, such as key word, topic or title. In this study, bibliometric analysis was used to evaluate literature in Web of Science (WoS) database from 1970 to 2019 regarding As removal from drinking water, groundwater and wastewater. This study aims to describe the publication pattern, to evaluate national and organizational contributions and to provide insights regarding most relevant technologies and future trends on As removal.

2. Materials and Methods

A bibliometric analysis was carried out using the Web of Science (WoS) database. The topic search that traces related information in the abstract, keywords and title was utilized to obtain publications from WoS database. Different combinations of words related to arsenic removal was used to retrieve publications. The key terms and the combinations of key terms are arsenic + removal + ("drinking water"/ "waste water"/ "ground water"/ groundwater / wastewater). "arsenic" and

"removal" were always used in the search and one of the given keywords were added to retrieve publications. Different combinations of key terms used in the study are given in Table 1.

Table 1. Different combination of key terms

Keywords	Number of Publications
Arsenic + removal + "drinking water"	2144
Arsenic + removal + "waste water"	463
Arsenic + removal + "ground water"	100
Arsenic + removal + groundwater	1011
Arsenic + removal + wastewater	365
Total	**4083**

As, water, groundwater, drinking water, wastewater and removal were not included in the frequency analysis as they were used in the database search. Different forms of words such as As (V), arsenic (V), As-V and arsenate; As (III), arsenic (III), As-III and arsenite; iron, ZVI, nZVI, zerovalent, zero-valent; nanoparticle, nanoparticles; membrane and membranes, ion exchange, ionexchange and ion-exchange were merged into one category in the frequency analysis. Publications from 1970 to 2019 were downloaded from WoS online database. Data retrieved from WoS database were pre-processed, each publication was evaluated, and duplications were removed. A total of 4739 publications were reduced to 4083 after removing duplications. Reference type of publications, distribution of major journals, contribution of countries were analyzed and visualization map analysis was conducted. Contribution of countries and institutions were identified by the country of the affiliation of at least one author of the publication [24]. Bibexcel that is freely available versatile bibliometric toolbox [25] was utilized for frequency analysis in keywords, titles, and abstracts. Network diagram of cooperation between countries was visualized by VOSviewer [26]. Retrieved publications were also evaluated in three separate terms for determination of research tendencies, hotspots and prospects on As removal studies

3. Results and Discussion

3.1. Publication Outputs

The overview of As removal research retrieved from WoS database is given in Fig. 1. A total of 4083 publications related to As removal from various water

resources including wastewater were found in the WoS database. The number of publications demonstrate a growing trend since 1990s, although there are some exceptions such as the year 2006 and 2015. The first publication was in 1973 and there were only 3 publications in 1993. A total of 85 publications were obtained in WoS database in the 1970-1999 period while 928 publications were obtained in the 2000-2009 period, and 3070 publications were obtained in the 2010-2019 period. The most productive year was 2019 with 449 publications. Time periods were chosen according to publication numbers and legislations regarding As limitations. Growing trend since 1990s is consistent with As legislations introduced by WHO in 1993, EU in 1998, and USEPA in 2001. The number of publications on arsenic removal has increased significantly after USEPA's legislation in 2001. This correlation might suggest

USEPA's drinking standard had the highest impact on the science community. However, synergistic effect of EU and WHO should be considered. In addition, advancing technologies that enable researchers to detect arsenic more accurately and social impacts of arsenic poisonings cannot be overlooked. Publication types were analyzed, and various types were found in the total of 4083 publications. Type of a publication is non-exclusive hence any given publication can be classified in more than one category. Thus, the number of publications in a category is more than total publication number. Article was the most favorable way of contribution to WoS, followed by proceedings papers and reviews. The most favorable research areas are Engineering, Environmental Science/Ecology and Chemistry, which are compatible with literature [15,27]**.**
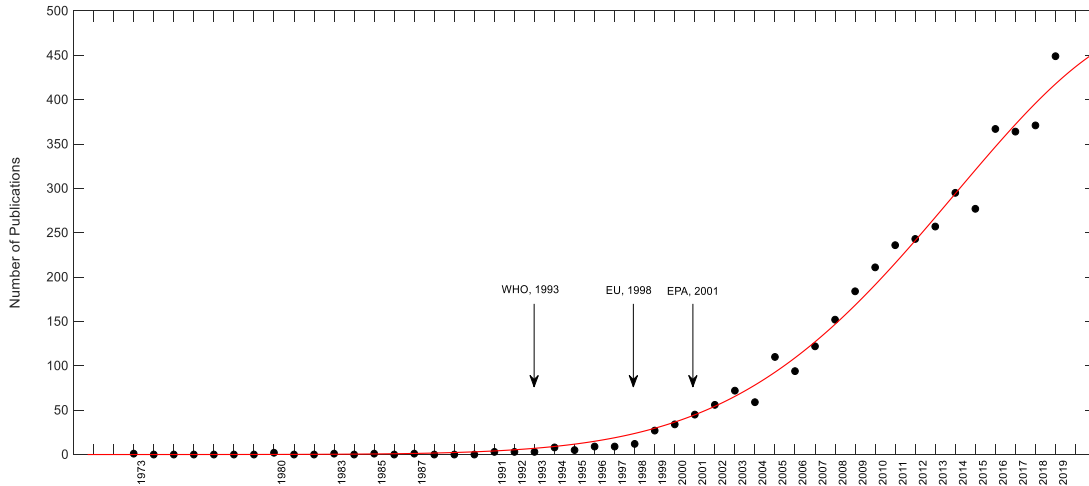
Figure 1. Worldwide overall publications on As removal
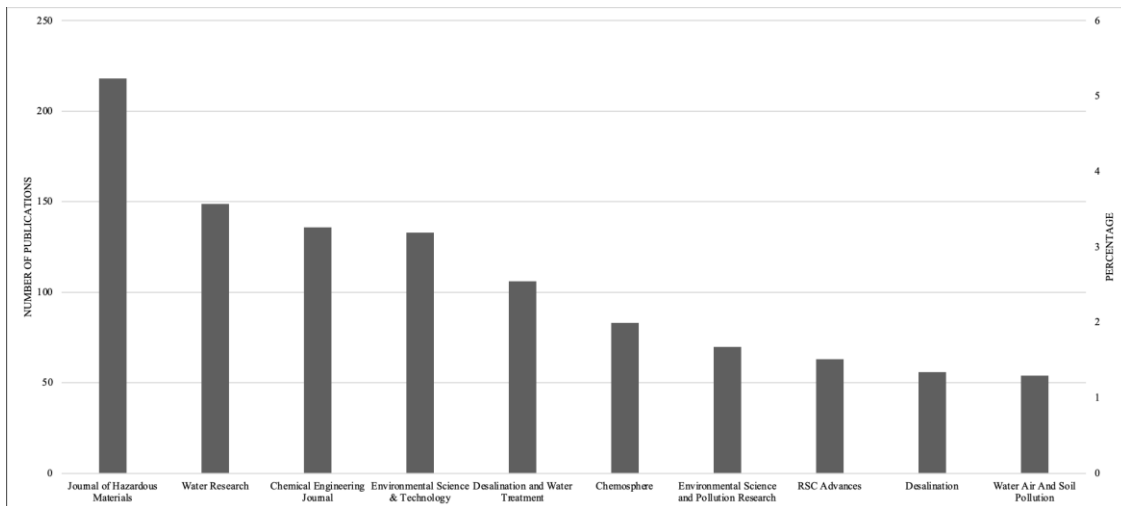
Figure 2. The most productive journals
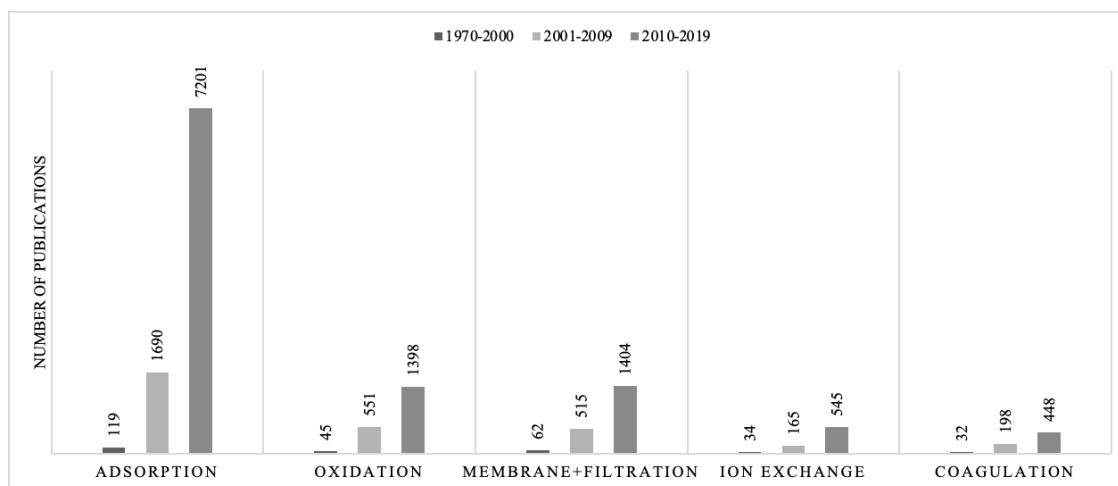
Figure 3. Evolution of As removal technologies since 1970
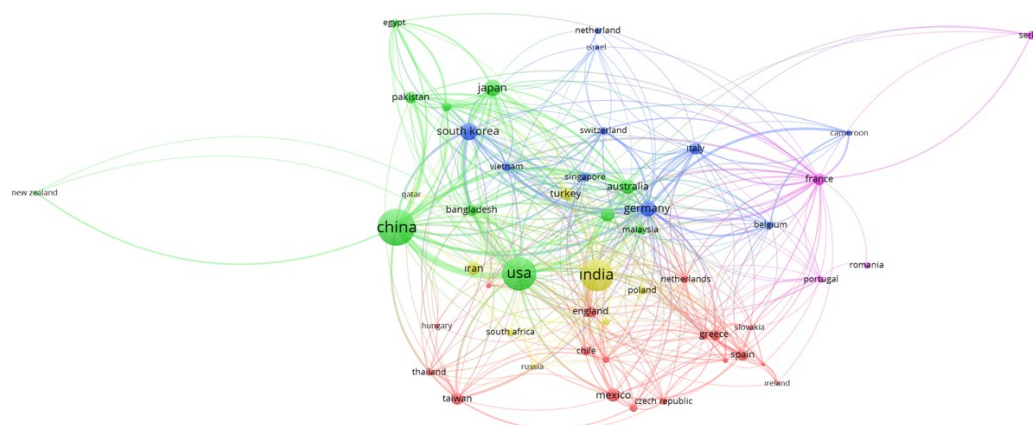
Figure 4. Visualization map analysis of collaboration of countries; minimum number of occurrences of 10

Table 2. The top 10 most cited articles on arsenic removal

Ranking	Articles	Times Cited
1	Arsenic removal from water/wastewater using adsorbents – A critical review Author(s): Mohan, Dinesh; Pittman, Charles U., Jr. Source: Journal of Hazardous Materials Year: 2007	2163
2	Water-dispersible magnetite-reduced graphene oxide composites for arsenic removal Author(s): Chandra, Vimlesh; Park, Jaesung; Chun, Young; et al. Source: ACS Nano Year: 2010	1382
3	Physico-chemical treatment techniques for wastewater laden with heavy metals Author(s): Kurniawan, TA; Chan, GYS; Lo, WH; et al. Source: Chemical Engineering Journal Year: 2006	1045

Table 2. (Cont.) The top 10 most cited articles on arsenic removal

Ranking	Articles	Times Cited
4	Applications of nanotechnology in water and wastewater treatment Author(s): Qu, Xiaolei; Alvarez, Pedro J.J; Li, Qilin Source: Water Research Year: 2013	985
5	Low-field magnetic separation of monodisperse Fe_3O_4 nanocrytals Author(s): Yavuz, Cafer T.; Mayo, J. T.; Yu, William, W; et al. Source: Science Year: 2006	918
6	Remediation technologies for metal-contaminated soils and groundwater: an evaluation Author(s): Mulligan, CN; Yong, RN; Gibbs, BF Source: Engineering Geology Year: 2001	861
7	Advances in water treatment by adsorption technology Author(s): Ali, Imran; Gupta, V.K. Source: Nature Protocols Year: 2006	826
8	Removal of arsenic (III) from groundwater by nanoscale zero-valent iron Author(s): Kanel, S.R; Manning, B; Charlet, L; et al. Source: Environmental Science & Technology Year: 2005	745
9	Arsenic contamination of groundwater and drinking water in Vietnam: A human health threat Author(s): Berg, M; Tran, HC; Nguyen, TC; et al. Source: Environmental Science & Technology Year: 2001	730
10	A review on nanomaterials for environmental remediation Author(s): Khin, Mya Mya; Nair, A. Sreekumaran; Babu V. Jagadeesh; et al. Source: Energy & Environmental Science Year: 2012	616

3.2. Distribution of Major Journals

The top ten productive journals with number of publications are given in Fig. 2. Journal of Hazardous Materials is the leading journal with 218 articles while Water Research is second with 149 articles, and Chemical Engineering Journal is third with 136 articles in the field of As removal. There are only 1068 articles within the top ten productive journals. Desalination and Water Treatment is in Quartile 4 (Q4), Water Air and Soil Pollution is in Q3, RSC Advances and Environmental Science and Pollution Research is in Q2 and remaning six of the top 10 journals are in Q1 category.

The top ten most cited papers present fundamental understanding of any given field [28,29]. Table 2 illustrates publications that have highest citations on As removal from water. The most cited article is a detailed review about types of adsorbents that have been used for As removal and was published in 2007. Two studies are related to environmental remediation of arsenic, one study is on the health and toxicity aspects of As in Vietnam, six of the top ten publications are related to nanotechnology enabled arsenic treatment from water. The list points out that adsorption which uses nanomaterials leads the field of arsenic removal water. Additionally, iron based nano adsorbents are the most frequently used nanomaterial in the top 10 cited articles.

3.3. Contribution of Countries

Distribution and collaboration of top productive countries which have more than 10 publications are illustrated in Fig. 4. A publication can be classified within more than one country, document type and research areas.

China is the most productive country with 880 publications, and it is followed by USA (734), India (649),

South Korea (193) and Japan (182). China, USA and India are well ahead on arsenic removal from water. Leading countries, except USA, are Asian countries with a noticeable momentum in recent years. In addition to these countries, contribution of Bangladesh (89) and Taiwan (87) should not be overlooked. High scientific contribution of these countries in academia is not common [37]. This attention is due to high As contamination in drinking water in South-East Asian countries [38]. Hence, Bangladesh and Taiwan contribute on arsenic related research more than other research areas. WHO considered As contamination in Bangladesh to be the largest mass population poisoning in the history [39]. WHO's limit for As in drinking water puts millions of people in the world and in Asia at risk for high As contamination in drinking water [40]. Figure 3 illustrates network of collaborations and links between international scientific communities. The size of the node represents the number of articles published by named country [41]. Different color grouping indicates frequent collaborations between different countries. The minimum document number of a country was set to 10 publications and countries that have met the threshold were shown in the figure below.

The thickness of lines illustrates the strength of collaboration whereas the size of nodes represents the number of publications. The distance between countries indicates the collaboration frequency [26]. Countries that are in the same cluster and closer to each other on the map have more frequent research collaboration. There are 52 countries that have met the 10-publication threshold and 5 different clusters with distinct colors. Leading countries China and USA are in the same cluster and have strong collaboration. Countries that suffer the most from As contamination such as; Bangladesh, Vietnam, Taiwan, Malaysia and Chile have strong links that suggest frequent collaborations with many different countries. Red cluster consists of 18 countries; green cluster consists of 11 countries; blue cluster consists of 10 countries; yellow cluster consists of 8 countries and purple cluster consists of 5 countries. A series of 118 articles for given keywords has been published between 1970 and 2019 from Turkey. Top 5 contributing universities are: Gebze Technical University, Ege University, Yildiz Technical University, Selcuk University and Yalova University. Highest number of publications were submitted to Desalination and Water Treatment, Journal of Hazardous Materials, Desalination, Separation Science and Technology and Chemical Engineering Journal. Approximately 30% of publications from Turkey were published in the top 10 journal list. The publication trend in Turkey correlates with global publication trend.

3.4. Research Tendencies and Hotspots

Nanotechnology provides effective and sustainable solutions for As removal technologies. It has enabled researchers to synthesize, tailor and modify very specific functionalities in nanoparticles [42]. Various nanomaterials which have unique and efficient properties were developed later to remove As from water. For instance, TiO_2 based nanomaterials increase their efficiency more than 200-fold under UV light, zirconium (Zr) based nanomaterials have the highest surface area, magnesium (Mg) based nanomaterials have the highest adsorption capacities and so on [22]. Iron based nanoparticles, mostly iron oxides, have super-paramagnetic properties [43] and it is the most favorable adsorbent in As removal studies. It is cheap and available, easy to produce, have high surface area and easy to separate in water due to magnetic properties [22]. Iron oxide nanoparticles (maghemite or magnetite) has gained momentum in biomedical applications due to their biocompatibility in the early 1990s and later found niche in engineering applications [42].

The top 5 As removal technologies are listed in Fig. 3 Frequency analysis of As removal technologies does not provide information about on-site applications, rather presents scientific approach for As removal. As a result, adsorption is the most used As removal technology with a total of 9010 appearances. It is followed by oxidation (1994), membrane and filtration technologies (1981), ion exchange (744), and coagulation (678). It is crucial to understand that usually these technologies do not operate as a single unit. For example, membrane technologies can require oxidation, As^{+3} to As^{+5}, to enhance removal efficiency. Similarly, adsorption can be used with filtration and in some cases ion exchange. This study only focuses on frequency of these words and does not include combination of these technologies. The evolution of research on As removal shows that until 2000, there wasn't a significant gap in the number of publications between various As removal technologies. However, since 2000, significant work has been done on developing adsorption-based treatment for As removal, making it favorable and dominant research topic for As removal. Majority (80%) of adsorption studies have been published after 2010 while other technologies are between 66 and 73 percent. This finding indicates that adsorption is not only the most studied As technology, it is also gaining more popularity in recent years.

Adsorption has gained popularity because it is efficient, easy to use, cost effective and does not produce toxic byproducts [44]. Nano adsorbents have improved upon limited efficiency of conventional adsorbents, such as the lack of selectivity and active sites [20]. The particle

size and pH value also have great importance on arsenic adsorption. Higher adsorption capacity can be achieved for As (III) and As(V) by simply reducing size of nanoparticles from 300 nm to 12 nm [45]. In addition to pH control, arsenic speciation, As (V) and As (III), for As removal is important. As has -III, 0, +III and +V oxidation states and the most common forms of As in natural waters are: arsenite and arsenate, referred to as As (III) and As (V) [46]. Arsenate species (AsO_4^{3-}, $HAsO_4^{2-}$, $H_2AsO_4^{-}$) are dominant and stable in aerobic environments while arsenite species dominate anaerobic environments like groundwater [19]. Bacteria can also reduce arsenate to arsenite in anoxic environment [6]. Redox potential and pH are driving forces in controlling As speciation [47]. When oxidizing conditions occur, $H_2AsO_4^{-}$ is predominant at pH lower than 7. $HAsO_4^{2-}$ becomes predominant at higher pH. The uncharged arsenite species predominate under reducing conditions at pH lower than 9.2 [48]. Also, pH_{pzc} values of iron oxide are between 6.8 and 7.5 depending on the type and production parameters of oxides. When pH value is greater than pH_{pzc}, the particle surface becomes negatively charged. Therefore, negatively charged As species lose electrostatic attraction to particle surface area. The optimum operating pH value ranges from around 7–9 for all the iron oxides except for commercial ones which can perform better in acidic conditions [49]. Nanomaterials perform better and usually can be found as powder which is not convenient for column applications due to low hydraulic conductivity and there is a problem of separation and regeneration of certain adsorbents [50]. Oxidation, photochemical, photocatalytic and biological reactions are mainly used to oxidize As (III) to As (V), followed by removal via precipitation. Ion exchange technology in drinking water treatment is mostly used for softening and As removal, but also requires pre-oxidation to enhance As removal performance [40]. These results suggest that when studying As removal from water, As speciation and pH control are fundamental steps towards efficient removal. Different membrane technologies exist for As removal such as nanofiltration (NF) and reverse osmosis (RO).

Nanofiltration require sensitive pH adjustment [51] and pre-oxidation [52]. Integrated membrane technologies, such as RO followed by membrane distillation, remove total As from water and produce less toxic by-products than oxidation followed RO. Nevertheless, high energy consumption, with addition of membrane fouling, is limiting worldwide application of membrane technologies [20,53]. Coagulation and flocculation, using a coagulant to form a floc, is a typical conventional method which produces excessive amount of sludge with high concentration of As [40].

3.5. Visualization Map Analysis

The network visualization map of keywords identifies tendencies in a research field of interest; and typically title, abstract and keywords are being used [53,54]. It was carried out within 4083 publications. Fig. 5 illustrates a network of the co-occurrence of keywords. The size of the node represents the number of repeating words. Different color grouping indicates co-occurrence links between keywords [55]. The minimum document number for keywords was set to 10 publications; and 27 keywords that have met the threshold were shown in the figure below. The result of visualization map analysis of keywords is coherent with frequency analysis of As removal technologies. Adsorption is the leading As removal technology with 264 occurrences and oxidation is the second with 100 occurrences. Water, arsenic, removal, and groundwater have high occurrence because they were used in keyword research. Adsorption, oxide, iron, nanoparticle, and bacterium keywords stand out in keyword analysis. Fig. 6illustrates a network of the co-occurrence of words in abstract. The minimum document number for words in abstract was set to 100 publications and 222 words that have met the threshold were shown in the figure below. There are three clusters with 87, 81 and 54 words respectively. The top 5 most repetitive words are arsenic, removal, water, concentration, and adsorption.

Figure 5. Visualization map analysis of all keywords; minimum number of occurrences of 10

Figure 6. Visualization map analysis of all words in abstracts; minimum number of occurrences of 100
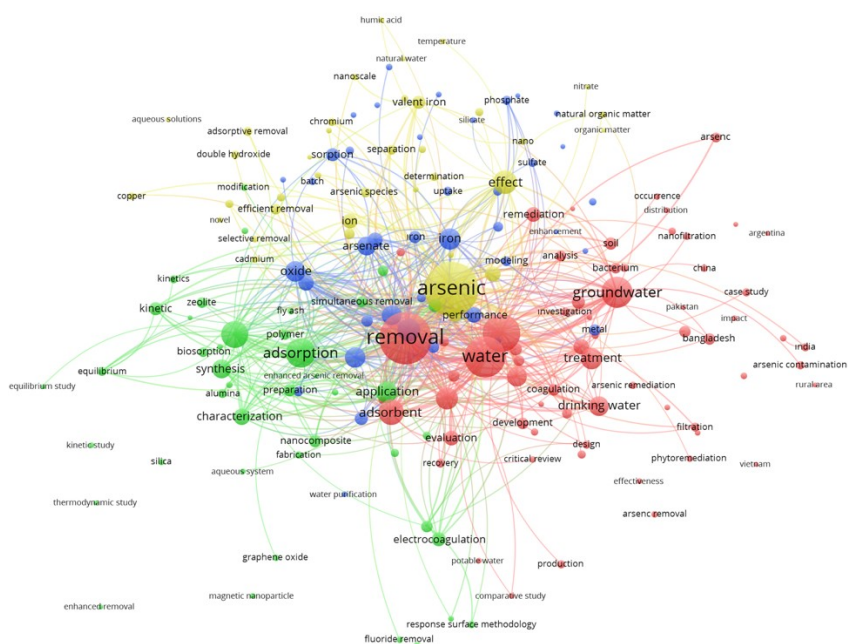
Figure 7. Visualization map analysis of all words in title; minimum number of occurrences of 10

abstract and keywords being used. Using clustering techniques with visualization map analysis points out technologies and methods that are more related to each other.

Fig. 7. illustrates a network of the co-occurrence of words in the title. The minimum document number for words in abstract was set to 10 publications and 186 words that have met the threshold were shown Fig. 7. There are four clusters with 65, 43, 40 and 38 words respectively. Adsorption, iron, and nanoparticle stand out in the title search. The highest number of occurrences and strong links in keyword, title and abstract search are the same keywords in Table 1. Since these words were used in topic search, they have higher occurrence numbers than other keywords as expected. It is crucial to investigate other high occurrence words and clusters when analyzing the visualization map. Taking everything into consideration, visualization map analysis illustrates that adsorption combined with nanotechnology is getting more attention from science community and the data is coherent with frequency analysis and top cited articles.

4. Conclusions

This study presents an overall evaluation of As removal technologies. Publications, journals, countries, and keywords were investigated, and research tendencies and prospects were discussed. A total of 4083 publications related to As removal technologies from 1970 to 2019

were evaluated using bibliometric analysis. The followings are the remarks and conclusions of this study:

▪ As removal research has a significantly increasing trend after 2000. It is assumed that is a cumulative effect of legislations enacted by WHO, EU and USEPA.

▪ Article is the most favorable publication type as expected and engineering is the most studied research area. Journal of Hazardous Materials has the highest number of publications with 218 articles.

▪ China is the leading country in the number of As related publication. Asian countries especially South-East Asian countries draw more attention on As removal studies and their contribution to literature should not be overlooked. Because this points out the obvious fact that these countries suffer from contaminated As water sources.

▪ It is safe to assume that adsorption techniques using nanoparticles would be the most likely leading As removal technology in that nanotechnology gives major advantages to adsorption compared with other technologies. However, pH sensitivity, cost, regeneration, separation, field applicability will be deciding factors over the years.

▪ The difficulties regarding As removal technologies are important but temporary, including high cost and limitations. Advancing nanotechnology can provide sustainable solutions to these issues and improve technological ability.

Conflict of Interests

Acknowledgement

Declaration of Ethical Standards

The authors of this article declares that the materials and methods used in this study do not require ethical committee permission and legal-special permission.

References

[1] Woolson E.A., 1975. Bioaccumulation of Arsenicals. In: Arsenical Pesticides. American Chemical Society.

[2] Goldberg S., Johnston C.T., 2001. Mechanisms of arsenic adsorption on amorphous oxides evaluated using macroscopic measurements, vibrational spectroscopy, and surface complexation modeling. J Colloid Interface Sci., **234**, pp. 204–216.

[3] Ahuja S., 2008. Arsenic Contamination of Groundwater: Mechanism, Analysis, and Remediation. Wiley, New Jersey.

[4] Choong T.S.Y., Chuah T.G., Robiah Y., et al. 2007. Arsenic toxicity, health hazards and removal techniques from water: an overview. Desalination, **217**, pp. 139–166.

[5] IARC. 1987. IARC Monographs on the Evaluation of Carcinogenic Risks to Humans; Overall Evaluation of Carcinogenicity: An updating of IARC Monographs Volumes 1 to 42, pp. 100-106.

[6] Stolz J.F., Oremland R.S., 1999. Bacterial respiration of arsenic and selenium. FEMS Microbiol., **23**, pp. 615–627.

[7] Mandal B.K., Suzuki K.T., 2002. Arsenic round the world: a review. Talanta, **58**, pp. 201–235.

[8] Smith A.H., Hopenhayn-Rich C., Bates M.N., et al. 1992. Cancer risks from arsenic in drinking water. Environ Health Perspect, **97**, pp. 259–267.

[9] Abbas G., Murtaza B., Bibi I., et al. 2018. Arsenic uptake, toxicity, detoxification, and speciation in plants: Physiological, biochemical, and molecular aspects. Int J. Environ Res. Public Health, **15**, pp 1.

[10] Smith A.H., Lingas E.O., Rahman M., 2000. Contamination of Drinking Water by Arsenic in Bangladesh: A Public Health Emergency. Bulletin of the World Health Organization 78: Contamination of drinking-water by arsenic in Bangladesh: a public health emergency. World Health Organ. Bull., **78**, pp. 1093.

[11] Stauber J.L., Florence T.M., Davies C.M., et al. 1996. Methylation study of a population environmentally exposed to Arsenic in Drinking water. Environ. Health Perspect., **91**, pp. 620–628.

[12] Chen C.J., Chen C.W., Wu M.M., Kuo T.L., 1992. Cancer potential in liver, lung, bladder and kidney due to ingested inorganic arsenic in drinking water. Br J Cancer, **66**, pp. 888–892.

[13] Berg M., Tran H.C., Nguyen T.C., et al. 2001. Arsenic contamination of groundwater and drinking water in Vietnam: A human health threat. Environ Sci Technol., **35**, pp. 2621–2626.

[14] Hopenhayn-Rich C., Biggs M.L., Fuchs A., et al. 1996. Bladder cancer mortality associated with arsenic in drinking water in Argentina. Epidemiology, **7**(2), pp. 117–124.

[15] Abejón R., Garea A., 2015. A bibliometric analysis of research on arsenic in drinking water during the 1992-2012 period: An outlook to treatment alternatives for arsenic removal. J. Water Process Eng., **6**, pp. 105–119.

[16] World Health Organization (WHO). 1993. Guidelines for Drinking-water Quality. Volume 1: Recommendations, 2nd edition. Geneva.

[17] European Union (EU). 1998. Council Directive 98/83/EC on the quality of water intended for human consumption. Brussels.

[18] United States Environmental Protection Agency (USEPA). 2001. National Primary Drinking Water Regulations; Arsenic and Clarifications to Compliance and New Source Contaminants Monitoring.

[19] Mohan D., Pittman C.U., 2007. Arsenic removal from water/wastewater using adsorbents-A critical review. J Hazard Mater., **142,** pp. 1–53.

[20] Qu X., Alvarez P.J.J., Li Q., 2013. Applications of nanotechnology in water and wastewater treatment. Water Res., **47**, pp. 3931–3946.

[21] Ali I., 2012. New generation adsorbents for water treatment. Chem Rev., **112**, pp. 5073–5091.

[22] Wong W., Wong H.Y., Badruzzaman A.B.M., et al. 2017. Recent advances in exploitation of nanomaterial for arsenic removal from water: A review. Nanotechnology, **28**, pp. 1–31.

[23] Reuters Thomson. 2008. White Paper Using Bibliometrics: A guide to evaluating research performance with citation data.

[24] Fu H.Z., Ho Y.S., Sui Y.M., Li Z.S., 2010. A bibliometric analysis of solid waste research during the period 1993-2008. Waste Management, **30**, pp. 2410-2417.

[25] Persson O., Danell R., Schneider W.J., 2009. How to use Bibexcel for various types of bibliometric analysis, in: Celebrating Scholarly Communication Studies. Danish National Research Database ID: 2398320558.

[26] Van Eck J.N., Waltman L., 2010. Software survey: VOSviewer, a computer program for bibliometric mapping. Scientometrics, **84**, pp. 523-538.

[27] Hu J., Ma Y., Zhang L., et al. 2010. A historical review and bibliometric analysis of research on lead in drinking water field from 1991 to 2007. Sci Total Environ., **408**, pp. 1738–1744.

[28] Garfield E., 1972. Citation analysis as a tool in journal evaluation. Science, **178**(4060), pp. 471-479.

[29] Ma J., Fu Z.H., Ho S.Y., 2013. The top-cited wetland articles in science citation index expanded: characteristics and hotspots. Environmental Earth Sciences, **70**(3), pp. 1039-1046.

[30] Chandra V., Park J., Chun Y., et al. 2010. Water-Dispersible Magnetite-Reduced Graphene Oxide Composites for Arsenic Removal. ACS Nano, **4**, pp. 3979–3986.

[31] Kurniawan T.A., Chan G.Y.S., Lo W.H., Babel S., 2006. Physico-chemical treatment techniques for wastewater laden with heavy metals. Chemical Engineering Journal, **118**, pp. 83-98.

[32] Yavuz C.T., Mayo J.T., Prakash A., et al. 2006. Low-Field Magnetic Separation of Monodisperse Fe3O4 Nanocrystals. Science, (80) **314**, pp. 964–967.

[33] Mulligan C.N., Yong R.N., Gibbs B.F., 2001. Remediation technologies for metal-contaminated soils and groundwater: an evaluation. Engineering Geology, **60**, pp. 193-207.

[34] Ali I., Gupta V.K., 2007. Advances in water treatment by adsorption technology. Nat Protoc., **1**, pp. 2661–2667.

[35] Kanel S.R., Manning B., Charlet L., Choi H., 2005. Removal of arsenic (III) from groundwater by nanoscale zero-valent iron. Environ Sci Technol., **39**, pp. 1291–1298.

[36] Khin M.M., Nair A.S., Babu V.J, Murugan R., 2012. Ramakrishna S. A review on nanomaterials for environmental remediation. Energy & Environmental Science, 5, pp. 8075-8109.

[37] Sun J., Wang H.M., Ho S.Y., 2012. A historical review and bibliometric analysis of research on estuary pollution. Mar Pollut Bull, **64,** pp. 13-21.

[38] Chappell R.W., Abernathy O.C., Calderon L.R., 2001. Arsenic exposure and Health Effects IV (First Edition). Elsevier, Amsterdam.

[39] Argos, M., Kalra, T., Rathouz, P.J., Chen, Y., et. al. 2010. Arsenic exposure from drinking water, and all-cause and chronic-disease mortalities in Bangladesh (HEALS): A prospective cohort study. Lancet, **376**, pp. 252–258.

[40] Singh R., Singh S., Parihar P., Singh P.V., Prasad M.S., 2015. Arsenic contamination, consequences, and remediation techniques: A review. Ecotoxicology and Environmental Safety, 112, pp. 247-270.

[41] Zyoud S.H., Hanush D.F., 2020. Mapping of climate change research in the Arab world: a bibliometric analysis. Environmental Science and Pollution Research, **27**, pp. 3523-3540.

[42] Gupta A.K., Gupta M., 2005. Synthesis and surface engineering of iron oxide nanoparticles for biomedical applications. Biomaterials, **26**(18), pp. 3995-4021.

[43] Bowell R.J., 1994. Sorption of arsenic by iron oxides and oxyhydroxides in soils. Appl Geochem., **9**, pp. 279-286.

[44] Jang M., Chen W., Cannon S.F., 2008. Preloading Hydrous Ferric Oxide into Granular Activated Carbon for Arsenic Removal. Environ Sci Technol., **42,** pp. 3369-3374.

[45] Yean S., Cong L., Yavuz C., Mayo J., Yu W., Kan A., Colvin V., Tomson M., 2005. Effect of magnetite particle size on adsorption and desorption of arsenite and arsenate. Journal of Material Research, **20**, pp. 3255–3264.

[46] Smedley P.L., Kinniburgh D.G., 2002. A review of the source, behaviour and distribution of arsenic in natural waters. Appl Geochemistry, 17, pp. 517–568.

[47] Yan X.P., Kerrich R., Hendry M.J., 2000. Distribution of arsenic (III), arsenic(V) and total inorganic arsenic in porewaters from a thick till and clay-rich aquitard sequence, Saskatchewan, Canada. Geochim Cosmochim Acta, **64,** pp. 2637–2648.

[48] Brookins D.G. 1988. Eh–pH Diagrams for Geochemistry, Springer-Verlag, Berlin.

[49] Chowdhury S.R., Yanful E.K., 2010. Arsenic and chromium removal by mixed magnetite-maghemite nanoparticles. Journal of Environmental Management, **91**, pp. 2238–47.

[50] Lata S., Samadder R.S., 2016. Removal of arsenic from water using nano adsorbents and challenges: A review. Journal of Environmental Management, **166**, pp. 387-406.

[51] Zhao S., Zou L., Tang C.Y., Mulcahy D., 2012. Recent developments in forward osmosis: Opportunities and challenges. J Membr Sci., **396**, pp. 1-21.

[52] Uddin M., Mozumder M., Islam M., Deowan S., Hoinkis J., 2007. Nanofiltration membrane process for the removal of arsenic from drinking water. Chem Eng Technol., **30**, pp. 1248-1254.

[53] Chiu W.T., Ho Y.S., 2007. Bibliometric analysis of tsunami research. Scientometrics, **7**, pp. 3-17.

[54] Li L.L., Ding G., Feng N., Wang H.M., Ho S.H., 2009. Global stem cell research trend: Bibliometric analysis as a tool for mapping of trends from 1991 to 2006. Scientometrics, **80** (1), pp. 39-58.

[55] Sanchez J.A.A., Munoz J.F.V., Urena L.J.B., Agugliaro F.M., 2019. Innovation and technology for sustainable mining activity: A worldwide research assessment. Journal of Cleaner Production, **221**, pp. 38-54.

Kocaeli University

Kocaeli Journal of Science and Engineering

http://dergipark.org.tr/kojose
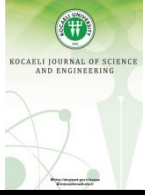
Cyber-Physical System based E-Health: Knee Joint Physical Therapy Monitoring

Fatih ATAMTÜRK [1] iD , Halil YİĞİT [2, *] iD

[1] *İzmit Vocational and Technical Anatolian High School, Kocaeli, 41001, Turkey*, **ORCID:** 0000-0001-5138-7231
[2] *Department of Information Systems Engineering, Kocaeli University, Kocaeli, 41001, Turkey*, **ORCID:** 0000-0003-0932-6966

Abstract

A cyber-physical system (CPS) uses sensors/actuators to associate the physical world with a system capable of computing. CPSs include software systems, communication technologies, and sensors/actuators, including intelligent embedded system technologies to interact with the real world. It is possible to monitor and control all physical processes without human factors by connecting the mechanical systems equipped with information technologies and establishing communication among themselves. In this study, a CPS system that offers a cost-effective and easy-to-apply physical therapy opportunity is proposed for post-hospital home follow-up of knee osteoarthritis, which can be seen in many people over a certain age. The proposed system consists of a hardware module consisting of two potentiometers, a microcontroller and a WiFi module, and a software module to monitor the movement of the knee joint point daily and to save the data in the database. Maximum knee flexion angle, exercise duration and success rate measurements were used to measure the progress of physical therapy. The CPS prototype developed for the healthcare field will make significant contributions to reducing the duration of physical therapy and increasing its reliability by eliminating the possibility of wrong/incomplete exercises.

1. Introduction

Cyber-Physical Systems (CPSs) are systems that seamlessly integrate computing components, network communication and physical processes for a specific purpose. CPS has four fundamental components. The first is the physical world, which refers to physical events to be monitored or controlled remotely. The second is the next generation of embedded devices that process information and communicate with the surrounding environments over a communication network. The third is a communication network and sensors/actuators, which is a bridge between cyber systems and the physical world. The last is the software [1]. With the concept of the Internet of Things (IoT), CPS, which started to remove the boundaries between the real and virtual world, is one of the cornerstones of Industry 4.0, one of the important issues of today's technology [2].

CPS, which is a highly complex and computationally intensive system, can be used in many healthcare applications. It offers stronger communication, more computation, and higher security compared to its current alternatives. Rapid advances in wireless communication technologies and wearable sensors used in healthcare make CPS a strong candidate for healthcare applications [3, 4]. In an exemplary CPS for healthcare, Patients who need home care or continue their treatment in the hospital can be monitored remotely and clinicians can offer treatment recommendations. First, patient data, which are collected using various sensors and sent to the cloud storage/remote server via a gateway over the wireless communication medium, is processed. By analyzing the sensor data, an alarm is generated and transmitted it to the observation center. The experts in the observation center can access patient data in real time via the cloud, and if needed, the patient's condition is evaluated according to the responses from other health systems, and the decision taken is sent to the control/activation component. Last, the patient is furnished with medical attention [5]. In this way, diseases

---

* Corresponding Author: halilyigit@kocaeli.edu.tr

can be categorized and treatment outcomes can be improved by collecting all data from patients and analyzing treatment methods and results [6, 7].

Osteoarthritis (OA), which is mostly seen in the elderly and affects the musculoskeletal system, causes health problems such as pain, joint stiffness, swelling, and difficulty in daily activities. In our body, this disease mostly affects the knee joints [8]. Medication and physical therapy come to the fore in the traditional treatment of OA patients. Physical therapy should be continued for a certain period at home after treatment. Many studies have shown that the knee can perform its normal physical functions by significantly reducing the pain caused by the disease with physical therapy [9-11]. Therefore, medical professionals should monitor the patient's knee movements in the home environment. Continuous evaluation of the knee joint angle allows immediate intervention in unwanted situations, allowing the treatment to achieve the desired result. Exercise performance in physical therapy can be characterized by monitoring changes in knee flexion/extension.

1.1. Related Works

[12] develops a novel approach, consisting of multiple flex-sensors mounted on a supportive cloth and microelectromechanical systems (MEMS) vibratory gyroscope, for measuring the knee joint angles for the surface electrical stimulator system. For the evaluation of knee angle motion, lower extremity joint angles and segment angles were estimated from data measured by wireless MEMS vibratory gyroscope and flex-sensors. These data were used to see the effectiveness of rehabilitation training, especially for spinal cord injury (SCI) patients.

[13] provides an approach to measure and monitor human body joint angles using inertial measurement unit (IMU) sensors that facilitate the remote assessment of patient activities for therapists and doctors. Euler angles are sent to the computer via Bluetooth to calculate the knee joint angle. In the experiments, it was determined that the IMU measurement system outperforms existing conductive fiber optic sensors and flexible sensors in accurately measuring knee joint angle.

Different joint monitoring methods and sensing technologies are compared in [14]. A discussion on the data processing, interpretation and analysis techniques of the sensors is also presented.

In [15], an accurate, low-cost, flexible wearable sensor has been developed that includes a retractable reel, a string, and a potentiometer to evaluate and monitor joint movements. The sensor estimates the joint angles in correlation with the amount of skin stretch measured by the

change in the length of the string. An optoelectronic system was used to evaluate the accuracy of the designed sensor in predicting knee joint angles.

[16] proposes a health monitoring system that can classify lower extremity movements such as assisting, lying and standing, using the angle and acceleration components of the knee joints of the elderly and physically disabled. Two potentiometers attached to a wearable frame and an IMU sensor attached to the thigh region were used to measure knee joint angles and accelerations. The data received from both sensors is transferred to the device via Bluetooth.

[17] proposed a novel sensing technique using e-textiles and triaxial accelerometers to analyze standing human motion. The proposed technique was used to measure the knee flexion-extension angle in different movement tasks (monopodalic flexions and walking at different speeds). The results were compared with a measurement system with an inertial measurement unit (IMU).

[18] evaluates the possibility of predicting 3D lower extremity joint kinematics during hip and knee exercises with data collected from a single inertial measurement unit (IMU). The proposed approach was applied to ten healthy young people. The results obtained were compared with measurements collected via a stereo photogrammetric system.

In [19], low-cost and non-invasive health and activity monitoring systems that the elderly can use at home were examined. A survey was conducted on textile-based sensors. At the same time, the future of remote monitoring systems and compatibility with communication technologies are discussed.

Apart from the studies detailed above, wearable sensors such as inertial measurement units (IMU) [20, 21], ultrasonic sensors [22], rigid electrogonometers [23, 24], flexible sensors [25], and e-textile sensors [26, 27] used to measure knee joint angle are evaluated in terms of power consumption, cost, safety, ease of use and compatibility with the human body.

Most of the studies mentioned above usually involve measuring and monitoring the joint angle. Some of these studies use smartphones and apps to provide an effective knee joint angle measurement system for real-time monitoring of knee angle. In our study, we propose an effective CPS that integrates two potentiometers, a WiFi module, and a Web interface for remote monitoring and analyzing the progress of physical therapy by a therapist/physician. Despite the limitation that potentiometers are not durable due to friction, the results obtained from the wearable sensor with a potentiometer are more reliable than accelerometers and flexible sensors affected by environmental conditions [28]. The proposed system includes measuring the knee joint angle, saving it in

the database on the remote server, and showing the daily exercise success rate and exercise duration information on the graph according to the maximum angle value (limit) entered by the doctor from a Web interface. The proposed system provides a very cost-effective and easy-to-apply physical therapy opportunity for the follow-up of the treatment of a health complaint that can be mostly seen in many people over a certain age. It allows the patient to continue the treatment processes without the need for any clinical environment and independent of the assistance of the therapist/physician.

2. The Proposed Model

Figure 1 shows an example scenario of the proposed CPS system. In this scenario, the system has three components. The first is the section where the knee joint angle measurement is calculated while the patient is exercising at home, and the data is sent to the network. The second is the process in which data is processed after reaching the remote server. The third part is the part of informing the experts who will guide the treatment process according to the data obtained after these two procedures. In-home operations form the hardware layer portion of the CPS. In this layer, the data coming from the array is taken by analog sensors and first converted into digital data with ADC, then these data are processed on the microcontroller to obtain angle information. Angle data is sent to the remote server over the internet via the WiFi module. The data coming to the remote server is taken into the database by the Web service. Instant training data recorded in the database is displayed graphically according to weekly, monthly and annual periods. The physician or therapist monitors the patient's treatment process remotely. Finally, they contact the patient via e-mail or telephone via the system to provide information about the treatment.

Figure 2 shows the hardware architecture of the proposed model. The system consists of (a) NodeMCU microcontroller card and ESP8266 WiFi module, (b) Analogue to Digital Converter - ADC, (c) Organic Light Emitting Diode - OLED display and (d) potentiometer.

Figure 1. The proposed CPS for healthcare.
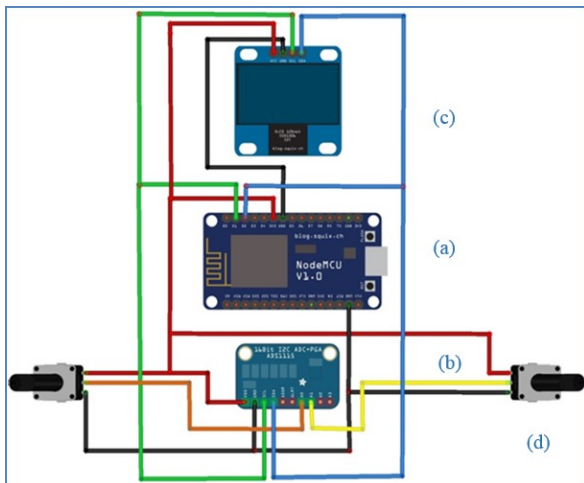
Figure 2. Hardware architecture.

NodeMCU (Node Micro Controller Unit) in Figure 3 is a microcontroller board, which is preferred because it is cheap, capable, and open source. It operates with low voltage. Thanks to the ESP8266 WiFi module, IoT applications can be performed. NodeMCU can work as a Web client or a Web server through HTTP libraries. NodeMCU has an advanced hardware I/O interface that can be adjusted and edited. It also has a simple API.

A typical single-turn potentiometer is often called a pot. It is a mechanically operated rotary analog device, which can be used in a wide variety of electrical and electronic circuits. Potentiometers can be used in two different ways, as a voltage divider and variable resistance. If the potentiometer is used as a voltage divider, the outer

terminals are connected to the + V and GND respectively. The middle terminal indicates the moveable contact called the screw and produces a value between 0 and +V depending on its physical position. In the case of the variable resistor, one of the outer terminals is short-circuited with the middle terminal. The resistance varies from 0 Ω to the maximum resistance of the pot as the screw is moved.
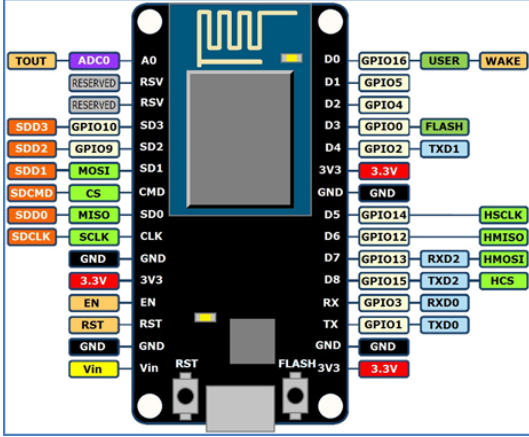
Figure 3. NodeMCU 1.0.

3. Angle Measurement with Potentiometer

Two potentiometers, which are analog circuit elements, are used to find the flexion angle from the knee joint point. Potentiometers are positioned symmetrically on both sides of the knee thanks to the specially designed mechanical parts with the 3D printer. Potentiometers that can rotate between 0-270 degrees in a single turn have a value of 100K. Analog values from potentiometers are converted into digital data with an n-bits ADC so that they can be processed in the microcontroller. As the potentiometer is rotated, the ADC converts this analog resistor value to a value between 0 and $2^n - 1$. These values are used to obtain the angle value of the potentiometer from 0 to 270 degrees. Eq. (1), (2), and (3) are used to make this calculation.

$$\theta_{rigth} = (X - in_{min})\left(\frac{out_{max}-out_{min}}{in_{max}-in_{min}}\right) + out_{min} \quad (1)$$

$$\theta_{left} = (X - in_{min})\left(\frac{out_{max}-out_{min}}{in_{max}-in_{min}}\right) + out_{min} \quad (2)$$

$$\theta_{mean} = \left(\theta_{rigth} + \theta_{left}\right)/2 \quad (3)$$

where θ_{rigth} is the angle value measured on the right side of the knee, θ_{left} is the angle value measured on the left side of

the knee, θ_{mean} is the average of the measured angle values, X is the measured value from the potentiometer, in_{min} is the minimum value measured from ADC, in_{max} is the maximum value measured from ADC. out_{min} shows the minimum angle value of the potentiometer while out_{max} is the maximum angle value of the potentiometer. The measured angle value with the potentiometer resistance value can be shown in Table 1.

Table 1. The measured angle value with the potentiometer resistance value.

Angle value measured from potentiometer (°)	The potentiometer resistance value (K)
5	1.2136296499
10	2.4272592999
15	3.6408889499
30	7.2817778999
45	10.9226668499
60	14.5635557999
90	21.8453336999
120	29.1271115999
135	32.7680005499
150	36.4088894999

4. Experimental Results and Analysis

Since there is one analog input on the NodeMCU microcontroller card used in the study, the values of the two potentiometers were read using a 16-bit four channel ADC. Therefore, the analog input is converted to a numerical value between 1 and 65536. The OLED screen displays the average knee joint angle value, number exercise repetitions, exercise status and IP number. The connection diagram of the designed circuit is shown in Figure 2. Socket cables and insulating tape are used for connections. After the connections were made, a prototype was produced as shown in Figure 4. The developed hardware is mounted on the knee brace and compatible with the knee joint point. Figure 5 shows the prototype wearable on the knee during exercise.
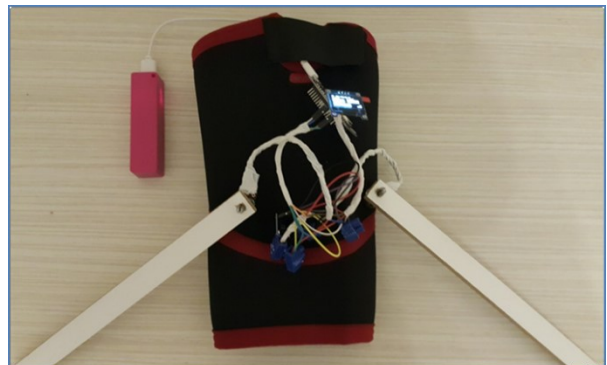
Figure 4. Experimental setup.
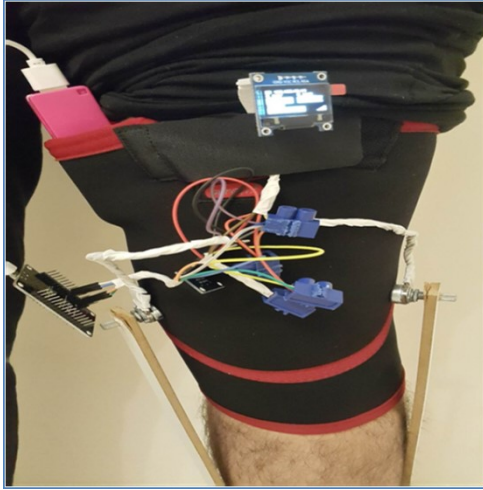
Figure 5. Wearable prototype on the knee.

The CPS software layer is used to receive data from potentiometers, convert these data to angle values in the microcontroller, connect to the internet with WiFi technology and send the data to the server, and save and analyze the data in the database. In our study, patient data are sent over the URL to the Web service on the server side via ESP8266. Using the PHP Web service, the angle, IP and user name information from the patient is retrieved from the URL using the GET method, and each data is stored in the database with the help of SQL commands. Then, the data in the database is analyzed and the treatment information is shown to the doctor / specialist as graphics/text. In addition, this information is sent via e-mail or SMS upon request.

After the Internet connection is established with the ESP8266 module, The patient's ID information, the targeted knee joint angle value and the Web service parameters during the exercise are entered into the interface shown in Figure 6 by the patient, doctor or specialist.

Figure 6. User general setting interface.

The Web interface shown in Figure 7 provides instant monitoring of the exercise over the Web. The physician / specialist can instantly monitor the exercise by connecting to the device via the IP address of the device registered on the Website.

Figure 7. Exercise tracking screen.

The Web interface where patient information is entered and recorded in the database is shown in Figure 8. An authorized person enters the patient's username and other personal information. This information is recorded in the database. With the password and user name specified in this section, the patient can log into the system via the Website and contact the doctor or authorized person. In addition, the person can view the tracking of past exercise information through the system.

As seen in Figure 9, authorized physicians or specialists can access the information of registered patients through the system. This information can be deleted or updated. The data recorded in the database are shown graphically in order to make it easier for patients and specialists to understand. The date and exercise data of the exercise information are recorded in the database. A single value is recorded in the database by taking the average of the data made during the exercise. Figure 10 shows the graphical representation of patient exercise information, time data on the x-axis, and angle values on the y-axis. The success time indicates to the first time to reach the limit value entered during exercise. Eq. (4) is used to calculate the success rate of the exercise.

$$SuccessRate = \frac{the\ number\ of\ angle\ values\ above\ the\ limit}{total\ number\ of\ angles} \quad (4)$$

Figure 8. Patient registration form.

Figure 9. Patient information monitoring.

5. Conclusions

The loss of mobility in the knee joints, which play an indispensable way in the daily life activities of people over a certain age, causes serious social, mental and physical consequences. It is very important to follow the condition of the knee joints in post-treatment physical therapy. In the study, CPS that is an effective and easy to implement, is developed that integrates two potentiometers, a WiFi module, and a Web interface to remotely monitor and analyze the progress of physical therapy by the therapist / physician. As a result, CPS studies in the field of health, which directly affect people's living standards, will save time and costs by ensuring that health services continue uninterruptedly after treatment, especially at home.

Declaration of Ethical Standards

The author(s) of this article declare that the materials and methods used in this study do not require ethical committee permission and/or legal-special permission.

Conflict of Interest

The authors declare that they have no known competing financial interests or personal relationships that could have appeared to influence the work reported in this paper.
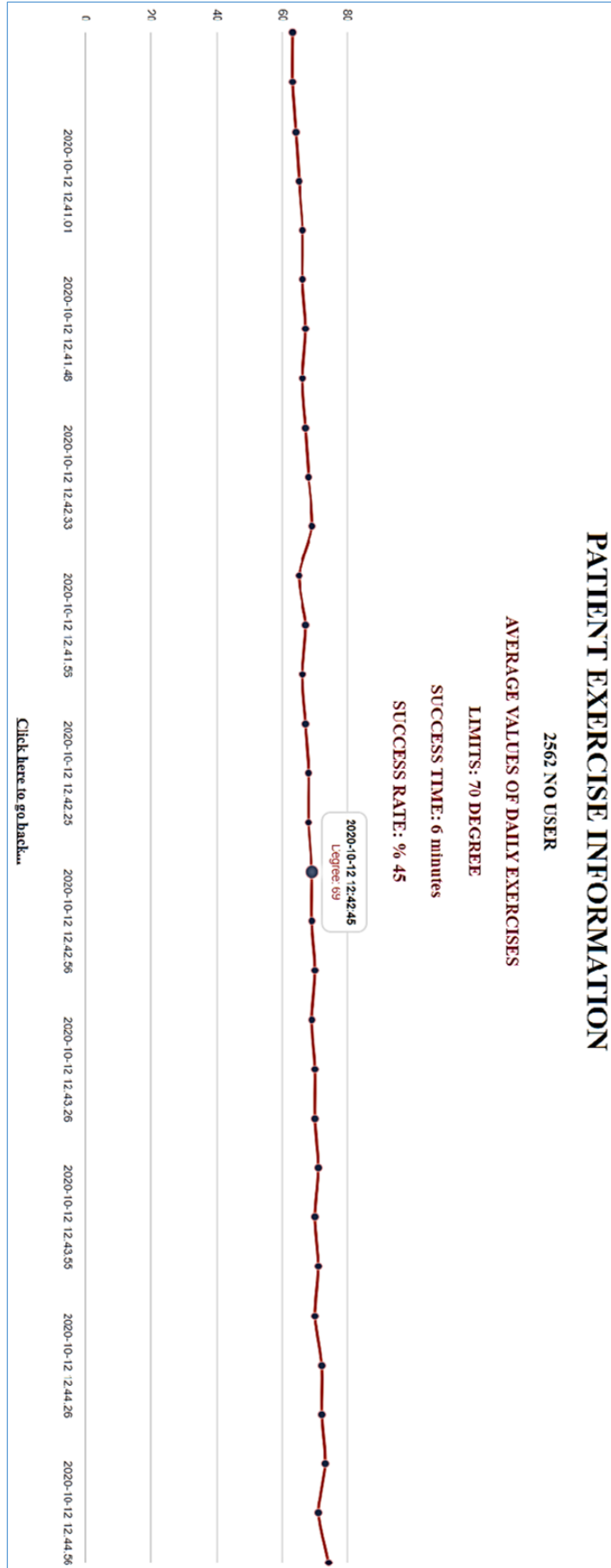
Figure 10. Patient exercise chart.

References

[1] Wang J., Abid H., Lee S., Shu L., Xia, F., 2011. A Secured Healthcare Application Architecture for Cyber-Physical Systems. Control Engineering and Applied Informatics, **13**(3), pp. 101–108.

[2] Jazdi N. 2014. Cyber Physical Systems in the Context of Industry 4.0. Proc. IEEE International Conference on Automation, Quality and Testing, Robotics, Cluj-Napoca, Romania, 22-24 May, pp. 1-4, DOI: 10.1109/AQTR.2014.6857843.

[3] Milenković A., Otto C., Jovanov E., 2006. Wireless Sensor Networks for Personal Health Monitoring: Issues and an Implementation. Computer Communications, **29**(13-14), pp. 2521–533.

[4] Jovanov E., Milenković A., Otto C., Groen P. C. D., 2005. A Wireless Body Area Network of Intelligent Motion Sensors for Computer Assisted Physical Rehabilitation. Journal of NeuroEngineering and Rehabilitation, **2**(1), pp. 1–10.

[5] Shah A. H., Syed M. A., Mustafizur R., 2014. Review of Cyber-Physical System in Healthcare. International Journal of Distributed Sensor Networks, 10, pp. 1–20.

[6] Lounis A., Hadjidj A., Bouabdallah A., Challal Y., 2012. Secure and Scalable Cloud-Based Architecture for E-Health Wireless Sensor Networks. 21st International Conference on Computer Communication Networks, Munich, Germany, 30 July-2 Aug., pp. 1-7, DOI: 10.1109/ICCCN.2012.6289252.

[7] Insup L., Sokolsky O., Chen S., Hatcliff J., et al., 2012. Challenges and Research Directions in Medical Cyber-Physical Systems. Proceedings of the IEEE, **100**(1), pp. 75–90.

[8] Tang L.-A., Yu X., Kim S., Han J., et al., 2012. Multidimensional Sensor Data Analysis in Cyber-Physical System: An Atypical Cube Approach. International Journal of Distributed Sensor Networks, **8**(4), pp. 1550–1329.

[9] Emmerzaal J., De Brabandere A., Vanrompay Y., Vranken J., Storms V., et al., 2020. Towards the Monitoring of Functional Status in a Free-Living Environment for People with Hip or Knee Osteoarthritis: Design and Evaluation of the JOLO Blended Care App. Sensors (Basel), **20**(23), pp. 6967.

[10] Bennell K., Hinman R. S., Wrigley T. V., Creaby M. W., Hodges P., 2011. Exercise and Osteoarthritis: Cause and Effects. Comprehensive Physiology, **1**(4), pp. 1943–2008.

[11] Zampogna B., Papalia R., Papalia G.F., Campi S., Vasta S., Vorini F., Fossati C., Torre G., Denaro V., 2020. The Role of Physical Activity as Conservative Treatment for Hip and Knee Osteoarthritis in Older People: a Systematic Review and Meta-Analysis. J. Clin. Med, **9**(4), pp. 1167.

[12] Masdar A., Ibrahim B. S. K. K., Hanafi D., Mahadi Abdul Jamil M., Rahman, K. A. A., 2013. Knee Joint Angle Measurement System Using Gyroscope and Flex-Sensors for Rehabilitation. The 6th Biomedical Engineering International Conference, Amphur Muang, Thailand, 23-25 Oct., pp. 1-4, DOI: 10.1109/BMEiCon.2013.6687719.

[13] Bakhshi S., Mahoor M. H., Davidson B. S., 2011. Development of a Body Joint Angle Measurement System Using IMU Sensors. Annual International Conference of the IEEE Engineering in Medicine and Biology Society. Boston, MA, USA, 30 Aug.-3 Sept., pp. 6923-6926, DOI: 10.1109/IEMBS.2011.6091743.

[14] Faisal A. I., Majumder S., Mondal T., et al., 2019. Monitoring Methods of Human Body Joints: State-of-the-Art and Research Challenges. Sensors (Basel, Switzerland), **19**(11), pp. 2629.

[15] Lee S. I., Daneault J., Weydert L., Bonato P., 2016. A Novel Flexible Wearable Sensor for Estimating Joint-Angles. IEEE 13th International Conference on Wearable and Implantable Body Sensor Networks (BSN), San Francisco, CA, USA, 14-17 June, pp. 377-382, DOI: 10.1109/BSN.2016.7516291.

[16] Kim J-N., Chong W. S., Kim S-H., Kim, K., 2019. Health Management Monitoring System for Use in Classifying Lower Extremity Movements of the Elderly. Journal of Mechanics in Medicine and Biology, **19**(7), pp. 1940028.

[17] Tognetti A., Lorussi F., Carbonaro N., De Rossi D., 2015. Wearable Goniometer and Accelerometer Sensory Fusion for Knee Joint Angle Measurement in Daily Life. Sensors, **15**(11), pp. 28435–28455.

[18] Bonnet V., Joukov V., Kulić D., Fraisse P., Ramdani N., et al., 2016. Monitoring of Hip and Knee Joint Angles Using a Single Inertial Measurement Unit during Lower Limb Rehabilitation. IEEE Sensors Journal, Institute of Electrical and Electronics Engineers, **16**(6), pp. 1557–1564.

[19] Majumder S., Mondal T., Deen M. J., 2017. Wearable Sensors for Remote Health Monitoring. Sensors (Basel, Switzerland), **17**(1), pp. 130.

[20] Cooper G., Sheret I., McMillian L., Siliverdis K., Sha N., Hodgins D., Kenney L., Howard D., 2009. Inertial Sensor-Based Knee Flexion/Extension Angle

Estimation. Journal of Biomechanics, **42**(16), pp. 2678–2685.

[21] Seel T., Raisch J., Schauer T., 2014. IMU-Based Joint Angle Measurement for Gait Analysis. Sensors Journal, **14**(4), pp. 6891–6909.

[22] Qi Y., Soh C. B., Gunawan E., Low K-S., Thomas R., 2015. Lower Extremity Joint Angle Tracking with Wireless Ultrasonic Sensors during a Squat Exercise. Sensors, **15**(5), pp. 9610.

[23] Toffola L. D., Patel S., Ozsecen M. Y., Ramachandran R., Bonato P., 2012. A Wearable System for Long-Term Monitoring of Knee Kinematics. IEEE-EMBS International Conference on Biomedical and Health Informatics, Hong Kong, China, 5-7 Jan., pp. 188-191, DOI: 10.1109/BHI.2012.6211541.

[24] Fennema M. C., Bloomfield R. A., Lanting B. A., Birmingham T. B., Teeter M. G., 2019. Repeatability of Measuring Knee Flexion Angles with Wearable Inertial Sensors. The Knee, **26**(1), pp. 97–105.

[25] Papi E., Bo Y. N., Mcgregor A. H., 2018. A Flexible Wearable Sensor for Knee Flexion Assessment during Gait. Gait & Posture, **62**, pp. 480–483.

[26] Watson A., Sun M., Pendyal S., Zhou G., 2020. TracKnee: Knee Angle Measurement using Stretchable Conductive Fabric Sensors. Smart Health, **15**, pp. 100092.

[27] Bergmann J. H., Anastasova-Ivanova S., Spulber I., Gulati V., Georgiou P., McGregor A., 2013. An Attachable Clothing Sensor System for Measuring Knee Joint Angles. IEEE Sensors Journal, **13**(10), pp. 4090–4097.

[28] Othman A., Hamzah N., Hussain Z., Baharudin R., Rosli A. D., Ani A. I. C., 2016. Design and Development of an Adjustable Angle Sensor Based on Rotary Potentiometer for Measuring Finger Flexion. The 6th IEEE International Conference on Control System, Computing and Engineering, Batu Ferringhi, Malaysia, 25-27 Nov., pp. 569-574, DOI: 10.1109/ICCSCE.2016.7893640.
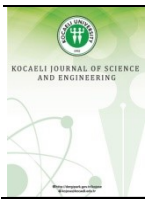
Promising La₂O₃ Nanocatalysts for Low-Temperature Oxidative Coupling of Methane Reaction: A Short Review

Emel ENGİNTEPE [1], * (iD), Ayşe Nilgün AKIN [2] (iD)

[1] Department of Chemical Engineering, Kocaeli University, Kocaeli, 41001, Turkey, **ORCID:** 0000-0001-6214-2117
[2] Department of Chemical Engineering, Kocaeli University, Kocaeli, 41001, Turkey, **ORCID:** 0000-0001-9392-5149

Abstract

This paper reviews the recent literature on La₂O₃ catalysts for the oxidative coupling of methane (OCM), which aims at ethylene production. The following subjects are discussed: (a) the main properties affecting the reaction mechanism such as oxygen vacancy, acid-base property, temperature, and morphology (b) prospects of nano-scale catalysts to improve the performance of the OCM process (c) the contribution of La₂O₃ nanocatalysts to the formation of ethane and ethylene (C₂ hydrocarbon) during the oxidative coupling of methane.

1. Introduction

Coal, then petroleum, and finally natural gas, have been utilized in energy generation and commodity chemical manufacture for the past two centuries. Due to strict environmental regulations and limited natural carbon reserves, the emergence of alternative processes based on renewable and/or "greener" technologies has been given priority for future industries [1]. With a continuous increase in natural gas resources (approximately 6×10^{12} cubic meters), chemical and fuel synthesis using methane as a feedstock has gotten a lot of attention from the petrochemical and energy industries throughout the world, in order to reduce our reliance on diminishing oil resources. Especially, the manufacturing of short-chain olefins, which are important building blocks in the modern chemical industry, immediately requires a synthesis method change from naphtha to methane. Due to the shortage of fossil fuel resources, attention has turned to alternate technologies that use more easily accessible feedstocks. Because methane is

the primary component of natural gas, methane is a promising feedstock alternative for short-chain olefins. [2-7]. Ethylene is a large-scale manufactured chemical with yearly global sales above 140×10^6 tons and a 3.5% annual growth rate [2,7-8]. Nowadays, ethylene is produced by the steam cracking method, which cracks naphtha to olefins and other hydrocarbons [3-5]. In this process, methane is industrially converted to olefins in an indirect way, in which methane first decomposes into the syngas (i.e., CO and H₂) via the catalytic steam or auto thermal reforming at temperatures above 700 °C, then syngas is converted to methanol and finally to olefins. However, the syngas pathway is energy inefficient, and such an indirect method results in low atom usage efficiency. Therefore, the direct conversion of methane to olefins is a highly desirable method, and done many studies to reach this aim. [7,9]. OCM makes it possible for a direct route from feedstock such as natural gas, biogas, or shale gas into value-added chemicals, avoiding the intermediate production of syngas [7,10]. The design of catalysts with high activity and

---

* Corresponding Author: emel.engintepe@kocaeli.edu.tr

selectivity is vital for improving the performance of the OCM reaction [10]. Although much research has been done on OCM for over 30 years due to the opportunity to lower ethylene production costs, unfortunately, these studies have not resulted in a suitable catalyst with the required performance for commercialization. Although these catalysts had promising performance and selectivity, they were limited by their very high operating temperature, low activity, and short lifetime (a few hours to a few days).

The overall yield must be at least 30% for economic efficiency. The necessity to solve these issues has led to the creation of new systems and OCM catalyst designs. Because high temperatures lead to decreasing selectivities of C_2 products, the development of novel catalysts that can run at low temperatures is critical to the economic viability of OCM. Low-temperature oxidative coupling of methane (LT-OCM) allows producing ethylene with an alternative process that converts methane (natural gas) to ethylene in a one-step operation. Siluria Technologies Inc. (shortly Siluria) applied a combination of innovations in the catalyst area to develop unique catalysts. The Company began running a factory in 2015 to demonstrate the low-temperature OCM reaction's industrial application. The factory has been designed to produce at least 350 tons of ethylene per year. Unfortunately, no information about the catalyst utilized is available. Siluria employs nanowire catalysts that operate at lower temperatures than traditional materials, according to multiple patents [1]. Siluria's OCM catalysts work at much lower temperatures (several hundreds of degrees lower) and operating pressures (5-10 atmospheres), and under these conditions, they show high performance and standard lifetimes (years) [11,12].

Recently, developments have had in heterogeneous catalysts with controlled morphologies are expected to improve the activity/selectivity and stability of the OCM catalysts. This review covers topics interested in the La_2O_3 catalysts strategies adopted for enhancement of methane conversion, increasing ethylene selectivity, and decreasing the reaction temperatures.

2. Ethylene Formation Mechanism During Oxidative Coupling of Methane Reaction

CH_4 is transformed to ethane, ethylene, and higher hydrocarbons (C_{2+} hydrocarbons) in a single step under OCM conditions, usually in the presence of oxygen (O_2) and a suitable catalyst [12]. The OCM reaction generally involves the formation of methyl radicals (CH_3·) via hydrogen extraction from methane by available active oxygen species on the surface of the oxide catalyst. The purpose of the OCM catalysts is to produce methyl radicals (CH_3·) while avoiding deep oxidation (the formation of CO,

CO_2, and H_2O) [7,9]. However, the oxidation of CH_4 to CO and CO_2 (CO_X) competes with the coupling of the CH_3 radical to C_{2+}, causing limitations on the selectivity of the desired hydrocarbon products. Furthermore, compared to CH_4, the over-oxidation of desirable hydrocarbon products such as ethane/ethylene is substantially more favorable [12]. Therefore, the most important performance of the OCM catalyst is to produce selective surface oxygen radicals that function as active sites for producing methyl radicals [7,9]. Then, the methyl radicals combine in the gas phase to form ethane (C_2H_6), which will be converted to ethylene (C_2H_4) by dehydrogenation as shown in Figure 1 [1,4,9]. However, OCM has long been limited to a low C_2 yield below economic feasibility, mainly due to the following reasons: (1) The catalyst capable of activating CH_4 also activate the generated C_2H_6 at a similar rate, resulting in the production of thermodynamically stable CO_X gases (2) Refilling generated vacant surface oxygen sites by gas-phase oxygen sometimes leads to adsorbed oxygen species, which promote CO_X formation as an undesirable scheme (3) Furthermore, diffusion of bulk lattice oxygen to the oxide surface is generally slow, leading to low overall activity, especially in the absence of oxygen flow in the gas phase (4) Because the OCM process requires high temperatures (over 800 °C), the probability of methane combustion is generally high [9].

It is generally believed that the OCM reaction consists of two typical steps, including the heterogeneous step of activating CH_4 molecules to CH_3· radicals in the gas phase at electrophilic oxygen sites on the active surface, followed by a homogeneous gas phase step to combine two CH_3· radicals to form C_2H_6 molecules, which are then dehydrogenated into C_2H_4 molecule. [13].

$$CH_4(g) \rightleftharpoons CH_4(a) \qquad (1)$$

$$O_2(g) \rightleftharpoons O_2(a) \qquad (2)$$

$$CH_4(a) + O_2(a) \rightarrow CH_3 \cdot + HO_2 \cdot \qquad (3)$$

$$CH_3 \cdot + CH_3 \cdot \rightarrow C_2H_6 \qquad (4)$$

$$CH_3 \cdot + O_2 \rightarrow CH_3O_2 \cdot \rightarrow CO, CO_2 \qquad (5)$$
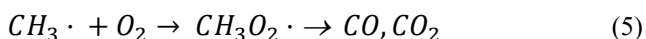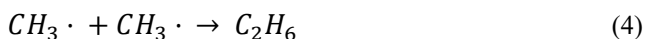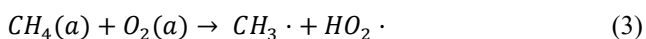
where the gas phase and the adsorbed species are represented by [g] and [a], respectively.

The oxygen species involved in the initiation of the reaction is suggested to be O_2^- or O_2^{2-} on the surface [14,15]. The dissociative adsorption of O_2 on the catalyst surface first produces a peroxy-type species, which subsequently activates the C-H bond. The challenge in OCM is separating C_2H_4 and C_2H_6 products, which undergo additional oxidation and are ultimately prone to CO_X Eqs. (1-5) describe the general steps in the OCM that leads to

production of C_2H_6 [16,17]. In equations (1) and (2), CH_4 and O_2 adsorptions occur on different active sites independently of one another. The abstraction of the hydrogen atom from CH_4 (equation (3)) appears to be the rate-determining step in the overall process. Because the C-H bond of CH_4 has a high dissociation energy (427 kJ/mol).

The initation (equation (3)) is considered to be caused by an adsorbed diatomic oxygen rather than monoatomic oxygen. C_2H_6 is produced by combining two $CH_3\cdot$ radicals (equation (4)). Two oxidation of $CH_3\cdot$ radicals can result in deep oxidation according to equation (5).Competition between reactions (4) and (5) determines selectivity for C_2-compounds.
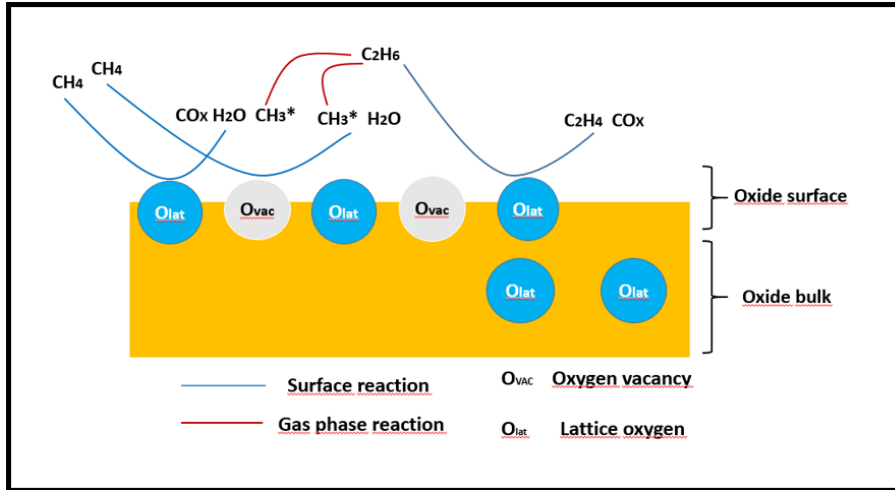
Figure 1. Schematic representation of OCM reaction over metal oxide catalyst surface [9].

2.1. Effect of Operating Temperature on Oxidative Coupling of Methane Reaction

The oxidative coupling of methane (OCM) is a direct way of converting methane into ethane or ethylene. Reaction 6 depicts the overall pathway. Since Keller and Bhasin's and Hinsen and Baerns's pioneer research, this reaction has gotten a lot of attention [18,19].

$$CH_4 + 0.5O_2 \rightarrow 0.5C_2H_4 + H_2O \qquad (6)$$
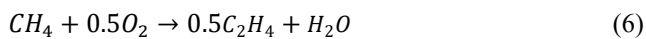
ΔH_r (800 ∘C) = −139 kJ/mol

ΔG_r (800 ∘C) = −153 kJ/mol

Methane coupling without an oxidizing agent is a strongly endothermic reaction, and due to thermodynamic constraints, the conversion is limited. By introducing an oxidant, the reaction becomes exothermic and the thermodynamic limitations can be overcome. However, partial oxidation (reaction (7)) and total oxidation (reaction (8)) are far more thermodynamically favorable than the oxidative coupling of methane.

$$CH_4 + 1.5O_2 \rightarrow CO + 2H_2O \qquad (7)$$

ΔH_r (800 ∘C) = −519 kJ/mol

ΔG_r (800 ∘C) = −611 kJ/mol

$$CH_4 + 2O_2 \rightarrow CO_2 + 2H_2O \qquad (8)$$
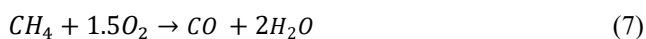
ΔH_r (800 ∘C) = −801 kJ/mol

ΔG_r (800 ∘C) = −801 kJ/mol

To obtain optimum yields of C_2 hydrocarbons (C_2H_6 and C_2H_4) the reaction needs to be controlled kinetically. This requires appropriate catalysts.

It is reported that high temperatures and multistage processes are necessary in order to activate the C–H bond in CH_4. These cause unwanted reactions that inhibit the formation of hydrocarbons and enhance the deeper oxidation of methane, thereby producing products of combustion like CO and CO_2 [20]. According to Ma et al., maximum C_2H_6+C_2H_4 yields have been obtained at two optimum temperatures (500°C and 950°C). Since active catalysts working at low temperatures have not been developed commercially, most OCM studies have been performed at higher temperatures [21]. To

decrease COx products and increase C_2 hydrocarbon yields, the OCM reaction should be performed at a low temperature. Researchers have attempted to lower reaction temperatures, however, spherical catalysts have not been able successfully to lower the temperature of OCM [20]. On the other hand, metal oxide nanocatalysts have recently been discovered to activate methane at lower temperatures. The advancement of OCM technology has been favored by the development of nanostructured catalysts. Siluria has recently developed the first commercial OCM process with a series of "nanowire catalysts" reported to work at temperatures below 600°C. The OCM catalysts are durable for long-run times at low process temperatures, according to Siluria's patent application, even though the single-pass C_2 yield did not reach the aim of 25%.

2.2. Catalysts for Oxidative Coupling of Methane

Oxide catalysts are the most often used catalysts in the OCM process. Transition metal oxides, either pure or modified, and mixed or promoted oxides of group IA and IIA elements, can be examples of these [22]. Some unmodified pure oxides of transition metals were investigated by Kus' et al [23]. Pure/unmodified La(III), Nd(III), Zr(IV), and Nb(V) oxides have catalytic efficiency in the OCM process in the following order: $La_2O_3 \geq Nd_2O_3 \gg ZrO_2 > Nb_2O_5$. Active oxide centers in modified transition metal oxide-based catalysts are thought to play a role in hydrogen abstraction, which has been identified as a key factor in the OCM process.

In this complex heterogeneous–homogeneous process, numerous catalysts have been examined and proven to be effective. Most of them are two-component or multi-component mixed or supported metal oxides, mainly containing components with basic properties like alkaline earth metal oxides, and rare earth metal oxides. The acid-base behavior of the oxide catalyst is largely determined by the kind and strength of the bond between the cationic and anionic species in the oxide. The acid-base characteristic of different oxide systems was discovered to be a critical factor

determining their reactivity in the OCM process [9]. Metal oxides are the catalysts most often studied in terms of their acid-base properties, with surface metal cations are commonly referred to as acid centers and surface oxide anions as basic centers [24]. Zavyalova et al. used a statistical technique to examine a large amount of data on OCM catalysts. They showed that excellent C_2 selectivity requires a strong basic character increased by doping with alkaline (Cs, Na) and alkaline earth (Sr, Ba) metals. Inserting a suitable dopant metal in the crystalline structure of the host oxide often changes the lattice and electronic structure, transforming it into a multifunctional hybrid material [9,25].

The simple and complex oxides of alkaline, alkaline-earth and rare-earth elements have been used to create a catalyst formula with such qualities. Hundreds of catalysts, including the typical Li/MgO and La-based oxides catalysts, have been studied in order to promote ethane, ethylene, propane, propylene (C_2-C_3) selectivity and decrease over-oxidation [7]. One of the most commonly studied catalysts for the oxidative coupling of methane is Li/MgO. The Li element in the Li/MgO catalysts functions as a structural modifier to improve the OCM performance of the catalyst, but it suffers from loss of Li metal because of evaporation during long-term operation; La-based catalysts have relatively lower C_2-C_3 selectivity. Mn_2O_3-Na_2WO_4/SiO_2 catalyst is regarded as the most promising one with a methane conversion of 20-30%, 60-80% C_2-C_3 selectivity, and hundreds of hours of stability and, in particular, stability of several hundred hours [7,19]. According to Ji et al., the existence of WO_4 tetrahedron in the metals promoted by W-Mn/SiO_2 offers an opportunity for high OCM performance due to energy matching with methane and the suitable geometric structure for hydrogen extraction. [22]. But, this catalyst must be run at temperatures over 800 °C, and even a minor decrease in temperature below 800 °C can significantly reduce the activity of the catalyst itself and even stop the OCM process. However, none of them have yet reached the commercialization stage, as their C_2 performance is still relatively poor [7,19]. In Table 1, oxide catalysts reported recently has been presented [19,22,26-29].

Table 1. Recent studies on the metal oxides during OCM reaction [19,22,26-29].

Catalyst	CH4/O2	T(°C)	CH4 Conversion (%)	C2 Selectivity (%)	C2 Yield (%)	References
BaSrTiO₃	2	800	47	29.5	14	[22,26]
4.49 wt.%Li/BaSrTiO₃	2	800	37	59.5	22	[22,26]
5.25 wt.%Mg/BaSrTiO₃	2	800	46.5	43	20	[22,26]

Table 1. (Cont.) Recent studies on the metal oxides during OCM reaction [19,22,26-29].

Catalyst	CH_4/O_2	T(°C)	CH_4 Conversion (%)	C_2 Selectivity (%)	C_2 Yield (%)	References
3.4 wt.%Mg/BaSrTiO₃	2	800	47	51	24	[22,26]
Sm₂O₃/MgO	4	700	24.3	52.3	11.1	[22]
Li-Sm₂O₃/MgO	4	700	24.4	62.5	13.2	[22]
Sm₂O₃	2,5	725	18	72	13	[27]
Na/W/Mn/SiO₂	7	850	43	71	30.4	[27]
Mn/Na₂WO₄/SiO₂	2.5	800	35	47	16.4	[27]
Ce/MgO	4	800	28	50	14	[28]
Li/MgO	2	750	37.8	50.3	19	[28]
CaO powder	4	800	40	50	20	[22,29]
30 wt.% CaO/silica	4	800	30	40	12	[22,29]
CaO fully-coated silica particles	4	800	40	70	28	[22,29]
Na₂WO₄/Mn/SiO₂	3.5	850	32	45	14.4	[22]
Na₂WO₄/Mn/SiO₂ modified with 3 wt.% Al₂O₃ (pellet)	2	850	41	47	19.3	[22]
Na₂WO₄/Mn/SiO₂ modified with 16.7 wt.% MgO (pellet)	2	850	50	38	19	[22]

3. La₂O₃ Catalysts

Many researches have shown that the activity of OCM catalysts is affected by the structural properties of the catalyst. In addition, basicity, surface oxgen and oxygen ion-conductivity, which has been identified as important factors for this reaction, are also impacted by the structural properties of the catalyst [18,26-27].

Zavyalova et al. demonstrated strong basicity as a critical factor for increasing the selectivity of C_2 products. Because CH_4 is a very weak acid, it's not unexpected that it requires a strong base to activate it. Rare earth oxides' basicity rises in the sequence Gd <Sn <Nd <Pr <La [14,24]. Since La₂O₃ is a strong base, it quickly reacts with CH_4. Lanthanum based materials have been studied widely in OCM. The La^{3+}-O^{2-} pair site can effectively activate CH_4, resulting in breaking of the CH_3–H bond and production of the CH_3^--La^{3+}-OH^- intermediate [24]. For surface reaction, the catalyst provides active oxygen and e^- vacancies via a mechanism $La_2O_3 \rightarrow 2La^{3+}O^{2-}e^- +[O]$ [30]. Metiu et al. recently performed periodic density functional theory (DFT) calculations and discovered that adsorption of CH_3^- at the La^{3+} site and H^+ at the O^{2-} site is the most stable dissociative adsorption configuration of CH_4 on the La₂O₃(001) surface [24].

La₂O₃ also prevents the formation of carbon on the metallic surface owing to basic characteristics and CO_2 absorption properties. La₂O₃ forms oxygen-containing species (La₂O₂CO₃) through the reaction and ultimately prevents the coke deposition on the catalyst surface. The reactions listed in Eqs. 9–10 are responsible for La₂O₃'s excellent property of inhibiting coke deposition [31-32]:

$$La_2O_3 + CO_2 \rightarrow La_2O_2CO_3 \qquad (9)$$

$$La_2O_2CO_3 + C \rightarrow La_2O_3 + 2 \qquad (10)$$
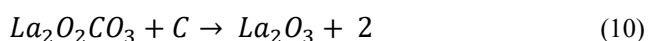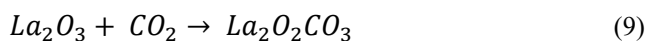
Song et al. also showed that the basic strength of OCM oxide catalysts could be effectively adjusted by optimal doping. They found that strongly basic centers in Sr-doped La₂O₃ nanofibers are essential to enhancing the performance of the OCM, particularly at temperatures exceeding 600 °C. It should be noted that the basicity of catalysts has a strong impact on the oxidative coupling of methane. Moderately alkaline active centers are necessary for a high C_2 yield [9]. The catalytic performances of some La₂O₃ catalysts studied in literature for OCM are shown in Table 2 [27-28,33-34].

Table 2. Reactivity and performance of La_2O_3 catalyts [27-28,33-34].

Catalyst	CH₄/O₂	T(°C)	CH₄ Conversion (%)	C₂ Selectivity (%)	C₂ Yield (%)	References
La_2O_3/MgO	4	800	24	63	15.1	[27]
La_2O_3/CaO	3	900	31	51	15.8	[27]
La/CaO	4	800	28	56	16	[28]
Sr/La_2O_3	4	800	29	59	17	[28]
La_2O_3	5.4	800	24	65	15.6	[28]
La_2O_3–CeO_2	-	775	22.3	66	14.7	[33]
La_2O_3	4	740	-	-	13.5	[34]
LaSrAlO₄	4	720	-	-	13	[34]

The goal of the study in this area has been to improve catalytic performance in terms of C_2 selectivity and better methane conversion in OCM. Since the OCM reaction typically takes place at temperatures of 800 °C and above, it is very difficult to control the selective oxidation of methane to the desired products (ethylene and ethane). Even while OCM performance is more considerable at higher temperatures, exothermic thermal effects can cause poor catalyst stability and, as a result, increased CO_X production. [9]. This high-temperature necessity is in connection with the chemical inertness of methane (due to its strong C−H bond, low electron affinity, high ionization energy, poor polarity, and lack of dipole moment in the methane molecule). Therefore, it is very difficult to obtain kinetic control over the selective conversion of methane. Among several options to meet this challenge, lowering the reaction temperature appears to be the best strategy. The focus of research has recently turned to OCM catalysts that allow low-temperature performance. It has been found that as well as metal content, particle size and shape, affected catalyst activity. In particular, the use of nanostructured catalysts (nanoparticles, nanorods, nanowires, and nanofibers) allows methane to be activated at lower temperatures and to be achieved higher OCM performance compared to powder catalysts. [9,35].

Nano-scale catalysts with modified morphology have a lot of potential for improving the low-temperature OCM performance. Due to having a large surface-to-volume ratio, nanowire and nanofiber morphologies seem to be the most promising [9]. This is because selectively exposed crystallographic facets generally have high defect sites, low atomic density, and high oxygen vacancies that facilitate methane activation. DFT computations and experimental studies have shown that the performance of heterogeneous catalysts strongly depends on the nature of the exposed catalyst surfaces, particularly for structure-sensitive reactions such as OCM. This means that the design of OCM catalysts with an optimized surface structure will provide lower reaction temperatures. Therefore, Siluria Technologies Inc. showed great improvement in LT-OCM performance with nanowire-based catalysts [9,35].

More detailed research was carried out about facet-dependent catalysis of nanocrystal and nanowire catalysts, the effect of crystal facets of CeO_2 for OCM reaction is also investigated by Sun et al. They found out that CeO_2 (doped with 10 wt.% Ca) in nanowire or nanorod forms performed better in terms of LT-OCM performance than CeO_2 catalysts in the form of nanoparticles. Fast Fourier transform (FFT) analysis of their High-Resolution Transmission Electron Microscopy (HRTEM) images showed that nanoparticles and nanowires had some exposed planes in common. But, compared to nanoparticles, CeO_2 in the form of nanowire mostly had (110) exposed facets. To explain the cause of the observed difference in performance, the group performed a DFT calculation and found that methane activation on the peroxided surface (110) is highly preferred due to the existence of moderate alkaline active sites. Also, the addition of Ca on the exposed facet (110) enhanced the basic strength substantially [9]. In addition, Hou et al. [35] researched the structural sensitivity of $La_2O_2CO_3$ catalysts at the nanoscale have various morphology for OCM. The result showed that $La_2O_2CO_3$ and La_2O_3 catalyst in the forms of nanoparticle has only 2% methane activity with zero yields at 500°C, indicated that they are inadequate for the reaction. The morphological changes resulting from hydrothermal nanoscale synthesis caused exposure to various types of crystallographic facets on the surface of the resulting oxide catalysts. Surprisingly, the rod-shaped catalyst performed better in LT-OCM performance (methane conversion of 30% and C_2 selectivity of 50% at

420°C). Sun et al. also investigated La_2O_3 oxide and found that nanorod morphology catalysts showed superior performance at lower temperatures below 650 °C lower than nanoparticles. Also, Hou et al. found that the La_2O_3 catalyst with the rod-shaped morphology exhibited twice the OCM performance (27.4% methane conversion and 43.4% C2

selectivity) relative to its plate-shaped equivalent at temperatures 500 °C lower thanks to its higher surface area to volume ratio [20,35]. Table 3 presents the catalytic performances of nanostructured La_2O_3 catalysts for LT-OCM reaction [35-38].

Table 3. The potential of nanostructured La_2O_3 catalysts for low-temperature OCM [35-38].

Catalyst	Morphology	T(°C)	CH₄ Conversion (%)	C₂ Selectivity (%)	C₂ Yield (%)	References
$La_2O_2CO_3$	Nanorod	420	29.7	48.4	14	[35]
	Nanoplate		0	0	0	
La_2O_3	Nanorods	500	27.4	43.4	12	[35]
	Nanoplate		16.2	24.6	4	
La_2O_3	Nanosheets	550	32.3	45.9	15	[36]
	Nanorods		29	40.5	12	
	Nanoflower		28.9	41.6	12	
	Nanoparticle		9.9	6.4	6	
Sr-La_2O_3	Nanofiber	500	35	47	16	[37]
La_2O_3-CeO_2	Nanofiber	470	27.7	65	12	[38]
		520	28.6	70	4	

Nanostructured catalysts, containing La_2O_3-CeO_2 nanofibers and metal oxide nanowires, have been suggested as a way to enhance the amount of surface catalytic active sites and make better use of the catalytic materials. Although nanostructured materials can increase catalytic activity, the high reaction temperature of OCM quickly degrades structures with a large surface area, making high nanostructured catalysts ineffective [39].

The catalytic performances of La_2O_3 nanorod and nanoparticle catalysts for OCM are compared in Sun et al. study. In the study, the lower initial reaction temperature was achieved with La_2O_3 nanorods than La_2O_3 nanoparticles. Methane was initially converted on La_2O_3 nanorods at 450°C while it was found higher than 550°C on La_2O_3 nanoparticles. Besides, La_2O_3 nanorods showed higher selectivity towards C_2 hydrocarbons than La_2O_3 nanoparticles at low temperatures. To produce C_2 hydrocarbons over La_2O_3 nanoparticles requires higher temperatures than La_2O_3 nanorods. In this study, the reusability of the La_2O_3 nanorod catalyst is also investigated. The catalytic activity over the used catalyst is similar to the fresh catalyst. The shape-specific impact of La_2O_3 nanorods should contribute to the higher rate of CH_4

conversion at low temperatures. It is thought that electrophilic oxygen species O^- and O_2^- are the most important species, and their abundance on the catalyst surface has a positive effect on C_2 selectivity. However, lattice oxygen (O^{2-}) causes total oxidation. Sun et al. showed that the proportion of electrophilic oxygen species (O^- and O_2^-) to lattice oxygen (O^{2-}) determined using XPS analysis is much higher for the La_2O_3 nanorods than La_2O_3 nanoparticle catalysts. Thanks to La_2O_3 nanorods having a high surface area, strong basic surface centers, electron-deficient surface oxygen species, and well-defined surface structures can be obtained better activity and selectivity for OCM reaction than La_2O_3 nanoparticles at low temperature [20]. By optimizing the size and shape of La_2O_3 nanocrystals, high methane activity and high C_2 selectivity for low-temperature OCM reaction can be achieved.

4. Conclusions

To summarize, one of the most difficult problems confronting the catalysis community today is direct methane activation and conversion to other valuable compounds. In addition, the plenty of methane has raised interest in the

development of methods for converting methane to higher hydrocarbons or chemicals. Because of the significant selectivity/conversion constraints associated with all studied catalysts, it has been concluded that traditional spherical catalysts have inadequate performance to obtain a desirable process economy. The catalysts studied in the literature for the oxidative coupling of methane are reviewed. It shows that nanoscale catalysts provide higher C_2 selectivity and methane conversion. Herein, we indicate the catalytic performance of La_2O_3 nanostructures for oxidative coupling of methane reaction. Catalytic properties of La_2O_3 nanocatalysts with different shapes have been compared and found that the activity and selectivity of the structure-sensitive OCM reaction are strongly related to the shape and size of La_2O_3 nanocatalysts. The ethylene yield at low temperature (<600°C) was increased with the invention of nanowire catalysts, and the commercialization of the OCM process was achieved by advanced nanowire catalysts.

Declaration of Ethical Standards

The authors of this article declare that the materials and methods used in this study do not require ethical committee permission and/or legal-special permission.

Conflict of Interest

The authors declare that they have no known competing financial interests or personal relationships that could have appeared to influence the work reported in this paper.

References

[1] Kondratenko V., Peppel T., Seeburg D., Kondratenko V. A., Kalevaru N., Martin A., Wohlrab S. 2017. Methane conversion into different hydrocarbons or oxygenates: current status and future perspectives in catalyst development and reactor operation. Catalysis Science & Technology, **7**(2), pp. 366–381. https://doi.org/10.1039/C6CY01879C

[2] Onoja O.P., Wang X., Kechagiopoulos P.N. 2019. Influencing selectivity in the oxidative coupling of methane by modulating oxygen permeation in a variable thickness membrane reactor. Chemical Engineering & Processing: Process Intensification, **135**, pp. 156–167. https://doi.org/10.1016/j.cep.2018.11.016

[3] Fleischer V., Steuer R., Parishan S., Schomäcker R. 2016. Investigation of the surface reaction network of the oxidative coupling of methane over $Na_2WO_4/Mn/SiO_2$ catalyst by temperature programmed and dynamic experiments. Journal of Catalysis, **341**, pp. 91–103. https://doi.org/10.1016/j.jcat.2016.06.014

[4] Alexiadis V.I., Chaar M., Van Veen A., Muhler M., Thybaut J.W., Marin G.B. 2016. Quantitative screening of an extended oxidative coupling of methane catalyst library. Applied Catalysis B: Environmental, **199**, pp. 252–259. https://doi.org/10.1016/j.apcatb.2016.06.019

[5] Sahebdelfar S., Ravanchi M.T., Gharibi M., Hamidzadeh M.. 2012. Rule of 100: An inherent limitation or performance measure in oxidative coupling of methane?. Journal of Natural Gas Chemistry, **21**, pp. 308–313. https://doi.org/10.1016/S1003-9953(11)60369-1

[6] Zhang H., Wu J., Xu B., Hu C. 2006. Simultaneous production of syngas and ethylene from methane by combining its catalytic oxidative coupling over $Mn/Na_2WO_4/SiO_2$ with gas phase partial oxidation. Catalysis Letters., 106, pp. 161-165. https://doi.org/10.1007/s10562-005-9624-2

[7] Wang P., Zhao G., Liu Y., Lu Y. 2017. TiO_2-doped Mn_2O_3-Na_2WO_4/SiO_2 catalyst for oxidative coupling of methane: Solution combustion synthesis and $MnTiO_3$-dependent low-temperature activity improvement. Applied Catalysis A, General, **544**, pp. 77–83. https://doi.org/10.1016/j.apcata.2017.07.012

[8] Penteado A., Esche E., Salerno D., Godini H. R., Wozny G. 2016. Design and Assessment of a Membrane and Absorption Based Carbon Dioxide Removal Process for Oxidative Coupling of Methane. Ind. Eng. Chem. Res., **55**, pp. 7473−7483. https://doi.org/10.1021/acs.iecr.5b04910

[9] Gambo Y., Jalila A.A., Triwahyono S., Abdulrasheed A.A. 2018. Recent advances and future prospect in catalysts for oxidative coupling of methane to ethylene: A review. Journal of Industrial and Engineering Chemistry, **59**, pp.218–229. https://doi.org/10.1016/j.jiec.2017.10.027

[10] Daneshpayeh M., Mostoufi N., Khodadadi A., Sotudeh-Gharebagh R., Mortazavi Y. 2009. Modeling of Stagewise Feeding in Fluidized Bed Reactor of Oxidative Coupling of Methane. Energy & Fuels, **23**, pp. 3745–3752. https://doi.org/10.1021/ef801060h

[11] U.S. Department of Energy, Ethylene via Low Temperature Oxidative Coupling of Methane. https://www.energy.gov/sites/prod/files/2016/08/f33/Ethylene%20via%20Low%20Temperature%20Oxidative%20Coupling%20of%20Methane.pdf

[12] Baser D.S, Cheng Z.,Fan Jonathan A., Fan L.-S. 2021. Codoping Mg-Mn Based Oxygen Carrier with Lithium and Tungsten for Enhanced C_2 Yield in a Chemical Looping Oxidative Coupling of Methane System. ACS Sustainable Chem. Eng., **9**, pp. 2651−2660. https://doi.org/10.1021/acssuschemeng.0c07241

[13] Xu J.,Zhang Y., Xu X., Fang X, Xi R., Liu Y., Zhang R., Wang X. 2019. Constructing $La_2B_2O_7$ (B = Ti, Zr, Ce) Compounds with Three Typical Crystalline Phases for the Oxidative Coupling of Methane: The Effect of Phase Structures, Superoxide Anions, and Alkalinity on the Reactivity. ACS Catal., **9**, pp. 4030−4045. https://doi.org/10.1021/acscatal.9b00022

[14] Otsuka K., Jinno K. 1986. Kinetic studies on partial oxidation of methane over samarium oxides. Inorganica Chimica Acta, **121**, pp. 237-241. https://doi.org/10.1016/S0020-1693(00)84528-4

[15] Yoon S., Lim S., Choi J.W., Suh D.J., Song K.H., Ha J.M. 2020. Study on the unsteady state oxidative coupling of methane: effects of oxygen species from O_2, surface lattice oxygen, and CO_2 on the C_{2+} selectivity. RSC Adv., **10**, pp. 35889-35897. https://doi.org/10.1039/D0RA06065H.

[16] Noon D., Zohour B., Senkan S. 2014. Oxidative coupling of methane with La_2O_3–CeO_2 nanofiber fabrics: A reaction engineering study. Journal of Natural Gas Science and Engineering, **18**, pp. 406-411. https://doi.org/10.1016/j.jngse.2014.04.004

[17] Ferreria V.J., Tavares P., Figueriedo J.L., Faria J.L. 2013. Ce-Doped La_2O_3 based catalyst for the oxidative coupling of methane. Catalysis Communications, **42**, pp. 50–53. https://doi.org/10.1016/j.catcom.2013.07.035

[18] Bosch C. E., Copley M.P., Eralp T., Bilbé E., Thybaut J.W., Marin G.B., Collier P. 2017. Tailoring the physical and catalytic properties of lanthanum oxycarbonate nanoparticles. Applied Catalysis A: General, **536**, pp. 104–112. https://doi.org/10.1016/j.apcata.2017.01.019

[19] Arndt S., Laugel G., Levchenko S., Harn R., Baerns M., Scheffler M., Schlögl R., Schomacker R. 2011. A Critical Assessment of Li/MgO-Based Catalysts for the Oxidative Coupling of Methane. Catalysis Reviews: Science and Engineering, **53**, pp.424–514. https://doi.org/10.1080/01614940.2011.613330

[20] Huang P., Zhao Y., Zhang J., Zhu Y., Sun Y. 2013. Exploiting shape effects of La_2O_3 nanocatalysts for oxidative coupling of methane reaction. Nanoscale, **5**, pp. 10844. https://doi.org/10.1039/C3NR03617K

[21] Ma Y.H., Moser W.R., Dixon A.G., Ramachandra A.M., Lu Y., Binkerd C., Oxidative coupling of methane using inorganic membrane reactors. U.S. Department of Energy Office of Scientific and Technical Information, DOI: 10.2172/766717.

[22] Galadima A., Muraza O. 2016. Revisiting the oxidative coupling of methane to ethylene in the golden period of shale gas: A review. Journal of Industrial and Engineering Chemistry, **37**, pp. 1–13. https://doi.org/10.1016/j.jiec.2016.03.027

[23] Kus´ S., Otremba M., Taniewski M. 2003. The catalytic performance in oxidative coupling of methane and the surface basicity of La_2O_3, Nd_2O_3, ZrO_2 and Nb_2O_5. Fuel, **82**, pp. 1331–1338. https://doi.org/10.1016/S0016-2361(03)00030-9

[24] Chu C., ZhaO Y., Li S., Sun Y. 2016. Correlation between the acid–base properties of the La_2O_3 catalyst and its methane reactivity. Physical Chemistry Chemical Physic, **18,** pp. 16509-16517. https://doi.org/10.1039/C6CP02459A

[25] Zavyalova U., Holena M., Schlögl R., Baerns M. 2011. Statistical Analysis of Past Catalytic Data on Oxidative Methane Coupling for New Insights into the Composition of High-Performance Catalysts. ChemCatChem, **3**(12), pp. 1935-1947. https://doi.org/10.1002/cctc.201100186

[26] Fakhroueian Z., Farzaneh F., Afrookhteh N. 2008. Oxidative coupling of methane catalyzed by Li, Na and Mg doped $BaSrTiO_3$. Fuel, **87**(12), pp. 2512–2516. https://doi.org/10.1016/j.fuel.2008.02.010

[27] Cruellas A., Melchiori T., Gallucci F., van Sint Annaland M. 2017. Advanced reactor concepts for oxidative coupling of methane. Catalysıs Reviews, **59**, pp. 234–294. https://doi.org/10.1080/01614940.2017.1348085

[28] Tiemersma T.P., Tuinier M.J., Gallucci F., Kuipers J.A.M., van Sint Annaland M. 2012. A kinetics study for the oxidative coupling of methane on a $Mn/Na_2WO_4/SiO_2$ catalyst. Applied Catalysis A: General, **433–434**, pp. 96–108. https://doi.org/10.1016/j.apcata.2012.05.002

[29] An B., Ryu KH., Kim YR., Lee SH. 2007. Activation of Methane to C_2 Hydrocarbons over Unpromoted Calcium Oxide Catalysts. Bulletin of the Korean Chemical Society, **28**(6), pp. 1049-1052. https://doi.org/10.5012/bkcs.2007.28.6.1049

[30] Traykova M., Davidova N., Tsaih J.-S., Weiss A. H. 1998. Oxidative coupling of methane – the transition from reaction to transport control over La_2O_3/MgO catalyst. Applied Catalysis A: General, **169**, pp. 237-247.
https://doi.org/10.1016/S0926-860X(98)00009-X

[31] Osorio-Vargas P., Campos C.H., Navarro R.M., Fierro J.L.G., Reyes P. 2015. Improved ethanol steam reforming on Rh/Al_2O_3 catalysts doped with CeO_2 or/and La_2O_3: Influence in reaction pathways including coke Formation. Applied Catalysis A: General, **505**, pp. 159–172.
https://doi.org/10.1016/j.apcata.2015.07.037

[32] Kumar A., Singh R., Sinha A.S.K. 2019. Catalyst modification strategies to enhance the catalyst activity and stability during steam reforming of acetic acid for hydrogen production. International Journal of Hydrogen Energy, **44**(26), pp. 12983-13010.
https://doi.org/10.1016/j.ijhydene.2019.03.136

[33] Holmen A. 2009. Direct conversion of methane to fuels and chemicals. Catalysis Today, **142**, pp.2–8.
https://doi.org/10.1016/j.cattod.2009.01.004

[34] Ghose R., Hwang H. T., Varma A. 2013. Oxidative coupling of methane using catalysts synthesized by solution combustion method. Applied Catalysis A: General, **452**, pp. 147– 154.
https://doi.org/10.1016/j.apcata.2012.11.029

[35] Hou Y.H., Han W.-C., Xia W.-S., Wan H.-L. 2015. Structure Sensitivity of $La_2O_2CO_3$ Catalysts in the Oxidative Coupling of Methane. ACS Catal., **5**(3), pp. 1663−1674.
https://doi.org/10.1021/cs501733r

[36] Jiang T., Song J., Huo M., Yang N.T., Liu J., Zhang J., Sun Y., Zhu Y. 2016. La_2O_3 catalysts with diverse spatial dimensionality for oxidative coupling of methane to produce ethylene and ethane. RSC Adv., **6**, pp. 34872-34876.
https://doi.org/10.1039/C6RA01805J

[37] Song J., Sun Y., Ba R., Huang S., Zhao Y., Zhang J., Sun Y. and Zhu Y.2015. Monodisperse Sr–La_2O_3 hybrid nanofibers for oxidative coupling of methane to synthesize C_2 hydrocarbons. Nanoscale, **7**, pp. 2260-2264.
https://doi.org/10.1039/C4NR06660J

[38] Noon D., Seubsai A., Senkan S. 2013. Oxidative Coupling of Methane by Nanofiber Catalysts. ChemCatChem, **5**, pp. 146 – 149.
https://doi.org/10.1002/cctc.201200408

[39] Yunarti R.T., Lee M., Hwang Y. J., Choi J.-W. , Suh D. J., Lee J., Kim I.W., Ha J.-M. 2014. Transition metal-doped TiO_2 nanowire catalysts for the oxidative coupling of methane. Catalysis Communications, **50**, pp.54–58.
https://doi.org/10.1016/j.catcom.2014.02.026

Kocaeli University

Kocaeli Journal of Science and Engineering

http://dergipark.org.tr/kojose

Natural Navigation System Design for Indoor Mobile Robots

F. Azeez ADEBAYO [1, *] (iD), H. Metin ERTUNÇ [2] (iD)

[1] *Department of Mechatronics Engineering, Kocaeli University, Kocaeli, 41001, Turkey,* **ORCID:** *0000-0002-8160-6949*
[2] *Department of Mechatronics Engineering, Kocaeli University, Kocaeli, 41001, Turkey,* **ORCID:** *0000-0003-1874-3104*

Article Info	Abstract
	Natural navigation simply refers to free navigation without the necessity of tapes, magnets, reflectors, or even wires. Many autonomous vehicles possess this as world maps are readily available and provide a perfect basis for machine learning solutions. However, this is not so much the case for indoor applications. Here, paths are often dynamic and more constrained; therefore, requiring the continuous identification, mapping and localization of the surrounding area. This work focuses on developing an indoor natural navigation system; the localization is achieved with a fusion of the wheel's odometry to the on-board Inertial Measurement Unit (IMU i.e., a combination of relative localization and absolute localization) using Unscented Kalman Filter (UKF) as system's encoder's accumulation of errors is desired to be nullified while employing a PID control in correcting reference state errors. The map is simultaneously constructed using laws of geometry based on static points obtained from a Lidar, subsequently converted to an occupancy grid layout for effective path planning. In operation, tangency is applied in the avoidance of dynamic obstacles. The simulation results obtained in this study confirms the possibility of a simple, educational, indoor navigation system approach easily integrable by other mobile robots of the differential drive model.

1. Introduction

Various studies have gone into autonomous navigation in vehicles for both indoor and outdoor use cases. These studies, while they have without doubt contributed to the success recorded in this area, also offer execution of complex equations and algorithms, which has made its adoption difficult and ultimately, hinder their reproducibility. Indoor mobile robot navigation particularly suffers here as the lack of satellite positioning signals, so discussed in [1] implies its localization and mapping calls for the inclusion of more sensors in its determination which further complicates and compounds the equations.

In this study, we attempt to build a simple indoor differential drive robot, using simplified steps and equations, for a better understanding of the literature, and to ultimately, ensure reproducibility in any coding language. A LiDAR-based navigation technology called

CoreSLAM [2] was studied and its variation, BreezySLAM [3] is implemented to generate an occupancy grid map [4] for which the robot will operate. Its feasibility and performance relative to other SLAM techniques is evaluated in [5].

Due to the accumulation of noise leading to drift errors that is accompanied by the use of encoder's wheel odometry alone in localization, a sensor fusion technique with the Unscented Kalman Filter, is applied to combine its results with an IMU [6-7]. The UKF, like the other filters such as Kalman, extended Kalman filter used in combining data of various sensors of similar targets, has been shown in [8] to require very basic governing equations on orientation and position in order to estimate robot states.

In getting the robot to move from one desired place to another, the A-star algorithm from [9] is employed. The algorithm plots the shortest walkable path between nodes, in this study, map pixels, depending on the distance measurement technique selected; Manhattan, Euclidean, etc. Also, the suitability of PID in minimizing error between target and reference robot speed state has been

---

*   Corresponding Author: hazeezadebayo@gmail.com

established in [10] while a simple Tangency approach is selected in avoiding obstacles as the need for a non-infrastructural change and cost-free solution is imperative.

The results obtained in this study showed a 70% improvement in path following accuracy of the sensor fused algorithm over the use of wheel odometry alone. This is further corroborated in [7], where for the square trajectory tested, an accuracy of 66.5% was observed, and a similar result is depicted in [11].

Similar works have also been demonstrated with some variation of the above techniques depending on the choice of sensor, often involving but not limited to; visual SLAM with cameras, sonar-based localization, or some hybrid integration into neural networks [11-15], as well as other combinations with more additions in terms of complexity and constraints, as in the use of RFID, Wi-Fi or Bluetooth whose accuracy and performance depends on implementing other external structures such as receivers [16-19]. The next section will highlight the methodology as well as offer calculation justifications in the design or the differential drive robot. After that, a section on results, followed by conclusions and recommendations marks the end of the paper.

2. Materials and Methods

2.1. Kinematics of Differential Drive Robot

The basic configuration of the mobile robot is with two drive wheels with encoders mounted on them and a free castor wheel for its stability. Drive wheels can be controlled independently, and they maintain a common axis as shown in Figure 1.
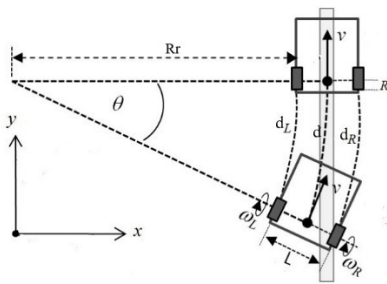
Figure 1. Differential Drive.

The kinematic model of differential drive mobile robot is therefore given by the relations:

$$\dot{x} = \frac{v_R + v_L}{2}\cos\theta = \frac{R}{2}(\omega_R + \omega_L)\cos\theta \tag{1}$$

$$\dot{y} = \frac{v_R + v_L}{2}\sin\theta = \frac{R}{2}(\omega_R + \omega_L)\sin\theta \tag{2}$$

$$\dot{\theta} = \frac{v_R - v_L}{L} = \frac{R}{L}(\omega_R - \omega_L) \tag{3}$$

where; ω_R is rate at which right wheel is turning, ω_L is rate at which left wheel is turning, R is radius of the wheels, and L is the wheel base distance.

Three notable cases associated with the differential drive are also stated below:

- When $v_R = v_L$, the robot moves in a straight line either forward or backward depending on the direction of wheel rotation.
- When $v_R = 0$, the robot moves about the right wheel and about the left wheel when $v_L = 0$. The robot will always move about the wheel with the smallest velocity and while this helps in steering, small errors in the relative velocities between the wheels can affect the robot trajectory.
- When $v_R = -v_L$, the robot rotates about the midpoint of the wheel.

Implementing this model helps us in translating from right and left wheel velocities, v_R and v_L into $\dot{x}$ and $\dot{y}$ describing changes along x and y as well as $\dot{\theta}$ describing changes in the robot orientation. However, since v_R and v_L, do not form inputs that are readily available to us in motion, using the unicycle model our inputs can be designed to be v and ω representing translational and angular velocities respectively. The model is given by:

$$\dot{x} = v\cos\theta \tag{4}$$
$$\dot{y} = v\sin\theta \tag{5}$$
$$\dot{\theta} = \omega \tag{6}$$

Equating both $\dot{x}$ in Eq. (1) and (4) and diving the through by $\cos\theta$. We have;

$$v = \frac{R}{2}(\omega_R + \omega_L) \Longrightarrow \frac{2v}{R} = \omega_R + \omega_L \tag{7}$$

$$\omega = \frac{R}{L}(\omega_R - \omega_L) \Longrightarrow \frac{\omega L}{R} = \omega_R - \omega_L \tag{8}$$

From which v_R and v_L are obtained as:

$$\omega_R = \frac{2v + \omega L}{2R} \Longrightarrow v_R = \frac{2v + \omega L}{2} \tag{9}$$

$$\omega_L = \frac{2v - \omega L}{2R} \Longrightarrow v_L = \frac{2v - \omega L}{2} \tag{10}$$

Thus, making our inputs governed by the combined action of both the linear velocity v and the angular velocity w. Of which, feedbacks are obtained from the wheels as ticks representing how many revolutions $s_{(time,t)}$, and by extension, distance d_L, d_R moved by the robot wheels of radius r over a certain amount of time. From these, the position and orientation are calculated by applying geometric techniques [20].

$$d_L = \frac{s_{l(t)} - s_{l(t-1)}}{n} * 2\pi r \tag{11}$$

$$d_R = \frac{S_{r(t)} - S_{r(t-1)}}{n} * 2\pi r \qquad (12)$$

where n, is the number of ticks of encoder per revolution.

For analysis, assuming the robot is at some position (x_0, y_0), headed in a direction making an angle θ with the x axis as described in Figure 1. From this, we can write:

$$d_L = R_r \Delta\theta \qquad (13)$$
$$d = (R_r + \frac{L}{2})\Delta\theta \qquad (14)$$
$$d_R = (R_r + L)\Delta\theta \qquad (15)$$

where R_r is the radius of movement, d_L and d_R are arc curvature or distance traveled by the left wheel, right wheel respectively and d is distance described by the center.

Making $\Delta\theta$ and d the subject of the formular yields the relations:

$$\Delta\theta = \frac{d_R - d_L}{L} \qquad (16)$$
$$d = \frac{d_R + d_L}{2} \qquad (17)$$

If distance traveled, d taken to be so infinitesimally small that it is assumed to be a straight line. We can write the change in x and y to be of the form:

$$\Delta x = d \cos\theta \qquad (18)$$
$$\Delta y = d \sin\theta \qquad (19)$$

Since coordinates (x_0, y_0) are the known starting point of the robot, the new pose is therefore estimated as:

$$x' = x_0 + d \cos\theta \qquad (20)$$
$$y' = y_0 + d \sin\theta \qquad (21)$$

However, ideally, we may also describe the position of a robot capable of moving in a particular direction $\theta(t)$ at a given velocity $v(t)$ by integrating Eq. (1), (2) and (3) as:

$$x(t) = \frac{1}{2}\int_0^t (v_R(t) + v_L(t)) \cos\theta(t)\, dt \qquad (22)$$
$$y(t) = \frac{1}{2}\int_0^t (v_R(t) + v_L(t)) \sin\theta(t)\, dt \qquad (23)$$
$$\theta(t) = \frac{1}{L}\int_0^t (v_R(t) - v_L(t))dt \qquad (24)$$

For the special case of a differential drive robot, the odometry which is the means by which we can obtain or estimate the pose information of the robot as in $(x, y$ and $\theta)$, essentially tracking the effect of the wheel velocities and updating pose accordingly, solving the forward kinematics problem is given as:

$$x(t) = x_0 + \frac{1}{2}\int_0^t (v_R(t) + v_L(t)) \cos\theta(t)\, dt \qquad (25)$$
$$y(t) = y_0 + \frac{1}{2}\int_0^t (v_R(t) + v_L(t)) \sin\theta(t)\, dt \qquad (26)$$
$$\theta(t) = \theta_0 + \frac{1}{L}\int_0^t (v_R(t) - v_L(t))dt \qquad (27)$$

Unfortunately, we cannot simply specify an arbitrary robot pose $(x; y; \theta)$ and find the velocities that will get us there as in the inverse kinematics problem since each individual wheel contributing to the robot's motion imposes constraints on the robot; which is that it cannot directly slide to the side. Described using Eq. (28) from Figure 2 below;
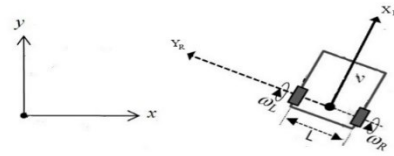
Figure 2. Non-holonomic nature of the differential drive.

$$\dot{Y}_R = \dot{y}\cos\theta - \dot{x}\sin\theta = \left(\frac{R}{2}(\omega_R + \omega_L)\sin\theta\right)\cos\theta - \left(\frac{R}{2}(\omega_R + \omega_L)\cos\theta\right)\sin\theta = 0 \qquad (28)$$

here, θ is the angle $\dot{X}_R$ makes with the horizontal axis, x.

Implying that the robot indeed cannot move laterally along its axle, it will require a more complicated set of steering maneuvers. Hence, imposing what is called a non-holonomic constraint. We may also confirm this by checking if the workspace velocity equation in Eq. (28) is integrable. Here we have:

$$f(x, y, \theta) \neq 0 \qquad (29)$$

2.2. PID

In section 2.1, we showed that our inputs are functions of both the linear velocity v and the angular velocity w. Since the linear velocity v, can be chosen as a constant valued number that represents the speed limit of our robot, the heading becomes the only controllable parameter as seen in Eq. (6). The difference between the desired direction and the current direction is known as the error and is written in Eq. (30).

$$e = \theta_d - \theta_o \qquad (30)$$

where θ_d is the desired orientation which can be obtained using Eq. (31) when waypoints in the form (x_g, y_g) are provided as goal states for the robot and θ_o is the robot's current orientation.

$$\theta_d = \arctan\left(\frac{y_g - y_o}{x_g - x_o}\right) \tag{31}$$

or set as $\theta(t)$ when v_R and v_L are directly inputted as in Eq. (27). If a PID is applied to correct this error, e, as shown in Eq. (32), to produce ω which will help in moving the current state to the desired state, Eq. (33).

$$PID(e) = K_p e(t) + K_I \int_0^t e(t)dt + K_D \dot{e}(t) \tag{32}$$
$$\omega = PID(e) \tag{33}$$

where error e, for correctness, is evaluated such that the angle is expected to remain between $-\pi$ and π to avoid ambiguities.

2.3. IMU

Now that we have all that is required to control the robot, it is imperative to state that these models only describe an ideal scenario where there is no drift or slip in the wheels or from the encoder reading. While further operating under the assumption that the time under consideration is infinitesimally small. In practice however, this is not always the case. Although the time can still be kept relatively infinitesimal, the slip cannot be so programmed. To overcome this, an IMU equipped with magnetometer, accelerometer and gyroscope is used externally to track the movement and its results fused. The plane XY is particularly of interest as the rotation is about the Z axis. First, we need to normalize the raw accelerometer data as:

$$accel\_x\_normalized = \frac{accel[x]}{\sqrt{(accel[x]^2 + accel[y]^2 + accel[z]^2)}} \tag{34}$$
$$accel\_y\_normalized = \frac{accel[y]}{\sqrt{(accel[x]^2 + accel[y]^2 + accel[z]^2)}} \tag{35}$$

where acceleration in X, Y and Z directions are given by $accel[x], accel[y]$ and $accel[z]$ with their resulting normalized acceleration in X and Y.
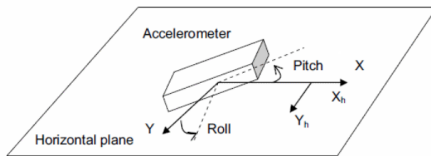
Figure 3. IMU at tilted position.

If the IMU device is tilted, then the pitch and roll angles are not equal to $0°$, as seen in Figure 3. The magnetic sensor measurements in all direction will need to be compensated. Hence, we first obtain the pitch and roll angle value as:

$$pitch = asin(accel\_x\_normalized) \tag{36}$$
$$roll = -asin\left(\frac{accel\_y\_normalized}{cos(pitch)}\right) \tag{37}$$

Next, we calculate the tilt compensated magnetometer in X and Y directions as:

$$magnxcomp = magn[x] * \cos(pitch) + magn[z] * sin(pitch) \tag{38}$$
$$magnycomp = magn[x] * sin(roll) * sin(pitch) + magn[y] * cos(roll) - magn[z] * sin(roll) * cos(pitch) \tag{39}$$

Finally, the earth's magnetic north is measured using the components of the magnetometer obtained above, from which our heading formular can then be written as:

$$heading = 180 * \frac{atan2(magnycomp, magnxcomp)}{\pi} \tag{40}$$

This, as well as the obtained longitudinal acceleration readings will be used in the sensor fusion model.

2.4. Sensor Fusion

The system is modeled in the UKF to have two sensors; IMU's linear acceleration, angular velocity measurement, and heading measurements as well as the encoders reading. The state vector is chosen to be:

$$x_n = \begin{bmatrix} p_x \\ p_y \\ \varphi \\ v \\ \dot{\varphi} \\ \dot{v} \end{bmatrix} = \begin{bmatrix} x + vt\cos\theta \\ y + vt\sin\theta \\ \theta + wt \\ v + at \\ w \\ a \end{bmatrix} \tag{41}$$

where p_x is the absolute x position, p_y is the absolute y position, φ is the yaw, v is the longitudinal velocity, $\dot{\varphi}$ is the yaw rate and $\dot{v}$ is the longitudinal acceleration.

Of which Gaussian noise with covariances representing uncertainties in our guess or estimates are subsequently introduced. That is:

$$x_{n+1} = f_n(x_n) + u_n \tag{42}$$
$$y_n = h_n(x_n) + v_n \tag{43}$$

where u_n is the process noise, v_n is the measurement noise, the process model is f_n and measurement model is h_n. x_{n+1} is the state vector and its measurement is denoted by y_n. Here, we wish to estimate the mean and covariances of both the state and its predicted estimated measurement.

2.4.1. Unscented Transformation

Suppose we know the mean $\bar{x}$ and covariance P of the state x, which could be either predicted or filtered estimates, we can find a set of points with a sample mean and covariance equal to $\bar{x}$ and P. the points are called sigma points, which are random in the sense that they depend on the current estimate of the state and state error covariance. We then apply our nonlinear function, Eq. (44), to each of these points. Once these are known, the calculations are deterministic i.e., no random generators are involved. The sample mean and covariance is a good estimate of the true mean and covariance of y. the biggest drawback here being the requirement of a matrix square root that requires $\mathcal{O}(n_x^3)$ operations.

$$y = h(x) \tag{44}$$
$$y^i = h(x^i) \tag{45}$$
$$\hat{y}_u = \frac{1}{2n_x}\sum_{i=1}^{2n_x} y^i \tag{46}$$
$$R_{\tilde{y},u} = \frac{1}{2n_x}\sum_{i=1}^{2n_x}(y^i - \hat{y}_u)(y^i - \hat{y}_u)^T \tag{47}$$

where y^i represents the output of every sigma point, $\hat{y}_u$ is the unscented estimated mean obtained from the sample average and $R_{\tilde{y},u}$ unscented estimated covariance. This also applies to the states in estimating its mean and covariance.

2.4.2. Unscented Kalman Filter

Although, there are three steps for the unscented Kalman filter; the Time update or prediction step, the sigma update and lastly, the measurement update or filter step. The sigma update step can be skipped with a bit of trade off on the accuracy while saving computation i.e., only the time update and measurement step are used and are shown below:
where n represents time. We start with what the mean and covariance initially are at time, $n = 0$:

$$\hat{x}_{0|0} = E[x_o] \tag{48}$$
$$P_{\tilde{x},0|0} = \left\|x_0 - \hat{x}_{0|0}\right\|^2 \tag{49}$$

Then, for $n = 1, ...$ the time update step is performed, then the mean is predicted and covariances of the state are estimated by running the sigma points into the process model, f_n as seen in Eq. (53).

$$x_{n-1}^i = \hat{x}_{n|n-1} + \tilde{x}^i \quad \text{for i} = 1, ..., 2n_x \tag{50}$$
$$\tilde{x}_n^i = \left[row_i\left(\sqrt{n_x P_{\tilde{X},n-1|n-1}}\right)^T\right] \text{ for i} = 1, ..., n_x \tag{51}$$

$$\tilde{x}_n^i = -\left[row_i\left(\sqrt{n_x P_{\tilde{X},n-1|n-1}}\right)^T\right] \text{ for i} = n_x + 1, ..., 2n_x \tag{52}$$
$$\hat{x}_n^i = f_n(\hat{x}_{n-1}^i) \tag{53}$$
$$\hat{x}_{n|n-1} = \frac{1}{2n_x}\sum_{i=1}^{2n_x}\hat{x}_n^i \tag{54}$$
$$P_{\tilde{x},n|n-1} = \frac{1}{2n_x}\sum_{i=1}^{2n_x}(\hat{x}_n^i - \hat{x}_{n|n-1})(\hat{x}_n^i - \hat{x}_{n|n-1})^T \tag{55}$$

where a $row_i(A)$ denotes the ith row vector of the matrix A and $\sqrt{n_x P_{\tilde{X},n-1|n-1}}$ is a matrix square root of $(n_x P_{\tilde{X},n-1|n-1})$ such that $\sqrt{n_x P_{\tilde{X},n-1|n-1}}^T\sqrt{n_x P_{\tilde{X},n-1|n-1}} = n_x P_{\tilde{X},n-1|n-1}$. n_x is the dimension of the state vector, $\hat{x}_{n|n-1}$ is the estimate of the mean and covariance $P_{\tilde{X},n-1|n-1}$ of the state error covariance at time $n-1$, lastly, x_{n-1}^i, represents the sigma point. Next, the measurement update is performed. Again, the predicted estimates are taken and then run through the measurement model h_n to obtain the measurement sigma points, y_n^i. Then the predicted estimated value of the measurement, $\hat{y}_{n|n-1}$ which is the sample average of the sigma points are calculated. R_{n-1} covariance representing the gaussian noise for each sensors introduced. It is a diagonal matrix. We also use a covariance $P_{\tilde{x}\tilde{y}}$ that is a combination of the state sigma points and the measurement sigma points to obtain the Kalman gain, K_n. This gain factor is basically used to decide final value for robot state. Subsequently we update the predicted state estimates and covariance.

$$y_n^i = h_n(x_n^i) \tag{56}$$
$$\hat{y}_{n|n-1} = \frac{1}{2n_x}\sum_{i=1}^{2n_x} y_n^i \tag{57}$$
$$P_{\tilde{y}} = \frac{1}{2n_x}\sum_{i=1}^{2n_x}(y_n^i - \hat{y}_{n|n-1})(y_n^i - \hat{y}_{n|n-1})^T + R_{n-1} \tag{58}$$
$$P_{\tilde{x}\tilde{y}} = \frac{1}{2n_x}\sum_{i=1}^{2n_x}(x_n^i - \hat{x}_{n|n-1})(y_n^i - \hat{y}_{n|n-1})^T \tag{59}$$
$$K_n = P_{\tilde{x}\tilde{y}}P_{\tilde{Y}}^{-1} \tag{60}$$
$$\hat{x}_{n|n} = \hat{x}_{n|n-1} + K_n(y_n - \hat{y}_{n|n-1}) \tag{61}$$
$$P_{\tilde{x},n|n} = P_{\tilde{x},n|n-1} - K_n P_{\tilde{y}} K_n^T \tag{62}$$

There are however other ways of evaluating sigma points e.g, upon computation of some scaling parameter, λ which is a function of n_x. For this, in the place of $\frac{1}{2n_x}$ the corresponding mean and covariance weights W_i are used. Every other thing does remain the same; calculate sigma points, time update, and measurement update wherein the final state represents the desired vectors. The UKF is favored as it facilitates implementation of the algorithms as non-linear transformations of a set of deterministically chosen sigma points which replaces calculations of Jacobian matrices [21].

2.5. Map Making

Basically, the Lidar obtains coordinates of static or non-dynamic obstructions as polar co-ordinates (r, θ) representing to what degree away from a specific datum within itself that it has spun. Hence, points of the Lidar's reading that falls below or within the Lidar's view-finder's range are collected and saved as landmarks, as the robot moves. In addition, every collected point is mapped or appended to the robot's location (x_i, y_i) at the time it was collected. The robot can be controlled to all locations of interest and an array of landmarks and corresponding robot locations are generated which are then casted into bytes to which an occupancy map can be created.

More specifically, the algorithm used is a variant of the CoreSLAM [2], and is called BreezySLAM [3], developed to implement a simple SLAM that can be integrated into a filter-based localization subsystem. This algorithm however, includes the use of the Random-Mutation Hill-Climbing search where a position S is initialized by m randomly selected instances from T. For each iteration, the algorithm randomly replaces one instance in S by another randomly selected instance in $T - S$. If this replacement can improve the predictive accuracy of the instances in T, the change will be retained [22]. This process is repeated for p times, where p is the maximum search iterations possible. This helps in establishing a better robot position based on a starting position as opposed the Monte Carlo localization (MCL). While, for each obstacle detected, the algorithm does not draw a single point, but a function with a hole whose lower point is at the position of the obstacle resulting in a grey-level map with holes dug to represent obstacle likelihood [2]. Bresenham algorithm is used to draw the view finder's rays. Furthermore, the conversion from real-world meters to pixels is also afforded the user. In this study, total map size in pixels and its equivalent in meters were chosen as 1000 and $10m$ respectively. Lastly, while the map algorithm is open loop, although not always required, the image generated may be further processed for a more perfect representation, in this case, with Opencv.

2.6. A-star

The name is derived from the algorithm being an optimal form of another common graph-search algorithm known as 'A'. Three functions are of interest and are given as the heuristic; a simple calculation of the distance or cost-to-go from the current node to the nth node or end node. It is often denoted by $H(n)$ and may employ different methods in obtaining a best estimate of the measured distance, in this case, Manhattan distance was

selected. The function $G(n)$; representing the estimate of the cost-to-come i.e., path cost estimate from start node to node under consideration or current node. Lastly, $F(n)$, which is the sum of the cost-to-go and cost-to-come, Eq. (63).

$$F(n) = G(n) + H(n) \qquad (63)$$

The $F(n)$ helps in prioritizing which node to move next upon looking up the queue in the open-set of available nodes for the node with the smallest *F score*. The open-set is an array of tuples of available nodes to move and their corresponding *F scores*, when at any given node of interest. An item is pulled from the open-set and expanded only once it has been selected, to which an open-set is generated again. Nodes can be thought of as grid co-ordinates or map intersects. In the end the taken path is made into an array of co-ordinates representing the best shortest distance from the start point to a goal or target point. These co-ordinates are what are called waypoints. The overall low computation time and the guarantee of producing optimal paths makes for A-star's selection for this study. The algorithm is demonstrated using Figure 4 below:
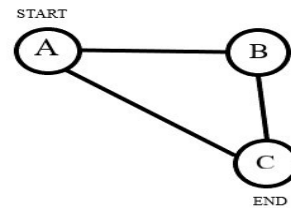
Figure 4. State transition graph illustrating the operation of the A-star.

Node A has two available nodes connected hence path AB and AC are considered and the respective $F(n)$ compared. Assuming all grid connectors have edge of 1 unit as they are equally spaced. It follows that:

- A→B: cost-to-come, $G(n)$, 1, representing the unit or edge of the path between A and B. then cost-to-go, $H(n)$, the heuristic, an estimate of the distance to the end or target point, C, also 1. Hence, from Eq. (63), $F(n) = 2$.
- A→C: cost-to-come, (n), 1, representing the unit or edge of the path between A and C. then cost-to-go, $H(n)$, the heuristic, an estimate of the distance to the end or target point, C, which is itself. Hence, 0. Therefore, $F(n) = 1$.
- The open-set will contain; $[(2, B), (1, C)]$. To which the candidate with the lowest *F score*, C, is selected and popped from the list. Hence, path chosen is A → C.

The map under consideration is an extract of the BreezySLAM generated image and processed using

Opencv in order to threshold the image. i.e., binarize; make it an image of just free spaces (white) and walls or obstructions (black). On this new map, co-ordinates become pixels to which the start point and goal point may be specified. The algorithm is run such that it checks a node or pixel's neighbor and avoids them if they are below a specified color threshold, in this case black pixels, then maps a path around it, i.e., path is strictly traced on the white spaces.

2.7. Obstacle Avoidance

The A-star algorithm generates waypoints for which already satisfies the avoidance of walls and other static obstacles. However, dynamic obstacles are not accounted and as such requires being addressed; when the Lidar or ultrasonic sensor detects an obstacle within a certain view range and angle, while the robot follows this predefined path, it first checks the distance between its current position and the next goal or target state in the waypoint, call it $p2t$ and compares it against the distance between its current position and the obstacle, $p2o$. If the distance $p2o$ is greater; it implies that the obstacle does not constitute an hinderance to its current trajectory hence, it is ignored. However, if $p2t$ is greater, a function is called that places a circle of a specified radius on the obstacle's location and draws a line tangential to the circle. The co-ordinate of the point of tangency is collected and appended to the waypoint as an intermediate stop for the robot to avoid the obstacle. The algorithm is demonstrated using Figure 5 below:
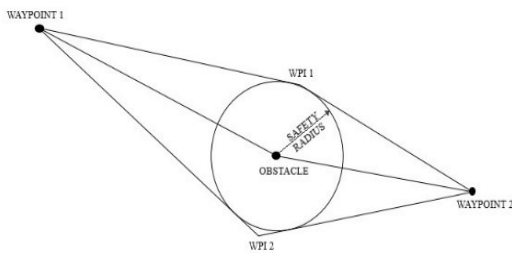
Figure 5. Obstacle avoidance illustration.

Let waypoint1 co-ordinate be (x_1, y_1) and obstacle co-ordinate be (x_o, y_o). Then let a line $w1o$ exist between these points, to which its center co-ordinate is $\left(\frac{x_1 + x_o}{2}; \frac{y_1 + y_o}{2}\right)$. Finally, let the distance between the center co-ordinate of $w1o$ and (x_o, y_o) be d.

1. Iterate for x from 0 to $(h + r)$ and y from 0 to $(k + r)$, in circle equation, $(x - h)^2 + (y - k)^2 = r^2$ with center co-ordinate of $w1o$ as the origin (h, k) and d as radius, r. and save all generated circle co-ordinates as tuples of an array, B.

2. Iterate for x from 0 to $(h + r)$ and y from 0 to $(k + r)$,

in circle equation, $(x - h)^2 + (y - k)^2 = r^2$ with obstacle co-ordinate as the origin (h, k) and *safety _radius* as radius, r. and save all generated circle co-ordinates as tuples of an array, C.

3. Compare arrays B and C and extract the two common co-ordinates marking the intersection of both circles, tuple co-ordinates w1i1 and w1i2.

4. Repeat $1 - 5$ for waypoint 2 as $w2o$ and extract arrays $w2i1$ and $w2i2$ intersection points.

5. Using the line equation, $y - y_1 = m(x - x_1)$, where (x_1, y_1) is $w1o$ and m is the gradient obtained between $w1o$ and intersection w1i1.

6. Similarly, $y - y_1 = m(x - x_1)$, where (x_1, y_1) is $w2o$ and m is the gradient obtained between $w2o$ and intersection $w2i1$.

7. Iterate for x and y in both cases to maximum limit above the sum of radius of both circles and save in an array, $w1l$ and $w2l$. Like in steps 1 and 2.

8. Compare $w1l$ and $w2l$ for a single point of intersection, i.e., waypoint $wpi1$.

9. Depending on the desired robot behavior; repeat steps *5, 6, 7* and *8* with the respective second point of intersection to *wpi2*. Decide which new waypoint, *wpi1* or *wpi2* to append as intermediary between waypoint1 and waypoint2.

2.8. Experimental Setup

Overall, the setup shown in Figure 6 includes:
- Raspberry pi
- Lidar
- Motor x2
- Incremental Encoder x2
- Ultrasonic sensor
- IMU
- L298n motor driver
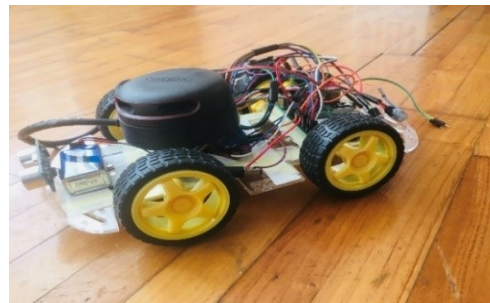
Figure 6. The assembled mobile robot.

The experiment was carried out in a room of size 5 by 4.4 m, with wooden demarcations which constituted part of the stationary obstacle, while the room's door opens to a corridor of about 6 by 1.2 m. Maximum and minimum

motor speed limits are set. The PID constants $K_p = 10$, $K_i = 0.01$, and $K_d = 0.1$, as well as the *previous error* and *cumulative error* for the calculation of the differential and integral errors respectively, were initialized at 0. The robot's dimensions (width, wheel radius etc.) were also initialized before the algorithm is run on the raspberry.

As the robot move, the encoder's feedback in combination with the IMU's data is served as input values into motion equations satisfying Eq. (41), to which state information is predicted. Furthermore, this information is then fed into the SLAM algorithm that obtains Lidar data and mapping ensues. Simultaneously, the PID is employed to correct the difference between the theoretical target state and the real-world execution. This generates a corrected w that helps in updating the robot's pose before the whole

process is repeated until a satisfactory map is obtained by the user.

3. Results and Discussion

Two main use cases are foreseen; Firstly, the user controls the robot around the intended spaces and the robot, as it moves, localizes, and generates a map as depicted in Figure 7 (Map 1-6), then saves the last copy of the generated map when satisfactory. Secondly, the user specifies any target co-ordinates or points within the map, declared as start and stop pixel co-ordinates respectively. The saved image, Figure 7 (Map 7), is then binarized by the robot, Figure 7 (Map 8), and a path is generated, and subsequently traced by the robot as seen in Figure 8.
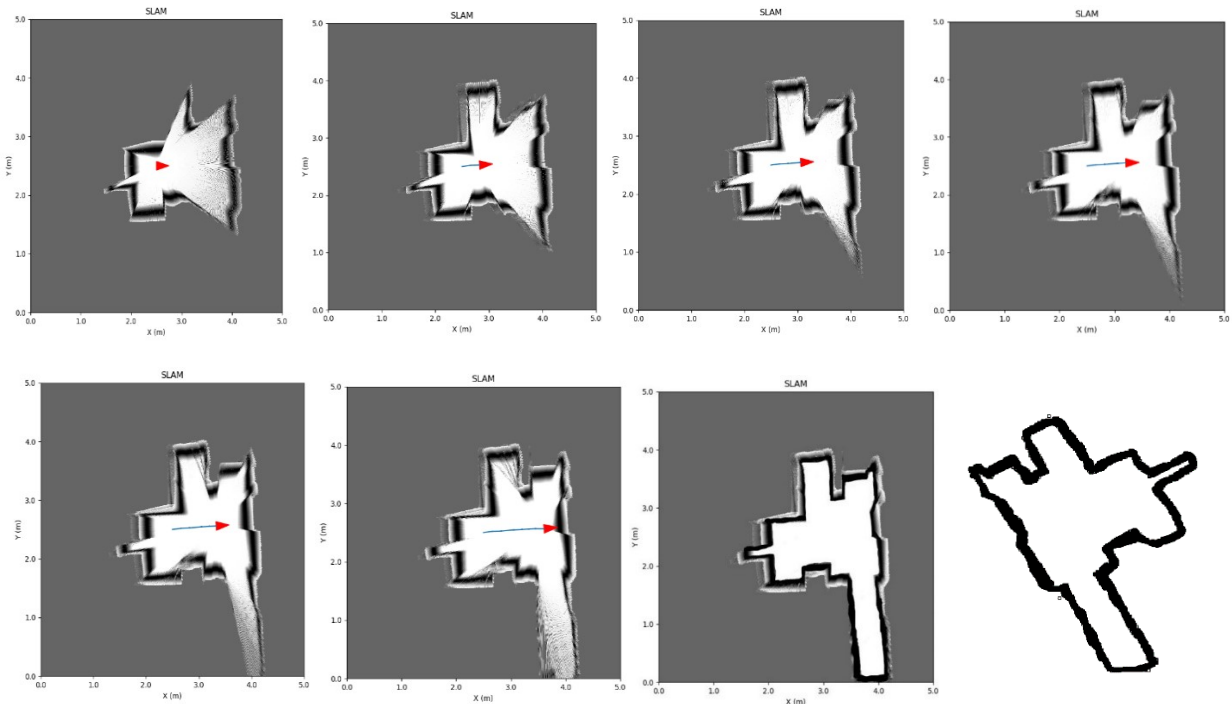
Figure 7. First use case or scenario.
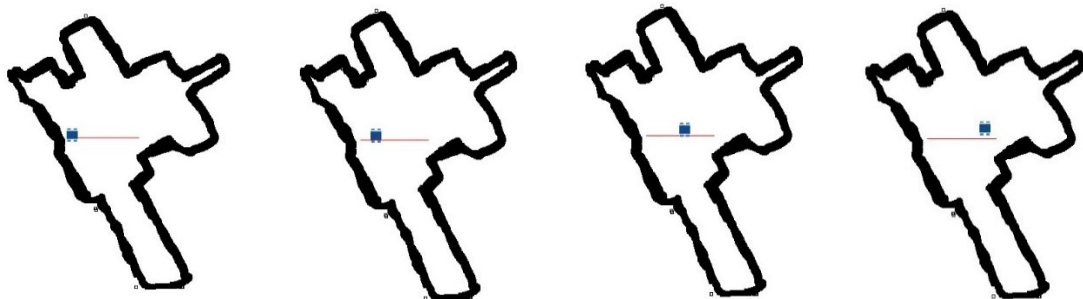
Figure 8. Second use case or scenario.

The measurement factors here would be the robot's ability to accomplish a mission or task without interaction with a human operator (i.e., navigate autonomously), as well as the closeness between the A-star algorithm

generated path (AGP) in the form of waypoints and the robot's real traced path (RTP) with and without sensor fusion, implying its accuracy. Although, its ability to alter

said waypoints if only to avoid dynamic obstacles is implied.

With its real-time progress shown in Figure 8, its behavior as observed is plotted in Figure 9, and 10. Essentially, indicating a success in the intention of the study, to some degree of accuracy, also estimated.
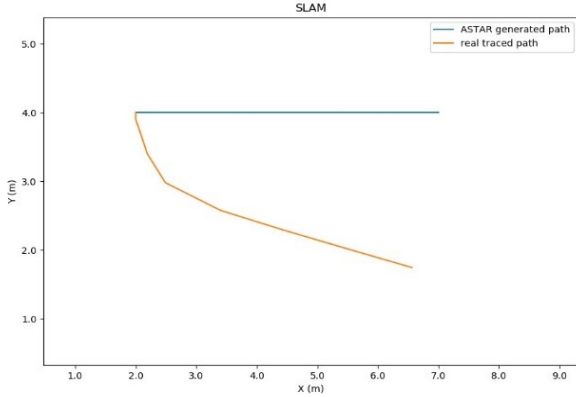
Figure 9. Performance for a straight trajectory (without sensor fusion).
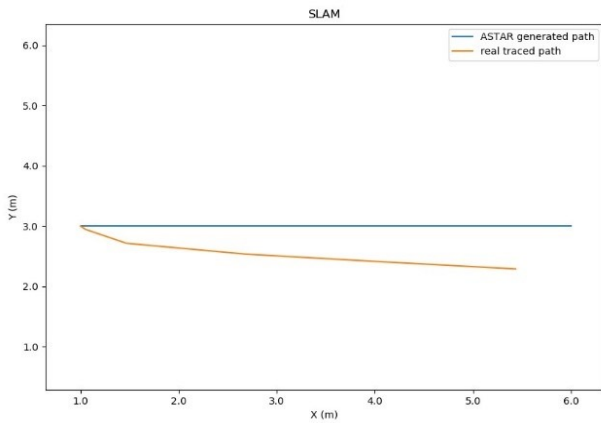
Figure 10. Performance for a straight trajectory (with sensor fusion).

In order to estimate the error, the mean deviation representing the average absolute deviation of points of the RTP from the AGP is calculated. For this, the mean Euclidean distance which is the sum of Euclidean distance at each corresponding point divided by the total number of the corresponding points, n, is employed.

$$\bar{x} = \frac{\sum_{i=0}^{n}(\sqrt{(x_{agp}-x_{rtp})^2+(y_{agp}-y_{rtp})^2})}{n} \quad (64)$$

where (x_{agp}, y_{agp}) are A-star algorithm's generated path co-ordinates and (x_{rtp}, y_{rtp}) represents the robot's real traced path co-ordinates.

The closer the estimates are to zero, the more accurate the trace is. Using Eq. (64) with four sample corresponding waypoints for AGP and RTP from Figure 9, and 10.

Table 1. Average Euclidean Distance Error.

Implementation	Average Euclidean Distance error (m)
Without sensor fusion	1.5
With sensor fusion	0.45

Table 1 shows the estimated error of the localization implementation. With the inclusion of sensor fusion bringing the error closer to zero, offering a comparative accuracy of about 70%.

The robot's behaviour is further demonstrated in Figure 11 for a zig-zag trajectory as the rigidity of the A-star algorithm does not allow for shapes such as square, circle etc. to be naturally selected. The algorithm resorts to finding the optimal path to the goal which may not necessarily be square, circular etc.
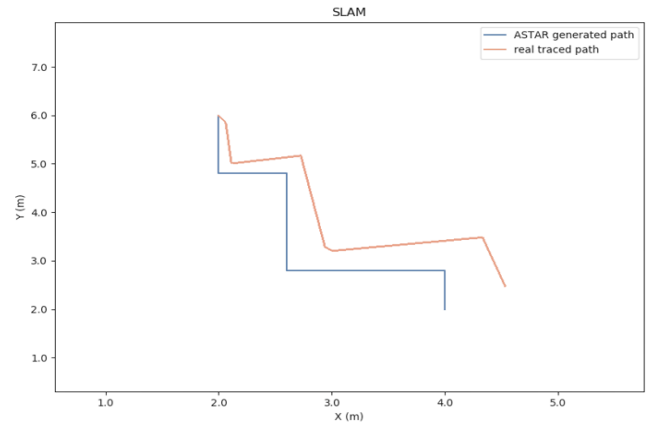
Figure 11. Performance for a zig-zag trajectory (with sensor fusion).

4. Conclusions

A differential drive robot with natural navigation was designed. The aim of which was educational, i.e., to ease intending engineer's approach on steps and calculations to be implemented for designing indoor mobile robots. The basic steps followed have been outlined and are reproducible. The code is also made available on GitHub, in python and is integrable in parts or as a whole in other differential drive robot related projects.

This study uses sensor fusion to limit the drift errors associated with encoder wheel odometry as it combines its results with the IMU. This in turn, successfully increased the accuracy of the localization and helped in map

creation. The natural navigation also included an ability to move from one specified point to another within the map while avoiding obstacle; this was achieved with the use of A-star search algorithm for the best estimated path and a tangency approach to avoiding obstacle. The approach utilized in this paper offers a not-so-simple yet not-so-complex combination of techniques that are computationally efficient and fast. However, more generally, the PID constant's values and the covariance matrix values of the sensors could be fine-tuned, with a further inclusion of the sigma update step in the UKF, for a more accurate trace. While employing a more flexible path search algorithm or technique might do even better for the robot's behavior.

Furthermore, in the future, the necessary research will be done to evaluate the best steps to analysis for stresses, feasible materials, weight considerations as well as aesthetics, also aimed at easing its integration for intending engineers designing mobile robots.

Declaration of Ethical Standards

The author(s) of this article declare that the materials and methods used in this study do not require ethical committee permission and/or legal-special permission.

Conflict of Interest

The authors declare that they have no known competing financial interests or personal relationships that could have appeared to influence the work reported in this paper.

References

[1] Wei L., Cappelle C.,Ruichek Y., 2013. Camera/Laser/GPS Fusion Method for Vehicle Positioning Under Extended NIS-Based Sensor Validation. IEEE Transactions on Instrumentation and Measurement, **62**(11), pp. 3110-3122. https://doi.org/10.1109/TIM.2013.2265476.

[2] Bruno S., Oussama H., 2010. CoreSLAM: a SLAM Algorithm in less than 200 lines of C code. Mines ParisTech - Center of Robotics, Paris, FRANCE.

[3] Bajracharya S., 2014. BreezySLAM: A Simple, efficient, cross-platform Python package for Simultaneous Localization and Mapping. Student Papers, Record Group 38, Special Collections and Archives, Leyburn Library, Washington and Lee University, Lexington, VA.

[4] Tsardoulias E. G., Iliakopoulou A., Kargakos A. et al., 2016. A Review of Global Path Planning Methods for Occupancy Grid Maps Regardless of Obstacle Density. Journal of Intelligent & Robotic Systems, **84**(1), p.p. 829–858. https://doi.org/10.1007/s10846-016-0362-z.

[5] Zou Q., Sun Q., Chen L., Nie B., and Li Q., 2021. A Comparative Analysis of LiDAR SLAM-Based Indoor Navigation for Autonomous Vehicles. IEEE Transactions on Intelligent Transportation Systems. https://doi.org/10.1109/TITS.2021.3063477.

[6] Guran M., Fico T., Chovancova A., Duchon F., Hubinsky P., Dubravsky J., 2014. Localization of iRobot create using inertial measuring unit, 2014 23rd International Conference on Robotics in Alpe-Adria-Danube Region (RAAD), 2014, pp. 1-7, doi: 10.1109/RAAD.2014.7002261.

[7] Suriya D., Srivenkata S., Sundarrajan G., Kiran S., Ragul B., Vidhya B., 2016. A Robust Approach for Improving the Accuracy of IMU based Indoor Mobile Robot Localization. ICINCO (2) 2016: 436-445. DOI:10.5220/0005986804360445.

[8] Urrea C., Agramonte R., 2021. Kalman Filter: Historical Overview and Review of Its Use in Robotics 60 Years after Its Creation. Journal of Sensors, **2021**. https://doi.org/10.1155/2021/9674015.

[9] Hart P. E.; Nilsson N. J.; Raphael B., 1968. A Formal Basis for the Heuristic Determination of Minimum Cost Paths. IEEE Transactions on Systems Science and Cybernetics, **4**(2), pp.100–107. https://doi.org/10.1109/TSSC.1968.300136.

[10] Purnama H. S., Sutikno T., Alavandar S. and Subrata A. C., 2019. Intelligent Control Strategies for Tuning PID of Speed Control of DC Motor - A Review. 2019 IEEE Conference on Energy Conversion (CENCON), pp.24-30. https://doi.org/10.1109/CENCON47160.2019.8974782.

[11] Berntorp K., Årzén K. E., & Robertsson A., 2011. Sensor Fusion for Motion Estimation of Mobile Robots with Compensation for Out-of-Sequence Measurements. 11th International Conference on Control, Automation and Systems, pp. 211-216.

[12] Janai J., Güney F., Behl A., Geiger A., 2020. Computer Vision for Autonomous Vehicles: Problems, Datasets and State of the Art. Foundations and Trends® in Computer Graphics and Vision, **12**(1–3), pp 1-308.

[13] Khan M. S., Chowdhury S. S., Niloy N., Aurin F. T. Z., Ahmed T., 2018. Sonar-based SLAM Using Occupancy Grid Mapping and Dead Reckoning. TENCON 2018 - 2018 IEEE Region 10 Conference, pp. 1707-1712.
doi: 10.1109/TENCON.2018.8650124.

[14] Mu X., He B., Zhang X., Song Y., Shen Y., Feng C., 2019. End-to-end navigation for Autonomous Underwater Vehicle with Hybrid Recurrent Neural Networks. Ocean Engineering, **194**. ISSN 0029-8018, https://doi.org/10.1016/j.oceaneng.2019.106602.

[15] Kang J. G., An S. Y., Kim S. and Oh S., 2009. Sonar based Simultaneous Localization and Mapping using a Neuro Evolutionary Optimization. 2009 International Joint Conference on Neural Networks, pp. 1516-1523,
https://doi.org/10.1109/IJCNN.2009.5178826.

[16] Wang J., Liu J., Kato N., 2019. Networking and Communications in Autonomous Driving: A Survey. IEEE Communications Surveys & Tutorials, **21**(2), pp. 1243-1274. doi: 10.1109/COMST.2018.2888904.

[17] Chiu C.C., Hsu J.C., Leu J.S., 2016. Implementation and analysis of Hybrid Wireless Indoor Positioning with iBeacon and Wi-Fi. 2016 8th International Congress on Ultra Modern Telecommunications and Control Systems and Workshops (ICUMT), pp. 80-84. doi: 10.1109/ICUMT.2016.7765336.

[18] Li J. et al., 2018. PSOTrack: A RFID-Based System for Random Moving Objects Tracking in Unconstrained Indoor Environment. IEEE Internet of Things Journal, **5**(6), pp. 4632-4641. doi: 10.1109/JIOT.2018.2795893.

[19] Lin P.T., Liao C.A. and Liang S.H., 2021. Probabilistic Indoor Positioning and Navigation (PIPN) of Autonomous Ground Vehicle (AGV) Based on Wireless Measurements. IEEE Access, **9**, pp. 25200-25207.
https://doi.org/10.1109/ACCESS.2021.3057415.

[20] Jensfelt P., 2001. Approaches to Mobile Robot Localization in Indoor Environments. (Doctoral thesis, Royal Institute of Technology (KTH), Stockholm, Sweden). Retrieved from http://www.diva-portal.org/smash/get/diva2:8964/FULLTEXT01.pdf

[21] Przemysławm P., Piotr K., 2020. Unscented Kalman filter application in personal navigation. Proc. SPIE 11442, Radioelectronic Systems Conference 2019, 114421C. DOI:10.1117/12.2564984

[22] Si L., Yu J., Wu W., Ma J., Wu Q., Li S., 2017. RMHC-MR: Instance selection by random mutation hill climbing algorithm with MapReduce in big data. Procedia Computer Science, **111**, pp.252-259. https://doi.org/10.1016/J.PROCS.2017.06.061.

Kocaeli University

Kocaeli Journal of Science and Engineering

http://dergipark.org.tr/kojose
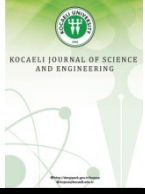
Evaluation of Seaway Passenger Transportation in Kocaeli Bay, By Using the Methods of Analytic Hierarchy Process and Analytic Network Process

Zafer AYDIN [1, *] (iD) , Güler ALKAN [2] (iD)

[1] Kocaeli Metropolitan Municipalıty, Kocaeli, 41040, Turkey, **ORCID:** 0000-0002-8155-0674
[2] İskenderun Technical University, Hatay, 31200, Turkey, **ORCID:** 0000-0001-6809-0784

Article Info	Abstract
Review paper *Received* : May 05, 2021 *Accepted* : March 08, 2022 **Keywords** *AHP* *ANP* *Public Transport* *Seaway Passenger Transport*	Municipalities are in charge of running and managing public transport activities. This study aims to identify the factors affecting seaway passenger transportation via scheduled high-speed sea buses, motorboats, and cityline from 11 points in Kocaeli Bay. To provide sea transportation service in Kocaeli at a sustainable cost, which is the legal obligation of Metropolitan Municipalities, framing the current transportation system as a whole in the light of these factors is another objective. In today's rapidly changing world, the criteria may quickly change over time. Many primary and secondary criteria affect public transportation systems. Therefore, it would be appropriate to use multi-criteria decision-making methods while dealing with Public Transport systems. In addition to the Analytic Hierarchy Process (AHP) method, it would be appropriate to use the Analytic Network Process (ANP) method, which is a structure that examines the interaction between criteria and allows systematic revealing of all types of dependencies and feedback between factors and sub-factors affecting the decision-making process. In the study, the results obtained by AHP and ANP methods were compared and evaluated, in order to determine the optimal alternative for the seaway passenger transportation in Kocaeli Bay to be economical, sustainable and continuous.

1. Introduction

By considering Kocaeli Bay as a whole, this study is prepared to determine the most suitable alternative or option in order to make seaway passenger transportation in Kocaeli Bay at a sustainable cost carried out by Kocaeli Metropolitan Municipality from 12 different piers as a component of public transportation activities.

Kocaeli Bay is a natural port and the farthest point that can be reached by sea in the Marmara Region as the industrial center of Turkey, a country where energy pipelines, rail system, and Ro-Ro lines which are the integration point of Trans-European highways with the seaway and intersect as a transfer center for long-distance flights.

The seaway passenger transportation in Kocaeli Bay is carried out by the Seaway Transportation Directorate of

Kocaeli Metropolitan Municipality. Urban public transport activities are among the main duties of the municipalities. The sea transportation directorate is an organization affiliated with the metropolitan municipality, and the metropolitan municipal council approves its budget. Damage arising from the seaway passenger transport activity is covered by the municipal budget. In this respect, there is no resource problem for seaway passenger transportation in Kocaeli Bay, but the fact that the income obtained is very low due to the fact that the resource spent for this activity is very high and the number of passengers is very low, it appears to be the biggest obstacle to the sustainable sea transport in Kocaeli Bay.

By examining the operations of the Seaway Transportation Directorate, it has been observed that the personnel structure is multifaceted and that it is subject to various regimes (permanent, contracted, subcontractor), resulting in ineffectiveness in personnel productivity. It is observed that there seem personnel subject to different working regimes, and the service produced is high in terms

---

* Corresponding Author: zfraydin61@gmail.com

of personnel costs. It has been determined that the professional competence and education level of the personnel of the Seaway Transportation Directorate is above the average and the average age is at the middle level. The Seaway Transportation Directorate has a mixed fleet structure and has four sea buses, three leased passenger motorboats and two city line ferries. The average age of the ships is above the economic life of 20 years, excluding leased passenger motorboats. The conditions and types of the ships are different from each other, which causes inefficiency in terms of management and operation.

There are 12 piers under the Seaway Transportation Directorate. Eight of these piers are open during summer and winter, and four of them are open only in summer. There is no integrity in the structures of the piers. All piers have separate technical features. The pier, which is suitable for berthing for a ship type, is not suitable for another ship type. This situation causes problems in berthing and departure maneuvers of ships and pier management. It has been determined that the number of piers is high on the Kocaeli Bay scale. There are four piers in the same district.

In Kocaeli Bay, except Kocaeli Metropolitan Municipality Directorate of Seaway Transportation, it has been determined that three maritime companies, namely Istanbul Sea Buses (İDO), İstanbullines A.Ş., Dentur Avrasya A.Ş., are operating in the field of passenger and vehicle transportation, and that there is no integration between these companies, and that each company operates independently.

Urban public transportation is a tool that is needed in every moment of our daily city life when traveling from point A to B, to go to work, school and any intercity transfer. Considering that the majority of people today live in cities, public transport is an integral part of city life. Intelligent transportation systems (electronic fare collection systems, smart stops, passenger information, etc.) are part of the public transportation system. Intelligent transportation systems play an important role in determining the urban public transportation fee policies and the implementation of these policies (single ticket, transfer, fare payment by distance, subscription). In the Seaway Transportation Directorate, money is collected according to the distance. A smart ticket system is used as a fare collection system, but transfers with other transport systems are not available. It is seen that the transfer is valid only between municipal vehicles. This situation is considered to be a factor in not achieving the desired increase in the number of passengers.

The only institution authorized to determine the local public transport ticket prices and fare policies is the Transport Coordination Center (UKOME), which is affiliated with the metropolitan municipalities. Since the decision-making mechanism of the Transportation Coordination Centers depends on the public, the increase in the ticket prices of the vehicles (metro, tram, sea bus, ferry, etc.) connected to the urban public transport modes is limited, and the management costs are determined in market conditions, this situation creates a serious problem for companies whose only item of income is ticket prices in terms of income-expenditure balance.

When the legal regulations on public transportation in the city are examined, there are basically three different passenger profiles (Adult, Student, 60 years and over). When Kocaeli Metropolitan Municipality's travel cards regulation is examined, it is stated that there are types of passengers transported free of charge in 14 different items (municipal officers, police, municipal employees, etc.), and, according to the Ministry of Family and Social Policies regulation, citizens aged 65 and over will benefit from public transportation free of charge. There is no government subsidy for passengers carried free of charge. The high number of passengers carried free of charge causes the income to be low and, this situation causes the number of resources to increase spent to perform the service.

The population is estimated to be 2.500.000 people in the 2025 projection of the Turkey Statistical Institution for Kocaeli province. With the impact of the 17 August 1999 earthquake, settlements tended to move away from the seashore and tended to be established on high mountain slopes. This trend continues. In addition, it is considered that the demand for sea transportation will not change much for the next ten years due to the lack of attraction centers between the opposite shores of the Kocaeli Bay that will increase urban population mobility. When planning transportation, the current and future population and zoning projections of the city should be taken into account.

2. Literature Review

In the literature, it is observed that there are many studies in various fields in which the solution of AHP and ANP methods with fuzzy numbers are applied. Evaluation of the contribution of IT departments to the organizational development and strategic goals of companies using fuzzy AHP and balanced scorecards (BSC) methods (Lee et al., 2008). The fuzzy AHP method has been used in the selection of the most suitable bridge construction method in bridge construction projects where many criteria are effective (Pan, 2008). In the selection of the most suitable hospital location, a solution was sought by the fuzzy logic AHP method (Vahidnia et al., 2009). The fuzzy AHP method was used in the selection of enterprise resource

planning in the textile company (Cebeci, 2009). To evaluate the performance of the production company, the fuzzy ANP method and the balanced objective cards methods were used (Yuksel and Dağdeviren, 2010). The fuzzy ANP method and TOPSIS methods were used together as a decision-making method in evaluating the education system (Chen and Chen, 2010). The fuzzy AHP method was used to evaluate the uncontrolled landfill area (Promentilla et al., 2008). There are also studies in the literature in which AHP and ANP methods are used together. In these studies, The role of production performance measurement systems in success was evaluated using AHP/ANP methods (Yang et al., 2009). AHP/ANP methods were applied as a decision-making method according to different conditions depending on time. (Saaty, 2007). Comparisons are done by showing the parallels between the AHP/ANP methods (Garuti & Spencer, 2007).

3. Materials and Methods

3.1. Multi-Criteria Decision-Making

Every person is constantly faced with the situation of making decisions both in his/her own life and in his/her business life. In their own lives, they decide on issues such as which products to meet their individual needs by purchasing, where they will spend their holidays, how to evaluate their savings, while they decide on issues such as organizational structure of institutions, marketing strategies, production planning, financing, and investments in their business lives. Multi-criteria decision problems are problems where a choice must be made between at least two criteria. Generally, all multi-criteria decision-making problems involve many criteria. For the most appropriate decision, the criteria must be determined very well. In the next step, the most suitable alternative should be determined for the solution of the problem. After that, the problem should be solved by making the necessary calculations and determining the most suitable alternative. In today's competitive environment, it is very important to make the right decisions for the success of the business. Therefore, to make the right decisions, decisions are made not only subjectively based on experience, but also based on objective and subjective criteria using quantitative and qualitative data as well as experience. For this, numerical methods have been developed to make the right decision. In today's world, due to the rapid development of time and events, the criteria that affect the problem can also change during the period of time the event continues. When handling the problem, variable events should also be considered. (Ozden, 2009).

Because the criteria are based on people's experiences and that people's experiences are different in multi-criteria problems, criteria in multi-criteria problems often conflict with each other. Therefore, there is usually no optimal solution for such problems. So, none of the alternative solutions is the best solution according to all the specified criteria. In addition, the effect (weight) of the criteria taken into consideration by the decision maker when choosing among the alternatives is not the same. These weights can often vary depending on the decision maker. (Ozden, 2009).

Multi-criteria decision-making methods used in the literature are mentioned below. The multi-criteria decision-making methods in Chene and Hwang's classification are; Dominance method, Maximin, Maximax, Conjunctive Method, Disconjunctive Method, Lexicographic Method, Semi Order Lexicographic Method, Elimination By Aspects- EBA Method, Simple Additive Weighting Method, Weighted Product Method, Distance from Target Method, AHP-Analytic Hierarchy Process, ELECTRE-Elimination and Choice Translating Reality, TOPSIS-Technique for Order Preference by Similarity to Ideal Solution, VIKOR -Vise Kriterjumska Optimizacija I Kompromisno Resenje, UTADIS- Utilities Additives Discriminantes, PROMETHEE- Preference Ranking Organization Method For Enrichment Evaluation and ANP-Analytic Network Process method. (Chen et al., 1992).

3.2. Multi-Criteria Decision-Making

Analytic Hierarchy Process is a structure with the objective function at the top, criteria and sub-criteria under this function, and various alternatives under the criteria. The Analytic Hierarchy Process was developed in 1971 by Thomas L Saaty. Saaty transforms AHP into a model in 1977, making it easier to solve decision-making problems. (Rencber, 2010). The main purpose of AHP is to contribute to the solution of multi-criteria decision-making problem. Analytic Hierarchy Process (AHP) is one of the multi-criteria decision-making methods. It is not a magical method (or model) that provides the correct answer. However, it is a process that helps decision-makers to find the "best" answer. (Formen and Sally, 2002).

AHP is a powerful and easy-to-understand method that allows groups and individuals to combine qualitative and quantitative factors in the decision-making process. (Saaty, 1996). The AHP method is used in decision-making problems where there are one or more decision makers and in environments with certainty or uncertainty where there are too many alternatives and criteria. It is an easy-to-use method allowing the decision-maker to

incorporate his/her intuition and instincts into the solution process and to act together by consensus on different ideas. (Dogan, 2004). One of the most important functions of AHP is being able to synthesize many factors in a single hierarchy. (Power, 2003).

The AHP method aims to ensure that this decision-making process is completed most efficiently by placing the related priorities on a scale for a given set of options, taking into account the intuitive judgments of decision-makers and the comparison consistency of the options in the decision-making process. This approach supports the decision maker's judgments based on his/her knowledge and experience. The strength of the AHP method is that it systematically organizes countable and uncountable factors and offers a simple and effective solution in the decision-making process by taking all factors into account. (Ozyurek et al., 2008)

AHP is a measurement theory based on binary comparison of alternatives according to a common criterion. AHP provides important assistance to the decision-maker in solving multi-criteria and multi-choice problems. AHP poses a problem with a hierarchical structure that consists of more than one level. In the Analytic Hierarchy Process, a hierarchical structure consisting of purpose, criteria, possible sub-criteria levels, and alternatives is used for each problem. (Saaty, 1990). It is a general method for complex, difficult to understand or unstructured problems. It is based on three basic principles, namely the establishment of hierarchies, determination of advantages, and logical and numerical consistency. (Guner and Yucel, 2007).

In AHP, the problem is structured hierarchically. Figure 1 shows a three-level hierarchical structure. There is a purpose at the top of the hierarchy, and the structure is completed with the criteria below the purpose and, alternatives at the bottom. (Felek et al., 2007).
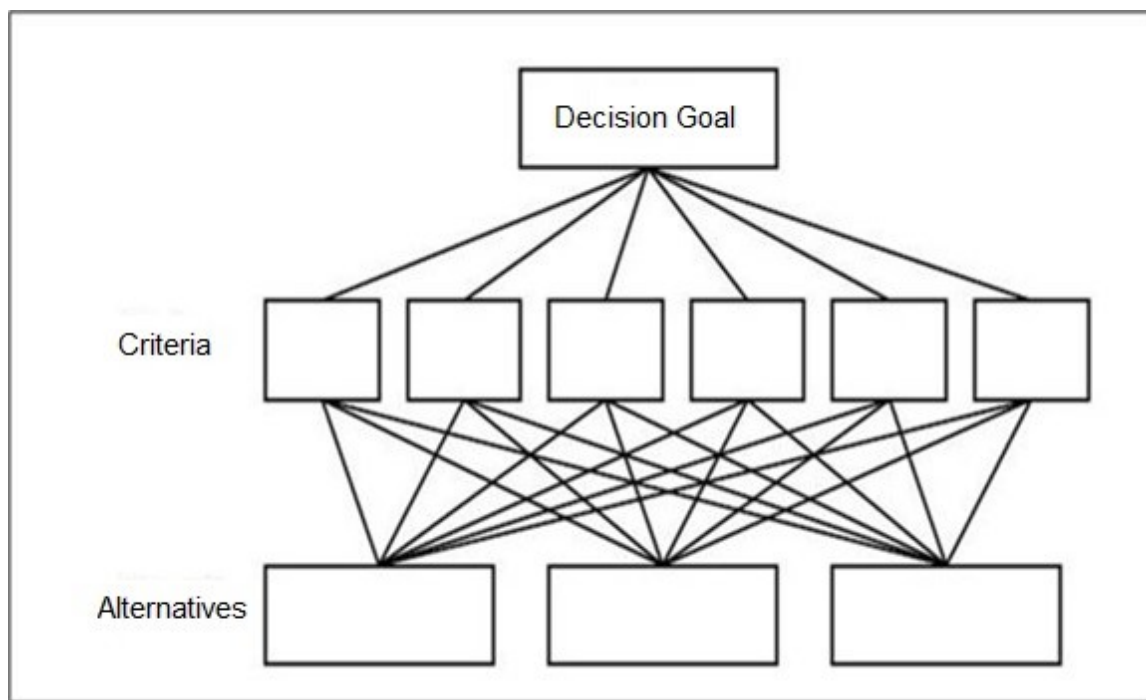
Figure 1. Three Level Analytic Hierarchy Model (Saaty and Vargas, 2001)

3.3. Analytic Network Process (ANP)

Analytic Network Process is a structure that examines the interaction between criteria. Making decisions quickly and effectively has been one of the most important goals of businesses in today's competitive environment. For businesses to quickly adapt to rapidly changing environmental conditions and take effective decisions in parallel with this change is possible by using scientific methods that can evaluate many qualitative and quantitative factors together in the decision process.

Analytic Network Process (ANP) is a method that can be used in this process. (Dagdeviren et al., 2005) The AHP method is used in environments with certainty or uncertainty where one or more decision makers are present. Likewise, it is used in decision problems where there are too many alternatives and criteria. It provides the opportunity to make decisions individually and as a group, to include the intuition and instincts of the decision maker in the solution process, and to act together by reconciling different ideas (Dogan, 2004).

ANP is a new multi-purpose decision-making method which is an extension of the Analytic Hierarchy Process (AHP) method. ANP is the first technique that allows systematically revealing all kinds of dependencies and feedback among factors and sub-factors affecting the decision-making process. (Bayazıt, 2002).

Analytic Network Process is a structure established to determine dependencies between criteria rather than assumptions in decision making. (Yang et al., 2009).

A decision problem in ANP consists of clusters, factors, and connections between them. A Cluster is formed by the combination of suitable factors in a network. ANP is based on feedback and dependency within each cluster. Thus, ANP enables easy modeling of complex decision problems that cannot be modeled hierarchically. (Alptekin, 2010).

ANP consists of two subsections. The first section is the control hierarchy formed by the factors that control the interactions in the model. The second is subgroups formed by interactions between factors and sets of factors. In ANP, the decision-making problem is modeled as a network and at this stage, external dependencies between factor groups, feedback, and internal dependencies within the same factor group are taken into consideration. With this structure, ANP enables more effective decisions to be made. Figure 2 shows a sample network structure presenting the relationships between factor clusters (C) consisting of different numbers of factors.
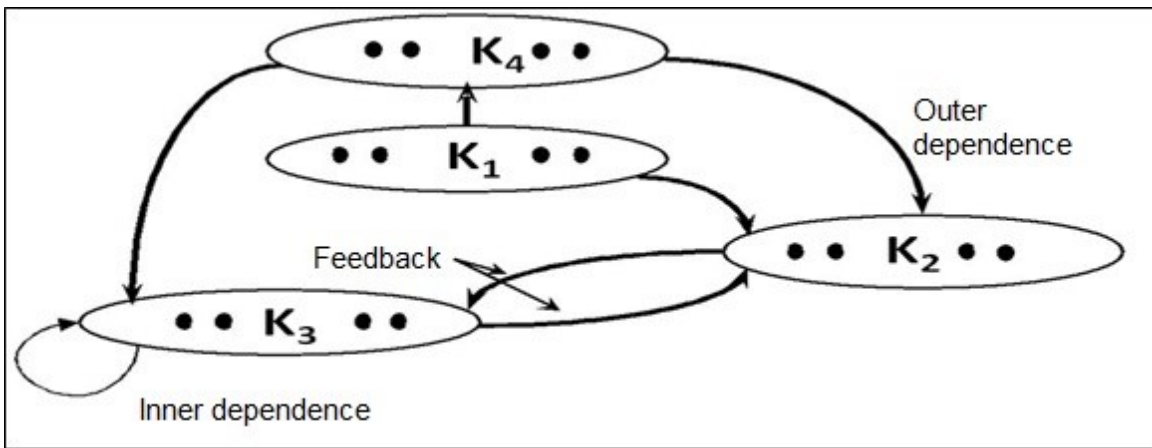
Figure 2. Example of a Network Model (Saaty, 1999)

The basic concept in ANP is the "effect". The fact that one component affects another component in a network structure indicates that there is an external dependency, the presence of two-way arrows between two components indicates that there is interdependence or feedback between those two components. If the elements in a component affect each other, it is said that there is an internal dependency in that component, and this situation is indicated by an arrow exported from the component and entering the same component. (Bayazıt and Yuzugullu, 2013). The difference between a hierarchical structure and a network structure is shown in Figure 3.
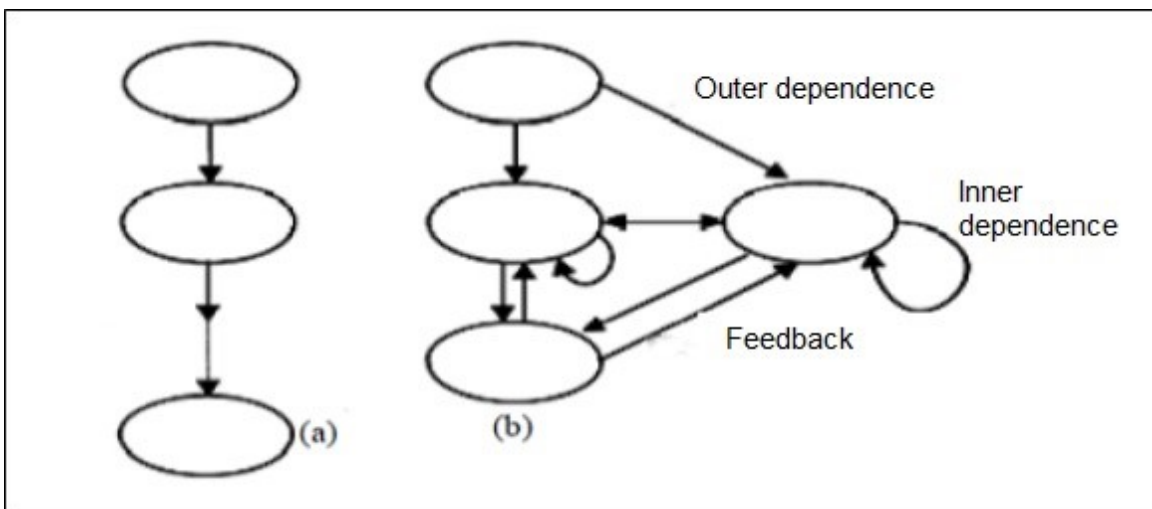
Figure 3. A Hierarchy and its Network Structure (Karsak et al., 2002).

4. Results

4.1. Description of the criteria and sub-criteria

It has been determined that 8 main criteria are evaluated as affecting maritime passenger means of transport in Kocaeli Bay, and additional 42 sub-criteria under these 8 main criteria have been identified. The determined criteria were evaluated together with the experts. Based on the expert opinions, the criteria were weighted in and the obtained data were finalized using the program called super decisions.

It is aimed to determine the factors affecting seaway passenger transportation in Kocaeli Bay and to make seaway passenger transportation in an economical and sustainable manner in line with these factors. For this, thirty-nine sub-criteria were determined under eight main criteria affecting the Kocaeli Bay seaway passenger means of transport. These criteria determined for the data were demonstrated practically using the Analytic Hierarchy Process and Analytic Network process methods, using the Super Decisions program. After examining these criteria and sub-criteria in detail, three different alternatives were determined for the most suitable alternative. These alternatives are:

Alternative 1 (X): Scheduled passenger transportation provided by the municipality, as an alternative to the service currently implemented by the Kocaeli Bay Seaway Transportation Directorate using the sea bus, passenger motorboat, and ferry,

Alternative 2 (Y): Scheduled passenger transportation service where this service is provided by the municipality using only passenger motorboats as an alternative to the mixed fleet of the passenger transportation service in Kocaeli Bay,

Alternative 3 (Z): Scheduled passenger transportation in Kocaeli Bay carried out using only passenger motorboats instead of a mixed fleet, is designated and named as an alternative to scheduled means of passenger transport where this service is provided by the private sector.

4.1.1. Operating Costs

Operating costs are among the most important cost items faced by businesses operating in the field of passenger transportation. Effectively managing the factors affecting operating costs leads to a reduction in operating costs, which makes the passenger means of transport service offered more economical.

Operating costs affecting Maritime Passenger means of transport in Kocaeli Bay consist of eight sub-criteria. These consist of personnel cost, fuel cost, maintenance and repair costs, class and certificate expenses, shipyard expenses, insurance costs, tax, drawing, and line permit costs, and SCT-free fuel costs. While personnel, insurance, tax, class, and certificate expenses are among the expenses that constitute the operating costs, fuel costs, maintenance, and repair costs, shipyard costs are variable costs that vary throughout the year and are determined according to market conditions.

4.1.2. Specifications of the Passenger Ships

The different types of passenger ships used in a seaway means of transport operation are an important factor affecting transportation costs. The different types of ships cause the type of the main engine used in passenger ships to be different, and the difference in the main engine type of passenger ships causes the speed of the ship to be high or low, the fuel consumption at the same distance to be different and the qualification of the personnel working on the ships to change. In the same type of passenger ships, the difference in age, machine condition, and sheet condition affects the number of resources spent on the operation of the ships.

Passenger ships consist of six sub-criteria such as the criteria of technical characteristics, different ship types, different ship's technical conditions, use of the high-speed main engine, ship passenger capacity incompatible with passenger frequency, and the average age of ships.

4.1.3. Passenger Schedule

The schedule includes the departure and arrival times, piers, and voyage times of passenger ships. The schedules are generally determined twice a year, taking into account the summer and winter times. The weekday schedules are determined according to working hours, and the number of voyages on weekdays is higher than the number of trips on weekends. The passenger schedule consists of six sub-criteria such as voyage times, voyage intervals, passenger safety, scheduled voyage, voyage cancellations, and seasonal effect.

4.1.4. Tariff System

In all modes of urban public transportation (bus, minibus, ferry, etc.), the right to determine the ticket price tariff belongs to the Municipalities. The Metropolitan Municipalities determine their tariffs through transportation coordination centers. While there are three

passenger types who pay (full, student, discounted) in urban public transportation, fourteen different passenger types do not pay any fees. There are no subsidies for passengers transported free of charge.

The wage system criterion consists of four sub-criteria such as fare collection system, ticket prices, transfer, and integration with other transportation systems.

4.1.5. Statutory Regulations

Statutory regulations determine how passenger means of transport (private transport, public transport, etc.) will be carried out, within which they will be performed, the rules and prohibitions, in short, they determine the legal framework of passenger transport. The implementation of every new rule introduced incurs a cost. Therefore, statutory responsibilities and obligations affect the unit transportation cost. The statutory regulation criterion consists of sub-criteria such as free transport passengers, UKOME effect, line permit, metropolitan municipality law, and financial structure.

4.1.6. Transportation Structure

Each transportation system has its unique features. When examining a transportation system, besides the features of the system, factors affecting other transportation systems should also be examined. When dealing with seaway transportation in Kocaeli Bay, besides the structure of seaway transportation, other factors affecting seaway transportation in Kocaeli Bay should be taken into consideration. These criteria consist of four sub-

criteria such as the number of piers, the different types of pier structures, the presence of other seaway transport companies operating in Kocaeli Bay, and the bay passage bridge.

4.1.7. Seaway Transportation Directorate

The Seaway Transportation Directorate is a directorate that has been carrying passengers at twelve different piers since 1998 in Kocaeli Bay affiliated with Kocaeli Metropolitan Municipality Public Transportation Department. The Seaway Transportation Directorate criterion consists of sub-criteria such as the difference of personnel regime, administrative structure, and age of the personnel, their professional and educational status, and previous planning studies.

4.1.8. Spatial Distribution of Kocaeli Bay

Each city has a specific spatial distribution. The topographic features of a city are one of the most important aspects affecting the transportation infrastructure. When examining the transportation structures of cities, there is a necessity to consider the spatial distribution of that city. Therefore, since the spatial distribution of each city is different, the solution for one city may not be the same for another. The Kocaeli Bay Spatial Distribution criterion consists of sub-criteria such as the settlement characteristic of Kocaeli, restricted areas, anchorage areas, and Kocaeli Bay traffic separation scheme, the absence of attraction centers between the opposite coasts, and the population structure of Kocaeli province.

4.2. Analytic Hierarchy Process Analysis and Implementation

4.2.1. Analytic Hierarchy Process Super Decision Computer Program Application
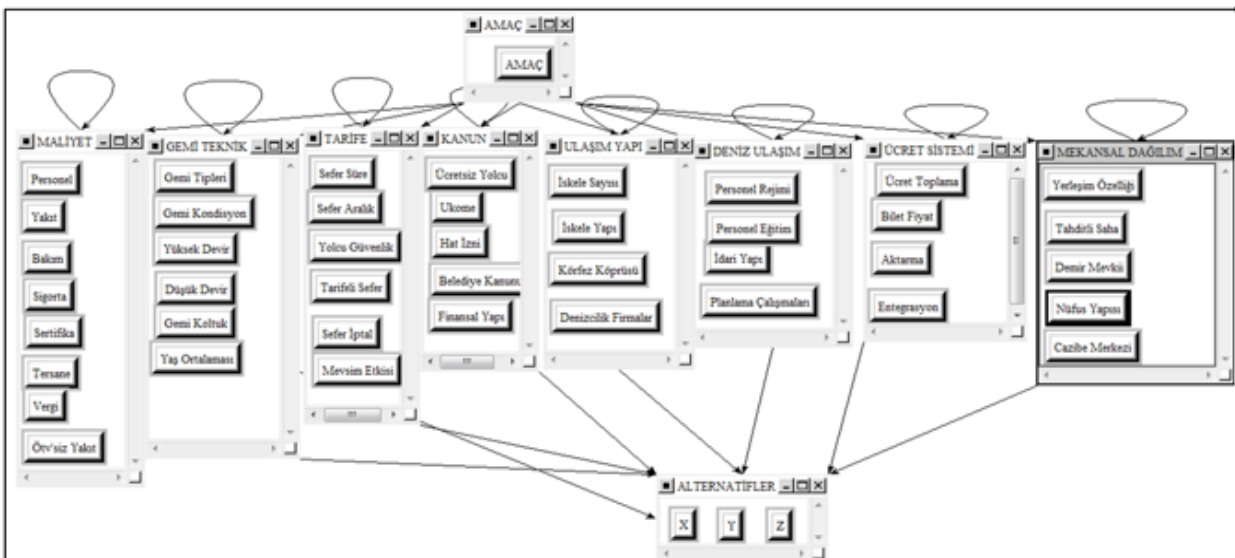
Figure 4: Analytic Hierarchy Process Purpose Function Display
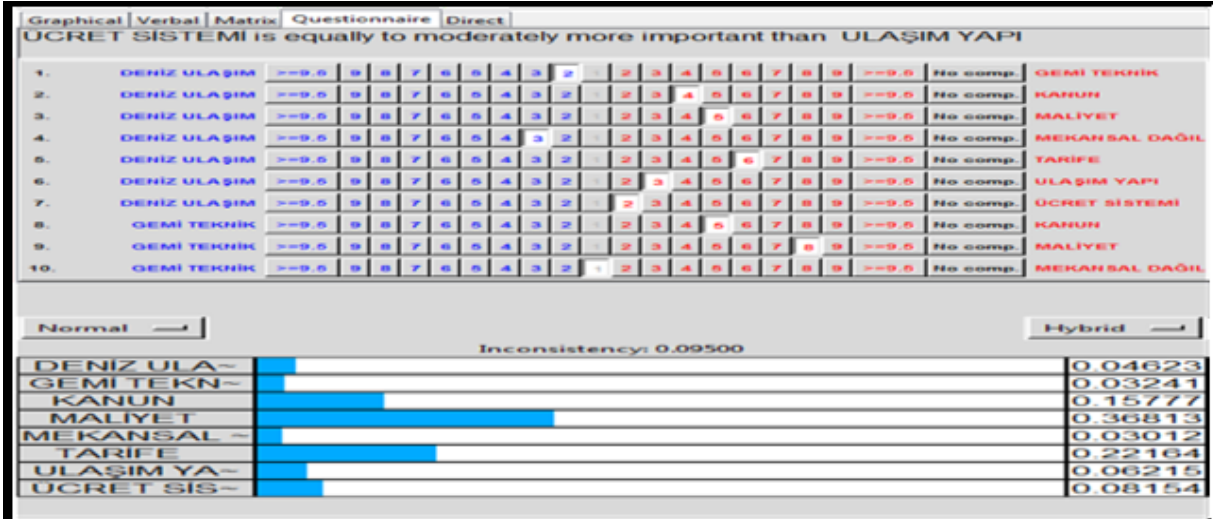
Figure 5: Analytic Hierarchy Process Key Criterion Paired Comparisons.

Analytic Hierarchy Process paired comparisons revealed that the main criterion Cost was 36%, Tariff 22%, Law 15%, Fee System 8%, Transport Structure 6%, Seaway Transportation 4% and Ship Technical key criterion 3%. Since the basis of the seaway passenger transportation service is determined by the announced tariff, it is of secondary importance in paired comparisons. As seen in paired comparisons, the main criterion of the

cost came out of first importance. The tariff main criterion has emerged at the second level of importance. In this respect, the service planned and the tariff to be implemented should be determined well. When the tariff is announced, the announced tariff must be executed, regardless of whether there is a passenger or not.
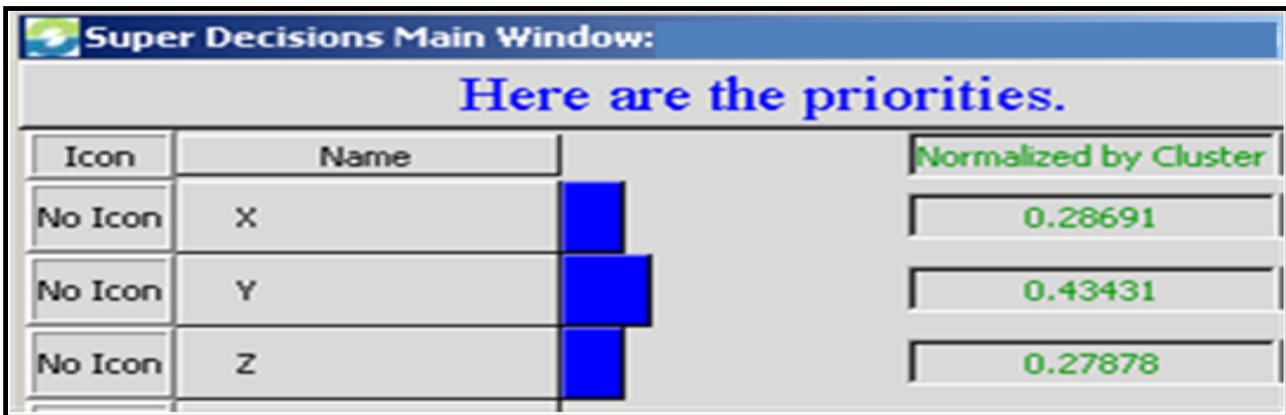
Figure 6: Analytic Hierarchy Process Purpose Function Displ

In the calculations made, it was determined that the best alternative among the three alternatives was the "Y" alternative. This alternative is considered appropriate to use the seaway passenger transportation in Kocaeli Bay not in the form of sea bus, passenger ferry, and passenger motorboat mixed fleet, but by leasing low-speed passenger engines. The most important reason for not choosing the "Z" alternative is that the nature of the Kocaeli Bay, the

voyages are long and the number of miles is high, the frequency of passengers is low, the income is low and the number of trips is high, all are making it difficult to provide the current service by the private sector. Since the "X" alternative has a mixed fleet structure within itself, it is considered that its implementation is not suitable for the efficient use of resources.

4.3. Analytic Network Process Analysis and Implementation

4.3.1. Analytic Network Process Super Decision Computer Program Application
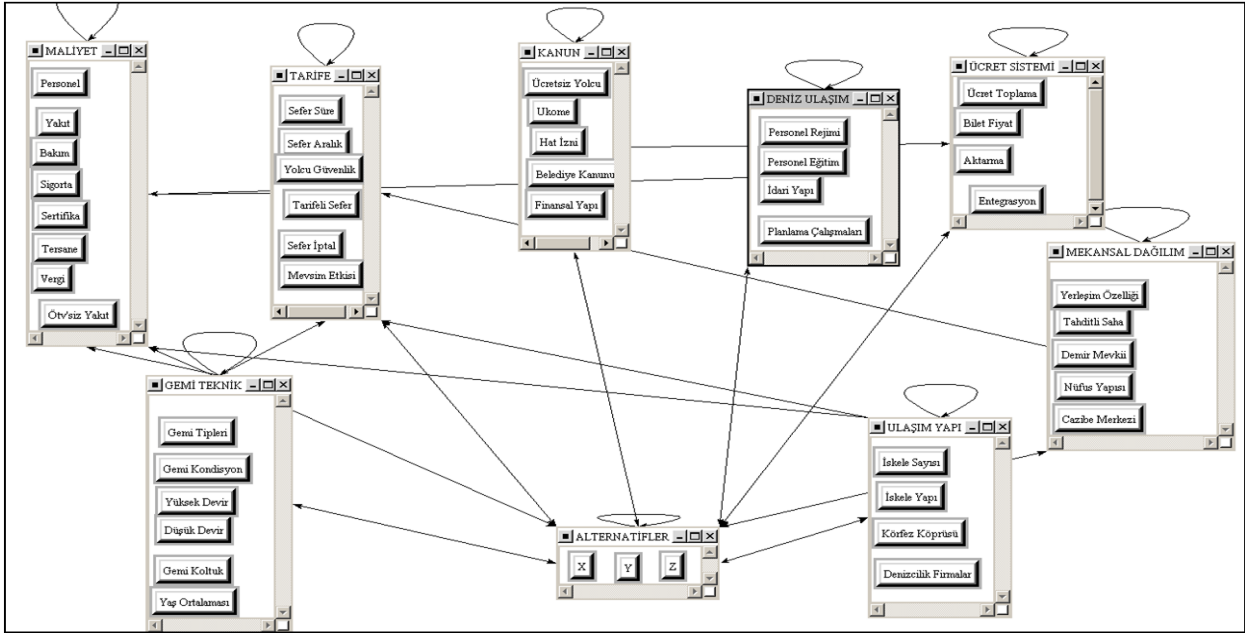


Figure 7: Analytic Network Process Function Display.
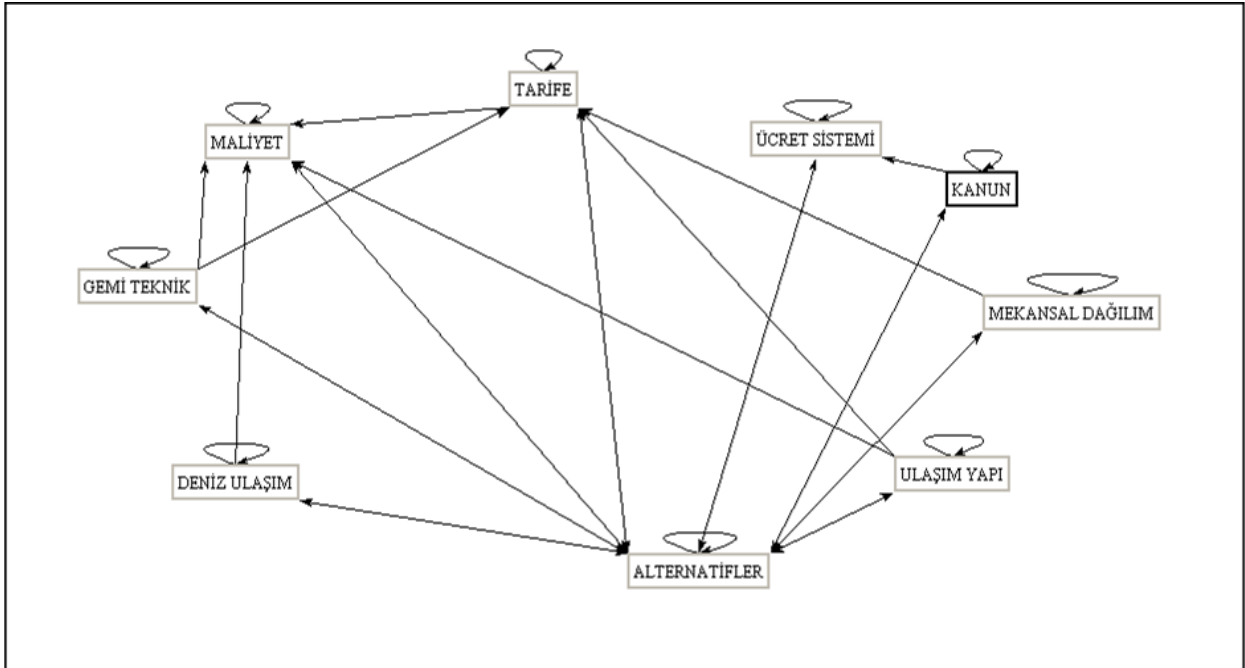
Figure 8: Analytic Network Process Network Function Display.
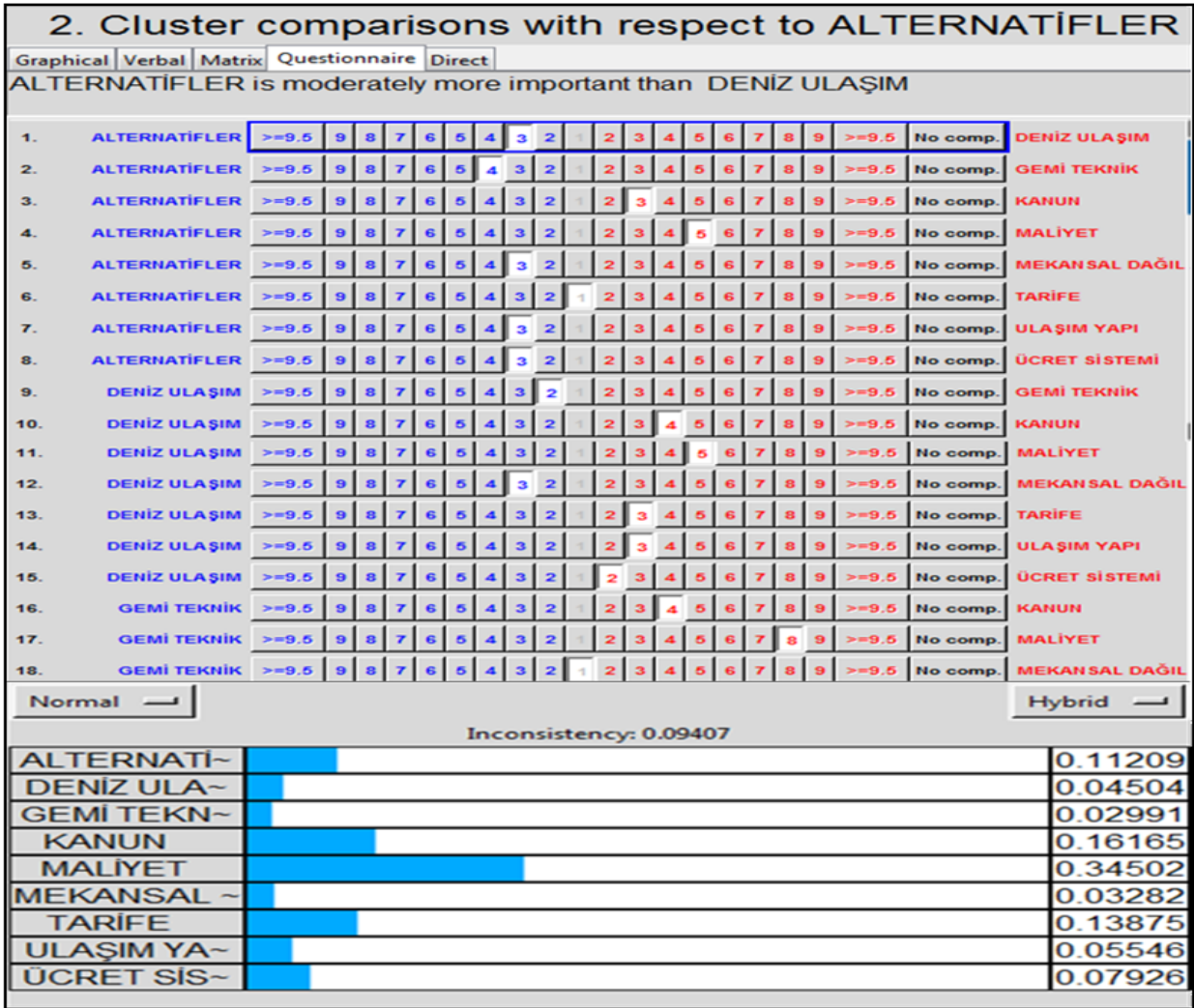
Figure 9: Analytic Network Process Alternatives and Criteria Comparisons.

When the paired comparisons of alternatives and main criteria of the Analytic Network Process are calculated, it is seen that the main criterion of Cost is 38%, the main criterion of the Law is 16%, the main criterion of the Tariff is 13%, the alternatives is 11%, the main criterion of the Wage System is 7%, the main criterion of the Transport Structure is 5%, the criterion is 4%, the Spatial Distribution main criterion is 3% and that the Ship Tech main criterion is 2% effective.
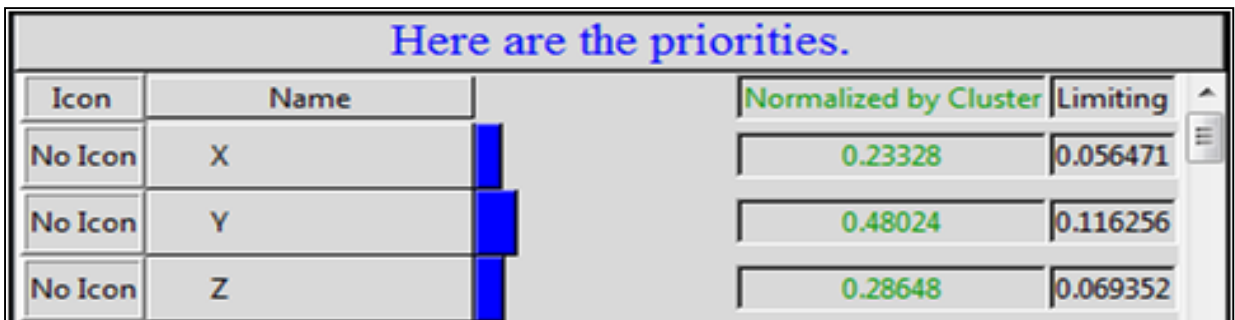
Figure 10: Analytic Network Process Display of Alternatives.

When the alternatives of the Analytic Network Process are evaluated, it is seen that the "Y" alternative is 48%, "Z" alternative is 28% and the "X" alternative is 23% effective. In the Analytic Hierarchy Process alternative evaluation, it was determined that the "Y" alternative was 43%, "X" alternative was 28%, and the "Z" alternative was 27% effective. In Analytic Network Process calculations, it was observed that the importance of "Y" and "Z" alternatives increased, and the importance of "X" alternatives decreased. The fact that the sub-criteria under the main criterion affect each other causes a change in the degree of importance among the alternatives. Another reason for the increasing importance of the "Y" alternative is that it is the most suitable model in terms of costs. The reason for the increase in the importance of the "Z" alternative and the decrease of the "X" alternative is that the "Z" alternative is similar to the "Y" alternative in terms of costs and, since the "X" alternative contains the sea bus option within itself, it is less likely to be preferred in terms of costs.

5. Discussion

By evaluating the Kocaeli Bay as a whole, this study was carried out to evaluate and determine the most suitable alternative or option for sea passenger transportation in Kocaeli Bay, which is carried out from 12 different piers as a component of public transportation activities by Kocaeli Metropolitan Municipality, at a sustainable cost.

To carry out at a sustainable cost the seaway passenger transportation in Kocaeli Bay, which is built in 12 different piers as a component of public transportation activities by Kocaeli Metropolitan Municipality, thirty-nine sub-criteria were determined under eight main criteria. Three different alternatives have been identified for these specified criteria. These alternatives are evaluated using analytic hierarchy and analytic network process methods.

When Analytic Hierarchy Process pair comparisons are made, it has been determined that the main criterion of cost is 36%, Tariff 22%, Law 15%, Wage System 8%, Transport Structure 6%, Maritime Transport 4%, and Ship Technical key criterion is 3%. As seen in the analytic network process pair of comparisons, the main criterion of the cost came out at the first level of importance. It has been seen that the best alternative in analytic network process calculations is the "Y" alternative. And, it has been determined that this is the scheduled passenger means of transport, the "Y" alternative in which sea passenger means of transport in Kocaeli Bay is provided by the metropolitan municipality using only a passenger motorboat as an alternative to the mixed fleet.

As a result of the pairwise comparisons of alternatives and main criteria of the Analytic Network Process are calculated, it can be seen the effectiveness of the criterion is as follow;

- Cost main criterion is 38%,
- Law main criterion is 16%,
- Tariff main criterion is 13%,
- Alternatives are 11%,
- Wage System main criterion is 7%,
- Transportation Structure main criterion is 5%,
- Main criterion of Maritime Transportation is 4%,
- Main criterion of Spatial Distribution is 3%
- Ship Technical key criteria is 2%.

When the alternatives of the Analytic Network Process are evaluated, it is seen that the "Y" alternative is 48%, the "Z" alternative is 28% and the "X" alternative is 23% effective. In the Analytic Hierarchy Process alternative evaluation, it was determined that the "Y" alternative was 43%, the "X" alternative was 28%, and the"Z" alternative was 27% effective. In Analytic Network Process calculations, it can be understood that the importance of "Y" and "Z" alternatives increased, and the "X" alternative decreased. By examining the analytic network process and the analytic hierarchy process together, it is concluded that the best alternative is the "Y" alternative in both methods.

6. Conclusions

It has been evaluated that it will be the most suitable solution at the scale of Kocaeli Bay to use the system in which passenger engines are supplied by leasing method and providing this service by the metropolitan municipality instead of the sea bus, ferry and passenger motorboat which are the current mixed sea fleet, and using low-speed passenger engines as marine vehicles, in order to ensure that the seaway passenger transportation service performed by the Kocaeli Metropolitan Municipality in the Kocaeli Bay is economical and sustainable, by considering seaway passenger transport as a component of urban public transport, by considering that the number of piers of Kocaeli Metropolitan Municipality Seaway Transportation Directorate is high and consequently the factors such as the high number of trips, the lack of attraction centers between the opposite coasts, the distancing of settlements from the coasts due to the earthquake, the low number of passengers, the lack of integration of urban public transport systems, the limited ticket increase price and ticket revenue and the absence of any other income than the ticket fee.

Declaration of Ethical Standards

The author(s) of this article declare that the materials and methods used in this study do not require ethical committee permission and/or legal-special permission.

Conflict of Interest

The authors declare that they have no known competing financial interests or personal relationships that could have appeared to influence the work reported in this paper.

References

[1] Akman G., Atakan A., 2006. Tedarik Zinciri Yönetiminde Bulanık AHP Yöntemi Kullanılarak Tedarikçilerin Performansının Ölçülmesi: Otomotiv Yan Sanayinde Bir Uygulama. İstanbul Ticaret Üniversitesi, Fen Bilimleri Dergisi, **9**, pp. 23-46.

[2] Aksoy Y., Özkan E.M., Karanfil S., 2014. Bulanık Mantığa Giriş, 2.Baskı., Yıldız Teknik Üniversitesi Basın- Yayın Merkezi, İstanbul.

[3] Alptekin N., 2010. Analitik Ağ Süreci Yaklaşımı ile Türkiye'de Beyaz Eşya Sektörünün Pazar Payının Tahmini. Doğuş Üniversitesi Dergisi, **11**(1), pp. 18-27.

[4] Bayazıt O., 2002. A New Methodology in Multiple Crieria Decision- Making Systems: Analytic Network Process (ANP) and an Applications, Ankara Üniversitesi Siyasal Bilimler Fakültesi Dergisi, **57**(1), pp. 15-34.

[5] Baynal K., Yüzügüllü E., 2013. Tedarik Zinciri Yönetiminde Analitik Ağ Süreci ile Tedarikçi Seçimi ve Bir Uygulama. İstanbul Üniversitesi İşletme Fakültesi Dergisi, **42**(1), pp. 77-92.

[6] Chen S. C., Hwang C. L., Beckmann M.J., Krelle W., 1992. Fuzzy Multiple Attrıbute Decısıon Makıng: Methods and Applıcatıons, New York: Sprınger-Verlag.

[7] Cinemre N., 2004. Doğrusal Programlama, Üçüncü Baskı., Beta Basım Yayım Dağıtım A.Ş, İstanbul.

[8] Daft R. L., 1991. Management, 2nd Edition., The Dryden Press, USA.

[9] Dağdeviren M., Eraslan E., Kurt M., Dizdar E., 2005. Tedarikçi Seçimi Problemine Analitik Ağ Süreci ile Alternatif Bir Yaklaşım. Teknoloji Dergisi, **8**(2), pp. 115-122.

[10] Doğan B., 2004. Karar Vermede Çok Kriterli Bir Yaklaşım Modeli Olarak Analitik Hiyerarşi Süreci ve Mayın Avlama Gemisi Seçiminde Analitik Hiyerarşi Yönteminin Uygulanması. Deniz Harp Okulu, Deniz Bilimleri ve Mühendisliği Enstitüsü, Yüksek Lisans Tezi, İstanbul.

[11] Dokuz Eylül Üniversitesi, 2014 www.deu.edu.tr/userweb/k.yaralioglu/dosyalar/bul_man.doc [05 Ağustos 2014]

[12] Elmas C., 2011. Yapay Zeka Uygulamaları, Ankara: Seçkin Yayıncılık.

[13] Enea M., Piazza T., 2004. Project Selection by Constrained Fuzzy AHP. Fuzzy Optimization and Decision Making, **3**(1), pp. 39-62.

[14] Eren E., 2005. Stratejik yönetim ve işletme politikası, Beta Basım Yayın, İstanbul.

[15] Ergin A., 2011. Tedarik Zincir Yönetiminde Konteyner Taşıyıcı Firma Seçimi ve Türkiye'deki Uygulaması, Doktora Tezi, İstanbul Üniversitesi Fen Bilimleri Enstitüsü, İstanbul.

[16] Evren R., Ülengin F., 1992. Yönetiminde Çok Amaçlı Karar Verme, İstanbul Teknik Üniversite Matbaası, İstanbul.

[17] Felek S., Yuluğkural Y., Aladağ Z., 2007. Mobil İletişim Sektöründe Pazar Paylaşımının Tahmininde AHP ve ANP Yöntemlerinin Kıyaslanması. Makine Mühendisleri Odası Endüstri Mühendisliği Dergisi, **10**(1), pp. 211-233.

[18] Formen E., Selly M.A., 2002. Decision by Objectives, World Scientific Publishing, Singapore.

[19] Güner M., Yücel O., 2007. Konfeksiyon Üretiminde Temel Kriterlerin Hiyararşik Modellenmesi İle Üretilecek En Uygun Ürünün Belirlenmesi. Gazi Üniversitesi Mühendislik Mimarlık Fakültesi Dergisi, **22**(1), pp. 73-79.

[20] Gürsoy M., Yardım M.S., Alçura G.A., 2012. İzmit Körfezi Feribot Taşımacılığı Taşıt ve Yolculuk Talebi ve Geleceğine İlişkin Teknik Rapor, Yıldız Teknik Üniversitesi, İstanbul, Türkiye.

[21] Harker P., Vargas L., 1987. The Teory of Ratio Scale Estimation, Saaty's Analytic Hierarchy Process Management. Management Science, **33**(11), pp. 1383-1403.

[22] Hwang C. L., Yoon K., 1981. Multiple Attribute Decision Making Methods and Applications, Springer Verlag, Berlin.

[23] İmrek M. K., 2003. Yöneticiler İçin Karar Verme Teknikleri El Kitabı,Beta Basım Yayım Dağıtım A.Ş, İstanbul.

[24] Jahanshahloo G. R., Lotfi F.H., İzadikhah M., 2006. An Algorithmic Method to Extend TOPSIS for Decision Making Problems with Interval Data. Applied Mathematics and Computation, **175**, pp. 1375-1384.

[25] Kahraman C., Demirel N. C., Ateş N. Y., 2008. A SWOT-AHP application using fuzzy concept: EGovernment in Turkey, Fuzzy Multi-Criteria Decision Making Book-Edited By Cengiz Kahraman, Springer Science-Business Media.

[26] Karsak E., Sözer S., Aladağ, Z., 2002. Product Plannig in Quality Function Deployment Using a Combined Analytic Network Process Goal Programming Approach. Computer& Industrial Engineering, **44**, pp. 171-190.

[27] Kocaeli Büyükşehir Belediyesi. 2012, Kocaeli Ulaşım Ana Planı Mevcut Bilgilerin Toplaması Çalışması 1. Ara Rapor. Kocaeli.

[28] Kocaeli Büyükşehir Belediyesi. 2012, Kocaeli Ulaşım Ana Planı Sonuç Raporu. Kocaeli.

[29] Kacakalay Ş., Özdemir M.S., Işık A., 2004. Analitik Serim Süreci Tekniği ile Pazar Payı Tahmini, Yöneylem Araştırması/Endüstri Mühendisliği Ulusal Kongresi, 15-18 Haziran 2004, Adana, 121-123.

[30] Koçel T., 2003. İşletme Yöneticiliği, Beta Basım Yayın Dağıtım A.Ş, İstanbul.

[31] Lin C., Tan B., Hsieh P.J., 2005. Application of the Fuzzy Weighted Average in Strategic Portfolio Management. Decision Sciences, **36**(3), pp. 489-511.

[32] Ömürbek T., Tunca M. Z., 2013. Analitik Hiyerarşi Süreci ve Analitik Ağ Süreci Yöntemlerinde Grup Kararı Verilmesi Aşamasına İlişkin Bir Örnek Uygulama. Süleyman Demirel Üniversitesi İktisadi ve İdari Bilimler Fakültesi Dergisi, **18**(3), pp. 47-70.

[33] Özden H.Ü., 2009. Türkiye'deki Mevduat Bankalarının Performansları, Detay Yayıncılık, Ankara.

[34] Özyürek B., Özcan C.E., 2008. Analitik Hiyerarşi Sürecinin Tedarikçi Seçiminde Uygulanması: Otomotiv Sektöründen Bir Örnek. Süleyman Demirel Üniversitesi İktisadi ve İdari Bilimler Fakültesi Dergisi, **13**(1) pp. 133-144.

[35] Power D.J., 2003. What is Analytic Hierarchy Proses (AHP)?, DSS News, 4, 13.

[36] Rençber Ö.F., 2010. Büyük Çaplı Projelerde Karar Verme: Analitik Hiyerarşi Süreci Uygulaması, Yüksek Lisans Tezi, Gebze Yüksek Teknoloji Enstitüsü, Sosyal Bilimler Enstitüsü, Gebze.

[37] Saaty T.L., 1990. How To Make A Decision: The Analytic Hierarchy Proses. European Journal of Operation Research, **48**, pp. 9-26.

[38] Saaty T.L., 1996. Decision Making with Dependence and Feedback: The Analytic Network Process, RWS Publications, Pittsburgh, PA.

[39] Saaty T.L., 1999. Fundamentals of The Analytic Network Process, ISAHP 1999, Kobe, Japan.

[40] Triantapjyllou E., 2000. Multi - Criteria Decision Making Methods: A Comparative Study, Kluwer Academic Publishers, 44, 1-3.

[41] Turanlı M., 1988. Pazarlama Yönetiminde Karar Alma, Beta Basım Yayım Dağıtım A.Ş, İstanbul.

[42] Yang C.L., Chuang S.P., Huang R.L., 2009. Manufacturing Evaluation System Based on AHP/ANP Approach for Water Fabricating Industry. Experts Systems with Applications, **36**, pp. 11369-11377.

[43] Yıldız Teknik Üniversitesi, 2014, http://www.enm.yildiz.edu.tr/~palcan/sistem_analizi. htm [7 Temmuz 2014]

Kocaeli University

Kocaeli Journal of Science and Engineering

http://dergipark.org.tr/kojose

Statistical Evaluation of Water Quality and Meteorological Conditions in Karacaören-II Dam Lake

Firdes YENİLMEZ [1], * (iD)

[1] Department of Environmental Engineering, Akdeniz University, Antalya, 07058, Turkey, **ORCID:** 0000-0002-1600-9419

Abstract

Karacaören-II Dam Lake is located on Aksu Stream within the borders of Burdur. The lake is planned to be a drinking water supply for Antalya in the near future. Some scientific studies carried out in recent years stated that the lake suffers from eutrophication problem due to the pressures within the basin.

This study examined the relationships between the selected water quality parameters (BOD_5, DO, pH, NH_4-N, NO_2-N, NO_3-N, TKN, TN, o-PO_4, TP and TSS) and the meteorological parameters (temperature, wind speed, precipitation, humidity, pressure, vaporization) measured between the years 2005 and 2014 using correlation analysis. The main factors contributing to the variation in the data set were also determined by principal component analysis and the trends in selected water quality parameters were analyzed using the Mann-Kendall test. The statistical tests indicated that nitrogen, phosphorus, pH, temperature, precipitation, and vaporization are the major parameters influencing the water quality in the dam lake. A very high correlation is found between NO_3-N and DO. Trend analysis showed an upward trend in TN and TP concentrations. The results of this study will be beneficial to decision-makers for better management of water quality and to those who will carry out studies on the lake in the future.

1. Introduction

European Union Water Framework Directive (numbered 2000/60/EC) and Surface Water Quality Regulation state the precautions to be taken to protect and achieve good water status in water resources. The balance between protection and use should be ensured for the sustainable management of water resources [1, 2]. The environmental objectives of Water Framework Directive include prevention of deterioration in the status of surface waters, protection, improvement and restoration of water bodies ensuring good water status in the first management cycle [3]. In order to achieve these environmental goals, it is essential to first determine the pressures by making the basin characterization, reveal the current situation in water quality and the trend in light of previous data, and take the necessary measures to reach the determined environmental

goals. Statistical methods are helpful tools to achieve these environmental targets. Correlation analysis, Principal Component Analysis (PCA), and trend analysis are widely used tools for this purpose especially when assessing the quality of surface waters and the relationship between water quality parameters and meteorological conditions [4-7]. They are instrumental in identifying necessary measures to prevent and improve water quality to achieve the environmental objectives.

When the projects and studies related to Karacaören-II Dam Lake were examined, it was seen that there have been limited number of studies that determine the distribution of pollutants in water and sediment. For example, Kır and Tumantozlu (2012) examined the accumulation levels of Fe, Cu, Zn, Mn, Al, Sr, Cr, Pb, Cd, Hg in water, sediment and some carp tissue samples in the lake between April 2009 – March 2010. In the study, it was determined that the metal concentrations increased in spring and summer and decreased in autumn and winter. The most accumulated metal in the sediment was

---

* Corresponding Author: firdesyenilmez@akdeniz.edu.tr

mentioned as Fe. According to the results, the metal ratios measured in the sediment were significantly higher than that in water and fish tissues. In the study, the heavy metal amounts detected in water samples and carp tissues were compared with the limit values for aquatic environments. According to the results, both Zn in water, Fe and Zn in sediment exceeded acceptable values in all seasons, while they were below acceptable values in carp tissues [8].

Ardıç (2013) assesed health risk potential caused by nitrate concentrations in drinking water resources of selected provinces in Turkey for 2009. The nitrate data were obtained from Duraliler Well, Aksu Stream, Karacaören II Dam. In the study, it was determined that nitrate values in these three stations do not pose any risk to human health [9].

Apaydın et al. (2019) investigated natural radioactivity levels in sediment of Karacaören II Dam Lake. They collected 12 sediment samples from the lake in May 2016 and measured natural radionuclides like ^{226}Ra, ^{232}Th and ^{40}K. In the study, radium equivalent activities (Ra$_{eq}$), absorber dose rate (D), internal (H$_{in}$) and external (H$_{ex}$) hazard index, annual effective dose rate (AED) and Excess life time cancer risk (ELCR) were calculated and compared with recommended values of international organizations in order to assess the radiological hazards resulting from natural radioactivity. Results indicated that all Raeq, Hex and Hin values were below the criterion values [10].

TÜBİTAK MAM (2013) prepared a basin protection plan for Karacaören-I and Karacaören-II Dam Lakes. For this purpose, the hydrological and hydrogeological water budget of the basin, limnological features, the pollution status of rivers and other water resources, the renewal time of the basin, the geometry of the basin, the point and diffuse pollution sources and the reasons affecting the water quality were evaluated. After that, the effect of the calculated pollution loads on the water quality was determined via water quality modelling study. Pollution maps were also created. Basin protection plan alternatives were created with the help of the modelling study. Then special provisions for the lakes were determined in accordance with the prepared basin protection plan to improve the existing water quality in the basin [11].

Previous studies evaluated distributions of pollutants in sediment and water column of Karacaören Dam Lake but have not conducted any statistical tests. There has been a gap in the statistical evaluation of water quality and meteorological conditions in Karacaören-II Dam Lake. Therefore, correlation between water quality data and meteorological data was examined by correlation analysis in this study. Trend analysis were also performed to evaluate the long-term trends in water quality parameters.

Effective parameters in representing the variation in data set were also determined using multivariate principal component analysis.

This study evaluates the long-term trends in Karacaören-2 Dam Lake for selected water quality parameters (BOD$_5$, DO, pH, NH$_4$-N, NO$_2$-N, NO$_3$-N, TKN, TN, o-PO$_4$, TP and TSS) using Mann-Kendall trend analysis. The study also determines meteorological variables that significantly affect water quality by correlation analysis, and specifies most deterministic principal components representing variation in data set. In this context, the SPSS program (version 23) was used to conduct correlation analysis, principal component analysis, and trend analysis using data sets belonging to the years 2005-2014. The long-term assessment of the change in water quality with this study will contribute to the protection of Karacaören-II Dam Lake, which has a high potential to be a drinking water source for Antalya in the future.

2. Materials and Methods

2.1. Study Area

Karacaören-II Dam Lake is located at 37°18' north latitude and 30°48' east longitude within the borders of Burdur Province. It was built on Aksu Stream between 1988-1993 for irrigation and energy purposes. It has been used as a recreation and aquaculture area as well. The surface area of the lake is 2.34 km^2. Karacaören-II Dam Lake is fed by Aksu Stream and Koca Stream. Aksu Stream joins with streams such as Dereboğazı Stream, Ağlasun Stream, Kovada Stream, Değirmen Stream, and enters firstly to Karacaören-I Dam Lake and then to Karacaören-II Dam Lake. Then, Aksu Stream outflows from the Karacaören-II Dam Lake and flows into the Mediterranean [12]. Figure 1 shows the locations of Karacaören-II Dam Lake and water quality monitoring stations of State Hydraulic Works.

The dam lake is significant because it is a recreational area used for irrigation, energy, and aquaculture [13]. In addition, it is planned to supply drinking water from the lake to Antalya Province in the future. There are many point and diffuse pollution sources within the basin borders of the lake that adversely affect the water quality. For this reason, determining the change of lake's water quality in the long term and identifying the significant water quality and meteorological parameters that are effective on the lake's water quality are extremely important for the management of the lake.
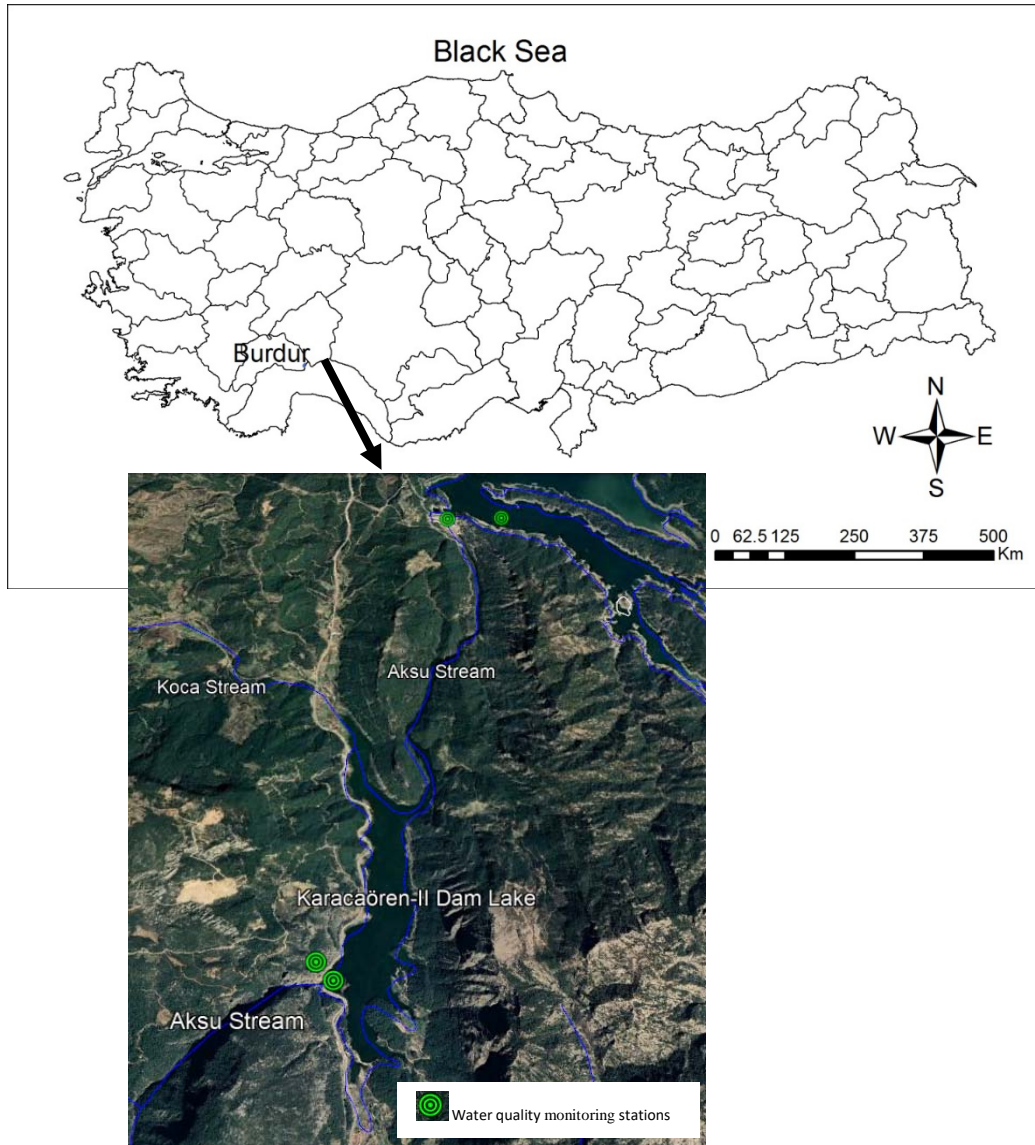
Figure 1. Karacaören-II Dam Lake and water quality monitoring stations

2.2. Methods

In this study, the relationship between water quality parameters and meteorological variables were examined by correlation analysis and principal component analysis. Thus, the most correlated and prominent parameters in explaining the change in the data set for 2005-2014 were determined. SPSS program (version 23) developed by IBM was used to perform correlation analysis and principal component analysis. As a first step, Pearson Correlation Coefficients were calculated to determine the degree and direction of the relationship between water quality parameters and meteorological data. The correlation values were tested within the 95% confidence limits to decide whether the relations between the variables were acceptable or not. The results obtained from the reliable correlations were discussed. The Pearson correlation coefficient is always between -1 and +1, and the closer the

coefficient is to -/+1, the closer to perfect correlation. Pearson correlation coefficient indicates a very high correlation above 0.8, a high correlation between 0.6-0.8, a moderate correlation between 0.4-0.6, a weak correlation between 0.2-0.4, and a very weak relationship below 0.2. If the correlation coefficient is negative, there is an inverse relationship between the two parameters, indicating that if one of the parameters increases, the other decreases. If the correlation coefficient is positive, there is a positive relationship in which one of the parameters increases as the other increases [14].

After the correlation analysis, the main components that can explain the change in the data set consisting of water quality and meteorological parameters were determined. Principal component analysis mathematically consists of five steps: (1) Standardization of the measurements to ensure that all variables are equally weighted in the analysis, that is, coding the variables as X_1,

X_2, …, X_p with zero mean and unit variance, (2) calculation of covariance matrix (C), (3) finding the eigenvalues (λ_1, λ_2,......, λ_p) and corresponding eigenvectors (a_1, a_2, …, a_p), (4) discarding components that makeup only a small part of the variation in the data set, and (5) developing the factor loading matrix and determining the principal components [15]. By following these steps, the main components that explain the change in the data set for the period 2005-2014 in Karacaören-II Dam Lake and the parameters that make up these components were determined using the SPSS program.

In the next step, the Mann-Kendall Trend Analysis test was applied to determine trends in DO, BOD_5, TN, TP, pH, and TSS parameters. A trend is defined as the long-term increase or decrease of a variable observed over time or space. Trend analysis helps to statistically determine whether the values of a random variable are decreasing or increasing over a period of time. A non-parametric Mann-Kendall test was choosen as it is not affected by the distribution of variables and is based on the calculation of the Kendall correlation coefficient. In addition, a non-parametric method was preferred in order not to be affected by situations such as not measuring water quality data at regular time intervals, missing data, not knowing the exact value of some values, expressing them as lower or higher than the lower and upper limit values [16-17]. The MK test is a widely used method for determining hydro-meteorological time series and water quality trends [18-19]. The null hypothesis for the Mann-Kendall test is that there is no change in the probability distribution of a random variable over time. In other words, the null hypothesis is that there is no trend in the data series. The test assumes that the random variables are independent and their values are from the same type of statistical distribution (normal, lognormal, etc.). The test makes all possible pairwise comparisons between variables in a time-series format. If the value of a particular variable is greater than the previous one at a given time, the plus sign is recorded (Equation (1)). If it is smaller, a minus sign is assigned. The test statistic is calculated as the difference between the total number of plus signs (representing the time increase) in the run time and the total number of minus signs (representing the time decrease). The zero test statistic shows no change over time (accepting the null hypothesis). The larger the deviation of the test statistic from zero, the more likely it is to observe a trend in the data and the more likely it is to reject the null hypothesis.

MK test statistic was calculated using Equation (2). In Equation (2), P is the total number of values marked positive, N is the total number of values marked as negative, and n is the total number of observations [16-20].

$$\text{sgn}(X_j - X_k) = \begin{cases} +1 & \text{If } (X_j - X_k) > 0 \\ 0 & \text{If } (X_j - X_k) = 0 \\ -1 & \text{If } (X_j - X_k) < 0 \end{cases} \quad (1)$$

$$MK = \frac{2(P-N)}{n(n-1)} \quad (2)$$

To perform trend and correlation analysis, water quality data between 2005 and 2014 years were obtained from the 13th Regional Directorate of DSI, and meteorological data from the 4th Regional Directorate of Meteorology. The 13th Regional Directorate of DSI has an accredited testing laboratory for water quality. Although the data obtained from the laboratory was accurate and reliable, it was also preprocessed before using in the statistical analysis. The units of water quality parameters were checked, and spikes were removed from the data. Water quality parameters with sufficient data were selected for trend analysis. BOD_5, DO, pH, NH_4-N, NO_2-N, NO_3-N, TKN, TN, o-PO_4, TP and TSS were the selected water quality parameters in this study. These parameters are the good indicators of productivity and water quality in lakes. They are commonly utilized in the determination of trophic status and pollution loads in lakes and reservoirs. Temperature, wind speed, humidity, pressure and vaporization are the meteorological parameters used in the study. These parameters have significant impact on productivity and water budget of lakes. In this study, annual average values were calculated for water quality and meteorological data, and correlation analysis, principal component analysis, and MK trend analysis were performed using these values.

3. Results and Discussion

The Pearson correlation coefficients calculated to show the degree and direction of the correlation between water quality parameters and meteorological data are given in Table 1. The correlation coefficient can be positive or negative, as seen in the table. When Table 1 is examined, it is seen that there is a very high positive correlation between nitrate nitrogen (NO_3-N) and dissolved oxygen (DO) with a correlation coefficient of 0.868, which is significant at the 0.01 level. The very high positive relationship between nitrate nitrogen and dissolved oxygen can be explained by the dependence of the nitrification process on oxygen supply [21]. Total Kjeldahl nitrogen (TKN) also represents high positive correlations significant at the 0.05 level with dissolved oxygen (DO), nitrate-nitrogen (NO_3-N), and total nitrogen (TN). Total Kjeldahl

nitrogen is the sum of organic nitrogen and NH_4-N. So, it determines both the organic and the inorganic forms of nitrogen. High positive correlation between TKN and NO_3-N can be attributed to the oxidation of the TKN (organic and inorganic nitrogen) to nitrate nitrogen by the nitrification process. Furthermore, total nitrogen has a high positive correlation with pH and temperature with correlation coefficients of 0.665 and 0.695, respectively. The positive relationships between TN, pH, and temperature can be readily explained by photosynthesis, since CO_2 assimilation increases pH values [21-22]. In addition, Total Suspended Solids (TSS) with a 0.707 correlation coefficient shows a significant positive correlation with total phosphorus (TP). This may be due to the fact that precipitation introduces TP to the lake via surface runoff [7]. The moderate correlations of TP and TSS with precipitation confirm this statement. However, BOD_5 has high negative correlations with dissolved oxygen and nitrate nitrogen (NO_3-N). BOD_5 represents the amount of oxygen consumed by microorganisms during decomposition of organic matter. While BOD_5 increases in lake, the decrease of DO and NO_3-N are expected [23].

Ammonium nitrogen (NH_4-N) give also high negative correlations with total Kjeldahl nitrogen (TKN), pH, total nitrogen (TN), total suspended solids (TSS), and total open surface vaporization with the varying correlation coefficients between -0.6 and -0.784. Nitrogen is usually removed from lakes by NO_3-N denitrification simultaneously with the oxidation of organic matter. On the other hand, high pH would favor N release to the atmosphere as NH_3 in highly productive surface waters [24]. This mechanism explains high negative correlation between NH_4-N and pH. The release of nitrogen to the atmosphere as ammonia (NH_3) also decreases NH_4-N, TKN and TN concentrations within lake. High negative correlation between open surface vaporization and NH_4-N can be as a result of the lost of ammonia (NH_3) nitrogen by volatilization.

Only temperature within meteorological parameters exhibited high correlation with TN. Temperature affects directly the growth rate of algae. Increase in temperature up to a certain level increases algal growth rates [25]. This can cause the increase of TN in lakes.

Table1. Correlations between water quality parameters and meteorological parameters

Parameter	BOD_5	DO	pH	NH_4-N	NO_2-N	NO_3-N	TKN	TN	o-PO_4	TP	TSS
BOD_5	1.000	**-.653***	-.311	.032	.226	**-.787****	**-.416**	-.189	.231	-.298	.291
DO	**-.653***	1.000	.059	-.173	-.211	**.868****	**.710***	.178	-.314	.002	-.078
NH_4-N	.032	-.173	**-.750***	1.000	.188	-.369	**-.732***	**-.784****	-.067	**-.507**	**-.600***
NO_2-N	.226	-.211	-.071	.188	1.000	-.369	-.344	**-.537**	-.087	-.306	-.241
NO_3-N	**-.787****	**.868****	.317	-.369	-.369	1.000	**.764***	**.456**	-.205	.371	.097
o-PO_4	.231	-.314	-.092	-.067	-.087	-.205	-.338	.144	1.000	-.272	-.015
TKN	**-.416**	**.710***	**.517**	**-.732***	-.344	**.764***	1.000	**.713***	-.338	**.445**	.396
pH	-.311	.059	1.000	**-.750***	-.071	.317	**.517**	**.665***	-.092	.398	.068
TSS	.291	-.078	.068	**-.600***	-.241	.097	.396	.442	-.015	**.707***	1.000
TN	-.189	.178	**.665***	**-.784****	**-.537**	**.456**	**.713***	1.000	.144	**.529**	**.442**
TP	-.298	.002	.398	**-.507**	-.306	.371	**.445**	**.529**	-.272	1.000	**.707***
Temperature	-.304	.199	**.578**	-.344	**-.490**	.373	**.437**	**.695***	.118	.002	-.255
Wind Speed	-.092	-.110	.287	.072	**-.467**	-.006	-.080	.276	.246	-.316	**-.525**
Precipitation	-.012	.124	-.097	.016	-.317	.248	.332	.295	**-.544**	**.502**	**0.400**
Humidity	-.186	.216	**-.525**	**.529**	.251	.067	-.085	**-.561**	**-.575**	.008	-.131
Pressure	-.304	.196	-.260	.149	.291	.165	-.213	-.266	**.567**	-.188	-.151
Total Open Surface Vaporization	.139	.016	**.477**	**-.600**	-.199	.015	.203	.373	**.478**	-.153	.108

*Correlation is significant at 0.05 level.
** Correlation is significant at 0.01 level.

Except tempretaure, all other meteorological parameters exhibited moderate, weak and very weak correlations with water quality prameters. For example, total open surface vaporization has a moderate positive correlation with orthophosphate phosphorus and pH with 0.478 and 0.477 correlation coefficients, respectively. As the total open surface vaporization increases, it means that the orthophosphate phosphorus and pH in the lake also increase. This can be attributed to the fact that vaporization enhance the conditions for eutrophication and increase algal productivity due to low lake volume. The increase in algal productivity rates increases water pH, as well.

After the correlation analysis, Principal Component Analysis (PCA) is performed. Principal components obtained from PCA analysis are depicted in Figure 2. Moreover, the variance in the data set explained by each principal component is given in Table 2. According to Table 2, the first component explains 31.768 % of the variance in the examined data set. In the first component, mostly nitrogen species such as NH_4-N, NO_3-N, TKN, and TN are present. pH and average temperature are also included in the first component. The TN: TP ratio indicates which nutrient limits growth in the lakes. If the ratio is less than 10, nitrogen is the limiting nutrient. If it is higher than 17, P is the limiting nutrient. If the ratio is between 10 and 17, this means that both N and P can limit the growth [26]. When TN: TP ratio is calculated based on the mean TN and TP concentrations given in Table 3, it is found as 15.86. This means nitrogen or phosphorus can be limiting nutrients for growth separately or together. Figure 2 confirms this statement because nitrogen locates in the first component and phosphorus in the second component. Both of them are very crucial for the lake's water quality.

The second component includes o-PO_4 and meteorological parameters like precipitation and open surface vaporization. The second principal component explains a 21.21% change in the data set in addition to the first component. The last component explaining 15.54% of the variance is composed of BOD_5, DO, and TSS. The three key components listed in Figure 2 describe 68.52 % of the variance in the examined data set.
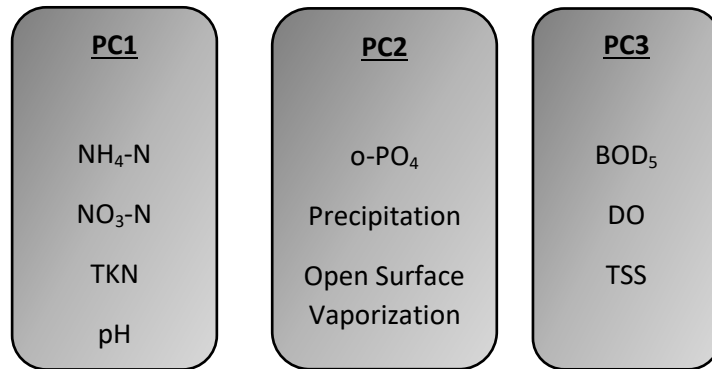

Figure 2. Principal Components

Table2. Total Variance Explained by each principal component

Principal Components	% of Variance	Cumulative %
1	31.768	31.768
2	21.211	52.979
3	15.543	68.522

Following principal component analysis, trend analysis was carried out to examine the changes in water quality of Karacaören-II Dam Lake during the 2005-2014 period. Mann Kendall test is used to determine the trends for TN, TP, DO, BOD_5, pH and TSS. Statistical data of water quality parameters and results obtained from trend analysis are given in Table 3. The H_0 hypothesis in the Mann-Kendall analysis is that there is no trend in the series. If the p-value calculated from the trend analysis is greater than the confidence level alpha value, the H_0 hypothesis is accepted. This indicates no trend in the water quality series in question. If the p-value is less than the alpha value, the trend is present in the water quality series studied [15]. Because the p values of the dissolved oxygen, BOD_5, pH, and total suspended solids parameters are greater than the alpha values, they do not show any trend between the 2005 and 2014 years. Whereas, the total nitrogen and total phosphorus parameters with the p values which are smaller than the alpha value show a positive increasing trend. NO_3-N: NH_4-N ratio is directly related to the TN: TP ratio for lakes [24]. So, the increase of TN and TP in the dam lake may cause the change in the concentrations of NO_3-N and NH_4-N, as well. As a result, lake trophic state can change. Therefore, some measures must be taken to reduce the total nitrogen and total phosphorus loads coming into Karacaören-II Dam Lake to improve the trophic level in the lake and to prevent

possible eutrophication problems in the near future.

Table3. Mann-Kendall trend analysis results for water quality parameters

Parameter	Min	Maximum	Mean	Std. Deviation	p-value	alpha	Trend
TP (mg/L)	0.000	0.205	0.052	0.068	0.032	0.05	↑
TN (mg/L)	0.000	1.430	0.825	0.541	0.008	0.05	↑
DO (mg/L)	7.000	10.650	8.293	1.034	0.242	0.05	-
BOD$_5$ (mg/L)	0.500	9.075	5.108	2.383	0.569	0.05	-
pH	7.663	8.375	8.022	0.223	0.122	0.05	-
TSS (mg/L)	1.500	15.750	5.902	4.542	0.054	0.05	-

4. Conclusions

The results obtained in this study show that the highest positive correlation is observed between nitrate nitrogen and dissolved oxygen. Additionally, the temperature is the most effective meteorological parameter on the lake water quality for the study period. The results of the principal component analysis indicate that nitrogen, phosphorus, pH, temperature, precipitation, and vaporization are the key variables effecting the water quality of the Karacaören-II Dam Lake.

It can be concluded from the study that the TN and TP indicate positive increasing trends at statistical significance. The increasing trends of these parameters can lead to water quality problems in the future, such as not achieving good water status and having high trophic status. Therefore, some precautions including improvements in current wastewater treatment plants discharging into streams flowing into the Dam Lake, modifications in the current irrigation technologies to reduce the loads coming from agricultural lands to the lake can be taken. Changes in the product pattern within agricultural areas located in the watershed of the lake may also contribute to the reduction of the total nitrogen and phosphorus loads reaching to the lake.

Declaration of Ethical Standards

The author of this article declares that the materials and methods used in this study do not require ethical committee permission and/or legal-special permission.

Conflict of Interest

The author declares that they have no known competing financial interests or personal relationships that could have appeared to influence the work reported in this paper.

References

[1] Water Framework Directive, European Union (WFD E.U.). Establishing a Framework for Community Action in the Field of Water Policy; Directive 2000/60/EC of the European Parliament and of the Council of 23 October 2000; EU: Brussels, Belgium, 2000.

[2] Surface Water Quality Regulation in Turkey, 2015. Official Gazette, No. 29327, 30 April Wednesday, Ankara, Turkey.

[3] Ministry of Agriculture and Forestry, General Directorate of Water Management. Yerüstü Su Kütlelerinin İyi Duruma Ulaşabilmesi İçin Sağlanması Gereken Çevresel Hedeflerin Belirlenmesine Yönelik Rehber Doküman. https://www.tarimorman.gov.tr/SYGM/Belgeler/kam ag/Rehber_Doküman_Çevresel_Hedefler.pdf [Last access date: 02.01.2020]

[4] Parinet B., Lhote A., Legube B., 2004. Principal component analysis: an appropriate tool for water quality evaluation and management—application to a tropical lake system, Ecological Modelling, **178** (3–4), pp. 295-311, ISSN 0304-3800, https://doi.org/10.1016/j.ecolmodel.2004.03.007.

[5] Wang J., Yang C., He L., Dao G., Du J., Han Y., Wu G., Wu Q., Hu H., 2019. Meteorological factors and water quality changes of Plateau Lake Dianchi in China (1990–2015) and their joint influences on cyanobacterial blooms, Science of The Total

Environment, **665**, 406-418, ISSN 0048-9697, https://doi.org/10.1016/j.scitotenv.2019.02.010.

[6] Tian L., Zhu X., Wang L., Du P., Peng F., Pang Q., 2020. Long-term trends in water quality and influence of water recharge and climate on the water quality of brackish-water lakes: A case study of Shahu Lake, Journal of Environmental Management, **276**, Article number:111290, ISSN 0301-4797, https://doi.org/10.1016/j.jenvman.2020.111290.

[7] Yenilmez F., Keskin F., Aksoy A., 2011. Water quality trend analysis in Eymir Lake, Ankara, Physics and Chemistry of the Earth, Parts A/B/C, **36** (5–6), 135-140, ISSN 1474-7065, https://doi.org/10.1016/j.pce.2010.05.005.

[8] Kır İ. ve Tumantozlu H., 2012. Karacaören-II Baraj Gölü'ndeki Su, Sediment ve Sazan (Cyprinus carpio) Örneklerinde Bazı Ağır Metal Birikiminin İncelenmesi. Ekoloji, **21** (82), 65-70.

[9] Ardıç C., 2013. Human Health Risk Identification of Nitrate Concentration in Drinking Water, M.S. Thesis, Hacettepe University, Department of Environmental Engineering, Ankara.

[10] Apaydın G., Köksal O. K., Cengiz E., Tıraşoğlu E., Baltas H., Karabulut K., Söğüt Ö., 2019. Assessment of natural radioactivity and radiological risk of sediment samples in Karacaören II dam Lake, Isparta/Turkey, ALKÜ Fen Bilimleri Dergisi, Özel Sayı (NSP 2018), 28-35.

[11] TÜBİTAK MAM, 2013. Karacaören I & II Baraj Gölleri Havza Koruma Planı ve Özel Hüküm Belirleme Projesi. Türkiye Bilimsel ve Teknolojik Araştırma Kurumu Marmara Araştırma Merkezi, Çevre ve Temiz Üretim Enstitüsü, Kocaeli.

[12] Çevre ve Şehircilik Bakanlığı, 2012. Isparta İl Çevre Durum Raporu 2012, Isparta Valiliği Çevre ve Şehircilik İl Müdürlüğü, Isparta.

[13] Tumantozlu, H., 2010. Investigation of some heavy metal accumulation in water, sediment and carp (cyprinus carpio) samples of karacaoren-II dam lake. Master Thesis, Süleyman Demirel University, Department of Biology, Isparta, Turkey.

[14] Wang C.N., Le T.M., Nguyen H.K., Ngoc-Nguyen H., 2019. Using the Optimization Algorithm to Evaluate the Energetic Industry: A Case Study in Thailand. Processes, **7**(2), 87.

[15] Ouyang, Y., 2005, Evaluation of river water quality monitoring stations by principal component analysis, Water Research, **39** (12), pp. 2621-2635, ISSN 0043-1354, https://doi.org/10.1016/j.watres.2005.04.024.

[16] Alemu Z.A., Dioha M.O., 2020. Climate change and trend analysis of temperature: the case of Addis Ababa, Ethiopia. Environ Syst Res, **9** (27), https://doi.org/10.1186/s40068-020-00190-5.

[17] Hirsch R. M., Slack J.R., 1984. A nonparametric trend test for seasonal data with serial dependence. Water Resources Research, **2**(6): 727-732.

[18] Yue S., Pilon P., Cavadias G., 2002. Power of the Mann-Kendall and Spearman's Rho Tests for Detecting Monotonic Trends in Hydrological Series, Journal of Hydrology, **259**, pp.254-271.

[19] Zhang X., Harvey K.D., Hogg W.D., Yuzyk T.R., 2001. Trends in Canadian Streamflow, Water Resources Research, **37** (4), pp. 987-998.

[20] Wang F., Shao W., Yu H., Kan G., He X., Zhang D., Ren M., Wang G., 2020. Re-evaluation of the Power of the Mann-Kendall Test for Detecting Monotonic Trends in Hydrometeorological Time Series, Front. Earth Sci., **8** (14), doi: 10.3389/feart.2020.00014.

[21] Rocha RRA., Thomaz SM., Carvalho P., Gomes LC, 2009. Modeling chlorophyll-a and dissolved oxygen concentration in tropical floodplain lakes (Paraná River, Brazil), Braz. J. Biol., **69** (2, Suppl.), pp. 491-500.

[22] Wetzel RG., 2001. Limnology: lake and river ecosystems, San Diego: Academic Press., 1006p.

[23] Maitera O. N., Ogugbuaja V. O., Barminas J.T., 2010. An assessment of the organic pollution indicator levels of River Benue in Adamawa State, Nigeria, Journal of Environmental Chemistry and Ecotoxicology **2** (7), pp. 110-116. ISSN-2141-226X

[24] Quirós R., 2003. The relationship between nitrate and ammonia concentrations in the pelagic zone of lakes, Limnetica **22** (1-2), pp. 37-50, ISSN: 0213-8409. DOI: 10.23818/limn.22.03

[25] Singh S. P., Singh P., 2015. Effect of temperature and light on the growth of algae species: A review, Renewable and Sustainable Energy Reviews, **50**, pp.431–444. https://doi.org/10.1016/j.rser.2015.05.024

[26] OECD, 1982. Eutrophication of Waters-Monitoring, Assessment and Control, Paris: Organisation for Economic Co-Operation and Development.

Kocaeli University

Kocaeli Journal of Science and Engineering
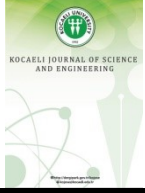
Classification of Tympanic Membrane Images based on VGG16 Model

Abidin ÇALIŞKAN [1, *]   iD

[1] *Department of Computer Engineering, Batman University, Batman, 72100, Turkey,* **ORCID:** *0000-0001-5039-6400*

Abstract

Otitis Media (OM) is a type of infectious disease caused by viruses and/or bacteria in the middle ear cavity. In the current study, it is aimed to detect the eardrum region in middle ear images for diagnosing OM disease by using artificial intelligence methods. The Convolution Neural Networks (CNN) model and the deep features of this model and the images obtained with the otoscope device were used. In order to separate these images as Normal and Abnormal, the end-to-end VGG16 model was directly used in the first stage of the experimental work. In the second stage of the experimental study, the activation maps of the fc6 and fc7 layers consisting of 4096 features and the fc8 layer consisting of 1000 features of the VGG16 CNN model were obtained. Then, it was given as input to Support Vector Machines (SVM). Then, the deep features obtained from all activation maps were combined and a new feature set was obtained. In the last stage, this feature set is given as an input to SVM. Thus, the effect of the VGG16 model and the features obtained from the layers of this model on the success of distinguishing images of the eardrum was investigated. Experimental studies show that, the best performance results were obtained for the fc6 layer with an accuracy rate of 82.17%. In addition, 71.43%, 90.62% and 77.92% performance criteria were obtained for sensitivity, specificity and f-score values, respectively. Consequently, it has been shown that OM disease could be accurately detected by using a deep CNN architecture. The proposed deep learning-based classification system promises highly accurate results for disease detection.

1. Introduction

The ear is an anatomical structure which exhibits the function of hearing and contains the balance organ. Sound waves pass through the outer ear and hit the eardrum and make it vibrate. When the sound reaches the middle ear, it is amplified by the ossicles in the middle ear and transmitted to the inner ear. Sound waves coming to the inner ear are also received by all the cells situated here and transmitted to the auditory nerve. Then, it is transferred to the auditory center in the brain via the auditory nerve. The overall structure of the ear is given in Figure 1 [1].

Symptoms of ear diseases and causes of ear diseases can be observed in different ways depending on the condition of the person. Ear diseases can occur due to seasonal reasons, infection or exposure to excessively loud noise [2]. One of the most common diseases among ear diseases is OM whishes an infectious disease caused by

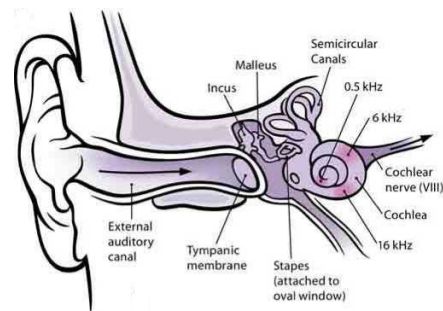viruses or bacteria in the middle ear cavity [3].

Figure 1. Ear internal structure [1].

The middle ear cavity is the inner part of the eardrum and contains the ear ossicles, which are filled with air. It can be classified as acute, subacute or chronic in accordance with the duration of the infection. Generally, middle ear infections lasting less than three weeks are called acute OM and middle ear infections lasting longer than 3 months are called chronic OM [4].

In the literature, Active Contour Segmentation has

---

* Corresponding Author: abidin.caliskan@batman.edu.tr

been used to detect the membrane region from middle ear images for the diagnosis of OM. After the membrane region was determined, the feature set was obtained by textural feature extraction algorithms. In addition, the images were classified using the AdaBoost method by adding Gabor features [5]. A portable video otoscopy platform is presented for better visual analysis of the images obtained with the video otoscope device [6]. By targeting and desiring the different regions of the eardrum of the clinical importance, the ossicles and the lesion area in the middle ear were clearly visualized by the linear Unsharp algorithm and low-pass filtering. Hierarchical tree diagram method was used for classification, by using average color value. Canny edge detection algorithm is imployed to in order to monitor the presence of bubbles in the image. An accuracy rate of 84% was obtained by this classification [7]. A new automatic algorithm with a classification success of 89.9% [8] has been proposed to recognize OM under three categories as normal, acute otitis media (AOM) and otitis media effusion (OME). The feature set obtained by subtracting the textural feature extraction algorithm and the average values of the color channels of the common ear images was determined by Başaran [9]. In this study, classification was made with the artificial neural network method with an accuracy rate of 76.14%. A classification model based on the usefulness and performance of a two-stage CNN has been developed for automatic diagnosis of OM from Tympanic Membrane (TM) images [10]. Based on the Class Activation Map, an accuracy of 93.4% was achieved using a two-stage classification model and a three-fold cross-validation network in order to improve accuracy and reliability and also to read TM images. Consequently, literature studies show that CNN has shown great success in the classification of diseases with biomedical images in recent years [11, 12].

In this study, the VGG16 CNN model, which has been proven to be successful in the literature, was used to distinguish OM images [13, 14].

Since different information about images is learned with each layer in CNN architectures, in this study, the success of the learning layers of the VGG16 model in distinguishing OM images was examined. In addition, normal and abnormal TM images were distinguished by combining the OM images and the features obtained with the learning layers.

2. Materials and Methods

Images have been resized in the proposed model to classify normal and abnormal images. After the activation maps of the layers were obtained, they were applied as an input to the SVM classifier model. The feature set obtained is given as an input to the SVM. Thus, the effect of the CNN model and the features obtained from the layers of this model to distinguish images was examined. In order to obtain the most effective results with CNN, tests were carried out with different parameter values. The block diagram of the proposed model is given in Figure 2.
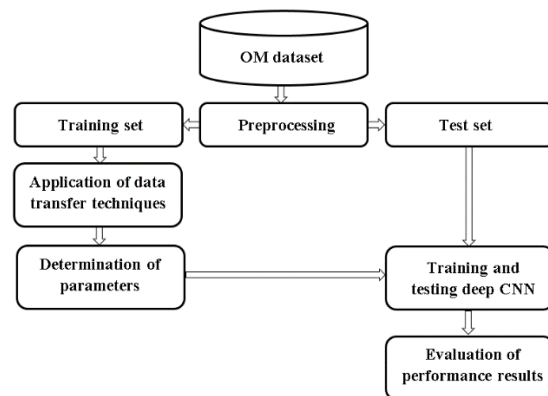

Figure 2. Block diagram of the proposed model.

2.1. Data Set

The data set consists of total 956 middle ear images which were obtained by otoscope device from volunteer patients who were examined in Van Akdamar Hospital in Turkey. The dataset includes 535 images belonging to the normal class and 421 images belonging to the abnormal class. Abnormal images include diseases such as "AOM, CSOM, Earwax, Otitis externa, Tympanoskleros, Ear ventilation tube, Pseudo-membranes, Foreign bodies in the ear" [15]. The number of images in the data set are given in Table 1 and the images of these classes are given in Figure 3.

Table 1. Total number of images in the dataset.

Class	Number of images
Normal	**535**
Abnormal	**421**
AOM	119
CSOM	63
Earwax	140
Otitis externa	41
Tympanoskleros	28
Ear ventilation tube	16
Pseudo-membranes	11
Foreign bodies in the ear	3

Normal images

Abnormal images

AOM   **CSOM**

Earwax   **Otitis externa**

Tympanoskleros   **Ear ventilation tube**

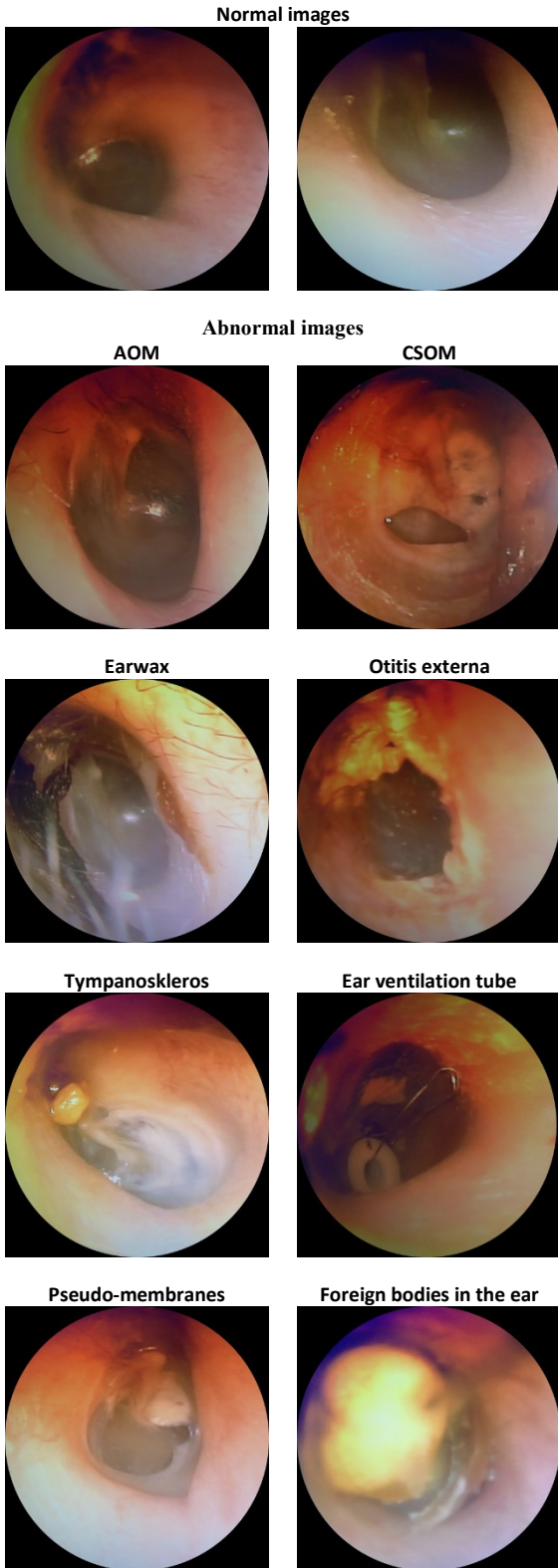**Pseudo-membranes**   **Foreign bodies in the ear**

Figure 3. Normal and abnormal Tympanic Membrane images.

2.2. Convolution Neural Networks

CNN is a feed-forward artificial neural network [16], which is a type of multi-layer perceptron. Each layer in the CNN architecture has different tasks. They work in three

dimensions in terms of depth, height and width. The CNN architecture performs well in many areas such as disease diagnosis, classification and segmentation in medical images [17, 18]. The architecture of an example VGG16 CNN model consisting of five convolutional layers and the fc6, fc7, fc8 and softmax layers are presented in Figure 4 [19, 20].
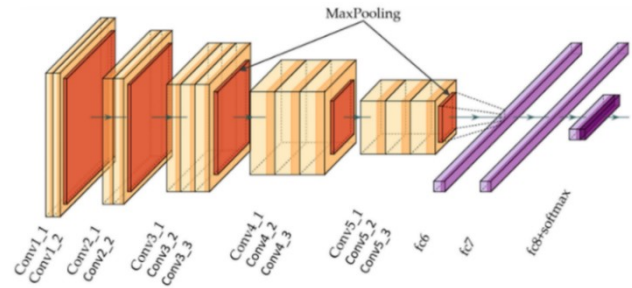

Figure 4. The architecture of the VGG-16 model.

Raw data is taken at the beginning of the CNN model and classification processes are performed after obtaining the layers and feature map. A typical CNN model includes input layer, convolution layer, pooling, fully connected layer and output layer. A feature map is obtained by scanning the image from left to right and top to bottom with the filters that are used to obtain the feature map in the convolution layer.

The first layers learn the edge and color information through the convolution layers of CNN and the kernels within the remaining layers learn the information about the image details [21]. The mathematical expression of the convolution is given in Eq. (1) [13].

$$(f * h)[m, n] = \sum_j \sum_k h[j, k], f(m - j, n - k) \tag{1}$$

Where *f* is the input image, *h* is the filter, *m* and *n* are the row and column indexes of the output matrix, respectively. *j* and *k* represent the location information of the filter.

The VGG16 network model, a CNN trained on more than one million images, was retrieved from the ImageNet database [22]. This model includes layers with learning weights, followed by layers with ReLu and pooling layers. Learnable layers consist of convolutional layers and fully-connected layers. Activations fc6 and fc7 in layers are used to extract feature vectors [23].

2.3. Support Vector Machines

SVM is designed to classify two-class linear data. Later on, it has been generalized to classify more classes and nonlinear data [24]. SVM tries to minimize the upper

bound of the error with the hyperplane. It is also a classification algorithm that maximizes the boundary separation between training data [25]. Unlike other machine learning methods, the performance of SVM, having a strong learning and generalization ability, is quite better [26]. The purpose of SVM is to find the plane with the largest distance between the two planes expressed in Eq. (2) [27].

$$\begin{cases} w.x_i + b = -1 \\ w.x_i + b = +1 \end{cases} \quad (2)$$

2.4. Performance Metrics

In this study, confusion matrix was used to test the performance of experimental studies. There are four different Performance Metrics in the Confusion matrix where actual and predicted records are kept to calculate various metrics. Here, True positive (TP) and True negative (TN) denote the number of correctly identified positive and negative records. False positive (FP) and False negative (FN) represent the number of records belonging to incorrectly predicted positive and negative classes [2]. Accordingly, the accuracy, sensitivity, specificity and F-Score metrics derived from the error matrix are calculated as shown in Eq. (3)-(6) [13].

$$Accuracy = \frac{TP + TN}{TP + TN + FP + FN} \quad (3)$$

$$Sensitivity = \frac{TP}{TP + FN} \quad (4)$$

$$Specificity = \frac{TN}{TN + FP} \quad (5)$$

$$F-Score = \frac{2*TP}{2*TP + FP + FN} \quad (6)$$

In addition to the performance criteria, the Receive Characteristic Curve (ROC) was used to measure the success of the model. The ROC curve is one of the most important evaluation criteria to control the performance of the classification model. A typical ROC curve has the FP rate on the x-axis and the TP rate on the y-axis. Area Under the Curve (AUC) can be considered as a summary of model performance. The size of the AUC area indicates the success of the machine learning model in distinguishing the classes. The ideal value for AUC is 1 [25].

3. Results and Discussion

In the first stage of the experimental study, the images obtained with the otoscope device via the VGG16 CNN model and the deep features of this model were directly used from the end-to-end VGG16 model in order to separate the images as normal and abnormal. In order to optimize the network, the number of data to be trained per iteration (mini-batch size) is set to 32, and the maximum epoch value (max-epoch) to train the entire dataset is 32. The initial learning rate value was $1x10^{-4}$ and the stochastic gradient descent was used as optimization. As a result of the experimental study, an accuracy rate of 78.67% was obtained, while the sensitivity, specificity and f-score values of the model were measured as 79.37%, 78.12% and 76.63%, respectively. In the second stage of the experimental study, the activation maps of the fc6 and fc7 layers consisting of 4096 features and the fc8 layer consisting of 1000 features of the VGG16 CNN model were obtained. Then, the activation maps were given as an input to SVM. After that, deep features from all activation maps were combined and a new feature set was obtained. Finally, this feature set was then given as an input to the SVM and the effect of the features obtained from the VGG16 model and its layers on the success of distinguishing the images of the eardrum was examined. As a result of the experimental study, the best performance results were obtained for the fc6 layer. An accuracy rate of 82.17% was obtained with the fc6 layer. In addition, 71.43%, 90.62% and 77.92% performance criteria were obtained for sensitivity, specificity and f-score values, respectively. The confusion matrix and ROC curve of the fc6 layer, which the best results are obtain illustrated in Figure 5 and Figure 6, respectively.

Normal	100	26
Abnormal	35	125
	Normal	Abnormal

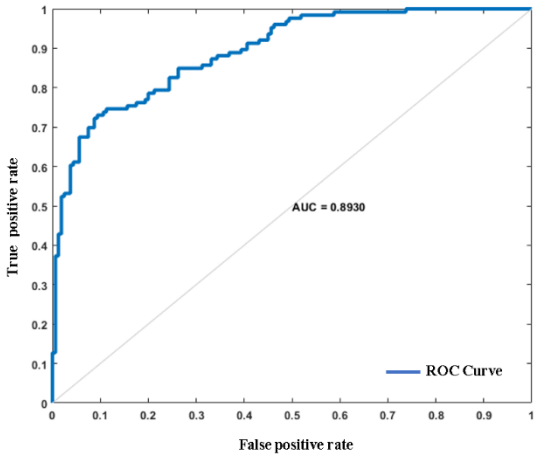**Figure 5.** The confusion matrix obtained with the VGG16 model.

Figure 6. ROC curve obtained with the VGG16 model.

The confusion matrix of the classification of deep features of the fc6 layer by SVM is given in Figure 7. The ROC curve is given in Figure 8.

Normal	90	36
Abnormal	15	145
	Normal	Abnormal

Figure 7. The complexity matrix of the classification of deep features of the fc6 layer by SVM.
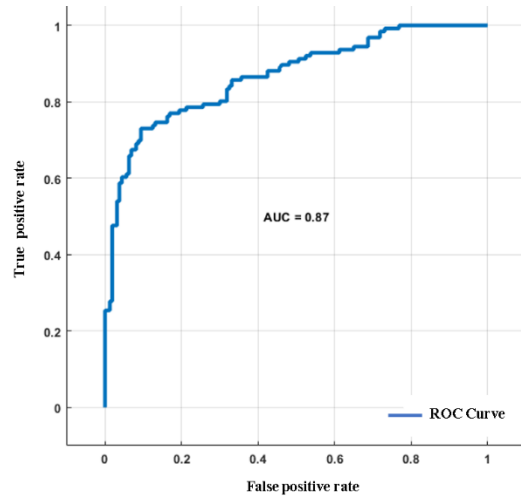

Figure 8. ROC curve of the classification of deep features of the fc6 layer by SVM.

The performance criteria obtained as a result of the classification of fc6, fc7, fc8 and the feature sets created by combining these layers with SVM are given in Table 2. In addition, the accuracy rates directly obtained with the VGG16 model and layers as a result of experimental studies are given in Figure 9.

Table 2. Classification results of the feature layers of the VGG16 model based on SVM.

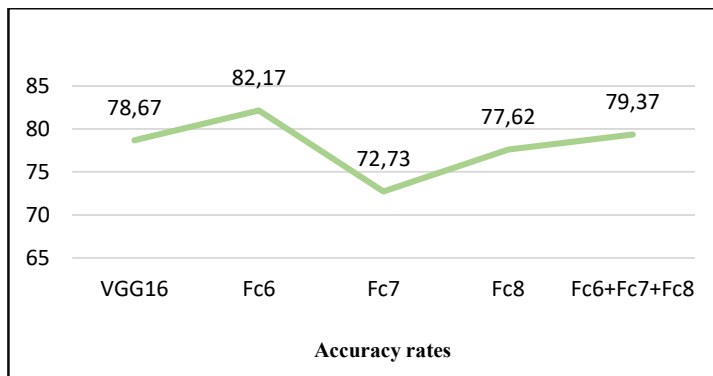| Layer	Number of Features	Accuracy (%)	Sensitivity (%)	Specificity (%)	F-Score (%)
fc6	**4096**	**82.17**	**71.43**	**90.62**	**77.92**
fc7	4096	72.73	65.08	78.75	67.77
fc8	1000	77.62	70.63	76.72	73.55
fc6+fc7+fc8	9192	79.37	73.02	84.38	75.72

Figure 9. Accuracy rates obtained with VGG16 and layers.

4. Conclusion

Accurate diagnosis of OM, which causes hearing loss, is extremely important for the correct treatment of the disease. In this study, the VGG16 model and its deep features were used to separate the images as normal and abnormal obtained by the otoscope device. Activation maps of fc6, fc7 and fc8 layers, which are the deep features of the VGG16 model, were obtained and given as an input to the SVM. A new feature set was derived by combining the deep features acquired from all activation maps. Then, as an input to the SVM, the success of the VGG16 model and the features obtained from the layers of this model in distinguishing the eardrum images was examined. The experimental study shows that the best performance results were obtained with the fc6 layer as 82.17%. In addition, 71.43%, 90.62% and 77.92% performance criteria were obtained for sensitivity, specificity and f-score values, respectively. In conclusion, a high-accuracy diagnostic model has been developed to help diagnose OM disease from the normal and abnormal images captured by the otoscope device.

Future studies may be conducted on different deep CNN architectures and to develop models that can give higher performance outputs.

Conflict of Interest

No conflict of interest was stated by the author.

Acknowledgements

Declaration of Ethical Standards

The author of this article declare that the materials and methods used in this study do not require ethical committee permission and/or legal-special permission.

References

[1] Chittka L., Brockmann, A., 2005. Perception space the final frontier. PLoS biology, **3**(4), pp. 564-568.

[2] Wu Z., Lin Z., Li L., Pan H., Chen G., Fu Y., Qiu Q., 2021. Deep learning for classification of pediatric otitis media. The Laryngoscope, **131**(7), E2344-E2351.

[3] Cetinkaya E. A., Topsakal V., 2022. Acute Otitis Media. In Pediatric ENT Infections, Springer, Cham, pp. 381-392.

[4] Manju K., Paramasivam M. E., Nagarjun S., Mokesh A., Abishek A., Meialagan, K., 2022. Deep Learning Algorithm for Identification of Ear Disease. In Proceedings of International Conference on Data Science and Applications, Springer, Singapore, pp. 491-502.

[5] Shie C. K., Chang H. T., Fan F. C., Chen C. J., Fang T. Y., Wang P. C., 2014. A hybrid feature-based segmentation and classification system for the computer aided self-diagnosis of otitis media. In 2014 36th Annual International Conference of the IEEE Engineering in Medicine and Biology Society, IEEE, pp. 4655-4658.

[6] Cheng L., Liu J., Roehm C. E., Valdez T. A., 2011. Enhanced video images for tympanic membrane characterization. In 2011 Annual International Conference of the IEEE Engineering in Medicine and Biology Society, IEEE, pp. 4002-4005.

[7] Kuruvilla A., Li J., Yeomans P. H., Quelhas P., Shaikh N., Hoberman A., Kovačević J., 2012. Otitis media vocabulary and grammar. In 2012 19th IEEE International Conference on Image Processing, IEEE, pp. 2845-2848.

[8] Kuruvilla A., Shaikh N., Hoberman A., Kovačević J., 2013. Automated diagnosis of otitis media: vocabulary and grammar. International Journal of Biomedical Imaging.

[9] Başaran E., Şengür A., Cömert Z., Budak Ü., Çelik Y., Velappan S., 2019. Normal and acute tympanic membrane diagnosis based on gray level co-occurrence matrix and artificial neural networks. In 2019 international artificial intelligence and data processing symposium (IDAP), IEEE, pp. 1-6.

[10] Cai Y., Yu J. G., Chen Y., Liu C., Xiao L., Grais E. M., Zhao F., Lan L., Zeng S., Zeng J., Wu M., Su Y., Li Y., Zheng Y., 2021. Investigating the use of a two-stage attention-aware convolutional neural network for the automated diagnosis of otitis media from tympanic membrane images: a prediction model development and validation study. BMJ open, **11**(1), e041139.

[11] Albashish, D., Al-Sayyed, R., Abdullah, A., Ryalat, M. H., Almansour, N. A., 2021. Deep CNN model based on VGG16 for breast cancer classification. In 2021 International Conference on Information Technology (ICIT), IEEE, pp. 805-810.

[12] Tripathi, S., Verma, A., Sharma, N., 2021. Automatic segmentation of brain tumour in MR images using an enhanced deep learning approach. Computer Methods in Biomechanics and Biomedical Engineering: Imaging & Visualization, **9**(2), pp. 121-130.

[13] Başaran E., Cömert Z., Çelik Y., 2020. Convolutional neural network approach for automatic tympanic membrane detection and classification. Biomedical Signal Processing and Control, **56**, 101734.

[14] Rehman, A., Naz, S., Razzak, M. I., Akram, F., Imran, M., 2020. A deep learning-based framework for automatic brain tumors classification using transfer learning. Circuits, Systems, and Signal Processing, **39**(2), pp. 757-775.

[15] Zafer C., 2020. Fusing fine-tuned deep features for recognizing different tympanic membranes. Biocybernetics and Biomedical Engineering, **40**(1), pp. 40-51.

[16] Hiremani V. A., Senapati K. K., 2021. Quantifying apt of RNN and CNN in Image Classification. In Proceeding of Fifth International Conference on Microelectronics, Computing and Communication Systems, Springer, Singapore, pp. 721-733.

[17] Singh S. P., Wang L., Gupta S., Goli H., Padmanabhan P., Gulyás B., 2020. 3D deep learning on medical images: a review. Sensors, **20**(18), 5097.

[18] Li Y., Sixou B., Peyrin F., 2021. A review of the deep learning methods for medical images super resolution problems, IRBM, **42**(2), pp. 120-133.

[19] Kattenborn T., Leitloff J., Schiefer F., Hinz S., 2021. Review on Convolutional Neural Networks (CNN) in vegetation remote sensing. ISPRS Journal of Photogrammetry and Remote Sensing, **173**, pp. 24-49.

[20] Lee J. Y., Choi S. H., Chung J. W., 2019. Automated classification of the tympanic membrane using a convolutional neural network, Applied Sciences, **9**(9), 1827.

[21] Tripathi, M., 2021. Analysis of convolutional neural network based image classification techniques. Journal of Innovative Image Processing (JIIP), **3**(02), pp. 100-117.

[22] Dhillon A., Verma G. K., 2020. Convolutional neural network: a review of models, methodologies and applications to object detection. Progress in Artificial Intelligence, **9**(2), pp. 85-112.

[23] Yao G., Lei T., Zhong J., 2019. A review of convolutional-neural-network-based action recognition. Pattern Recognition Letters, **118**, pp. 14-22.

[24] Nalepa J., Kawulok M., 2019. Selecting training sets for support vector machines: a review. Artificial Intelligence Review, **52**(2), pp. 857-900.

[25] Uçar M., Akyol K., Atila Ü., Uçar E., 2021. Classification of different tympanic membrane conditions using fused deep hypercolumn features and bidirectional LSTM. IRBM.

[26] Wang Z., Cha Y. J., 2021. Unsupervised deep learning approach using a deep auto-encoder with a one-class support vector machine to detect damage. Structural Health Monitoring, **20**(1), pp. 406-425.

[27] Alhudhaif A., Cömert Z., Polat K., 2021. Otitis media detection using tympanic membrane images with a novel multi-class machine learning algorithm. PeerJ Computer Science, **7**, e405.